

70-18,340

SISKA, Peter Emil, 1943-
KINEMATICS AND DYNAMICS OF REACTIVE COLLISIONS.

Harvard University, Ph.D., 1970
Chemistry, physical

University Microfilms, A XEROX Company, Ann Arbor, Michigan

THIS DISSERTATION HAS BEEN MICROFILMED EXACTLY AS RECEIVED

KINEMATICS AND DYNAMICS OF REACTIVE COLLISIONS

A thesis presented

by

Peter Emil Siska

to

The Department of Chemistry

in partial fulfillment of the requirements

for the degree of

Doctor of Philosophy

in the subject of

Chemistry

Harvard University

Cambridge, Massachusetts

November, 1969

PLEASE NOTE:

**Not original copy. Several pages
have indistinct print. Filmed as
received.**

University Microfilms.

KINEMATICS AND DYNAMICS OF REACTIVE COLLISIONS

A Summary

Research Director

Peter Emil Siska

Professor D. R. Herschbach

November, 1969

Crossed molecular beam experiments with velocity analysis of the alkali chloride products from the reactions of K, Rb and Cs with CCl_4 are described. New methods of kinematic analysis applied to the data reveal a strong coupling between the center-of-mass (c.m.) angular distributions of the products and the speed with which they recoil away from the c.m., in contrast to what has been found for other alkali atom reactions with halogen-containing molecules. The new kinematic methods are developed in detail, and are applied to several other reactions for which product velocity spectra have been measured.

Angular distribution measurements on the alkali atom products from the reactions of hydrogen and deuterium atoms with alkali halide molecules are reported. Pronounced anisotropies and chemical trends are brought out by a kinematic analysis, and dynamical arguments based on the small mass and fast motion of the H atom relative to the heavy-atom reactant diatomic are used as evidence that molecular orientation effects may play a role in producing these features. This speculation is supported by potential energy surface calculations based on a one-electron pseudopotential model for the entrance channel of these reactions, which show pronounced wells (stable regions) for a triangular configuration of the atoms and more or less repulsive interactions for other geometries. Quantitative calculations utilizing the special mechanical features of these systems together with an assumed orientational preference for reaction are able to fit the observed product distributions for values of the orientation parameter which correlate well with the potential surfaces. These results indicate that a concerted electron transfer in a definite preferred geometrical configuration may govern these reactions.

ACKNOWLEDGEMENTS

Professor Dudley Herschbach has been a continuing source of insight and inspiration throughout the course of this research. Without his chemical intuition and unfailing enthusiasm none of this work would have been possible. It has been a privilege and a pleasure to work with him.

Sincere thanks go to my good friend and colleague Steve Riley, with whom I collaborated in the work on the CCl_4 reactions and in much of the development of the new kinematic analysis methods. His know-how and good humor were essential to the success of these efforts.

I am grateful to Yuan Lee and George Fisk for many experimental pointers and suggestions which were invaluable in studying the hydrogen atom-salt reactions, to Walt Miller and Sanford Safron for enlightening discussions on the production of salt beams, and to Bill Stwalley and Arendt Niehaus, who provided my introduction to "Faith". A special word of thanks is due to Professor Doug Carlson for his assistance during most of these latter experiments.

Many other members of the Herschbach group, past and present, have contributed in some way to this thesis. Outside the group, I am particularly indebted to Eugene Switkes for information which aided in the calculations of Chapter VI, and to Gabriel Balint-Kurti for making available some of his results in advance of publication.

Also invaluable to the completion of this work were the friendly services of the machine, electronics and glass shop personnel, the high-quality drafting and photography by Joan Sheahan and Dave Lang, and the excellent and rapid typing of Gwen Diggs.

The support of the National Science Foundation for four years and

of the Emerson fund at Harvard for one semester is gratefully acknowledged.

Finally, my deepest gratitude and appreciation go to my wife Jeanne, who would provide a bright moment to an often discouraging day, and whose patience in listening to my problems of itself often led me to their solutions.

TABLE OF CONTENTS

Chapter	Page
I. Introduction	I-1
II. Coupling of Product Angle and Energy Distribution in Reactions of Alkali Atoms with Carbon Tetrachloride	II-1
A. Introduction	II-2
B. Experimental Conditions	II-4
C. Results and Kinematic Analysis	II-7
Method A: Nominal Transformation	II-11
Method B: Least Squares Fit	II-12
D. Discussion	II-20
Rainbow Analysis	II-22
Elastic Spectator Model	II-29
E. Conclusion	II-35
III. Kinematic Analysis of Reactive Scattering	III-1
A. Introduction	III-2
B. Notation and Coordinate Transformation	III-3
C. Intensity Transformation	III-7
D. Methods of Analysis: Nominal and Stochastic	III-9
E. Methods of Analysis: Least Squares Fit	III-12
F. Computational Details	III-22
G. Analysis of Primitive Experiments	III-24
H. Discussion	III-31
Appendix: Computer Programs for Kinematic Analysis	III-34

Chapter	Page
IV. Kinematic Analysis: Applications	IV-1
A. Introduction	IV-2
B. Data Analysis and Discussion	IV-4
C. Details and Comments	IV-16
D. Conclusion	IV-19
V. A Molecular Beam Study of the Reactions of Hydrogen and Deuterium Atoms with Alkali Halides	V-1
A. Introduction	V-3
B. Experimental Conditions	V-7
C. Elastic Scattering	V-16
D. Reactive Scattering	V-22
E. Total Reaction Cross Sections	V-38
F. Discussion	V-40
G. Comparison with M + HX Reactions	V-46
H. Correlation with Electronic Structure	V-52
Appendix: Elastic Scattering Transformation	V-54
VI. One-electron Potential Energy Surfaces for the Reactions of Hydrogen Atoms with Alkali Halides	VI-1
A. Introduction	VI-2
B. Pseudopotential Formulation	VI-5
C. Evaluation of Integrals	VI-8
D. Pairwise Core Interactions	VI-10
E. Three-Center Polarization	VI-21
F. Summary of Empirical Parameters	VI-24
G. Calculations on MH ⁺ Molecule Ions	VI-24
H. Results and Discussion	VI-29
Appendix: Computational Details	VI-37

Chapter	Page
VII. Impulsive Model for Hydrogen Atom Reaction Dynamics	VII-1
A. Introduction	VII-2
B. Kinematic Formulation	VII-5
C. Comparison with Experimental Data on H + MX	VII-15
D. Discussion	VII-16
Appendix: H Atom Impulsive Model Calculation	VII-21
General Appendix: Possible Observability of KHBr	A-1

CHAPTER I
INTRODUCTION

The study of chemical reactions in crossed molecular beams has opened up unprecedented possibilities for interpretation in terms of molecular dynamics and correlation with the electronic structures of the reactants and products.¹ With the beam method one can study the outcomes of single collisions, and is thus enabled to look at the so-called "elementary processes" of classical chemical kinetics.² For more than a decade the technique had been limited almost exclusively to reactions involving alkali atoms and/or their compounds because of ease of detection,¹ but due to recent technological improvements in mass spectrometric detection the chemical scope of scattering experiments has been greatly enlarged³ and the focus of this field is now rapidly moving "beyond the Alkali Age".

The experimental work of this thesis still belongs to the "Alkali Age", but may in some respects represent a bridge between the old and new eras. The results presented in Chapter II are a refinement of earlier experiments⁴ on the reactions of alkali atoms with CCl_4 , which had indicated that these systems were of particular interest because the product angular distribution peaked sideways with respect to the initial relative velocity vector (rather than backwards

-
1. For recent reviews, see (a) D. R. Herschbach, *Advan. Chem. Phys.* 10, 319 (1966); (b) E. F. Greene and J. Ross, *Science* 159, 587 (1968); (c) J. P. Toennies, in "Chemische Elementarprozesse", H. Hartmann, Ed. (Springer-Verlag, Heidelberg, 1968), p. 157.
 2. An up-to-date reference is H. S. Johnston, "Gas Phase Reaction Rate Theory" (Ronald Press, New York, 1966).
 3. See for example, Y. T. Lee, P. R. LeBreton, J. D. McDonald and D. R. Herschbach, *J. Chem. Phys.* 49, 2447 (1968), 51, 455 (1969) on halogen atom-molecule exchange reactions.
 4. K. R. Wilson and D. R. Herschbach, *J. Chem. Phys.* 49, 2676 (1968).

or forwards as in the other reactions that had been studied). In collaboration with S. J. Riley, we measured the velocity spectrum of the scattered MCl produced in reactions of CCl_4 with M = K, Rb, and Cs. These more detailed data revealed a well-defined structure in the form of the differential reactive scattering cross sections of a kind which had previously been observed in only one other chemical scattering study, a theoretical calculation for the $\text{H} + \text{H}_2$ reaction.⁵ The position of the peak of the product angular distribution, θ_p (in the center-of-mass system), was found to vary strongly with the relative translational energy of the products, E' . For a given reaction, θ_p shifted from wide angles to forward angles as E' increased and for $\text{K} \rightarrow \text{Rb} \rightarrow \text{Cs}$ the whole pattern shifted towards the forward hemisphere. At least qualitatively, we find these results for M + CCl_4 and also the calculated pattern for $\text{H} + \text{H}_2$ can be correlated with a phenomenological model which resembles the rainbow effect familiar in elastic scattering.

The strong coupling between product emission angle and energy found in the CCl_4 study, besides bringing out the kinship with $\text{H} + \text{H}_2$, led to another bridge to the new era since it required the development of more general methods for transforming the experimental scattered intensities measured in the laboratory coordinate system into a differential cross section for reactive scattering in the center-of-mass coordinate system. The kinematic transformations and numerical

5. M. Karplus and K. T. Tang, Disc. Faraday Soc. 44, 56 (1967).

techniques, much of which were again developed in collaboration with S. J. Riley, are described in Chapter III. Applications to several prototype alkali reactions for which detailed experimental information is available are given in Chapter IV.

The final three chapters present a study of a new family of reactions,



As this involves conversion of the ionic bond of an alkali halide (MX) to the dominantly covalent bond of a hydrogen halide (HX), these reactions represent the reverse of the much-discussed "electron-jump" mechanism for alkali atom reactions. Also, there is an opportunity for revealing comparisons with results for two other families of hydrogen atom reactions currently being studied in this laboratory, reactions with alkali dimer molecules (M_2)⁶ and with diatomic halogens (X_2 or XY).⁷ Angular distribution measurements for reactions of H and D with five alkali halides and a kinematic analysis of the data are presented in Chapter V. The principal finding is that the product angular distributions are decidedly anisotropic, with the emitted M atoms preferring the backward hemisphere ($\theta > 90^\circ$) with respect to the incoming H or D atoms. The preferred direction varies from near 180°

6. Y. T. Lee, R. J. Gordon, and D. R. Herschbach, *J. Chem. Phys.* (to be published).

7. J. D. McDonald, P. R. LeBreton, Y. T. Lee, and D. R. Herschbach, *J. Chem. Phys.* (to be published).

to almost 90° as $X = Br \rightarrow Cl \rightarrow F$. Dynamical arguments (based on the rapid motion of H compared with M or X atoms) suggest that a preferred molecular orientation plays an important role in producing the anisotropy.

On the reactant side, the $H + MX$ systems have an appealingly simple electronic structure, since H possesses only one electron and MX can be accurately represented by a polarizable ion-pair model,⁸ corresponding to M^+X^- , a "no-electron" bond. In Chapter VI we present potential energy surfaces calculated from a one-electron pseudopotential treatment for the entrance channel of the reactions of H with KF, KC_l, and KBr. The treatment is patterned after that of Roach and Child for the K + NaCl system.⁹ The significant features of these surfaces are distinct wells (stable regions) for triangular configurations and more or less repulsive interactions for linear H-X-K configurations. The wells shift in position as the halogen atom is varied in a way which can be qualitatively correlated with the experimental data, as interpreted in the light of the dynamical constraints alluded to above.

Finally, in Chapter VII, the qualitative features of light atom-heavy molecule reaction mechanics are formulated in a dynamic model which makes use of the motions of the reactant atoms, the nature of

8. E. S. Rittner, J. Chem. Phys. 19, 1030 (1951). See also C. Maltz, Chem. Phys. Letters 3, 707 (1969).

9. A. C. Roach and M. S. Child, Mol. Phys. 14, 1 (1968).

the chemical energy release, and the conservation laws to predict the possible form of the observed reactive scattering. An orientation-angle parameter is varied to give the best fit to the data of Chapter V, and it is found that the shapes and peak positions of the angular distributions can be reproduced quite well for all the systems experimentally studied. The resulting orientation angles are in quite satisfactory semiquantitative agreement with the potential surfaces, and show the same qualitative trends.

It is tentatively concluded that a highly concerted electron-transfer mechanism in a definite preferred geometrical configuration governs reaction in the H + MX systems. For other H atom reactions it is expected, and evidence already has been found^{6,7} that such orientation effects should often be prominent in reactive scattering.

CHAPTER II

COUPLING OF PRODUCT ANGLE AND ENERGY DISTRIBUTIONS IN

REACTIONS OF ALKALI ATOMS WITH CARBON TETRACHLORIDE

Abstract

Velocity distributions of alkali chloride scattering from crossed thermal beams of alkali atoms (K, Rb, Cs) and CCl_4 have been measured over the range 100-1000 m/sec at 8-10 laboratory angles from 10° to 100° with respect to the parent alkali beam. Two approximate kinematic methods are used to derive the differential cross section for reactive scattering, $I_{\text{cm}}(u, \theta)$, as a function of recoil velocity u and angle θ in the center-of-mass coordinate system. In one method, the LAB \rightarrow c.m. transformation is carried out directly by selecting a single representative velocity in each of the parent beams in order to make the transformation unique. The other method uses the c.m. \rightarrow LAB transformation, with $I_{\text{cm}}(u, \theta)$ represented by a many-term polynomial in powers of $ucos\theta$ and $usin\theta$ and the coefficients determined by a least-squares fit to the experimental data. The cross sections obtained by the two methods agree well and confirm the qualitative interpretation of previous experiments made without velocity analysis.

In contrast to the results obtained for the stripping reactions of alkali atoms with halogen molecules, where the angular distributions are nearly independent of product recoil energy E' , and are sensitive only to the identity of the halogen, these data show a strong coupling between angular peak position θ_p and E' , and marked sensitivity to the identity of the alkali atom. For a given alkali, θ_p shifts to smaller angles as E' increases, and as K \rightarrow Rb \rightarrow Cs the entire pattern shifts toward the forward hemisphere. The results are qualitatively correlated by a phenomenological analysis similar to that used for the rainbow effect in elastic scattering, and also by a modification of the spectator model.

A. Introduction

The first quantitative estimate of product recoil energy from a chemical reaction was made more than fifteen years ago in a pioneering but generally unheralded beam experiment carried out on the $\text{Cs} + \text{CCl}_4$ reaction by Bull and Moon.¹ Since then the burgeoning field of molecular beam kinetics, in an extensive series of studies, has identified two limiting types of reactions between alkali atoms and halogen-containing molecules.² "Stripping" reactions (for example, $\text{K} + \text{Br}_2$) are characterized by forward-peaked center-of-mass product distributions and large cross sections ($\sim 150 \text{ \AA}^2$). Much smaller cross sections ($\sim 30 \text{ \AA}^2$) and backward scattering of products, on the other hand, are the main features of the "rebound" reactions (prototype, $\text{K} + \text{CH}_3\text{I}$). Both are categorized as proceeding by dominantly direct or impulsive mechanisms, and their center-of-mass differential cross sections both have been approximately described as consisting of a product of independently varying angle- and recoil energy-dependent terms.^{3,4} Recent product velocity analysis experiments on these

-
1. T. H. Bull and P. B. Moon, Disc. Faraday Soc. 17, 54 (1954).
 2. For a review, see D. R. Herschbach, Advan. Chem. Phys. 10, 319 (1966).
 3. E. A. Entemann, Ph.D. Thesis, Harvard University, Cambridge, Mass., 1967.
 4. This has now been shown not to be strictly true for the $\text{M} + \text{Br}_2$ reactions; see Ref. 5 and Chapter IV, this thesis.

reactions^{5,6} indicate that the energy disposal also shifts markedly, from predominantly internal excitation for the stripping case to translational recoil for the rebound type.

The reaction of alkali atoms with CCl_4 promised to be an interesting "transition" case. More recent angular distribution measurements⁷ indicated that the products prefer to recoil sideways in the center-of-mass (c.m.) system, producing a bimodal laboratory distribution on account of the required azimuthal symmetry of the scattering about the relative velocity vector. In addition, the inferred c.m. angular peak position, θ_p , (measured with respect to the incident alkali) varied strongly with the identity of the alkali atom, going from $\theta_p \sim 90^\circ$ to $\theta_p \sim 30^\circ$ as $\text{K} \rightarrow \text{Cs}$, in contrast to the stripping results, where only the identity of the halogen seemed to matter in determining the c.m. angular dependence. The size of the reactive cross sections, also found to be intermediate between the rebound and stripping limits, showed definite variation with alkali, going from 60 to 150 \AA^2 as $\text{K} \rightarrow \text{Cs}$, in direct parallel with the trend toward the forward hemisphere in θ_p .

The present experiments confirm this general behavior, and show further a marked nonseparability of the cross section into angle- and velocity-dependent factors. For a given alkali atom, the preferred emission angle of the MCl product shifts to smaller angles as the

-
- 5. Ch. Ottinger, R. Grice and D. R. Herschbach, J. Chem. Phys. (to be published), on $\text{K}, \text{Cs} + \text{Br}_2, \text{ICl}$.
 - 6. Ch. Ottinger, P. M. Strudler and D. R. Herschbach, J. Chem. Phys. (to be published), on $\text{K}, \text{Rb}, \text{Cs} + \text{RI}$, R a series of hydrocarbon groups.
 - 7. K. R. Wilson and D. R. Herschbach, J. Chem. Phys. 49, 2676 (1968).

recoil energy, E' , increases, and the entire pattern shifts toward the forward hemisphere as $K \rightarrow Rb \rightarrow Cs$. Structure of this kind had previously been found in only one other chemical system, the $H + H_2$ theoretical study of Karplus and Tang.⁸

The fraction of available energy going into product translation also places these reactions in the transition realm, being somewhat larger than for, e.g., the $M + Br_2$ cases,⁵ but with most of the exo-ergicity remaining in internal degrees of freedom. Comparison with the early Bull and Moon results¹ shows good agreement within the uncertainties of both experiments.

B. Experimental Conditions

The apparatus and experimental procedures have been described elsewhere.⁵ Briefly, the beams, which intersect at 90° , are formed in ovens mounted on a rotatable lid. The CCl_4 beam is collimated by passage through "crinkly-foil" slits and a further defining slit. The alkali oven is double-chambered, the lower chamber temperature determining the pressure (intensity) and the upper chamber determining the translational temperature of the beam.

The velocity analyzer is a slotted-disk type, with a resolution of 20%. Velocities from 20 to 1000 m/sec can be conveniently measured, the upper limit corresponding to a selector rotational frequency of 450 cps. Differential surface ionization is used to distinguish the product MC_1 signal from the total signal $M + MC_1$. Product velocity

8. M. Karplus and K. T. Tang, Disc. Faraday Soc. 44, 56 (1967).

distributions were measured every 10° from $\Theta = 10^\circ$ to 100° , except at 90° (the position of the CCl_4 beam). In some cases, measurements were taken every 5° in the vicinity of the product peak.

In order to attain sufficient beam intensities for velocity analysis experiments, the oven pressures are normally too high to assure "effusive flow" conditions. For example, during one run the mean free path of Cs in the oven was $\sim 8 \times 10^{-3}$ cm, whereas the oven slit width is 30×10^{-8} cm. The resulting beams do not have Maxwellian velocity distributions, but supersonic or "Laval" distributions characteristic of "free jet flow" conditions.⁹ Such velocity profiles have higher velocity peaks and narrower widths than thermal distributions for the same temperatures. This effect is desirable, since the narrower velocity spreads better approximate the ideal of velocity-selected, monoenergetic parent beams.

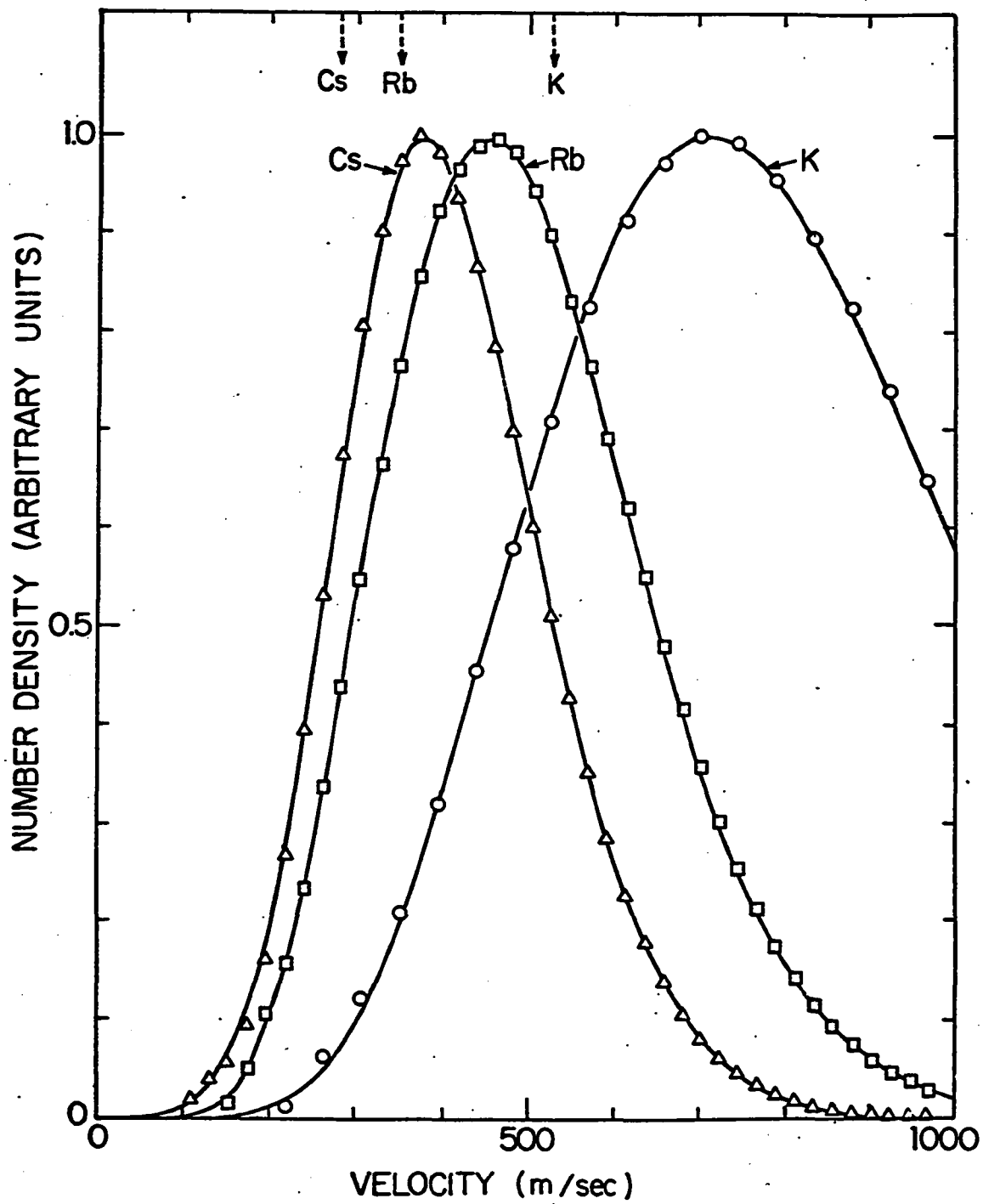
The alkali beam velocity distributions were measured as a part of each experiment, and are shown in Fig. 1. As indicated, the peaks are shifted upward from thermal by 30-35%, indicating a Mach number on the order of unity. The number density distributions were fit to the convenient functional form

$$P(v) = (v/v^*)^n \exp\left\{-\frac{n}{m}[1 - (v/v^*)^m]\right\} \quad (1)$$

where v^* is the peak velocity and n and m are determined by choosing a value of m and optimizing, in a least squares sense, the value of n ,

9. For a review on supersonic beams, see J. B. Anderson, R. P. Andres and J. B. Fenn, *Advan. Chem. Phys.* 10, 275 (1966).

Fig. 1. Velocity distributions of the parent alkali beams. Solid curves are calculated from Eq. (1) with parameters from Table I. The acceleration due to jet flow is illustrated by comparison with the dashed arrows, which show calculated position of peaks for the corresponding Maxwell-Boltzmann distributions.



repeating the process until an absolute minimum in the standard deviation is achieved. Different values of n and m are used in the regions $v < v^*$ (subscript 1) and $v > v^*$ (subscript 2). The resulting parameters, together with oven conditions, are given in Table I. For a thermal beam, $n_1 = m_1 = n_2 = m_2 = 2$, and $v^* = a$.

For the purposes of the kinematic analysis to be described, the CCl_4 beam was assumed to have a thermal velocity profile. More recently, its distribution has been measured under about the same pressure conditions using negative surface ionization, and has been found to be Laval also, with a Mach number ≈ 1.10 . Kinematic calculations were performed comparing the cross sections generated using thermal and Laval crossed-beam distributions; they show that the results presented below are not appreciably affected by the change, because of the favorable kinematics in these systems.

C. Results and Kinematic Analysis

The product laboratory velocity distributions for positive laboratory angles are shown in Fig. 2. Within each system, intensities are absolute, the data being normalized in each case to ten units at the largest peak. Open circles denote "raw" data; i.e., total $M + MX$ signal minus M signal. The method of determining the subtraction factor has been described elsewhere.⁵ Relative normalization was achieved by comparing the integrated flux (area under the curve) at each angle with the total flux as measured in the "primitive"

10. S. J. Riley, Ph.D. Thesis, Harvard University, Cambridge, Mass., 1970.

Table I. Velocity distributions in parent alkali beams.^a

Beam	T_U (°K)	T_L (°K)	α (m/sec)	v^* (m/sec)	n_1	m_1	n_2	m_2
Cs	623°	533°	281	376	4.5	3.2	10.4	1.0
Rb	623°	543°	348	456	11.7	0.7	10.9	0.9
K	653°	613°	527	712	9.8	0.8	5.3	1.5

^aTemperatures T_U and T_L refer to the upper (source) and lower (supply) chambers of the beam oven; $\alpha = (2kT_U/M)^{1/2}$ is the most probable velocity for a Maxwell-Boltzmann velocity distribution; other parameters are defined in Eq. (1).

Fig. 2. Product velocity distributions as indicated laboratory angles. Open circles are experimental points, solid curves are smoothed data. Dashed curves show distributions back-calculated from the kinematic analysis based on the polynomial cross section of Eq. (5), dotted curves from the nominal cross section of Eq. (4). The ordinate scale is such as to assign 10 units to the largest experimental peak for each reaction (60° for K, 50° for Rb, 30° for Cs).

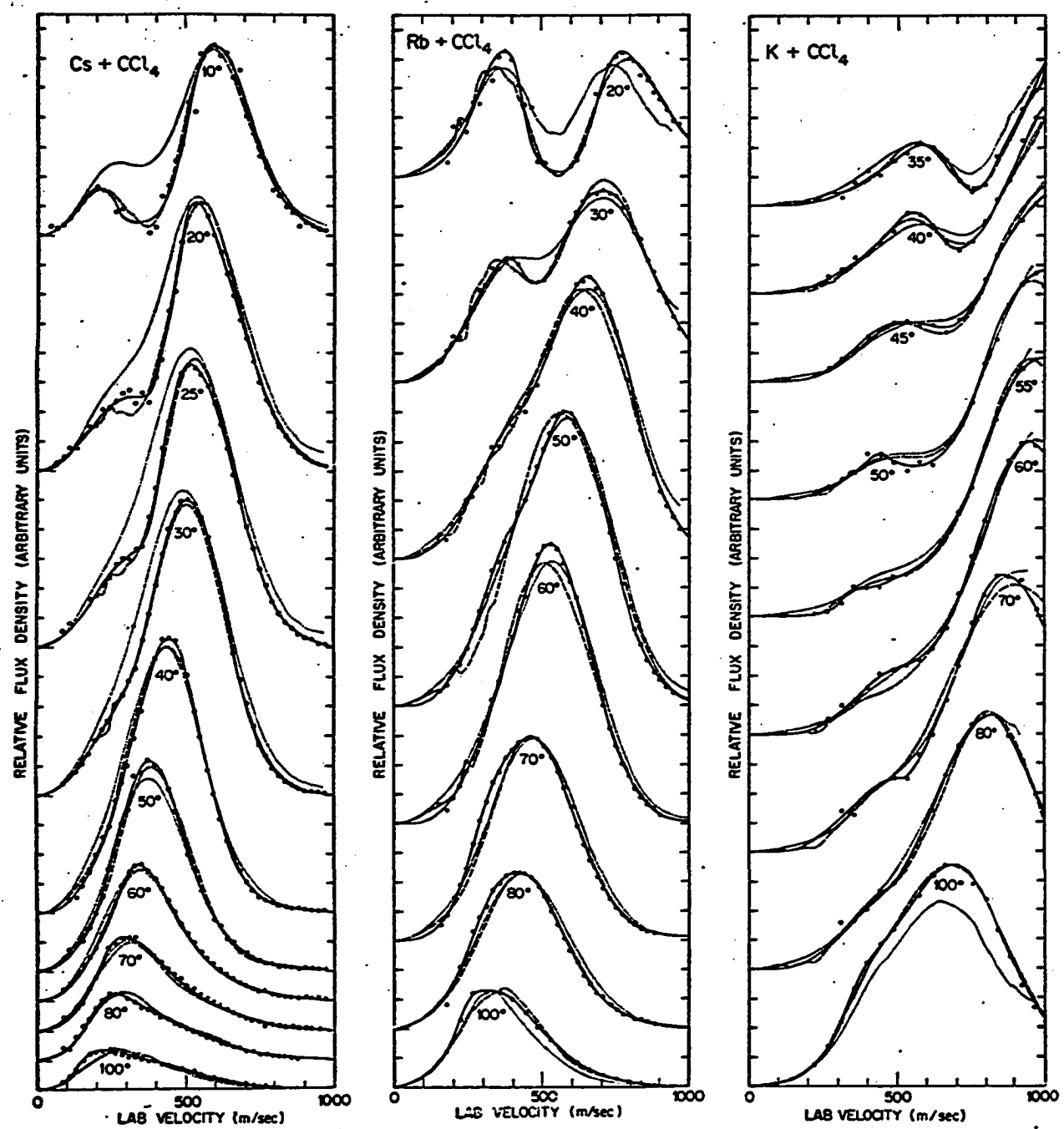


Fig. 2

experiment.⁷ The solid lines are smooth curves (hand-drawn) through the data, from which all subsequent data was taken for kinematic analysis.

Three features are immediately apparent in these distributions.

- 4 Peak velocities shift considerably with laboratory angle, a behavior which, as described below, is reflected in the center-of-mass cross section. Translational energies are quite high. At 60°, the peak velocity of KCl corresponds to 8 kcal/mole. The appearance of low velocity "bumps" at small laboratory angles suggests a Jacobian effect, but kinematic analysis indicates that there may be such structure in the center-of-mass cross section.

Obtaining this cross section from the laboratory data is complicated by the velocity averaging inherent in non-velocity selected parent beams. The expression relating the observed intensity at a laboratory angle Θ and velocity v to the center-of-mass cross section $I_{cm}(u, \theta)$ is given by Entemann as³

$$I_{LAB}(v, \Theta) = \int_0^{\infty} dv_1 \int_0^{\infty} dv_2 n_1(v_1) n_2(v_2) v \frac{v^2}{u^2} I_{cm}(u, \theta) \quad (2)$$

where v_1 and v_2 are the velocities of the parent beams, n_1 and n_2 the number density distributions, $V = (v_1^2 + v_2^2 - 2v_1 v_2 \cos\gamma)^{1/2}$ is the magnitude of the initial relative velocity (γ is the angle of intersection of the beams), and v^2/u^2 is the Jacobian factor for transforming intensities from the center-of-mass to the laboratory system. Once the beam velocities are specified the coordinate transformation

$v, \Theta \leftrightarrow u, \theta$ can be performed. (θ is measured relative to the initial center-of-mass direction of the alkali atom.) Entemann and others have given the transformation equations.³

Kinematic analysis of primitive total flux data usually involves assuming a form for the center-of-mass cross section and back-calculating via Eq. (2) to predict the laboratory flux

$$I_{LAB}(\Theta) = \int_0^\infty I_{LAB}(v, \Theta) dv. \quad (3)$$

The stochastic procedure, repeating this process until the calculated flux matches the laboratory data, is often time-consuming and sometimes unsuccessful. Velocity analysis data permits a more straightforward determination of the center-of-mass cross section, although Eq. (2) is still not analytically invertible.

Method A: Nominal Transformation

The simplest procedure is to assume no velocity averaging in the main beams - the situation that would exist in an experiment with velocity selected beams. Eq. (2) then becomes

$$I_{CM}(u, \theta) \approx \frac{u^2}{v^2} I_{LAB}(v, \Theta) \quad (4)$$

and the center-of-mass cross section can be obtained uniquely from the laboratory cross section. The resulting "nominal" cross section is to some extent dependent upon the main beam velocities used to perform the transformation, but for velocities corresponding roughly to the most probable velocities in the beam distributions it should approximate qualitatively the true center-of-mass cross section. In fact,

the "best fit" nominal cross section, determined as before by back-calculation with Eq. (2), corresponds very closely to the least squares polynomial cross section, described below. The advantage of this stochastic procedure is that only two parameters, the main beam velocities, need be adjusted. The resulting best fit parameters are given in Table II.

Method B: Least Squares Fit

In the second method of data analysis employed, the center-of-mass cross section was given the functional form of a polynomial:

$$I_{cm}(u, \theta) \equiv I_{cm}(u_x, u_y) = \exp[-(u/u_0)^2] \sum_{i,j} a_{ij} u_x^i u_y^j \quad (5)$$

where (u_x, u_y) are the planar Cartesian components of the recoil velocity vector u , and u_0 is a width parameter, chosen beforehand, whose inclusion in the exponential factor allows the cross section to become vanishingly small at high recoil energy. The coefficients a_{ij} are determined through a least squares calculation which matches an observed intensity $I_{LAB}(v, \theta)$ with the transformed and velocity-averaged intensity calculated from Eqs. (2) and (5).

In this procedure the integrations indicated in Eq. (2) are performed numerically using a Simpson's rule quadrature over $v_i = 0$ to $2.5 v_i^*$. In practice 100 grid points (10 along each beam) were sufficient to produce convergent results; no significant change was noted in either the LAB fit or the resulting center-of-mass cross section when the number of grid points was increased to 196. The values of u_0 were usually chosen to be $\sim 10\%$ less than the peak of the center-of-mass distribution, as determined by the nominal

Table II. Velocity parameters for kinematic analysis.^a

System	v_1	v_2	u_o
Cs + CC ₁ ₄	450	260	250
Rb + CC ₁ ₄	500	200	400
K + CC ₁ ₄	800	187	500

^aUnits are meters/sec; v_1 and v_2 are velocities of the parent beams ($1 \leftrightarrow M$, $2 \leftrightarrow CC_1_4$) used in Method A, Eq. (4); u_o is the width parameter for Method B, Eq. (5).

transformation, and are given in Table II. The coefficient matrix a_{ij} was allowed to be a full square one, to allow maximum anisotropy by including more cross terms. In all calculations presented here the dimensionality of the a_{ij} matrix was six. For the systems considered, the standard errors of the laboratory fits were: Cs, 2.7%; Rb, 5.1%; K, 3.4%. (Standard error $\equiv \frac{\text{standard deviation}}{\text{size of avg. pt.}} \times 100$). Chapter III of this thesis contains a detailed discussion of these methods; see also Ref. 10.

The calculated laboratory distributions are shown in Fig. 2. The polynomial cross section in general fits the data better than the nominal cross section, which, as expected, tends to be too broad and incapable of reproducing fine structure. The interpolation scheme employed in the back calculation of the nominal cross section fails at the edges of the data, such as at high velocities and at 100° in the laboratory. This is particularly noticeable in the K + CCl₄ system, where the flux density at high velocity does not go to zero. The polynomial cross section circumvents this problem because as an analytic form it is still evaluable near the edges of the data.

The center-of-mass differential cross sections are shown in Fig. 3. As is evident, the nominal and polynomial cross sections are quite similar, indicating the value of the nominal procedure as a straightforward way to obtain the main features of the c.m. cross section in systems with favorable kinematics.

Figure 4 shows constant-angle contours of the energy density distribution, expressed in terms of the fraction of recoil energy

Fig. 3. Angular distributions of reactively scattered alkali chloride for various velocities u in the c.m. system. Dashed curves are derived from the polynomial cross section, dotted curves from the nominal cross section.

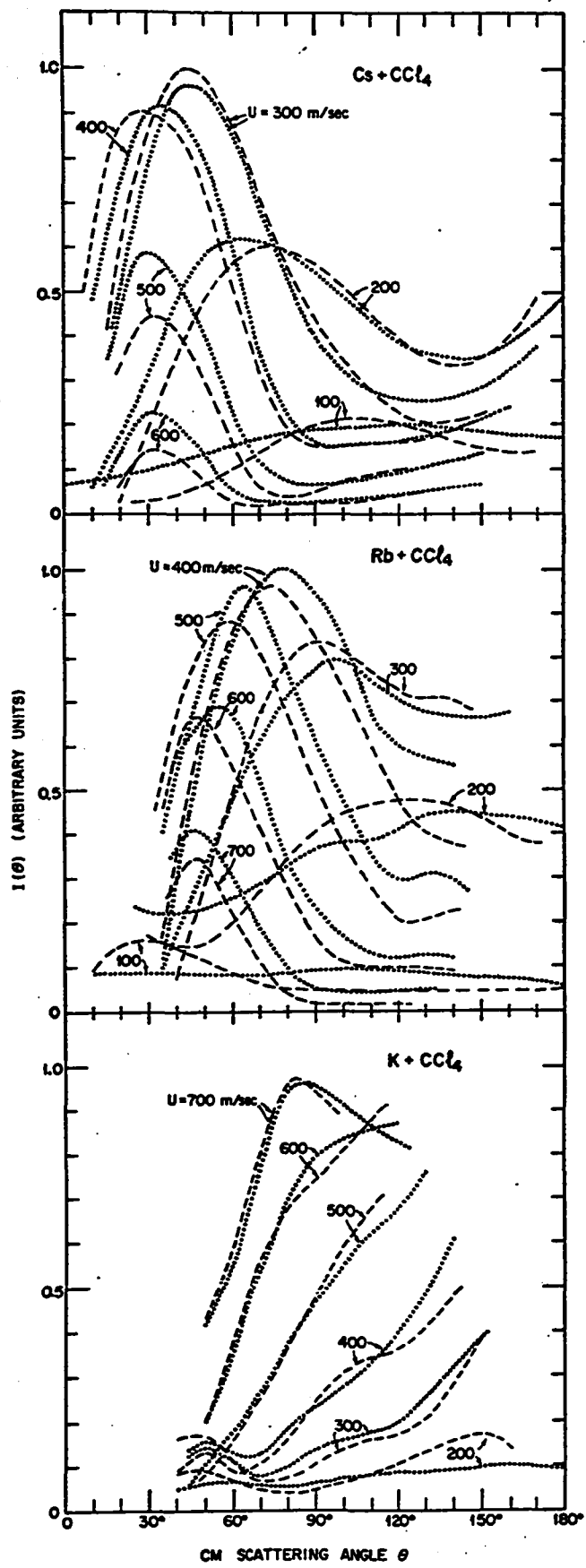
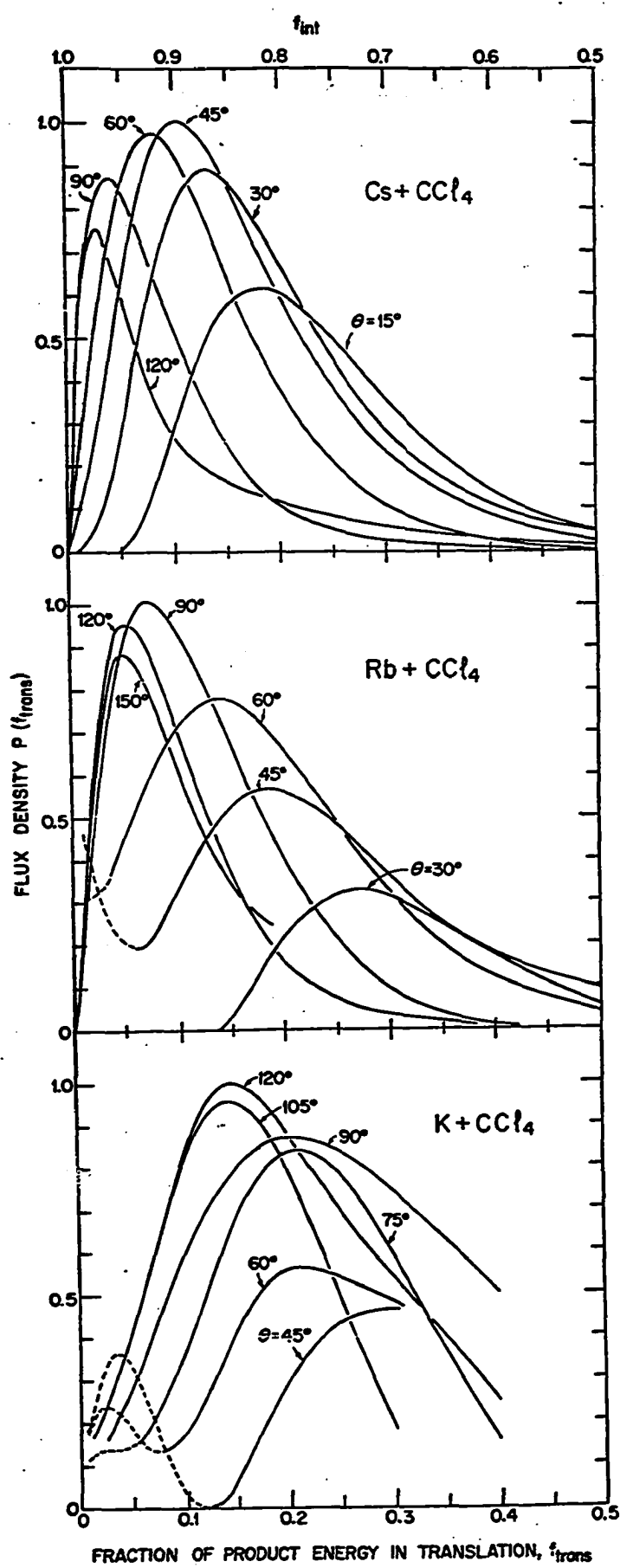


Fig. 4. Distributions of relative translational energy of the reaction products for various scattering angles in the c.m. system, as derived from the polynomial cross section.



appearing in translation

$$f_{\text{trans}} = \frac{E'}{(E + W + \Delta D_0)_{\text{ref}}} \quad (6)$$

where E' is the recoil energy, E the initial energy (both in the center-of-mass) W is the initial internal energy of the CCl_4 and ΔD_0 is the exothermicity of the reaction. E and W are average values for the experimental beam conditions. The values used are given in Table III. The energy flux density is derived from the center-of-mass cross section via

$$P_f(\theta, E') = I_{\text{cm}}(\theta, u)/u.$$

The polynomial cross section was used in these calculations.

Figure 5 shows contour maps of the center-of-mass differential cross section, again using the polynomial expression. The maps are arbitrarily normalized to 100 at the peak, and tic marks appear every 100 m/sec. The dashed line and open circles represent the "mountain ridge" or path of largest intensity, giving an indication of the change in peak velocity with angle.

It is of interest to compare these results to those of the ingenuous Bull and Noon experiment¹ on $\text{Cs} + \text{CCl}_4$. In their experiment, a pulsed, accelerated CCl_4 beam produced by "swatting" with a rapidly rotating paddle was intersected at right angles with a Cs beam effusing from an oven. Time-of-flight signal pulses were recorded by a surface ionization detector located downstream from the CCl_4 beam source. Although there was no way of distinguishing Cs from CsCl , kinematic analysis of the data and blank runs with the CCl_4 replaced

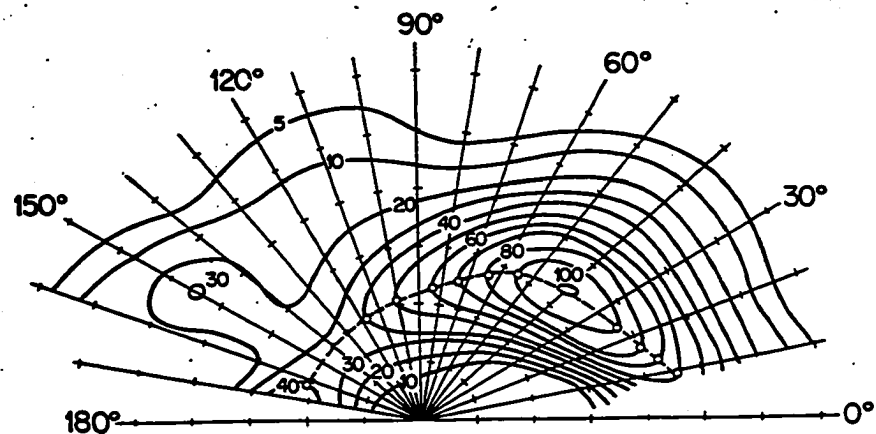
Table III. Energy parameters.^a

System	E	W	ΔD_0
Cs + CCl ₄	1.5	0.6	37.0
Rb + CCl ₄	1.6	0.6	33.0
K + CCl ₄	2.0	0.6	32.0

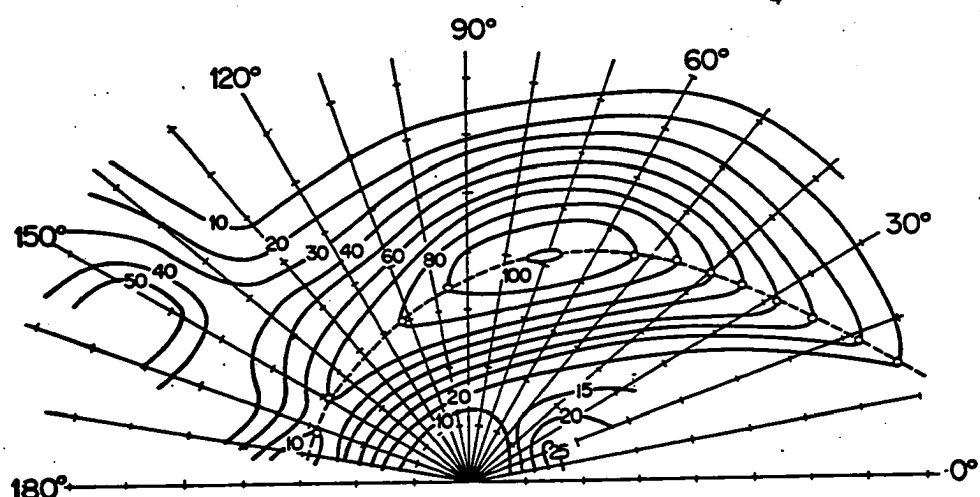
^aUnits of kcal/mole.

Fig. 5. Contour maps of the differential reaction cross section in
the c.m. system. Tic marks are every 100 m/sec.

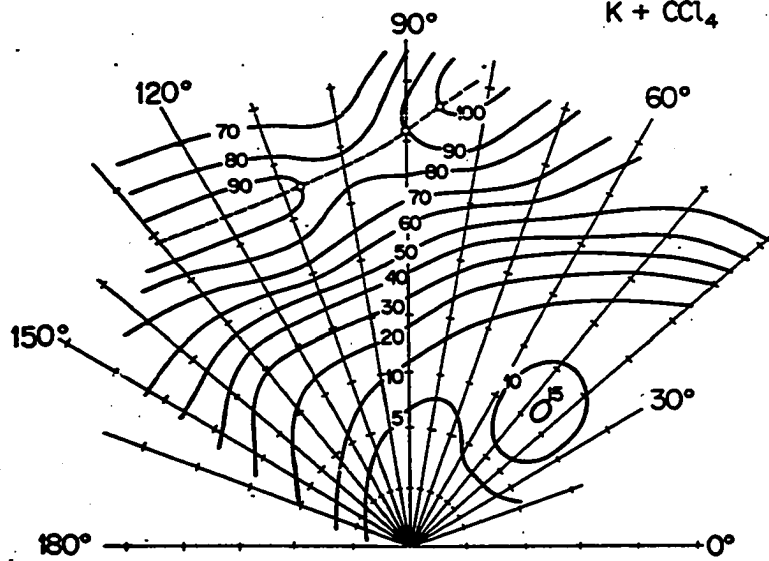
$\text{Cs} + \text{CCl}_4$



$\text{Rb} + \text{CCl}_4$



$\text{K} + \text{CCl}_4$



by Hg indicated the signal was primarily due to product CsCl. The more recent "traditional" molecular beam experiments⁷ have confirmed this: at 90° from the Cs beam elastically scattered Cs accounts for less than one-fifth of the total signal. The broader angular width of the Cs beam in the Bull and Moon experiment would change this ratio slightly, but not significantly.

Using the polynomial cross-section, a calculation based on Eq. (2) was made to predict the CsCl LAB velocity expected in the paddle source experiments. The velocity of the CCl_4 beam was taken to be that of the paddle tip with a thermal distribution superimposed, and the Cs beam (thermal) was given a sine distribution in intensity about 0°. Product velocities at 80°, 90° and 100° were averaged to approximate the degree of collimation used by Bull and Moon. The calculated distributions were multiplied by two additional factors of velocity to correspond to time-of-flight signal pulses. The results, shown in Table IV, show clear correlation, but caution must be used in any further analysis, as the approximations used were only qualitative, and the Bull and Moon data, centered at $\Theta = 90^\circ$, lies just at the fringe of our data, where the cross section is rather uncertain. It is nonetheless remarkable that these early results, generally ignored in reactive scattering literature, have now been corroborated by our data.

D. Discussion

In obtaining the center-of-mass differential cross sections, it was assumed that the c.m. scattering occurs independently of the

Table IV. Comparison with Bull and Moon experiment

Rotor tip speed $\times 10^4$ cm/sec	Pulse speed $\times 10^4$ cm/sec	Bull and Moon	Calculation
1.52	4.7		4.6
2.92	4.9		5.1
4.33	5.2		5.6
6.52	6.7		6.2

magnitude of the initial relative velocity, which seems reasonable for the relatively narrow range of reactant energies involved in a thermal beam experiment. Nonetheless it is possible that the observed strong coupling between the recoil velocity and scattering angle is due at least in part to an initial velocity dependence of the cross section. It is clear, then, that we can approach the interpretation of these results from two quite different directions. The first to be discussed is based on an analogy with the "rainbow effect" found in elastic scattering, in which the same sort of angle-energy correlation occurs, and is a phenomenological attempt to analyze these data via the same "potential barrier" connection as is well-known in the semiclassical theory of rainbow scattering. The second approach makes use of an extension of the Spectator Stripping model, which also gives the same sort of "nonseparability" of the angle and recoil dependences of the scattering, but which is totally dependent on the magnitude of the initial relative velocity.

Rainbow Analysis

The most striking feature in the center-of-mass cross sections, as shown in the contour maps, is the definite sideways peaking and rapid fall-off in intensity towards small angles and velocities. A definite trend exists in the three systems: from Cs to K the region of peak intensity shifts to larger angles and velocities, in contrast to other alkali systems studied,² where the nature of the alkali species little affects the form of the center-of-mass cross section. This suggests that the reactive scattering of alkali atoms and CCl_4 is dominated, at

least in part, by some form of pseudo-elastic scattering in the entrance or exit channel (or both) determined by potential interactions. One would expect, for example, the interaction between CsCl and CCl_3 to be quite different from that between KCl and CCl_3 because the dissociation energy of the salt affects the position of the first-order crossing between the $\text{M} + \text{Cl}-\text{CCl}_3$ and $\text{M}-\text{Cl} + \text{CCl}_3$ potential curves. It seems plausible to suggest this interaction produces a barrier along the reaction trajectory off which elastic-type scattering can occur. This situation is quite different from the prototype stripping mechanism, where the alkali atom essentially "picks up" the halogen atom in transit, the trajectory following a downhill potential surface, and the rebound mechanism, where a barrier exists that is so high the product alkali halide bounces backwards from it. What is being suggested, then, for the CCl_4 reaction is a barrier in the exit channel of height comparable to or less than the recoil translational energy, which affects the scattering of the products.

The distinguishing feature of elastic scattering involving potential barriers lower than the translational energy is a focussing of the scattered species into a narrow angular region beyond which there is a rapid falloff in intensity - a behavior referred to as the rainbow effect by analogy with optics,¹¹ and explained in terms of a local minimum (or maximum) in the deflection function versus impact

11. See, for example, J. O. Hirschfelder, C. F. Curtiss, and R. B. Bird, *Molecular Theory of Gases and Liquids* (New York, Wiley, 1954).

parameter curve. At such an extremum the classical cross section¹²

$$I(\theta) = \frac{b}{|\sin \theta \frac{d\theta}{db}|}$$

becomes infinite. A semiclassical treatment of barrier scattering¹³ rounds off this infinity and predicts the cross section in the neighborhood of a rainbow angle will be of the form

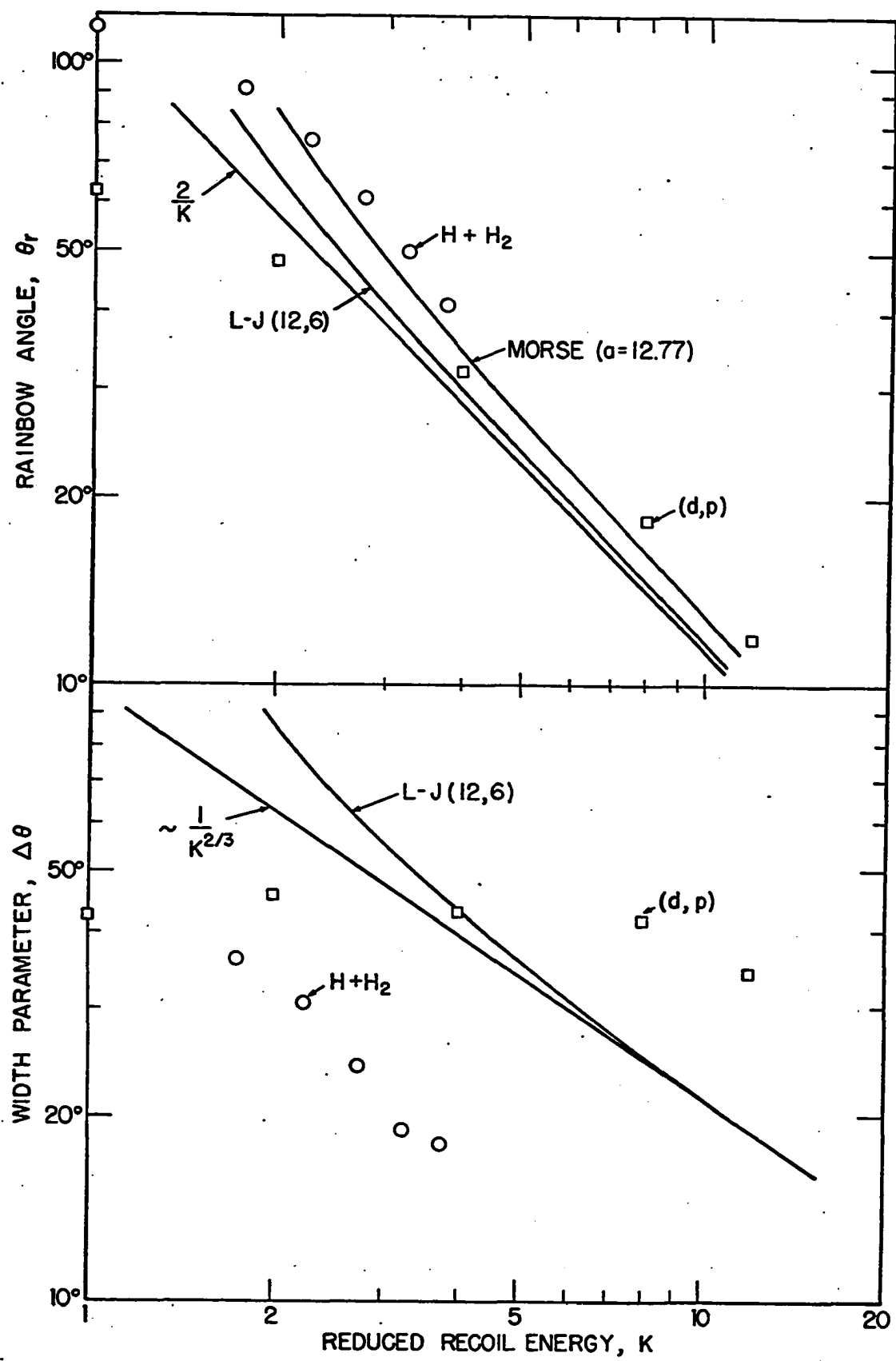
$$I(\theta)\sin\theta = C_1 A_i^2(C_2(\theta - \theta_r))$$

where C_1 and C_2 depend on potential and deflection function parameters, as well as the energy, and θ_r is the rainbow angle. A_i is the Airy function, and from its properties the rainbow angle is shown to be the angle on the "dark" side of the rainbow peak that corresponds to 44% of the peak intensity of the $I(\theta)\sin\theta$ curve.¹³ Further analysis¹² shows that the rainbow angle is inversely proportional to the energy in the limit of high energy, and that the width parameter $\Delta\theta = \theta_{peak} - \theta_{rainbow}$ is also inversely proportional to the energy. Figure 6 shows the results of calculations of rainbow parameters for the Morse¹⁴ and Lennard-Jones¹⁵ potentials, together with the high-energy approximations for the Lennard-Jones (12,6) potential:

$$\theta_r = \frac{2}{K} \text{ and } \Delta\theta \propto K^{-2/3}$$

12. H. Pauly and J. P. Toennies, Adv. Atomic and Mol. Phys. 1, 201 (1965) and references cited therein.
13. K. W. Ford and J. A. Wheeler, Ann. Phys. (N.Y.) 7, 259 (1959).
14. R. B. Bernstein in M. R. C. McDowell, Ed., Atomic Collision Processes (Amsterdam, North Holland Publishing Co., 1964), p. 895.
15. F. A. Morse and R. B. Bernstein, J. Chem. Phys. 37, 2019 (1962).

Fig. 6. Rainbow parameters for the Morse and Lennard-Jones potentials (Ref. 14 and 15), and for the $H + H_2$ reaction (circles, Ref. 8) and deuteron stripping reaction (squares, Ref. 20). For the $H + H_2$ reaction, the characteristic energy ϵ is taken as 0.4 eV, the minimum saddle-point height for the potential surface used in Ref. 8. For the (d,p) reaction, the points are shifted an arbitrary amount, corresponding to an ϵ of 25 MeV.



where K is the reduced energy E/ϵ . In these approximations θ_r is dependent only on K , whereas $\Delta\theta$ is also a function of the range of the potential. The curves in the lower half of Fig. 6 have thus been shifted vertically so that the $K^{-2/3}$ curve matches the exact semi-classical result¹⁶ at high reduced energy.

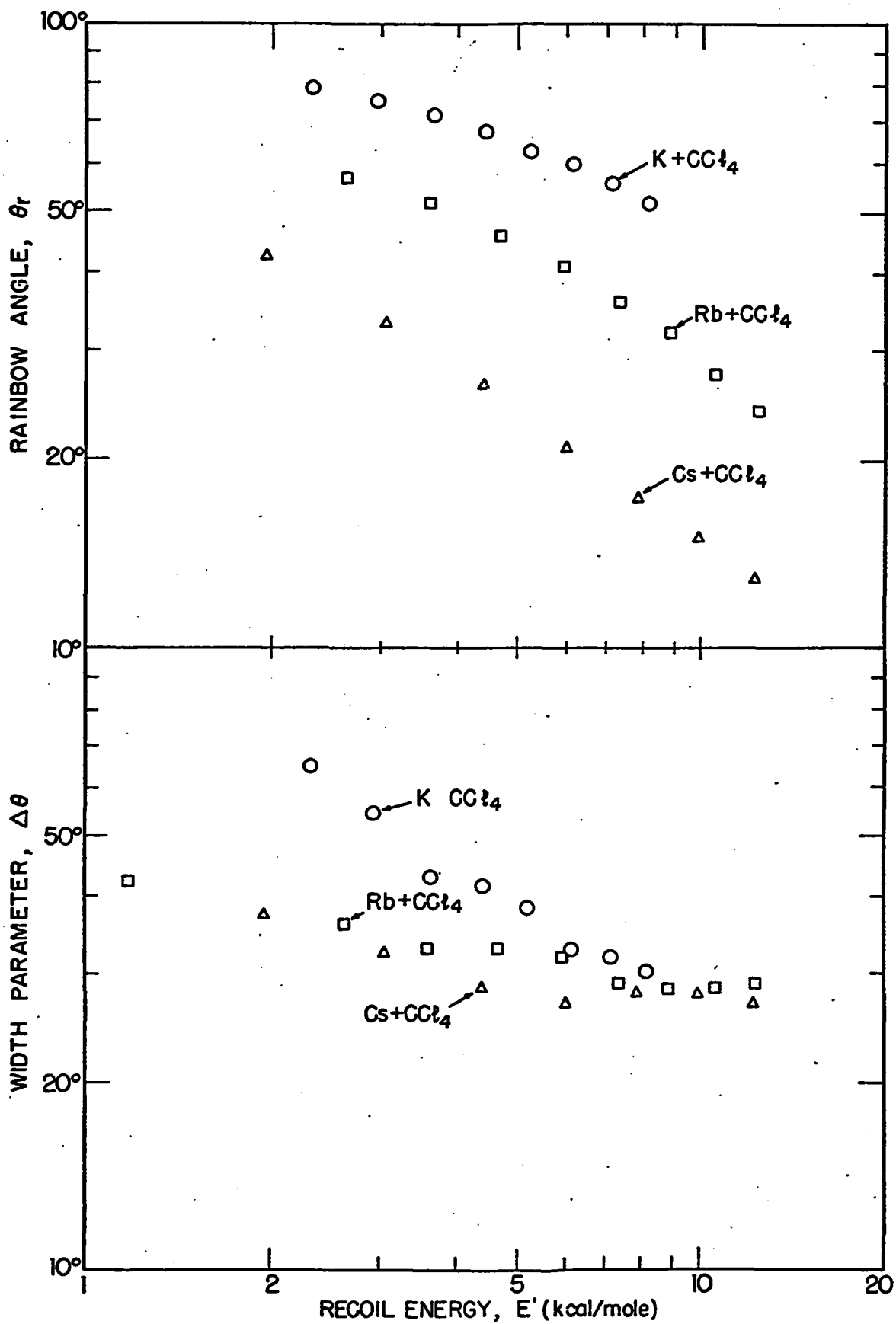
In the $M + CCl_4$ system, the postulated potential barrier might be expected to produce rainbow-like behavior in the scattering cross section. And indeed, further inspection of Fig. 3 suggests that the rapid falloff in intensity at small angles is the "dark" side of a rainbow maximum. This would correspond to a "positive" rainbow, in which the deflection function and its curvature in the rainbow region are of the same sign.¹¹ This is exactly the behavior expected for a barrier in an attractive region of the outgoing two-body potential.

A rainbow analysis¹⁷ was therefore done on the polynomial cross sections for Cs, Rb, and $K + CCl_4$. Plots of $I_u(\theta)\sin\theta$ were prepared and the quantities θ_r and $\Delta\theta$ determined for various values of u . The results, shown in Fig. 7, suggest a definite similarity to rainbow behavior. θ_r appears to be proportional to $E^{-1/2}$, not to E^{-1} as in the elastic rainbow effect. But a similar analysis of theoretically calculated reactive cross sections for the system $H + H_2 \rightarrow H_2 + H^8$ may explain this behavior. This cross section, based on a potential surface having a definite barrier at the crossover point, bears striking resemblance to the $M + CCl_4$ cross sections. Peaking is

16. E. A. Mason, R. J. Munn, and F. J. Smith, *J. Chem. Phys.* 44, 1967 (1966).

17. The procedure is described in, e.g., E. F. Greene, G. P. Reck and J. L. J. Rosenfeld, *J. Chem. Phys.* 46, 3693 (1967).

**Fig. 7. Rainbow parameters for the $M + CCl_4$ reactive scattering
derived from the polynomial cross sections.**



predominantly sideways, shifting to larger angles for lower energies. As the rainbow analysis indicates (circles in Fig. 6) the barrier produces a negative deviation from a linear relationship at low energies, as opposed to the positive deviation for potentials having wells. It may be then, that the recoil energies accessible to measurement in the $N + CCl_4$ reactions are not high enough for the characteristic rainbow effect to be completely evident.

Reactive barrier scattering has been noted in other systems, particularly in high energy nuclear reactions.¹⁸ In the case of deuteron stripping reactions, notably (d,p) and (d,n) reactions, the Coulomb barrier produces scattering cross sections remarkably similar to elastic rainbow cross sections. Most theoretical models¹⁹ for these systems are fully quantum mechanical in nature and lead, after considerable effort, to reasonable agreement with experimental data. But it would appear that, here too, a simple rainbow analysis provides valuable insight into the main feature of the scattering. One such model²⁰ for the (d,p) reaction produces a calculated cross section which is very similar to the $H + H_2$ system. A rainbow analysis (as shown by the squares in Fig. 6) of this cross section strengthens this similarity.

It should be emphasized that these rainbow analysis are meant to be purely phenomenological. We have intended to show that the general

18. See, for example, Freemantle, Prouse, Hossain, and Rotblat, Phys. Rev. 97, 1270 (1954).

19. (a). S. T. Butler, Proc. Roy. Soc. (London) A208, 559 (1951); (b) K. A. Ter-Martirosian, J. Exptl. Theoret. Phys. (USSR) 29, 713 (1955); Soviet Phys.-JETP 2, 620 (1956).

20. L. C. Biedenharn, K. Boyer, and M. Goldstein, Phys. Rev. 96, 1270 (1954).

behavior of our differential reaction cross sections is very reminiscent of the elastic rainbow effect - perhaps pointing to the existence of a potential barrier in the reaction trajectory (a conclusion supported by the similar behavior of calculated distributions based on such barriers) but not implying any quantitative relationship. The replacement of a reactive six-body potential surface by an elastic two-body curve clearly is a severe approximation, but should suffice for such a qualitative correlation.

Elastic Spectator Model

It has been pointed out that the ordinary Spectator Stripping model can easily be extended to include chemical reactions in which the AB product distribution from



does not peak at $\theta = 0^\circ$ in the c.m. system.²¹ This is done simply by relaxing the requirement that the magnitude and direction of the initial c.m. velocity of atom C be conserved, the defining assumption in the ordinary model, and allowing C to be elastically scattered, thus conserving only the magnitude of its velocity. This modification has been dubbed the "Elastic Spectator" model²¹ (ES). It is proposed to calculate c.m. angular distributions for ES, and show that the model can qualitatively reproduce the coupling between recoil velocity and scattering angle found in the M + CCl₄ reactions.

21. D. R. Herschbach, Appl. Optics, Suppl. 2 of Chemical Lasers, 128 (1965).

The momentum transfer to the products may be written as

$$q = \mu' V' - \mu V, \quad (7)$$

where μ is a reduced mass, V a relative velocity and the primes denote product quantities. Conservation of the magnitude of atom C's velocity is equivalent to

$$V = \gamma_A V', \quad (8)$$

$\gamma_A \equiv m_{AB}/m_A$; we note that Eq. (8) is written for the scalar magnitudes of the velocities only. Using the law of cosines to relate the magnitudes in (7) together with (8), we obtain

$$V' = V_t [\gamma_C^2 + 1 - 2\gamma_C \cos\theta]^{-\frac{1}{2}} \quad (9)$$

where $V_t \equiv q/\mu'$ is the transferred velocity, and $\gamma_C \equiv m_{BC}/m_C$. Since the minimum of the radicand is at $\theta = 0^\circ$ and the maximum at $\theta = 180^\circ$ (θ is the c.m. scattering angle), this relationship provides an inverse correlation between recoil velocity and angle, as observed in the CCl_4 systems, as long as V_t (or q) is not strongly angle- or energy-dependent. Development of angular distributions should allow an independent choice to be made for V_t , so that Eq. (9) can be quantitatively compared with the data.

Assuming that the momentum transfer can be taken as constant, if then the beam experiment had been performed with monochromatic initial conditions (velocity-selected, well-collimated parent beams), ES in this form would predict a δ -function product peak at an angle θ and velocity V' determined by the unique V through Eqs. (8) and (9). The only way in which a distribution in angle and recoil energy can arise

is through a spread in the incoming energy; this situation is completely analogous to that of the ordinary Spectator Stripping model. For simplicity we neglect the internal motion of the polyatomic species, so that

$$I(\theta) \sin \theta d\theta \approx P(V) dV, \quad (10)$$

where $P(V)$ is the flux density of the initial relative velocity magnitude. Using $P(V)$ for Maxwellian beams intersecting at 90° ,²² we arrive at the simple expression

$$I(\theta) \approx \xi^7 \exp(-\frac{1}{2} \xi^2) I_1(\frac{1}{2} \delta \xi^2), \quad (11)$$

where

$$\xi(\theta) = \gamma_A V_t^* [\gamma_C^2 + 1 - 2\gamma_C \cos \theta]^{-\frac{1}{2}} \quad (12)$$

$I_1(x)$ is a first order modified Bessel function, $\delta = (\alpha_A^2 - \alpha_{BC}^2)/(\alpha_A^2 + \alpha_{BC}^2)$, $\alpha_i = \sqrt{2kT_i/m_i}$, $V_t^* = V_t/\alpha$, and $1/\alpha^2 = 1/\alpha_A^2 + 1/\alpha_{BC}^2$.

For the sake of obtaining a tidy analytic expression, we have neglected the possible non-effusive character of the beam distributions; considering the crudity of the model, this appears justified.

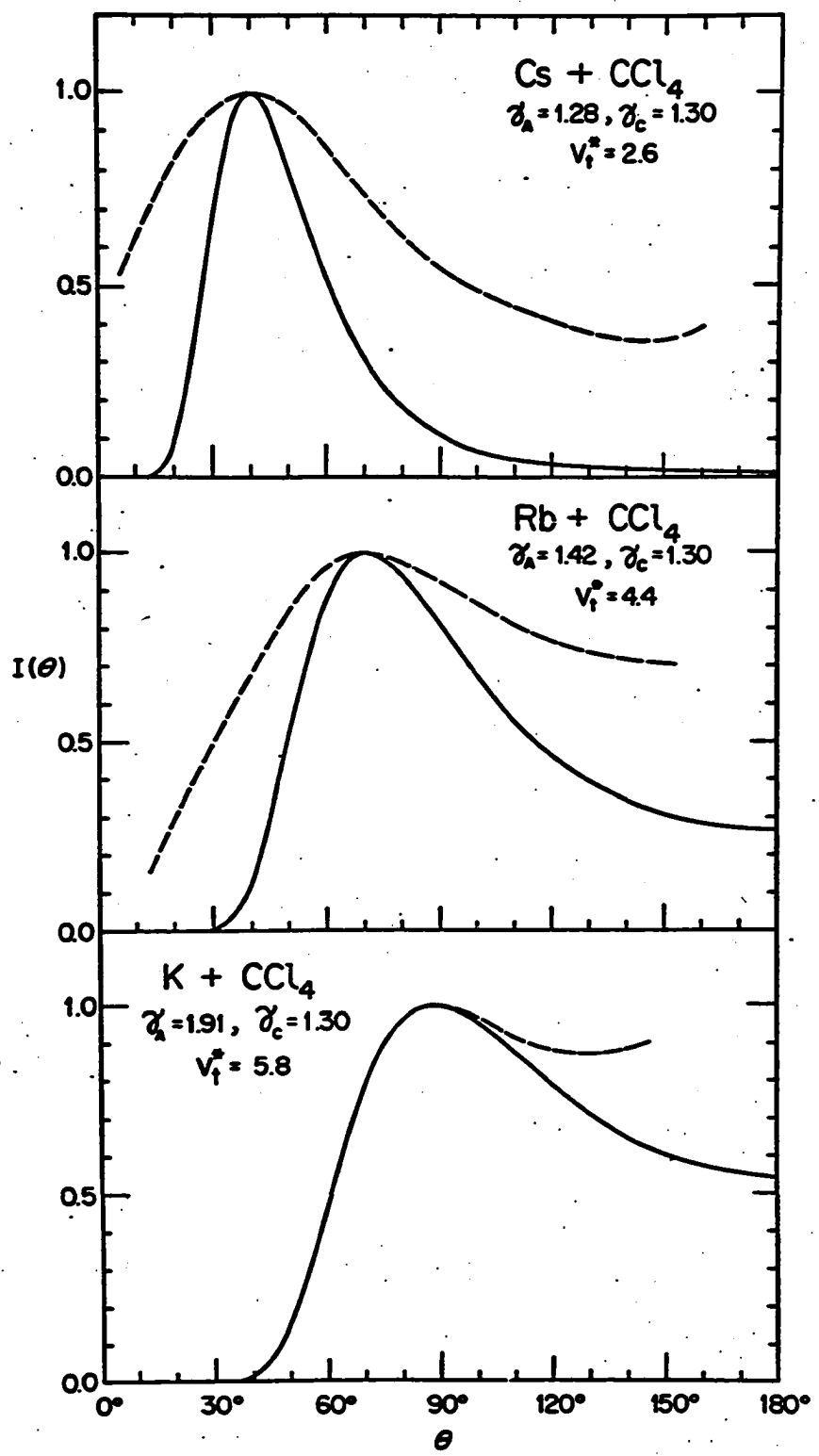
For these reactions the necessary mass ratios are easily calculated, and the α_M 's are taken from Table I with $\alpha_{CCl_4} = 187$ m/sec.

The Bessel function of Eq. (11) was evaluated using rational polynomial approximations.²³ By adjusting the value of V_t^* , the peaks of the angular distributions can be fit, as shown in Fig. 8; the values

22. W. B. Miller, Ph.D. Thesis, Harvard University, Cambridge, Mass., 1969.

23. M. Abramowitz and I. A. Stegun, Eds. "Handbook of Mathematical Functions" (National Bureau of Standards Appl. Math. Ser. 55, 1964), p. 378.

Fig. 8. Elastic Spectator c.m. angular distributions of MC1 calculated from Eq. (11) (—) for the indicated parameter values, compared with the peak recoil intensity as a function of angle (---) taken from Fig. 5.

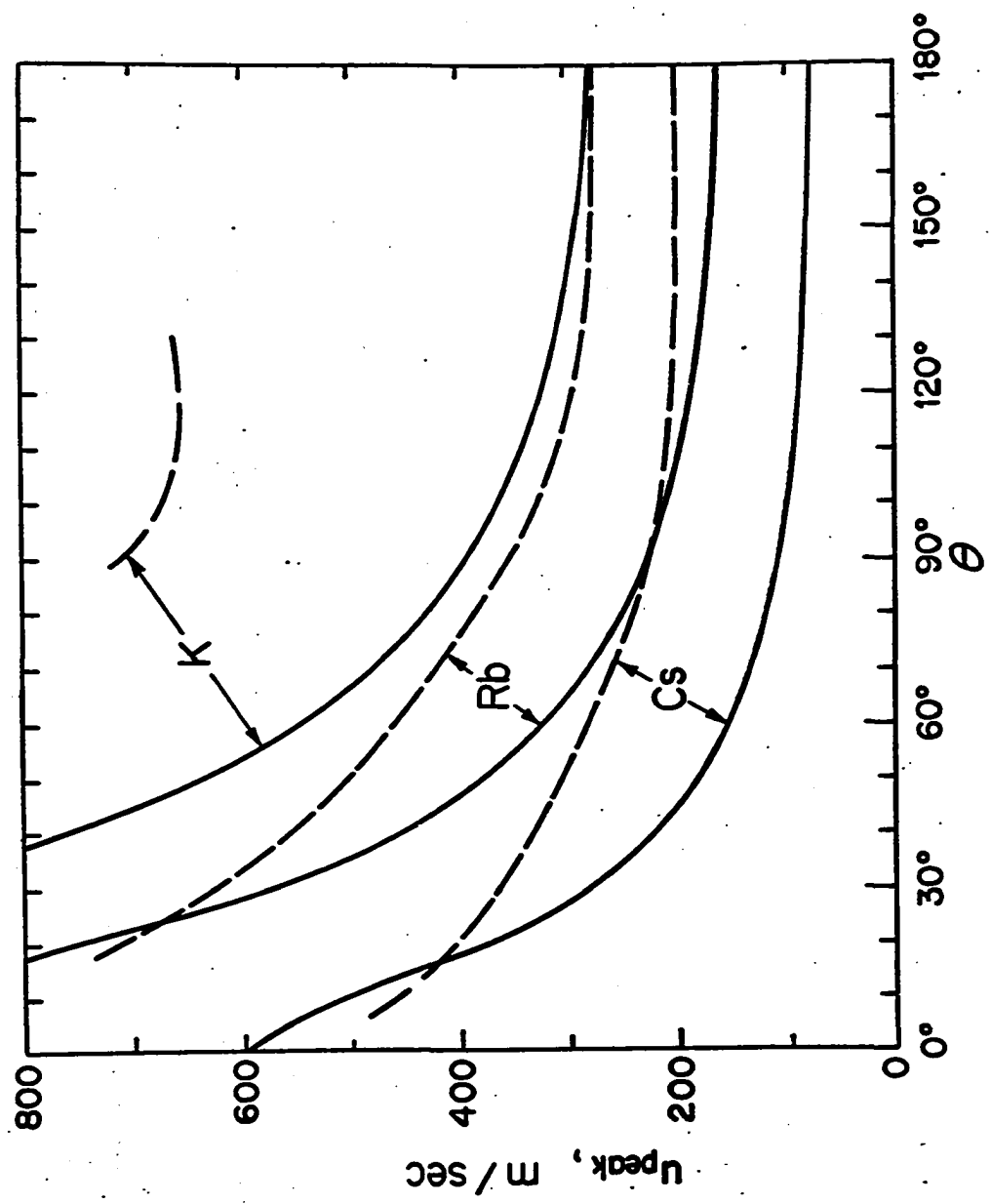


of the experimental parameters are as given. The experimental curves represent the intensity distribution of the peaks in the recoil velocity distributions at various angles; these were read off the c.m. contour plots (Fig. 5). The model curves are all too narrow, as might be expected, since the internal motions of $\text{Cl}-\text{CCl}_3$ have been ignored.

The values of v_t^* which best fit the angular data were then used to determine the quantitative relation between V' and θ (Eq. (9)). The results are shown in Fig. 9, where again the data curves are taken from the contour plots. The predicted falloff in $u (= \frac{m_{\text{CCl}_3}}{m} V')$ with θ is too rapid, but the general qualitative shapes are similar. The KCl product is certainly going much too fast to be compatible with the model, but the quantitative agreement is somewhat better for Rb and Cs. The fact that the model consistently predicts too low a recoil velocity at wide angles is perhaps not surprising, since the chemical energy release into translation generally seems to be greatest for backward scattering.⁶

The model, as might be expected, also gives $E' - \theta$ relations qualitatively similar to those found in the $\text{H} + \text{H}_2$ calculation and in the (d,p) and (n,p) reactions cited earlier. Its most glaring weaknesses are (1) its assumption about the constancy of the momentum transfer and (2) its lack of any initial impact parameter (b) dependence. In an impulsive mechanism one naturally associates backward scattering ($\theta \sim 180^\circ$) with small b 's, and smaller θ 's with larger b 's, as in the hard-sphere case.² Therefore, weaknesses (1) and (2) may

Fig. 9. Variation of NCl recoil velocity with angle predicted by the Elastic Spectator model (—) as obtained from Eq. (9) for the same values of the parameters as in Fig. 8, compared with the experimental variation in recoil peak position with angle (---) from Fig. 5.



be related in that, if, as one might intuitively expect, the momentum transfer were larger for small- b collisions than for large, the angular dependence of the momentum transfer would be such as to cancel out the strong V' - θ correlation of Eq. (9). Nonetheless the model represents a way of qualitatively correlating the data in terms of a kinematic effect depending on the initial relative velocity.

E. Conclusion

In conclusion, we summarize the main results:

(1) These experiments confirm the "intermediate" status of the $M + CCl_4$ reactions between the limits of "stripping" and "rebound" mechanisms, both in terms of angular peak position and energy disposal. In contrast to the alkali-halogen stripping reactions, the angular distributions are strongly influenced by the identity of the alkali atom. These reactions put a greater fraction of the available energy into product translation than do the stripping reactions, but internal excitation still dominates, unlike the case for rebound reactions.

(2) Two new methods of kinematic analysis applied to the data show that a pronounced correlation exists between recoil energy and scattering angle in the center-of-mass system. Superimposed on the known angular peak shifting toward the forward hemisphere as $K \rightarrow Rb \rightarrow Cs$ is a steady increase in recoil energy with decreasing angle.

The dilemma encountered in attempting to interpret point (2), as to whether or not to regard the coupling as due to a strong initial energy dependence remains unresolved. Further experiments with a velocity-selected K beam, in order to narrow the initial

energy distribution, should rule out one or the other of the two possible interpretations we have put forth. In addition, trajectory studies on surfaces which give sideways peaking would be helpful in determining whether the $E'-\theta$ correlation is a chemical or purely kinematic effect.

CHAPTER III
KINEMATIC ANALYSIS OF REACTIVE SCATTERING

Abstract

A simple coordinate transformation is presented to convert LAB velocity-space coordinates to their c.m. counterparts in the kinematic analysis of reactive scattering in crossed molecular beams. The transformation of intensities between the two frames is reviewed, and these two results are applied to the kinematic problem, obtaining the c.m. reactive scattering cross section as a function of scattering angle and speed of recoil from observed data.

For an experiment with monochromatic initial conditions and velocity analysis of the product, the straightforward application of kinematic relations suffices to determine the c.m. function to within the precision of the data. If there is a spread in initial conditions, the problem becomes more complicated. The simplest approach in this case is to ignore this spread and proceed exactly as in the ideal case. A more rigorous method is expounded which employs the least squares fitting technique to give a c.m. cross section which reproduces the data after velocity-averaging.

If the experiment considered has not employed product velocity analysis, one must settle for a more approximate determination of the c.m. function. Previous analytical schemes are reviewed, and the least squares method is again applied to this problem, resulting in an approximate c.m. cross section which reproduces the LAB angular distribution upon averaging over initial conditions.

The implications of these procedures for kinematic analysis as to the desirability of various experimental arrangements are discussed, and the effect of velocity-averaging assessed. Finally, a recently developed method employing iterative deconvolution is reviewed.

A. Introduction

Reactive scattering experiments using crossed molecular beams fall into two main categories: the so-called "primitive" experiments, performed without any state selection of either the reactants or products, and other experiments (which will be dubbed "sophisticated") employing some type of state analysis of the detected product and perhaps one (but not yet both) of the reactants. The most common method of selection used has been velocity analysis, usually with a slotted-disk type analyzer, and it will be our concern here. Also, virtually all of these experiments have used a detector placed in the place defined by the intersecting beams; therefore our discussion will be confined to the in-plane case.

Before any quantitative interpretation can be made of the results of such studies, the measured intensities must be transformed from the laboratory (LAB) coordinate system to the center-of-mass (c.m.) system of the reacting aggregate of atoms. This kinematic transformation is necessary since it is only the relative motion of the products which contains information about the reaction dynamics. Statements about the magnitude and directional preference of recoil of the reaction products in the c.m. system are thus the primary objective. These features of the scattering hopefully can characterize some of the important qualities of the potential surface governing the reaction; Monte Carlo trajectory studies at present seem to provide the best

means to establish such correlations.¹ Then, ultimately, one may speculate about the chemical dynamics of the reaction, bond breakage and formation, which is the *raison d'être* for these experiments. But before these succeeding stages of analysis can be approached successfully, the initial kinematic problem must be solved with some accuracy.

B. Notation and Coordinate Transformation

We will follow almost without exception the notation of Entemann,^{2,3} whose pioneering work on kinematic analysis made the present study feasible. For the convenience of the reader, the relevant symbols are defined in Table I. The velocity vector relation governing the c.m. \leftrightarrow LAB transformation is

$$\chi = \mu + \xi, \quad (1)$$

which simply expresses the kinematic problem: the (desired) distribution in μ vectors is coupled to the (known) distribution in ξ , and all we can measure is the distribution in χ . The objective then is to eliminate the contribution ξ makes to χ . Let us imagine for a moment that we have done the ideal sophisticated experiment (ISE): we have velocity selected each parent beam as well as velocity analyzed the product. Assuming also that the beams are nearly

1. P. J. Kuntz, M. H. Mok, E. M. Nemeth and J. C. Polanyi, *J. Chem. Phys.* **50**, 4607, 4623 (1969), and references cited therein.
2. E. A. Entemann, Ph.D. Thesis, Harvard University, Cambridge, Mass., 1967.
3. E. A. Entemann and D. R. Herschbach, *Disc. Faraday Soc.* **44**, 289 (1967).

Table I. Definition of kinematic symbols

(see Fig. 1 for pictorialization)

χ_i , $i = 1, 2$: initial LAB velocities of the reactants. Conventionally the LAB polar components of χ_1 are taken to be $(v_1, 0^\circ)$ and those of χ_2 (v_2, γ) , where γ is the angle of intersection of the reactant beams. This convention serves to define the polar axis and the sense of rotation of the LAB velocity-space coordinate system.

m_i , $i = 1, 2, 3, 4$: masses of the reactants (1,2) or products (3,4); $i = 3$ indicates the detected product. Omission of the subscript denotes total mass of the system.

$\chi = \chi_1 - \chi_2$: initial relative velocity of the reactants; the polar components of χ in the LAB are (V, Θ_V) and in the c.m. $(V, 0^\circ)$. This serves to define the c.m. coordinate system analogously.

The initial relative kinetic energy $E = \frac{1}{2} \mu V^2$, where $\mu = m_1 m_2 / m$.

$\xi = \frac{1}{m}(m_1 \chi_1 + m_2 \chi_2)$: center-of-mass vector of the system; its LAB polar components are (C, Θ_C) . The magnitude and direction of this vector remain constant regardless of the outcome of any collision.

χ (no subscript): the LAB velocity of the detected product; (v, Θ) are its LAB polar components.

ψ : the c.m. recoil velocity of the detected product; its c.m. polar components are (u, θ) . In terms of the final relative velocity χ' , $\psi = \frac{m_4}{m} \chi'$. The final relative kinetic energy $E' = \frac{1}{2} \mu' V'^2 = \frac{1}{2} (\mu m_3 / m_4) u^2$, where $\mu' = m_3 m_4 / m$.

perfectly collimated, we can now draw a unique vector diagram (which we are fond of calling a Newton Diagram), shown in Fig. 1. This illustrates Eq. (1) in both the LAB and c.m. frames. Symbols are as defined in Table I. For now we will consider only the geometry of the transformation, and leave the implications of the knowledge of the distributions in ξ and η for the next section.

It is clear from Fig. 1 that the planar LAB \leftrightarrow c.m. coordinate transformation is merely a translation by ξ followed by a rotation through Θ_V , which we can write in matrix notation as

$$\begin{pmatrix} \tilde{x} \\ \tilde{y} \end{pmatrix} = R(\Theta_V) \begin{pmatrix} x - \xi \\ y \end{pmatrix} \quad (2)$$

where $R(\alpha)$ is the rotation matrix, whose Cartesian representation is

$$R(\alpha) = \begin{pmatrix} \cos\alpha & -\sin\alpha \\ \sin\alpha & \cos\alpha \end{pmatrix}.$$

Writing the velocities in terms of their Cartesian components, we have

$$\begin{pmatrix} u_x \\ u_y \end{pmatrix} = \begin{pmatrix} \cos\Theta_V & -\sin\Theta_V \\ \sin\Theta_V & \cos\Theta_V \end{pmatrix} \left[\begin{pmatrix} v_x \\ v_y \end{pmatrix} - \begin{pmatrix} c_x \\ c_y \end{pmatrix} \right]. \quad (2a)$$

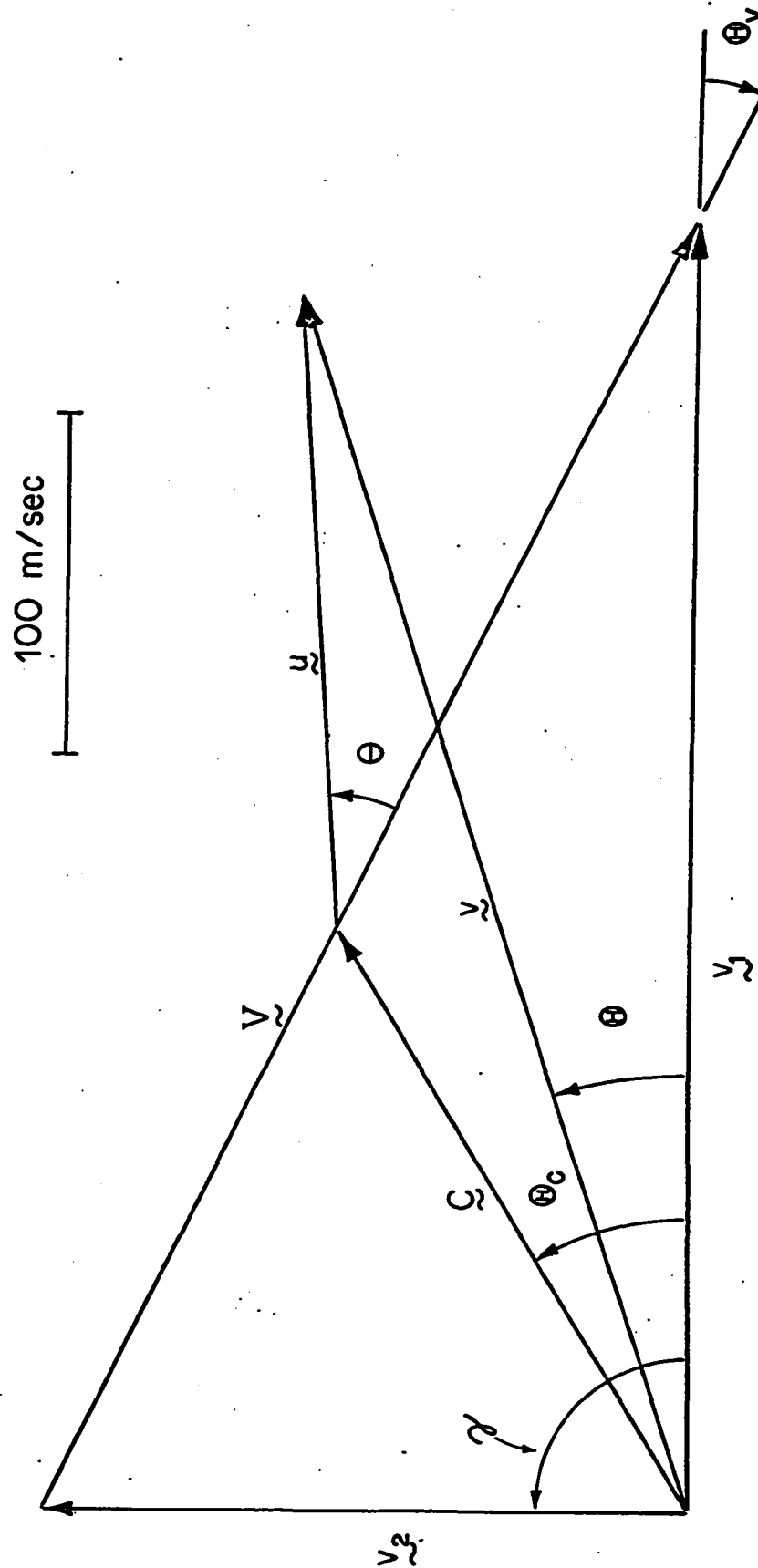
The polar components of u are easily obtained from

$$u = \sqrt{u_x^2 + u_y^2}, \quad (3)$$

$$\theta = \tan^{-1} \left(\frac{|u_y|}{u_x} \right).$$

θ is easily recognized as the c.m. scattering angle. For non-polarized reactant beams, cylindrical symmetry about η is required for

**Fig. 1. Newton diagram, drawn here for the masses and velocities
of the Cs + CCl_4 reaction of Chapter II. The labeled quantities
are defined in Table I.**



the scattering, and therefore our in-plane measurements may suffice to determine the nature of all scattering occurring, whether in- or out-of-plane. The computational convenience of the use of (2a) and (3) in kinematic calculations is discussed in the Appendix to this chapter.

C. Intensity Transformation

Having confined ourselves to the case of in-plane scattering, we can think of the measured LAB intensities as a function of v obtained from our ISE as forming a surface in LAB velocity coordinate space, i.e.,

$$I_{LAB} = f(v_x, v_y) \equiv f(v, \theta) \equiv f(\chi).$$

Since we are dealing with the scattering of particles, $I_{LAB}(v)$ should be expressed as a flux density,⁴ so that we can utilize the conservation of flux in transforming to c.m. intensity, denoted by $I_{cm}(u)$. The conservation of flux implies that the intensity in the LAB with speed between v and $v + dv$ scattered into the LAB solid angle $d\Omega$ is equal to that in the c.m. with speed between u and $u + du$ scattered into the corresponding c.m. solid angle $d\omega$, i.e.,

$$I_{LAB}(\chi)dv d\Omega = I_{cm}(u)dud\omega, \quad (4)$$

where χ and u are understood to be related through Eq. (1). Since the coordinate transformation preserves the volume element, we have

4. A surface ionization detector (SI) measures flux; an electron bombardment detector (EB) measures number density. The transmission of a velocity selector (VS) is proportional to v . Hence, for SI-VS data the observed intensity must be divided by v to obtain flux, whereas for EB-VS the data is already in flux form.

$$v^2 dv d\Omega = u^2 du d\omega. \quad (5)$$

This yields, together with (4),

$$I_{cm}(u) = \frac{u^2}{v^2} I_{LAB}(v). \quad (6)$$

This relation was first recognized by Entemann.²

We have thus quite simply solved the problem of obtaining the c.m. reactive scattering differential cross section as a function of scattering angle and speed of recoil for our ISE. All we need do is apply Eqs. (2a) and (3) and multiply all of our LAB intensities by the Jacobian factor u^2/v^2 as in Eq. (6). In this way we generate another surface, this one in the c.m. system. Such surfaces are conveniently displayed as polar constant-intensity-contour maps.

(See Chapters II and IV for examples.)

Unfortunately, we must be content with something less than an ISE at the present level of technological development, due primarily to the very low intensities concomitant with energy-analyzed reactants.⁵ Allowing one or both of the reactant beams to have distributions in velocity enormously complicates the kinematic problem, for we can no longer rigorously consider a single Newton Diagram as before, but must now take into account an infinite set of them. This implies that ξ and η no longer have uniquely defined magnitudes or directions in the LAB frame, and hence both the translation and rotation transformation relations differ for different Newton Diagrams. In effect, the c.m.

5. The well-known narrowing of the velocity distribution in a supersonic beam offers a promising way out of the monochromatization-intensity dilemma.

cross section $I_{cm}(u)$ has been averaged over the beam distributions, and the $I_{LAB}(v)$ we observe is related to it, not by Eq. (6), but by an integral equation,^{2,6}

$$I_{LAB}(v) = \int_0^{\infty} dv_1 \int_0^{\infty} dv_2 n_1(v_1)n_2(v_2) v \frac{v^2}{u} I_{cm}(u, v), \quad (7)$$

where n_1 and n_2 are the number density speed distributions of the reactant beams, and other symbols have been previously defined. It has also become necessary to include any initial energy dependence of the c.m. cross section, such as would be caused by a chemical activation energy barrier, since V potentially can vary from zero to infinity. The product $n_1(v_1)n_2(v_2)V$ can be regarded as the probability for occurrence of the Newton Diagram corresponding to (v_1, v_2) .

Entemann² has written a Fortran IV computer program which uses an assumed parametric form for $I_{cm}(u, v)$ and averages it over a finite number of Newton Diagrams to obtain $I_{LAB}(v)$. This program has formed the basis for all of the present work.

D. Methods of Analysis: Nominal and Stochastic

Let us assume that we have still been able to velocity analyze one of the reaction products, while allowing one or both of the reactant beams to retain their normal distributions; we will refer to this arrangement as an "ordinary" sophisticated experiment (OSE). The

6. The averaging effect of beam divergence has not been included, since trial calculations have shown that this effect is negligible compared with that of the velocity-averaging.

simplest approximation we can make to get some idea of the c.m. scattering is one we shall call the Nominal Newton Diagram Approximation (NNDA). In this method we select the parent beam velocities corresponding roughly to the most probable Newton Diagram,⁷ and do the transformation exactly as in the ISE case. Depending on the character of the actual $I_{cm}(u, V)$, this procedure yields a more or less accurate approximation to the "true" cross section.^{8,9} A notable virtue of the NNDA is that no assumptions about the functional form of $I_{cm}(u, V)$ need be made. An adaptation of the Entemann program written by Riley⁹ to velocity average the NNDA cross section, assuming it is independent of initial velocity, has shown that it also reproduces the main features of the LAB data fairly well. It is important to realize, at this point in our discussion, that the only criterion we have for the validity of the $I_{cm}(u, V)$ is how well it can reproduce the observed intensities. In testing the above and later methods, however, we can always start with a known c.m. function, use the Entemann program to obtain the LAB intensities which would result from it, and then see how well a given method of analysis will do, both in recovering the c.m. function and then reproducing the LAB data. It has been found empirically, as might be expected, that, due to the blurring effect of

7. Entemann, Ref. 2, gives a convenient graph for determining these velocities.

8. See Fig. 2 and Chapter IV.

9. S. J. Riley, Ph.D. Thesis, Harvard University, Cambridge, Mass., 1970.

the velocity averaging, the derived c.m. function can be fairly far from the "true" one, and still give percentagewise a decent fit to the LAB intensities.

In order to make further progress toward improved analytical procedures, it has been convenient to make assumptions about the functional form of $I_{cm}(u, v)$. The usual ansatz has been that the cross section can be written as a product of independently varying functions,^{2,10} as

$$I_{cm}(u, v) = T(\theta)U(u)V(v). \quad (8)$$

In the so-called "stochastic procedure" of Entemann,² convenient parametric forms are chosen for T , U and V , and one then proceeds to iterate between Mallinckrodt and the Computation Center until the hand-adjusted parameters reproduce the LAB data more or less well, or one becomes weary, whichever comes first. For our OSE, where there are often 400 or more LAB data points to be fitted, the latter case has held more often than not. In addition, recent experimental results¹¹ and trajectory studies¹ indicate that the "separability" assumption of Eq. (8) does not hold in general. The initial relative velocity may well influence the shape of the c.m. surface, and the first two factors of (8) can be strongly coupled.¹¹ It has been shown experimentally, however, for the $K + Br_2$ reaction, that the form of $I_{LAB}^{(KBr)}(v)$ is substantially unaffected by varying the initial

10. See, for example, K. T. Gillen, C. Riley and R. B. Bernstein, J. Chem. Phys. 50, 4019 (1969).

11. See Chapters II and IV.

velocity in the thermal range.¹² In practice, $\gamma(V)$ invariably has been set equal to unity.

E. Methods of Analysis: Least Squares Fit

It is clear that a procedure which would allow the computer to adjust the c.m. cross section parameters would be a great improvement over the stochastic method, and might also eliminate the necessity for assuming Eq. (8). In order to develop such a procedure, it is also apparent that we must use our OSE LAB data as input. These two facts point to the method of least squares¹³ as ideally suited to the problem. In this well-known method, we begin the analysis by forming the sum of the squares of the differences between the observed quantity $p_i^{(o)}$ and that which is calculated from some assumed parametric function, $p_i^{(c)}$, i.e.,

$$S = \sum_{i=1}^N w_i (p_i^{(o)} - p_i^{(c)})^2, \quad (9)$$

where $p_i^{(c)} = p_i^{(c)}(a_1, a_2, \dots, a_n)$. Here N is the total number of data points, w_i is a weighting assigned to each point (usually determined on the basis of an error analysis), and the $\{a_j\}$ are the n parameters on which $p_i^{(c)}$ depends. Our fitting criterion is the minimization of S , from which the method derives its name, so we proceed to set the derivative of S with respect to each of the

- 12. (a) J. H. Birely and D. R. Herschbach, *J. Chem. Phys.* 44, 1690 (1966); (b) A. E. Grosser and R. B. Bernstein, *J. Chem. Phys.* 43, 1140 (1965).
- 13. See for example, A. Ralston, "A First Course in Numerical Analysis", Ch. 6, McGraw-Hill, New York, 1965.

parameters a_j equal to zero. This gives rise to a set of n simultaneous equations, often called the normal equations, in the n parameters,

$$\sum_{i=1}^N w_i (p_i^{(o)} - p_i^{(c)}) \frac{\partial p_i^{(c)}}{\partial a_j} = 0, \quad j = 1, 2, \dots, n, \quad (10)$$

the solutions of which will yield the best fit to the data according to our criterion. To simplify the problem, we would like to make Eqs. (10) linear in the $\{a_j\}$. Since (10) contains terms linear in $p_i^{(c)}$, the only way this can be done is to make $p_i^{(c)}$ a linear function of the $\{a_j\}$, i.e.,

$$p_i^{(c)} = \sum_{k=1}^n a_k f_{ki}, \quad (11)$$

where the $\{f_{ki}\}$ are functions of the independent variables in the problem only. Since

$$\frac{\partial p_i^{(c)}}{\partial a_j} = f_{ji}, \quad (12)$$

independent of the $\{a_j\}$, this choice of parametric form does indeed make Eqs. (10) linear in the $\{a_j\}$. Substituting (11) and (12) into (10), we obtain

$$\sum_{k=1}^n \sum_{i=1}^N w_i f_{ki} f_{ji} a_k = \sum_{i=1}^N w_i f_{ji} p_i^{(o)}, \quad j = 1, 2, \dots, n, \quad (13)$$

which is succinctly written in matrix notation as

$$\begin{aligned} \mathbf{T} \mathbf{a} &= \mathbf{b}, \\ \text{where } (\mathbf{T})_{kj} &= \sum_{i=1}^N w_i f_{ki} f_{ji}, \quad (\mathbf{a})_k = a_k \text{ and } (\mathbf{b})_j = \sum_{i=1}^N w_i f_{ji} p_i^{(o)}. \end{aligned} \quad (13a)$$

\tilde{T} is called the normal matrix and is clearly a symmetric matrix; by effectively inverting it we may solve Eqs. (13) for the desired parameter vector \tilde{a} . The standard deviation, which we define as

$$\sigma = \left[\frac{S}{N-n} \right]^{\frac{1}{2}}, \quad (14)$$

can then be calculated as a measure of the goodness of the fit. Note that this definition of σ guards against "over-fitting" the data (reproducing insignificant noise) with too many parameters through the denominator $N-n$. Since there will be a certain amount of random noise in any experimental data, we would like to allow our calculated function to retain any smoothing properties it might have.

We are now ready to apply these results to the kinematic problem. To begin with, it is apparent that in order to make the calculated LAB intensities linear functions of the parameters, which we shall again refer to as the $\{a_j\}$, it suffices to write the c.m. cross section as a linear function of the parameters. Since from a single OSE run at a given nominal initial kinetic energy, we have no sufficient criterion for determining the exact (possibly coupled) V dependence of $I_{cm}(u, V)$, we will assume that V has no influence whatever on the cross section, and take¹⁴

$$I_{cm}(u, V) = \sum_{j=1}^n a_j f_j(u), \quad (15)$$

14. Note that there is no need to make the "separability" assumption for the u dependence.

which yields, from Eq. (7)

$$I_{LAB}^{(c)}(v) = \sum_{j=1}^n a_j F_j(v), \quad (16)$$

where

$$F_j(v) \equiv \int dv_1 \int dv_2 n_1 n_2 v \frac{v^2}{u^2} f_j(u). \quad (17)$$

With the cross section in this form, it is a simple matter, once the $F_j(v)$ have been calculated, to apply the above least squares procedure to obtain the best \vec{a} vector. It remains for us to choose an analytic form for the $f_j(u)$.

Chronologically, the first form chosen was such as to make $I_{cm}(u)$ a weighted two-dimensional polynomial in the c.m. cartesian components of u , i.e.,

$$f_j(u) = \exp[-(u/u_0)^2] u_x^k u_y^l, \quad (18)$$

where k and l are independently limited (rather than their sum) and u_0 is a scaling parameter. It was found empirically that the inclusion of the Gaussian form factor, which realistically forces the cross section to die off at large u , improved the fits obtained with this functional form. Though this form for $I_{cm}(u)$ seemed adequate for fitting most of the LAB data to which it was applied,¹¹ several aspects of the analysis made it less desirable. The first and most easily noticed difficulty is the tendency for the polynomial to oscillate badly near and beyond the edge of the region of velocity space covered by the LAB data, and also in regions requiring a good deal of interpolation, as at 0° and γ in the LAB (the beam positions). A further discussion of this latter problem will be given later when

prevalent data collection techniques are taken up. The second and more fundamental problem is the fact that, as the degree of the polynomial is raised, the normal matrix T becomes increasingly ill-conditioned, in exact analogy with the one-dimensional polynomial case.¹³ It was not strictly determined whether double precision arithmetic on the IBM 7094 computer is sufficient to solve the normal equations accurately for a 36-term function ($k_{\max} = l_{\max} = 5$), the order usually used in the data analysis. But in a test calculation on computer-generated "data" using both single and double precision the two sets of coefficients obtained did not compare very well; many differed by an order of magnitude or more and some changed sign. The resulting c.m. function and LAB fits were less affected, the double precision calculation being somewhat better. In any event, whether this form could rigorously recover the original cross section cannot be tested through increasing the number of terms because of the ill-conditioning problem.

It is well known¹³ that the use of series of functions which are rigorously or even approximately orthogonal over the range of the argument of a "sampled" function such as $I_{LAB}(y)$ to fit it in a least squares sense circumvents the ill-conditioning difficulty incurred in using the polynomial form. It was also expected that the use of such functions would produce a smoother $I_{cm}(u)$ which would converge uniformly to the "true" cross section with a sufficient number of terms. For these reasons we chose

$$f_j(u) = \exp(-u/u_0) \left(\frac{2u}{u_0} \right)^2 L_n^{(4)} \left(\frac{2u}{u_0} \right) P_\ell(\cos\theta), \quad (19)$$

where¹⁵ $L_n^{(\alpha)}(x)$ is the generalized Laguerre polynomial of degree n and order α , orthogonal over $(0, \infty)$ with respect to the weight function $x^\alpha e^{-x}$, $P_\ell(x)$ is the Legendre polynomial of degree ℓ , orthogonal over $(-1, 1)$ with respect to unit weight function, the premultiplying factors are just the square root of the Laguerre weight function, and u_0 is again a scaling parameter. As before, n and ℓ are independently limited. The order 4 was chosen for the Laguerre function in order to eliminate the often-troublesome Jacobian singularity encountered in the evaluation of $F_j(y)$ (Eq. (17)) by cancellation of the u^{-2} factor. Although an OSE can never span all of velocity space, over which (19) are orthogonal, use of (19) results in $F_j(y)$ which are approximately orthogonal over the range of LAB data for typical OSE experiments (such as those of Chapter II). Inspection of the T matrix reveals that the diagonal elements are usually larger than any off-diagonal elements by an order of magnitude or more; the ill-conditioning has thus been eliminated. Moreover, calculations performed with 16 ($n_{\max} = \ell_{\max} = 3$), 36 ($n_{\max} = \ell_{\max} = 5$), and 100 ($n_{\max} = \ell_{\max} = 9$) terms in $I_{cm}(y)$ show that this functional form is smoothly convergent on the original c.m. function (a different functional form involving Gaussian angular dependence, fractional powers of u , and

15. M. Abramowitz and I. A. Stegun, eds., "Handbook of Mathematical Functions", National Bureau of Standards, A. M. Series No. 55, 1964.

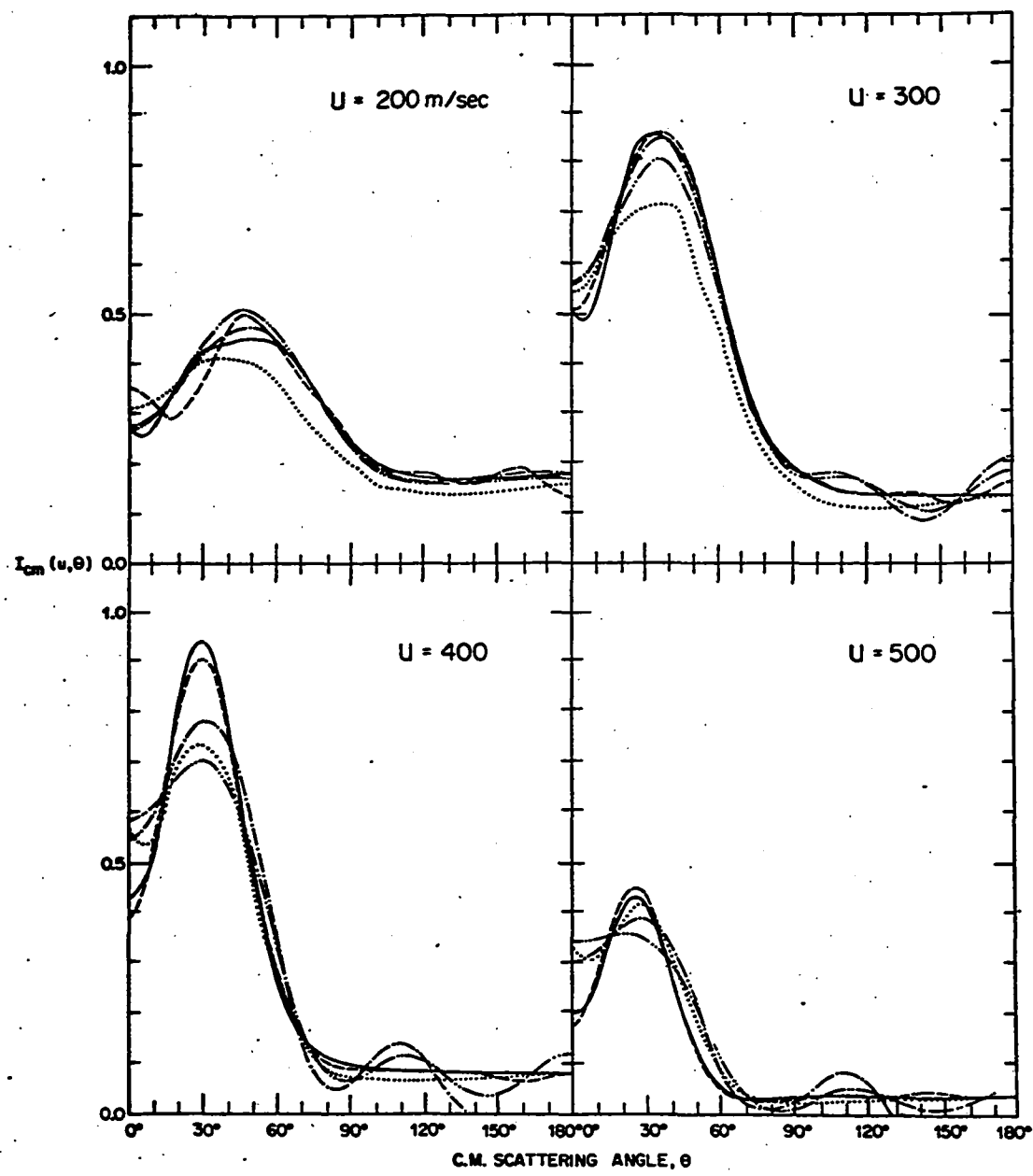
nonseparability). Figure 2 shows plots of the 36-term and 100-term c.m. results along with those from the NNDA analysis and the original $I_{cm}(u)$ as a function of scattering angle θ for various values of u . Defining the standard error of the LAB fit by $\sigma/I \times 100\%$, where I is the average magnitude of $I_{LAB}(y)$, the 36-term function fitted the data within 5%, the 100-term function within 0.5%. Plots of the data were virtually indistinguishable from those of the velocity-averaged 100-term function. (These are not shown, but see Chapter IV for examples of data plots.) More details of the calculation will be presented below.

Now regarding the form (19) as more desirable, the remainder of the OSE discussion will concern it only. So far the parameter u_0 has remained unspecified. It was decided to use the NNDA cross section as a criterion for choosing u_0 ; noting that the square root of the Laguerre weight function has its maximum at $u = 2u_0$, a good choice for u_0 should be one-half of the value of u at which the NNDA cross section peaks. The "form factor" for the orthogonal polynomial series thus is made to peak near the maximum of the "true" $I_{cm}(u)$. In practice, both the c.m. cross section and the LAB fits have been found to be rather insensitive to the exact value of u_0 .

We also have not specified a choice for the least-squares weights w_i in Eq. (9). It should be noted that the least-squares procedure inherently weights the larger data points: a given percentage error in fitting a large point gives a greater contribution to the sum in (9) than the same error in fitting a small point. Hence for $w_i \equiv 1$

Fig. 2. Center-of-mass reproductions by the NNDA and least-squares (LS) methods of a trial c.m. cross section (—) from which artificial laboratory data was generated for the analysis.

Kinematic conditions were appropriate to the Cs + CCl_4 reactions of Chapter II., NNDA; - - -, 100-term LS; - - -, 36-term LS, $w_i = 1$; - - -, 36-term LS, $w_i = [p_i^{(0)}]^{-1}$. The curves shown are constant velocity contours at four representative recoil velocities.



the procedure will minimize the absolute differences between calculation and observation, and observed points with relatively small magnitude will receive little weight. In an experiment, the signal-to-noise ratio may be quite favorable, and the small points may have absolute errors comparable to or even smaller than those of the large ones. This suggests that, for such experiments, we should weight the data points inversely as their magnitudes. For our case, the cross section parameters themselves have no physical significance; only the shape of the cross section has meaning. It has been found empirically that, although the choice of data weights has an appreciable effect on the numerical values of the individual parameters, the cross section shape and LAB fits are much less affected. Two weighting schemes have been tried, $w_i = 1$ and $w_i = [P_i^{(0)}]^{-1}$, and the LAB fits for all systems so far analyzed using both schemes are quite comparable; one or the other weighting will give a slightly better fit, depending on the character of the data. The $I_{cm}(\mu)$'s obtained are somewhat less similar, but with no striking differences. The latter weighting has been generally preferred.⁹

In order to clarify further the exact nature of the kinematic problem, it is necessary to take into account the prevailing methods used to sample the $I_{LAB}(v)$ surface, i.e., methods of data collection. S. J. Riley⁹ has given a complete description of the two-filament method of surface ionization detection used for alkali atom-halogen compound reactions. The almost universal method used to sample $I_{LAB}(v)$ has been to take complete velocity spectra at various LAB

angles Θ ,¹⁶ a natural extension of the technique used for primitive experiments, which are described below. The data point positions can be represented on the Newton Diagram of Fig. 1 as lying along rays emanating from the LAB origin at the tails of x_1 and x_2 . The region of velocity space accessible to measurement is usually limited by the mutual physical interference of the detector and the beam sources, and by the limiting rotor frequency of the velocity analyzer. For the Harvard molecular beam apparatus "Bertha"^{9,17} these limits are approximately $-30^\circ \leq \Theta \leq 100^\circ$ (the sense of Θ is defined in Table I) and $0 < v < 1000$ m/sec. The Wisconsin apparatus¹⁰ is limited to $0^\circ \leq \Theta \leq 90^\circ$ with similar limits on v , the smaller angular range apparently due to the presence of the primary beam velocity selector. The regions within $\pm 10^\circ$ of each beam are also generally inaccessible, at least in the alkali experiments, due to the huge background of (detected) small-angle elastic scattering near the alkali beam, and to the "poisoning" effects associated with long exposure of the filaments to the intense crossed beam. Data has usually been taken every 10° , occasionally every 5° .

These circumstances combine with a specific kinematic effect to make certain regions of $I_{cm}(\mu)$ as determined by the least squares procedure less reliable. The kinematic effect is the "blurring out" of the low-velocity region of the c.m. cross section due to the

16. See for example Refs. 9, 10, 12 and Chapter IV.

17. K. R. Wilson, Ph.D. Thesis, University of California, Berkeley, California, 1964; R. Grice, Ph.D. Thesis, Harvard University, Cambridge, Mass., 1967.

comparable-in-magnitude spread in C ; the uncertainty of the velocity-space origin of the c.m. frame as viewed in the LAB system makes itself felt most strongly here. In addition, the gaps in the data at the beam positions force an interpolation by the c.m. functional form, the results of which will very much depend on the exact analytic form used. Finally, significant regions of the cross section may lie outside the range of the LAB data. For these reasons the results of the analysis of an OSE using the above method, i.e., the $I_{cm}(\nu)$ obtained, must be interpreted with some caution. A consideration of the velocity spread in the reactant beams to get an approximate idea of the spread in C , along with a most probable Newton Diagram with data rays drawn in, can easily show which regions of $I_{cm}(\nu)$ are not to be trusted.

F. Computational Details

We can now discuss in more detail the actual calculations. The Entemann program,² as modified by the author,¹⁸ has provided the basic framework for the present calculations. The main task is the calculation of the $F_j(\nu)$ of Eq. (17). The beam velocity distributions n_1 and n_2 are entered in parametric form, and the integrations performed using a trapezoidal rule out to twice the peak velocity for each beam. In practice, the use of ten-point grids along each beam has proven to

18. See the Appendix to this chapter for a listing of the computer program and discussion of details.

be sufficient to produce an $I_{cm}(u)$ and a back calculation nearly completely insensitive to further increases in grid density. For the test calculation alluded to earlier, computer "data" was generated using the modified Entemann program at 10° intervals for $-30^\circ < \theta < 110^\circ$, excluding 0° and 90° , the assumed beam positions. The least-squares analysis results, as mentioned, are shown in Fig. 2. The noticeable discrepancies near $\theta = 0^\circ$ and 180° for $u = 200$ m/sec, even for the 100-term function, in light of the preceding discussion, are easily accounted for, since examination of the most probable Newton Diagram for the system (Fig. 1) shows that $\theta = 0^\circ$, $u = 200$ m/sec lies directly in the primary-beam gap, and $\theta = 180^\circ$, $u = 200$ m/sec in the crossed-beam gap. There is also some effect due to the low-velocity blurring. This latter is particularly noticeable at $u = 100$ m/sec (not shown), where the calculated 100-term function shows a steady oscillation, or "ringing", about the original. When one considers that the LAB "data" in this region is very well fit (often to three figures), the seriousness of the blurring effect becomes apparent. The 36-term function is smoother at small u , but the fit to the "data" is also not as good. It seems clear that, were the "true" cross section to have much structure at low recoil velocities, it could not be recovered very well with this method. These points serve to underline the fact that extreme care must be used in interpreting a c.m. function obtained in this way.

In use, the 36-term function has been adequate for fitting virtually all the LAB data to which it has been applied;⁹ standard

errors were usually less than 10%, well within experimental error, for 400 or more data points covering about a 100° range on the average. The 36-term Laguerre-Legendre series is therefore recommended for general use; in Chapter IV specific examples are given where the optimum number of parameters can be objectively chosen.

G. Analysis of Primitive Experiments

We now turn to the consideration of the so-called primitive experiments (PE), those in which the product is not velocity-analyzed but only the total flux is measured as a function of LAB scattering angle Θ . We are forced to include in this category even those experiments in which one or both of the parent beams is velocity-selected. It is quite clear that much less information is to be had from such an experiment, for one no longer has any information concerning the distribution in magnitude of v , but only its direction in the LAB. What we measure in a PE are the areas under the velocity spectrum curves of the OSE (or ISE), and we learn nothing about their shapes or peak positions. We can write the measured intensities as

$$\mathcal{J}_{LAB}(\Theta) = \int_0^{\infty} I_{LAB}(v, \Theta) dv. \quad (20)$$

In this case one has no way of assessing the degree to which the magnitude and angle of v are coupled or uncoupled; we therefore must resort to restricting the form of $I_{cm}(u, v)$ in order to obtain any information whatever about its functional dependence. It seems natural to adopt Eq. (8) as our assumption.

Prior to the later work of Entemann² the analysis which had been followed is known as the Fixed Velocity Approximation¹⁹ (FVA). It assumes that the cross section has the form

$$I_{cm}(u, v) = T(\theta) \delta(u - u_0), \quad (21)$$

in which case the LAB \rightarrow c.m. coordinate transformation is unique for a given Newton Diagram, since, for a given θ , χ is fixed by Eqs. (1) and (21). Choosing the most probable Newton Diagram, and using the intensity transformation appropriate for a fixed recoil velocity,^{2,19}

$$I_{cm}(v) = \frac{u^2 \cos(u, v)}{v^2} I_{LAB}(\chi), \quad (22)$$

the PE data can be transformed directly into a c.m. angular distribution for a given value of u_0 . The best u_0 is determined by requiring symmetry about v : data taken on the positive and negative c.m. angle sides of χ should fall on the same curve.

The FVA analysis for PE's is in much the same spirit as the NNDA for OSE's; in the latter case one has measured the surface $I_{LAB}(\chi)$ and obtains an approximate $I_{cm}(v)$ surface, while in the former one has only an angular distribution $I_{LAB}(\theta)$ and obtains an approximate c.m. angular distribution $T(\theta)$.

Subsequent OSE's¹² and analysis^{2,9} on the K + Br₂ reaction have indicated that the FVA angular distribution for this system is too broad, as expected, and that the value of u_0 obtained from this analysis is not reliable. The most probable recoil energy as obtained from u_0 was too low by almost a factor of two when compared with that

19. J. H. Birely, R. R. Herm, K. R. Wilson, and D. R. Herschbach, J. Chem. Phys. 47, 993 (1967); see Ref. 2 for details.

obtained from analysis of the OSE's.

Entemann's "stochastic" procedure² represents some improvement over the FVA, the c.m. \rightarrow LAB transformation being performed rigorously with velocity averaging, while allowing for a spread in recoil speeds. As mentioned earlier, the form (8) is used in this analysis, with $\gamma(V)$ usually set equal to unity. The main disadvantage of this method, as before, is that the cross section parameters must be hand-adjusted. In addition, it would seem that allowing both $T(\theta)$ and $U(u)$ to be completely free parametric functions permit a little too much freedom in fitting a PE angular distribution. This fact becomes apparent in comparing some of the c.m. functions used to fit PE data² with subsequent results from OSE's.¹¹

As mentioned above, our approach will also begin with the assumption of (8) as the form for $I_{cm}(u, V)$, again with $\gamma(V) = 1$. We would like to apply a method similar to that used for the OSE analysis here also. We begin by noting that the function $U(u)$ is more easily characterized than $T(\theta)$; the former must go to zero at $u = 0$ and $u = \infty$ and can generally be expected to have a unique maximum (at least in an average sense), while the latter is not similarly constrained as a function of θ . The work of J. C. Polanyi and collaborators²⁰ on hydrogen-halogen reactive systems with an HX product (X = halogen) to obtain the (angle-averaged) internal energy distributions in HX serve to determine essentially completely the $U(u)$ function through energy

20. K. G. Anlauf, P. J. Kuntz, D. H. Maylotte, P. D. Pacey, and J. C. Polanyi, Disc. Faraday Soc. 44, 183 (1967); K. G. Anlauf, J. C. Polanyi, W. H. Wong and K. B. Woodall, J. Chem. Phys. 49, 5189 (1968).

conservation. Alternatively, if the reaction is suspected to proceed via a long-lived collision complex, one can use the RRKM theory or the phase-space theory of reactions to predict $U(u)$.²¹ If neither of the above is the case for the reaction being analyzed, as a matter of convenience one can assume a (flux) Boltzmann shape for $U(u)$ and retain the peak position as a free parameter.

Assuming one knows the $U(u)$ function, the least-squares determination of $T(\theta)$ by fitting the LAB data can then be attempted. We again desire a linear form for the normal equations (10), so we write

$$T(\theta) = \sum_{j=1}^n a_j f_j(\theta). \quad (23)$$

Again using Eq. (7) with Eq. (20) we obtain

$$\mathcal{J}_{\text{LAB}}^{(c)}(\theta) = \sum_{j=1}^n a_j \mathcal{F}_j(\theta), \quad (24)$$

where

$$\mathcal{F}_j(\theta) = \int_0^\infty dv \left[\int dv_1 \int dv_2 n_1 n_2 V \frac{v^2}{u^2} U(u) f_j(\theta) \right]. \quad (25)$$

As before, once the $\mathcal{F}_j(\theta)$ are calculated, we can easily determine the best a vector from the least squares analysis.

Enlightened by our previous experience with choosing an optimum form for each term in the series used to represent $I_{\text{cm}}(u)$, we choose

$$f_j(\theta) = P_j(\cos\theta), \quad (26)$$

where $P_j(x)$ is again the Legendre polynomial of degree j , orthogonal

21. S. A. Safron, Ph.D. Thesis, Harvard University, Cambridge, Mass., 1969.

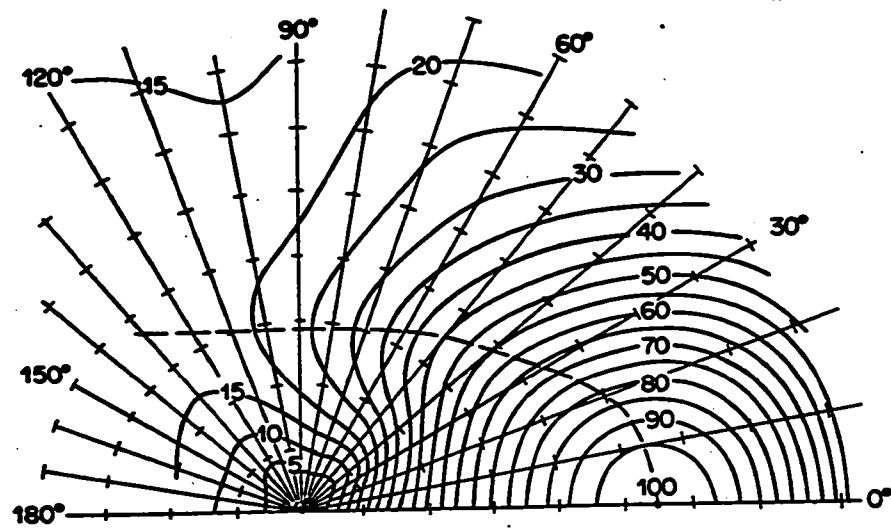
on $(-1,1)$ with unit weight. Again, since our measurements cannot cover the entire velocity space, the use of (26) results in $\tilde{F}_j(\theta)$ only approximately orthogonal over the range of θ ; but this choice nonetheless again eliminates the ill-conditioning difficulty that would have been encountered in using a polynomial in $\cos\theta$.

Computer-generated "data" were again used to test the method. It was found that a six-term function for $T(\theta)$ ($l_{\max} = 5$) provided a fit to the data within 1% standard error and reproduced the original $T(\theta)$ (a Gaussian form) to about 5%. An eight-term function fitted the data exactly to 4 significant figures, while providing a $T(\theta)$ differing by at most 0.5% from the original. These calculations were performed, of course, using the "true" $U(u)$. Varying the shape and peak position of the $U(u)$ used in the least squares procedure as compared to the original function resulted in $T(\theta)$'s quantitatively quite different from the "true" one, but qualitatively similar (as in peak position) if the changes in $U(u)$ were not too drastic. Any such alterations, of course, worsened the fit to the data. Figure 3 presents the c.m. results of these calculations for both narrow and broad $T(\theta)$'s. The examples shown are somewhat unfavorable kinematically (low recoil velocity), so that the $T(\theta)$ obtained would usually not be as sensitive to changes in $U(u)$ as in Fig. 3.

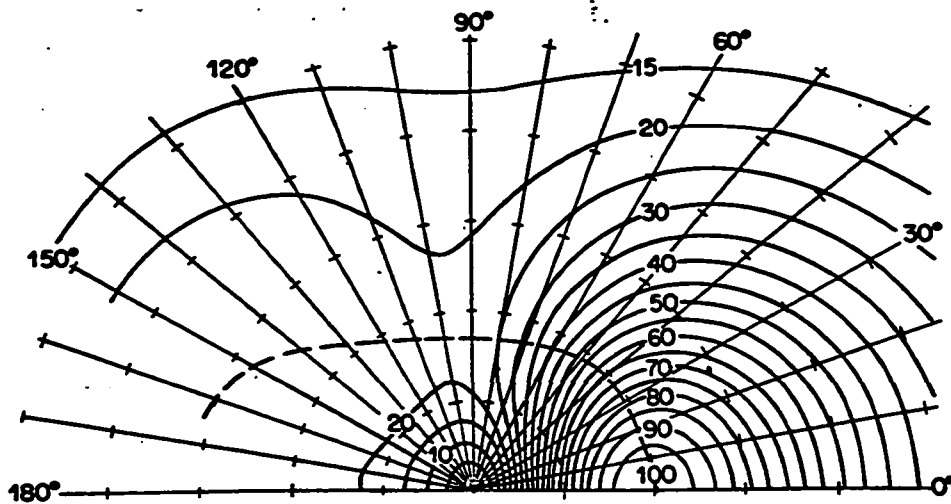
Except for systems with very small cross sections, the experimental difficulty associated with measuring signals near the beams is not nearly so severe as in the OSE case. For the two-filament surface ionization method, the increase in intensity over the OSE usually

Fig. 3. "Optimum" center-of-mass constant-intensity contour maps for MBr from K and Cs + Br₂ generated from 36- and 16-term functions, respectively. Tic marks define 100 m/sec intervals. Note change in velocity scale in going from K to Cs. To get recoil distribution at a given angle, read out along an angular ray; for angular distribution at constant velocity, follow tic marks around origin. Dashed lines represent loci of recoil peaks.

$K + Br_2$



$Cs + Br_2$



allows measurements within 5° of the alkali beam, and the fact that a long exposure of the filaments to the crossed beam is not required to make measurements there generally permits a determination of $\mathcal{I}_{LAB}(\theta)$ which includes $\theta = \gamma$, the intersection angle. In the test calculations an angle spacing of 5° between data points was used; many experiments have been done using a smaller spacing, and all have used at most 5° .

In practice, it has been found that a six-term function for $T(\theta)$ has been adequate to fit experimental data within 5% standard error for a reasonably good choice of $U(u)$. In the absence of a priori information, a Boltzmann flux shape has been used and the peak varied to give the best fit to the data (see Chapter IV of this thesis). This approach is analogous in form to that of the FVA, except that the cross section obtained is rigorously related to the LAB data.

A computer program to carry out the above analysis, very similar to that previously cited for the analysis of OSE's, is presented in the Appendix. The calculational procedure used here differs slightly from that described above; a coarser grid was used for the integration over the beam distributions (six points along each beam) and the additional integration required in Eq. (25) was again performed using a trapezoidal rule, this with a 32-point grid to average out any inconsistencies caused by the coarser beam grids. It was found that increasing any of the grid densities further had no significant effect on either the $T(\theta)$ obtained or the LAB fit.

H. Discussion

The least squares methods of kinematic analysis of reactive scattering presented above seem capable of extracting the maximum amount of information about the c.m. cross section consistent with the kind and quality of data being analyzed. These procedures essentially represent an extension of the work of Entemann.² The NNDA method for OSE's, however, is a simple new approach for obtaining an approximate c.m. map; more detail on this method can be found elsewhere.⁹

All the calculations presented here lead to some natural conclusions regarding the experiments under consideration. It was clear from the outset of our discussion that any kind of velocity selection would yield better information than would be had in its absence, but in the light of this work it appears that velocity analysis of the reaction products allows a far more accurate determination of the c.m. scattering than the selection of one or even both of the reactant beams. As was made clear in the section on PE analysis, an OSE measures the (velocity-averaged) shape of the $I_{LAB}(v)$ surface, while an experiment without product velocity analysis (which we have referred to as a PE), even though both beams may have been monochromatized, measures only the areas under certain cuts across $I_{LAB}(v)$, and is thus inherently less sensitive to the exact shape of $I_{cm}(u)$.

Another main result of these calculations has been the fairly quantitative determination of the effects of velocity-averaging on our ability to extract the correct c.m. cross section from the data. It has been found from the test calculations that a least-squares

determined $I_{cm}(y)$ which reproduces the data to a certain standard error, is usually about a factor of 2-10 worse percentagewise in reproducing the original c.m. cross section. The averaging, particularly at low c.m. velocities, has the effect of "covering up" discrepancies between the actual scattering function and an approximation to it. If the data were completely noiseless (referring now to an OSE), most of $I_{cm}(y)$ could be determined quite accurately, as demonstrated by the test calculations; since this can never be the case, the uncertainties in $I_{LAB}(y)$ will lead to much larger ones in $I_{cm}(y)$ due to the averaging inherent in an OSE. In an ISE, of course, the errors in the LAB and c.m. frames would be identical (both probably very large, due to the low intensities likely to accompany any attempt at such an experiment).

The kinematic problem with velocity-averaging can be regarded as a problem in "deconvolution" or "unfolding". The flux distribution in y vectors has been "folded in" with the distribution in ζ to give $I_{LAB}(y)$. McDonald²² has developed an iterative deconvolution scheme for OSE's based on the one-dimensional method of Ioup and Thomas.²³ But the method is severely noise-limited; random noise is magnified at each iteration and can cause the method to diverge before the "unfolded" $I_{LAB}(y)$ is reached. An iterative smoothing technique similar in form to the unfolding has been tried,²² but it can remove only that noise which is "incompatible" with the beam distributions, and tends

22. J. D. McDonald, unpublished work.

23. G. E. Ioup and B. S. Thomas, J. Chem. Phys. 46, 3959 (1967).

to allow a certain amount of noise to remain. The least squares procedure does not suffer from this problem; it is expected to smooth out any random uncertainties in the LAB back-calculation.

APPENDIX

Computer Programs for Kinematic Analysis

This appendix presents three Fortran IV computer programs for kinematic analysis of reactive scattering in crossed molecular beams. The first, which has many features common to all three, is a direct adaptation of the Entemann program; its main advantages over the original program are its increased simplicity and about a factor of two in speed. Its one disadvantage is its inability to handle out-of-plane scattering; in view of prevalent experimental techniques, this is not considered a serious drawback.

The basic operation of this program is as follows. The user specifies the initial conditions (beam velocity distributions, masses, and other system parameters), the c.m. cross section parameters, the grid density to be used in the velocity averaging, and a set of LAB velocity vectors γ at which the product intensity is to be calculated, in the form of constant-LAB-angle (Θ) rays with a set of γ 's along each ray. Then, for each grid point (Newton Diagram), the specified LAB velocity is transformed to a c.m. velocity u using the relations outlined in Section B of this chapter, and the c.m. cross section calculated from u and the input parameters, multiplied by the intensity Jacobian to convert it to LAB units, and weighted according to the probability of the Newton Diagram under consideration. Included in this weighting is a damping factor which allows internal energy of an assumed diatomic reactant to contribute if the energy corresponding to the u called for exceeds the available kinetic and chemical energy.

When the weighted sum over the grid is taken, the result is the desired LAB product intensity at the given velocity, averaged over initial conditions. An intensity-versus-velocity curve for a given Θ generated in this way can then be integrated to give a total intensity at Θ . The output of the program thus consists of a set of velocity spectra at various Θ , comparable to the results of a product velocity analysis experiment, and a LAB angular distribution, to be compared with primitive experiment measurements.

As mentioned in the text, the functional form for the c.m. cross section is taken to be a "separable" one, as in Eq. (8). Entemann² describes in detail and gives typical plots of the particular parametric forms used in this program.

For reference the program has been given the main deckname "CMLB". Table II gives a complete description of punched card input for CMLB, followed by a Fortran listing; the user should note that the formats used for input are arbitrarily chosen and can easily be changed for convenience. For a typical run with 20 angles, 20 velocities at each angle (400 LAB points), averaged over 36 Newton Diagrams, the program shows a time (including tape access) of ca. 0.8 minutes on the IBM 7094 computer. The time expended rises roughly linearly as the number of LAB points and the grid density; thus a 100-Newton-Diagram, 800 point run would take ca. 4.5 minutes. The increased efficiency over the original version is due largely to the simplification of the coordinate transformation through the in-plane restriction.

The second program, which embodies the least squares procedure

Table II. CMLB input and listing

<u>Variable</u>	<u>Meaning</u>
.....	(The first card to be read contains a "1" in col. 1, followed by user's comments).
IPUNCH.....	IPUNCH.NE.0 indicates punched-card output is desired.
NVA,NVB.....	The number of grid points to be taken along the primary ($\theta = 0^\circ$) beam and crossed beam velocity distributions for the velocity averaging; must be even integers, and are usually equal.
NGAM.....	The number of intersection angles to be averaged over for an assumed triangular distribution; must be an odd integer. <u>Note:</u> The product NVA*NVB*NGAM must not exceed 400.
GA, GB.....	Reactant masses for the primary and crossed beams, resp., in a.m.u.
GAMMA.....	Most probable intersection angle, in deg.
HWIDB.....	FWHM of the triangular distribution in intersection angle.
VAPAR, VBPAT arrays..	Velocity distribution parameters for the primary and crossed beams, resp.; five parameters for each beam. Denoting the parameters by P_i , $i = 1,5$, the functional form used is

$$n(v) = \begin{cases} \left(\frac{v}{P_1}\right)^{P_2} \exp\left\{\frac{P_2}{P_3}\left[1 - \left(\frac{v}{P_1}\right)^{P_3}\right]\right\}, & v \leq P_1, \\ \left(\frac{v}{P_1}\right)^{P_4} \exp\left\{\frac{P_4}{P_5}\left[1 - \left(\frac{v}{P_1}\right)^{P_5}\right]\right\}, & v > P_1, \end{cases}$$

where the units of v are 10^4 cm/sec. For a Maxwell-Boltzmann beam, the parameters are α , P_2 , P_3 , P_4 , P_5 , where $\alpha = 1.2987/T/M$. For a measured distribution the parameters are easily determined by a least squares fit.

NTHL.....Number of LAB angles at which intensities are to be calculated, < 100 .

NV.....Number of LAB velocities for each angle.

XXV.....LAB velocity increment in units of 10^4 cm/sec; the velocities at which intensities are calculated are equally spaced from XXV to NV*XXV.

GC.....Mass of the product for which the calculation is to be done, in a.m.u.

DELTD0.....Reaction exothermicity in kcal/mole.

T.....Temperature of the polyatomic beam, °K.

THL array.....Set of LAB angles.

THPAR array.....c.m. angular distribution parameters, six in number. Again denoting the parameters by P_i , $i = 1, 6$, the functional form is

$$T(\theta) = \begin{cases} (1-P_4) \exp \left[-\ln 2 \frac{(\theta-P_1)^2}{P_3} \right] + P_4, & \theta < P_1, \\ 1, & P_1 < \theta < P_2, \\ (1-P_6) \exp \left[-\ln 2 \frac{(\theta-P_2)^2}{P_5} \right] + P_6, & \theta > P_2 \end{cases}$$

where θ is in degrees.

UPAR array.....c.m. recoil speed distribution parameters, five in number. The same functional form as for VAPAR and VBPAR.

```

C CMLB
C MODIFIED ENTEMANN CM-LAB TRANSFORMATION.
C FOR IN-PLANE REACTIVE SCATTERING ONLY.
    DIMENSION P(400),THL(100)
    DIMENSION FABG(400),CX(400),CY(400),E(400),COSTV(400),SINTV(400)
    DIMENSION VAPAR(5),VBPART(5),UPAR(5),THPAR(6)
    DATA R,Y/.0019872,.017453292/
100 READ(5,1000)
    READ(5,1001)IPUNCH
    READ(5,1001) NVA,NVB,NGAM,GA,GB,GAMMA,HWIDB
    G=GA+GB
    NGRID=NVA*NVB*NGAM
    READ(5,1002) (VAPAR(I),I=1,5)
    READ(5,1002) (VBPART(I),I=1,5)
C CALCULATION OF NEWTON DIAGRAM WEIGHTS AND TRANSFORMATION PARAMETERS.
    CALL CNEWT(NVA,NVB,VAPAR,VBPART,GA,GB,NGAM,GAMMA,HWIDB,FABG,CX,CY,
1 E,COSTV,SINTV)
    READ(5,1004) NTHL,NV,XXV,GC,DELTD0,T
    RT=R*T
    GFAC=.00119503*G*GC/(G-GC)
    READ(5,1003) (THL(I),I=1,NTHL)
    READ(5,1002) (THPAR(I),I=1,6)
    READ(5,1002) (UPAR(I),I=1,5)
    WRITE(6,1000)
    WRITE(6,1020)
    WRITE(6,1001) NVA,NVB,NGAM,GA,GB,GAMMA,HWIDB
    WRITE(6,1012) (VAPAR(I),I=1,5)
    WRITE(6,1022) (VBPART(I),I=1,5)
    WRITE(6,1021)
    WRITE(6,1004) NTHL,NV,XXV,GC,DELTD0,T
    WRITE(6,1024) (THPAR(I),I=1,6)
    WRITE(6,1025) (UPAR(I),I=1,5)
1000 FORMAT(55H
1001 FORMAT(3I5,5X,5F10.4)
1002 FORMAT(8F10.5)
1003 FORMAT(16F5.0)
1004 FORMAT(2I5,10X,5F10.4)
1012 FORMAT( 6HOVAPAR,5F10.5)
1022 FORMAT(6H VBPART,5F10.5)
1020 FORMAT( 5H0 NVA2X3HNVB1X4HNGAM9X2HGA8X2HGB7X5HGAMMA5X5HHWIDB)
1021 FORMAT(5H0NTHL3X2HNV13X3HXXV8X2HGC6X6HDELT07X1HT)
1024 FORMAT(6H0THPAR,6F10.5)
1025 FORMAT(2X4HUPAR,5F10.5/1H0)
C LAB ANGLE LOOP.
    DO 30 ITHL=1,NTHL
    TL=THL(ITHL)*Y
    CT=COS(TL)
    ST=SIN(TL)
    FLX=0.
C LAB VELOCITY LOOP.
    DO 20 IV=1,NV
    VL=FLOAT(IV)*XXV

```

```

VX=VL*CT
VY=VL*ST
F=0.0
C  VELOCITY-AVERAGING LOOP.
    DO 10 IJK=1,NGRID
C  COORDINATE TRANSFORMATION.
    UX=VX-CX(IJK)
    UY=VY-CY(IJK)
    U=SQRT(UX*UX+UY*UY)
    THCM=ATAN2(ABS(UX*SINTV(IJK)+UY*COSTV(IJK)),
1   UX*COSTV(IJK)-UY*SINTV(IJK))/Y
    DELTE=GFAC*U**2-E(IJK)-DELTDO
    PRB=1.0
    IF(DELTE.GT.0.) PRB=EXP(-DELTE/RT)*(1.+DELTE/RT)
C  CALCULATION AND WEIGHTING OF C.M. CROSS SECTION.
10  F=F+FABG(IJK)*PRB*(VL/U)**2*THDIST(THCM,THPAR)*UDIST(U,UPAR)
    FLX=FLX+F*XXV
20  P(IV)=F
C  OUTPUT LAB INTENSITIES.
    WRITE(6,1010) THL(ITHL),FLX
1010 FORMAT(5H THL=,F6.1,4X5HFLUX=,1PE11.4)
    WRITE(6,1011) (P(I),I=1,NV)
1011 FORMAT(1P8E10.3)
    IF(IPUNCH.EQ.0) GO TO 30
    WRITE(7,1010) THL(ITHL),FLX
    WRITE(7,1011) (P(J),J=1,NV)
30  CONTINUE
    GO TO 100
    END

C  CALCULATION OF NEWTON DIAGRAM WEIGHTS AND TRANSFORMATION PARAMETERS.
SUBROUTINE CNEWT(NVA,NVB,VAPAR,VBPAR,GA,GB,NGAM,GAMMA,HWIDB,FABG,
1 CX,CY,E,COSTV,SINTV)
DIMENSION FABG(400),CX(400),CY(400),E(400),COSTV(400),SINTV(400)
DIMENSION VA(10),VB(10),FA(10),FB(10),GAM(3),FG(3)
DIMENSION VAPAR(5),VBPAR(5)
Y=.017453292
G=GA+GB
GFAC=.00119503*GA*GB/G
NH=NGAM/2+1
FNH=NH
DO 1 K=1,NGAM
    GAM(K)=GAMMA+FLOAT(K-NH)*HWIDB/FNH
    FG(K)=1.0
1 IF(HWIDB.NE.0.0) FG(K)=1.0-ABS(GAM(K)-GAMMA)/HWIDB
    FNH=(NVA+1)/2
    DO 2 I=1,NVA
        VA(I)=VAPAR(1)*FLOAT(I)/FNH
2 FA(I)=UDIST(VA(I),VAPAR)
    FNH=(NVB+1)/2
    DO 3 J=1,NVB
        VB(J)=VBPAR(1)*FLOAT(J)/FNH
3 FB(J)=UDIST(VB(J),VBPAR)
    SUM=0.0

```

```

IJK=0.
DO 4 K=1,NGAM
GMK=GAM(K)*Y
CG=COS(GMK)
SG=SIN(GMK)
DO 4 I=1,NVA
V1=VA(I)
DO 4 J=1,NVB
V2=VB(J)
IJK=IJK+1
V=SQRT(V1**2+V2**2-2.*V1*V2*CG)
E(IJK)=GFAC*V**2
FABG(IJK)=V*FA(I)*FB(J)*FG(K)
CX(IJK)=(GA*V1+GB*V2*CG)/G
CY(IJK)=GB*V2*SG/G
COSTV(IJK)=(V1-V2*CG)/V
SINTV(IJK)=V2/V*SG
4 SUM=SUM+FABG(IJK)
NGRID=NVA*NVB*NGAM
DO 5 IJK=1,NGRID
5 FABG(IJK)=FABG(IJK)/SUM
RETURN
END

```

C PARAMETRIC FORM FOR VELOCITY DISTRIBUTIONS.

```

FUNCTION UDIST(U,PAR)
DIMENSION PAR(5)
R=U/PAR(1)
IF(R.GT.1.0) GO TO 10
A=PAR(2)
B=PAR(3)
20 UDIST=R**A*EXP((1.0-R**B)*A/B)
RETURN
10 A=PAR(4)
B=PAR(5)
GO TO 20
END

```

C PARAMETRIC GAUSSIAN FORM FOR C.M. ANGULAR DISTRIBUTIONS.

```

FUNCTION THDIST(THCM,THPAR)
DIMENSION THPAR(6)
X1=THCM-THPAR(1)
X2=THCM-THPAR(2)
IF(X1.GE.0..AND.X2.LE.0..) GO TO 2
IF(X2.GT.0.) GO TO 3
H=THPAR(3)
C=THPAR(4)
X=X1
GO TO 4
2 THDIST=1.
RETURN
3 H=THPAR(5)
C=THPAR(6)

```

```
X=X2
4 THDIST=(1.-C)*EXP(-.69314718*(X/H)**2)+C
RETURN
END
```

for velocity analysis data, has been given the nickname "LSLBCM". A detailed description of its operation would be very similar to that for CMLB; the chief difference is that in LSLBCM two complete calculation cycles are executed. During the first cycle, the $F_j(v)$ of Eq. (17) are calculated and used to fill the normal matrix and the R.H.S. vector in the normal equations. After solution of the equations using the SHARE Library matrix subroutines PODTAS and PODTB (which take computational advantage of the symmetry of the normal matrix), the second cycle is strictly analogous to the CMLB routine, the LAB intensities being calculated using the least-squares determined parameter vector. In addition to the LAB back-calculation, the program also outputs the parameter vector and the c.m. cross section, in the form of angular distributions at a set of recoil speeds specified by the user.

A description of the punched card input and a Fortran listing for LSLBCM are presented in Table III. Any input parameters already covered in Table II and not needing further explanation are not included; the subroutines CNEWT and UDIST, which are used in both programs, are not listed in Table III. Again, input card formats, particularly for reading in the experimental data, are arbitrary; an array has been set aside so that LAB velocities may be read in and stored if they are unevenly spaced for a given θ . For purposes of economy of output, the numbers of data points at each angle (NV) are required to be equal; if they are not, all the angles sets should be filled in with zeroes until they are as large as the largest set

Table III. LSLBCM input and listing.

<u>Variable</u>	<u>Meaning</u>
IWGT.....	Determines the weighting for each data point P: for IWGT.EQ.0, unit weights are assumed; IWGT.EQ.1 implies each point P is to be weighted by $P^{-1/2}$; IWGT.EQ.2 gives P^{-1} weights. Unit or $P^{-1/2}$ weights are preferred.
PE(ITHL,IV) array....	Experimental data to be fitted, in flux units, where the polar velocity-space coordinates of each point are specified by the indices. A maxi- mum of 20 angles with 50 velocities at each angle is allowed.
VL(ITHL,IV) array....	LAB speeds corresponding to the PE(ITHL,IV).
NU.....	Number of c.m. recoil speeds at which the cross section is to be calculated.
UCM array.....	The set of c.m. recoil speeds.
NLEG,NLAG.....	The number of Legendre and Laguerre polynomials, resp., to be included in the c.m. function; are usually equal. Both ≤ 10 .
U0.....	Scaling parameter for the Laguerre weight func- tion; usually set equal to one-half the value of u at the peak of the NNDA cross section. Units are 10^4 cm/sec.

All other input parameters have been previously defined in Table II.

```

C LSLBCM
C LEAST SQUARES DETERMINATION OF C.M. REACTIVE DIFFERENTIAL CROSS
C SECTION FROM PRODUCT VELOCITY ANALYSIS DATA. FUNCTIONAL FORM IS
C A LAGUERRE-LEGENDRE SERIES.
      DIMENSION P(20,50),PE(20,50),VL(20,50),THL(20)
      DIMENSION FABG(400),CX(400),CY(400),E(400),COSTV(400),SINTV(400)
      DIMENSION VAPAR(5),VBPAR(5),PLC(10),UNC(10),UCM(20)
      DIMENSION A(100,100),B(100),X(100)
      LOGICAL SING,SWITCH,W1,W2,PCH
      DATA NM,NB,TOL,Y/100,1,1.E-8,.017453292/
99 READ(5,1000)
      READ(5,1001) IPUNCH,IWGT
      W1=IWGT.EQ.1
      W2=IWGT.EQ.2
      PCH=IPUNCH.NE.0
      READ(5,1001) NVA,NVB,NGAM,GA,GB,GAMMA,HWIDB
      NGRID=NVA*NVB*NGAM
      G=GA+GB
      READ(5,1002) (VAPAR(I),I=1,5)
      READ(5,1002) (VBPAR(I),I=1,5)
C CALCULATION OF NEWTON DIAGRAM WEIGHTS AND TRANSFORMATION PARAMETERS.
      CALL CNEWT(NVA,NVB,VAPAR,VBPAR,GA,GB,NGAM,GAMMA,HWIDB,FABG,CX,CY,
      1 E,COSTV,SINTV)
C DATA READ-IN.
      READ(5,1006) NTHL,NV,DV,VO
      DO 110 ITHL=1,NTHL
      READ(5,1007) THL(ITHL)
      DO 105 IV=1,NV
      .105 VL(ITHL,IV)=FLOAT(IV)*DV+VO
      110 READ(5,1011) (PE(ITHL,IV),IV=1,NV)
      READ(5,1001) NU
      READ(5,1003) (UCM(IU),IU=1,NU)
      100 READ(5,1005) NLEG,NLAG,UO
      IF(NLEG.EQ.0) GO TO 99
      WRITE(6,1000)
      WRITE(6,1020)
      WRITE(6,1001) NVA,NVB,NGAM,GA,GB,GAMMA,HWIDB
      WRITE(6,1012) (VAPAR(I),I=1,5)
      WRITE(6,1022) (VBPAR(I),I=1,5)
      WRITE(6,1021)
      WRITE(6,1001) NTHL,NLEG,NLAG,UO
      WRITE(6,1023)
1000 FORMAT(55H
1001 FORMAT(3I5,5X,5F10.4)
1002 FORMAT(8F10.5)
1003 FORMAT(16F5.0)
1005 FORMAT(2I2,F10.0)
1006 FORMAT(2I5,7F10.3)
1007 FORMAT(5X,F6.1)
1011 FORMAT(1P8E10.3)
1012 FORMAT(6HOVAPAR,5F10.5)
1020 FORMAT(5HO NVA2X3HNVB1X4HNGAM9X2HGA8X2HGB7X5HGAMMA5X5HHWIDB)

```

```

1021 FORMAT(5H0NTHL1X4HNLEG1X4HNLAG10X2HU0)
1022 FORMAT(6H VBPAR,5F10.5)
1023 FORMAT(1H0)
C INITIALIZATION.
SWITCH=.FALSE.
NA=NLEG*NLAG
DO 115 I=1,NA
B(I)=0.
DO 115 J=1,I
115 A(I,J)=0.
C LAB ANGLE LOOP.
120 DO 30 ITHL=1,NTHL
TL=THL(ITHL)*Y
CT=COS(TL)
ST=SIN(TL)
C LAB VELOCITY LOOP.
DO 20 IV=1,NV
PX=PE(ITHL,IV)
IF(PX.LE.0.) GO TO 195
IF(SWITCH) GO TO 6
DO 5 LL=1,NA
5 X(LL)=0.
6 V=VL(ITHL,IV)
VX=V*CT
VY=V*ST
V2=((V+V)/U0)**2
F=0.
C VELOCITY-AVERAGING LOOP.
DO 10 IJK=1,NGRID
C COORDINATE TRANSFORMATION.
UXL=VX-CX(IJK)
UYL=VY-CY(IJK)
U=SQRT(UXL**2+UYL**2)
COSTH=(UXL*COSTV(IJK)-UYL*SINTV(IJK))/U
R=U/U0
WT=FABG(IJK)*V2*EXP(-R)
R=R+R
C CALCULATION OF LAGUERRE AND LEGENDRE POLYNOMIALS.
CALL LEGNDR(NLEG,COSTH,PLC)
CALL ALAGER(NLAG,R,UNC)
LL=0
C IF SWITCH=.F., CALCULATION OF DERIVATIVES FOR NORMAL EQUATIONS.
C IF .T., CALCULATION OF LAB INTENSITIES.
DO 9 N=1,NLAG
WU=WT*UNC(N)
DO 9 L=1,NLEG
LL=LL+1
IF(SWITCH) GO TO 7
X(LL)=X(LL)+WU*PLC(L)
GO TO 9
7 F=F+B(LL)*WU*PLC(L)
9 CONTINUE
10 CONTINUE
WGT=1.
IF(W1) WGT=1./PX

```

```

IF(W2) WGT=1./(PX*PX)
IF(SWITCH) GO TO 19
C FILLING NORMAL MATRIX AND RHS VECTOR.
DO 15 I=1,NA
B(I)=B(I)+WGT*PX*X(I)
DO 15 J=1,I
15 A(I,J)=A(I,J)+WGT*X(I)*X(J)
GO TO 20
19 P(ITHL,IV)=F
NPTS=NPTS+1
SD=SD+WGT*(PX-F)**2
SUMP=SUMP+PX
SUMPF=SUMPF+ABS(PX-F)
GO TO 20
195 P(ITHL,IV)=0.
20 CONTINUE
30 CONTINUE
IF(SWITCH) GO TO 400
C SOLVE NORMAL EQUATIONS.
CALL PODTAS(TOL,A,A,NM,NA,SING)
IF(SING) GO TO 300
CALL PODTB(A,NM,NA,B,B,NB,NB)
WRITE(6,1500)
1500 FORMAT(3HO N2X1HL8X11HCOEFFICIENT)
LL=0
DO 250 N=1,NLAG
N1=N-1
DO 250 L=1,NLEG
L1=L-1
LL=LL+1
WRITE(6,1052) N1,L1,B(LL)
1052 FORMAT(2I3,1PE20.7)
250 CONTINUE
C CALCULATION OF C.M. CROSS SECTION.
CALL DXSEC(NU,UCM,B,NLAG,NLEG,U0)
NPTS=0
SD=0.
SUMP=0.
SUMPF=0.
SWITCH=.TRUE.
GO TO 120
300 WRITE(6,1013)((A(I,J),I=1,NA),J=1,NA)
1013 FORMAT(1X,1P10E10.3)
STOP
400 CONTINUE
C OUTPUT LAB INTENSITIES.
NPG=NTHL/3
IF(3*NPG.LT.NTHL) NPG=NPG+1
DO 500 IP=1,NPG
NT1=3*(IP-1)+1
NT2=MINO(NT1+2,NTHL)
WRITE(6,1030) (THL(ITHL),ITHL=NT1,NT2)
WRITE(6,1031)
DO 450 IV=1,NV
450 WRITE(6,1032) (PE(ITHL,IV),P(ITHL,IV),VL(ITHL,IV),ITHL=NT1,NT2)

```

```

500 CONTINUE
IF(.NOT.PCH) GO TO 550
WRITE(7,1000)
WRITE(7,1100) (B(I),I=1,NA)
1100 FORMAT(4E20.8)
DO 525 ITHL=1,NTHL
WRITE(7,1033) THL(ITHL)
525 WRITE(7,1011) (P(ITHL,IV),IV=1,NV)
1030 FORMAT(10H1LAB ANGLE,3(12X,F6.1,18X))
1031 FORMAT(1H09X,3(2X4HEXPT8X4HCALC6X5HLAB V7X))
1032 FORMAT( 7X,3(1P2E12.3,0PF8.3,4X))
1033 FORMAT(5H THL=,F6.1)
550 CONTINUE
SD=SQRT(SD/FLOAT(NPTS-NA))
SUMP=SUMPF/SUMP*100.
WRITE(6,1053) SD,SUMP,NPTS
1053 FORMAT(22H1STANDARD DEVIATION IS,1PE10.3/5X17HSTANDARD ERROR IS,
1 0PF8.3,9H PER CENT/1H0,I4,12H DATA POINTS)
GO TO 100
END

```

C LEGENDRE POLYNOMIALS BY RECURSION.

```

SUBROUTINE LEGNDR(N,X,PL)
DIMENSION PL(10)
PL(1)=1.
IF(N.EQ.1) RETURN
PL(2)=X
IF(N.EQ.2) RETURN
DO 1 I=3,N
1 PL(I)=(FLOAT(2*I-3)*X*PL(I-1)-FLOAT(I-2)*PL(I-2))/FLOAT(I-1)
RETURN
END

```

C ASSOCIATED LAGUERRE POLYNOMIALS BY RECURSION. ALPHA=4.

```

SUBROUTINE ALAGER(N,X,UN)
DIMENSION UN(10)
UN(1)=1.
IF(N.EQ.1) RETURN
UN(2)=5.-X
IF(N.EQ.2) RETURN
DO 1 I=3,N
1 UN(I)=((FLOAT(2*I+1)-X)*UN(I-1)-FLOAT(I+2)*UN(I-2))/FLOAT(I-1)
RETURN
END

```

C CALCULATES C.M. CROSS SECTION FROM LEAST SQUARES LAGUERRE-LEGENDRE
C SERIES.

```

SUBROUTINE DXSEC(NU,U,B,NLAG,NLEG,U0)
DIMENSION B(100),U(20),PLC(10),UNC(10),TH(19),CTH(19),D(19,20)

```

```

DATA Y/.017453292/
DO 1 ITH=1,19
  TH(ITH)=10*(ITH-1)
1 CTH(ITH)=COS(TH(ITH)*Y)
  DO 10 IU=1,NU
    R=U(IU)/U0
    EX=EXP(-R)
    R=R+R
    EX=EX*R**2
    CALL ALAGER(NLAG,R,UNC)
    DO 10 ITH=1,19
    CALL LEGNDR(NLEG,CTH(ITH),PLC)
    DXS=0.
    LL=0
    DO 2 N=1,NLAG
    DO 2 L=1,NLEG
    LL=LL+1
2 DXS=DXS+B(LL)*UNC(N)*PLC(L)
    DXS=DXS*EX
    D(ITH,IU)=DXS
10 CONTINUE
  WRITE(6,1100)
  NR=1
  IF(NU.GT.10) NR=2
  DO 30 IR=1,NR
    N1=10*(IR-1)+1
    N2=MIN0(N1+9,NU)
    WRITE(6,1000) (U(IU),IU=N1,N2)
    WRITE(6,1001)
    DO 20 ITH=1,19
20 WRITE(6,1002) TH(ITH),(D(ITH,IU),IU=N1,N2)
30 CONTINUE
1100 FORMAT(19H1C.M. CROSS SECTION)
1000 FORMAT(1H08X1HU,10F10.2)
1001 FORMAT(1H 3X4HTHCM)
1002 FORMAT(1H ,F7.0,2X,10F10.5)
  RETURN
END

```

```

SUBROUTINE PODTAS (TOL,A,AI,NMAX,N,SING)
DIMENSION A(NMAX,NMAX),AI(NMAX,NMAX)
LOGICAL SING
IF (TOL.LE.0.0) TOL=1.E-8
20 SING=.FALSE.
  IF (ABS (A(1,1)).GT.TOL) GO TO 40
30 SING=.TRUE.
  GO TO 999
40 DO 50 I=1,N
50 AI(I,1)=A(I,1)
  IF (N-1) 30,999,60
60 IJLAST=N-1
  DO 300 IJ=1,IJLAST
    I=IJ

```

IMP10
IMP10

```

JFIRST=I+1
DO 100 J=JFIRST,N
100 AI(I,J)=AI(J,I)/AI(I,I)
   J=IJ+1
   KLAST=IJ
   DO 200 I=J,N
   AI(I,J)=-AI(I,J)
   DO 180 K=1,KLAST
180 AI(I,J)=DBLE(AI(I,K))*DBLE(AI(K,J))+DBLE(AI(I,J))
200 AI(I,J)=-AI(I,J)
   IF (ABS (AI(J,J)).LE.TOL) GO TO 30
300 CONTINUE
999 RETURN
END

```

```

SUBROUTINE PODTB (AI,NMAX,N,B,X,NBMAX,NB)
DIMENSION AI(NMAX,NMAX),B(NMAX,NBMAX),X(NMAX,NBMAX)
DO 10 J=1,NB
10 X(1,J)=B(1,J)/AI(1,1)
NLAST=N-1
IF (NLAST.EQ.0) GO TO 999
DO 300 J=1,NB
DO 100 I=2,N
KLAST=I-1
X(I,J)=-B(I,J)
DO 80 K=1,KLAST
80 X(I,J)=DBLE(X(I,J))+DBLE(AI(I,K))*DBLE(X(K,J))
100 X(I,J)=-X(I,J)/AI(I,I)
DO 200 II=1,NLAST
I=N-II
KFIRST=I+1
X(I,J)=-X(I,J)
DO 180 K=KFIRST,N
180 X(I,J)=DBLE(X(I,J))+DBLE(AI(I,K))*DBLE(X(K,J))
200 X(I,J)=-X(I,J)
300 CONTINUE
999 RETURN
END

```

...LSBCM ALSO USES THE FOLLOWING SUBROUTINES...

CNEWT
UDIST

(zeroes are ignored by the program). A typical run, with 400 data points, a 100-point grid, and using a 36-term series (the latter two conditions having proven satisfactory; see text), uses about 8 minutes of 7094 computer time. As before, the calculation timing depends approximately linearly on the number of LAB points, the grid density, and also on the number of terms taken. The test calculation described in the text consumed 24 minutes with 624 data points, 100 Newton Diagrams, and 100 terms, indicating slightly less than linear dependence. It is possible that the program time could be cut nearly in half if the $F_j(v)$ could all be stored in high-speed memory; the LAB intensities could then be quickly calculated from Eq. (16). But there might be as many as 60,000 numbers to be stored, which exceeds the capacity of the 7094 excluding the core used by the program as it stands, (about 25K); use of magnetic tape or disk would be prohibitive timewise for this amount of data. This improvement awaits a larger machine.

The third program, decknamed CMLB1, performs a least squares analysis for primitive experiments. Its operation is almost identical to that of LSLBCM, except that the quantities calculated in the first cycle are the $\mathcal{I}_j(\theta)$ of Eq. (25). Besides the LAB velocity spectra and total intensity fit, the program also outputs the Legendre coefficient vector and the c.m. angular distribution.

A code listing for CMLB1 is given in Table IV. The only undefined parameter is NL, the number of Legendre polynomials to be included in the $T(\theta)$ series, <8. All CMLB1 subroutines previously listed, namely,

...CMLB1 FORTRAN IV LISTING...

```

C CMLB1
C LEAST SQUARES DETERMINATION OF APPROXIMATE C.M. CROSS SECTION FOR
C REACTION FROM 'PRIMITIVE' LAB ANGULAR DISTRIBUTION. THE C.M. ANGULAR
C DISTRIBUTION IS REPRESENTED BY A LEGENDRE POLYNOMIAL SERIES. THE
C C.M. RECOIL DISTRIBUTION IS GUESSED.
    DIMENSION P(400),THL(100),FLX(100)
    DIMENSION FABG(400),CX(400),CY(400),E(400),COSTV(400),SINTV(400)
    DIMENSION VAPAR(5),VBPAR(5),UPAR(5),X(8),XX(8),A(8,8),B(8),PLC(8)
    LOGICAL SING,SWITCH,W1,W2
    DATA NM,NB,TOL,Y/8,1,1.E-8,.017453292/
99 READ(5,1000)
    READ(5,1001) IWGT
    W1=IWGT.EQ.1
    W2=IWGT.EQ.2
    READ(5,1001) NVA,NVB,NGAM,GA,GB,GAMMA,HWIDB
    NGRID=NVA*NVB*NGAM
    G=GA+GB
    READ(5,1002) (VAPAR(I),I=1,5)
    READ(5,1002) (VBPAR(I),I=1,5)
C CALCULATION OF NEWTON DIAGRAM WEIGHTS AND TRANSFORMATION PARAMETERS.
    CALL CNEWT(NVA,NVB,VAPAR,VBPAR,GA,GB,NGAM,GAMMA,HWIDB,FABG,CX,CY,
1 E,COSTV,SINTV)
    READ(5,1001) NTHL,NV
    READ(5,1003) (THL(ITHL),FLX(ITHL),ITHL=1,NTHL)
    READ(5,1002) GC,DELTD0,T,XXV
    RT=.0019872*T
    READ(5,1001) NL
100 READ(5,1002) (UPAR(I),I=1,5)
    IF(UPAR(1).EQ.0.) GO TO 99
    WRITE(6,1000)
    WRITE(6,1004)
    WRITE(6,1001) NVA,NVB,NGAM,GA,GB,GAMMA,HWIDB
    WRITE(6,1005) (VAPAR(I),I=1,5)
    WRITE(6,1006) (VBPAR(I),I=1,5)
    WRITE(6,1007)
    WRITE(6,1001) NTHL,NL,NV,GC,DELTD0,T,XXV
    WRITE(6,1008) (UPAR(I),I=1,5)
1000 FORMAT(5H
1001 FORMAT(3I5.5X,5F10.4)
1002 FORMAT(8F10.4)
1003 FORMAT(2F10.0)
1004 FORMAT(5H0 NVA2X3HNVB1X4HNGAM9X2HGA8X2HGB7X5HGAMMA5X5HHWIDB)
1005 FORMAT(6HOVAPAR,5F10.4)
1006 FORMAT(6H VBPAR,5F10.4)
1007 FORMAT(5H0NTHL3X2HNL3X2HNV9X2HGC6X6HDELTDO8X1HT6X3HXXV)
1008 FORMAT(6H0 UPAR,5F10.4/1H0)
C INITIALIZATION.
    SWITCH=.FALSE.
    GFAC=.00119503*G*GC/(G-GC)
    DO 101 I=1,NL
    B(I)=0.
    DO 101 J=1,I

```

```

101 A(I,J)=0.
C LAB ANGLE LOOP.
110 DO 30 ITHL=1,NTHL
    TH=THL(ITHL)*Y
    CT=COS(TH)
    ST=SIN(TH)
    FLC=0.
    IF(SWITCH) GO TO 5
    DO 4 L=1,NL
        4 X(L)=0.
C LAB VELOCITY LOOP.
5 DO 20 IV=1,NV
    VL=FLOAT(IV)*XXV
    VX=VL*CT
    VY=VL*ST
    F=0.
    IF(SWITCH) GO TO 7
    DO 6 L=1,NL
        6 XX(L)=0.
C VELOCITY-AVERAGING LOOP.
7 DO 10 IJK=1,NGRID
C COORDINATE TRANSFORMATION.
    UX=VX-CX(IJK)
    UY=VY-CY(IJK)
    U=SQRT(UX*UX+UY*UY)
    COSTH=(UX*COSTV(IJK)-UY*SINTV(IJK))/U
    DELTE=GFAC*U*U-E(IJK)-DELTDO
    PRB=1.
    IF(DELTE.GT.0.) PRB=EXP(-DELTE/RT)*(1.+DELTE/RT)
    WT=FABG(IJK)*PRB*(VL/U)**2*UDIST(U,UPAR)
C CALCULATION OF LEGENDRE POLYNOMIALS.
    CALL LEGNDR(NL,COSTH,PLC)
    SUM=0.
C IF SWITCH=.F., CALCULATION OF DERIVATIVES FOR NORMAL EQUATIONS.
C IF .T., CALCULATION OF LAB INTENSITIES.
    DO 9 L=1,NL
        IF(SWITCH) GO TO 8
        XX(L)=XX(L)+WT*PLC(L)
        GO TO 9
8 SUM=SUM+X(L)*PLC(L)
9 CONTINUE
10 IF(SWITCH) F=F+WT*SUM
    IF(.NOT.SWITCH) GO TO 18
    P(IV)=F
    FLC=FLC+F*XXV
    GO TO 20
18 DO 19 L=1,NL
19 X(L)=X(L)+XX(L)*XXV
20 CONTINUE
    FX=FLX(ITHL)
    WGT=1.
    IF(W1) WGT=1./FX
    IF(W2) WGT=1./FX**2
    IF(SWITCH) GO TO 29
C FILLING NORMAL MATRIX AND RHS VECTOR.

```

```

DO 25 I=1,NL
B(I)=B(I)+WGT*FX*X(I)
DO 25 J=1,I
25 A(I,J)=A(I,J)+WGT*X(I)*X(J)
GO TO 30
29 SD=SD+(FX-FLC)**2*WGT
C OUTPUT LAB INTENSITIES.
WRITE(6,1050) THL(ITHL),FX,FLC
WRITE(6,1051) (P(IV),IV=1,NV)
1050 FORMAT(5H0THL=,F6.1,2X10HEXPT FLUX=,1PE11.4,2X10HCALC FLUX=,E11.4)
1051 FORMAT(1X,1P8E11.3)
30 CONTINUE
IF(SWITCH) GO TO 60
C SOLVE NORMAL EQUATIONS.
CALL PODTAS(TOL,A,A,NM,NL,SING)
IF(SING) GO TO 50
CALL PODTB(A,NM,NL,B,B,NB,NB)
WRITE(6,1052)
DO 40 L=1,NL
X(L)=B(L)
L1=L-1
40 WRITE(6,1053) L1,X(L)
1052 FORMAT(2H0L9X11HCOEFFICIENT)
1053 FORMAT(I2,1PE20.7)
C CALCULATION OF C.M. ANGULAR DISTRIBUTION.
CALL ANGDIS(NL,X)
SD=0.
SWITCH=.TRUE.
GO TO 110
50 WRITE(6,1054) ((A(I,J),I=1,NL),J=1,NL)
1054 FORMAT(1P8D11.3)
STOP
60 SD=SQRT(SD/FLOAT(NTHL))
WRITE(6,1055) SD
1055 FORMAT(20H0STANDARD DEVIATION=,1PE20.7)
GO TO 100
END

C CALCULATES C.M. ANGULAR DISTRIBUTION FROM LEAST SQUARES LEGENDRE
C SERIES.
SUBROUTINE ANGDIS(N,A)
DIMENSION A(8),DXS(37),TH(37),PLC(8)
WRITE(6,1000)
DO 2 I=1,37
TH(I)=5.*FLOAT(I-1)
COSTH=COS(TH(I)*.017453292)
CALL LEGNDR(N,COSTH,PLC)
SUM=0.
DO 1 L=1,N
1 SUM=SUM+A(L)*PLC(L)
DXS(I)=SUM
2 CONTINUE
DMAX=DXS(1)
DO 3 I=1,37

```

```
3 IF(DMAX.LT.DXS(I)) DMAX=DXS(I)
DO 4 I=1,37
DXS(I)=DXS(I)/DMAX
4 WRITE(6,1001) TH(I),DXS(I)
RETURN
1000 FORMAT(6HO THCM4X3HDXS)
1001 FORMAT(F6.1,F10.4)
END
```

...CMLB1 ALSO USES THE FOLLOWING SUBROUTINES...

CNEWT
UDIST
LEGNDR
PODTAS
PODTB.

CNEWT, UDIST, LEGNDR, PODTAS, PODTB, are omitted from this table. The program time on the 7094, for 20 LAB angles with 32 velocities at each, a 6-term Legendre series, and a 36-point grid, is about 3 minutes. The dependence on each of these conditions is about linear, as before. Again, the program time could be halved if the $\mathcal{F}_j(\theta)$ were stored and then used to calculate the LAB angular distribution from Eq. (25). In this case there is no storage capacity problem, but, if the back-calculation were performed in this way, the velocity spectra at each angle would be lost. These spectra are important for judging the accuracy of their integral; one has no advance knowledge of precisely where the peaks of these will fall, and if an integration has been cut off while a curve is still significant in size, the results of the analysis may not be accurate. In addition, these velocity profiles can be of value for comparison with subsequent velocity analysis results.

CHAPTER IV
KINEMATIC ANALYSIS: APPLICATIONS

Abstract

The methods evolved in the preceding chapter for treating reactive scattering data are applied to some extensively studied systems. Velocity analysis data for the systems K, Cs + Br₂ and K + HBr, DBr are used to generate center-of-mass velocity-space intensity maps for the scattered products. The sensitivity of the features of these maps to the quality of the data and to the kinematics of the scattering are discussed, and comparisons are made with previous analyses. In particular, it is shown that the nominal analysis, described in the preceding chapter, which does not account for the effects of velocity-averaging, nonetheless is at least semiquantitative in predicting the center-of-mass scattering behavior for systems with favorable kinematics.

A. Introduction

Much experimental data from crossed-molecular beam reactive scattering studies employing product velocity analysis are becoming available,¹⁻⁶ and large scale computer trajectory calculations on a variety of potential surfaces have now become feasible.⁷⁻¹² In order

1. K. T. Gillen, C. Riley and R. B. Bernstein, J. Chem. Phys. 50, 4019 (1969), on K + HBr, DBr.
2. R. Grice, C. Ottlinger, and D. R. Herschbach, J. Chem. Phys. (to be published), on K, Cs + Br₂, ICl.
3. C. Ottlinger, P. M. Strudler and D. R. Herschbach, J. Chem. Phys. (to be published), on K, Rb, Cs + RI, R a series of alkyl groups.
4. S. J. Riley, Ph.D. Thesis, Harvard University, Cambridge, Mass., 1970, on K, Cs + CBr₄, CHBr₃, CH₂Br₂, CH₂I₂, and K, Rb, Cs + SF₆, SnCl₄.
5. Chapter II, this thesis, on K, Rb, Cs + CC₁₄.
6. J. D. McDonald, P. R. LeBreton, Y. T. Lee, and D. R. Herschbach, on D + Cl₂, Br₂, I₂, IBr.
7. M. Karplus and L. Raff, J. Chem. Phys. 41, 1267 (1964), on K + CH₃I.
8. N. C. Blais, J. Chem. Phys. 49, 9 (1968); 51, 856 (1969), on K + Br₂.
9. M. Godfrey and M. Karplus, J. Chem. Phys. 49, 3602 (1968), on K + Br₂.
10. P. J. Kuntz, M. H. Mok, E. M. Nemeth and J. C. Polanyi, Disc. Faraday Soc. 44, 229 (1967); J. Chem. Phys. 50, 4607, 4623 (1969), on K + Br₂.
11. K. G. Anlauf, P. J. Kuntz, D. H. Maylotte, P. D. Pacey, and J. C. Polanyi, Disc. Faraday Soc. 44, 183 (1967); K. G. Anlauf, J. C. Polanyi, W. H. Wong and K. B. Woodall, J. Chem. Phys. 49, 5189 (1968), on H + X₂, X + HY, X and Y halogens.
12. J. C. Polanyi and W. H. Wong, J. Chem. Phys. 51, 1439 (1969); M. H. Mok and J. C. Polanyi, J. Chem. Phys., 51, 1451, on the effects of energy barriers.

to compare experiment and theory it is convenient to be able to express the experimental results in the center-of-mass (c.m.) coordinate system. Due to the velocity-averaging present to some extent in each of the experiments cited, however, the kinematic problem of transforming the laboratory (LAB) data to the c.m. system becomes ambiguous because of the ill-defined position of the c.m. in the LAB frame.¹³ In addition, the correct Jacobian factor for conversion of intensities had not been realized until fairly recently.¹⁴ Thus the seemingly trivial problem of kinematic analysis at times has barred an easy comparison with the trajectory results.^{7,10}

In the preceding chapter two methods have been outlined for mapping a fairly complete set of LAB intensities $I_{\text{LAB}}(v)$ into the c.m. system to get the corresponding $I_{\text{cm}}(u)$. The first, the Nominal Newton Diagram Approximation (NNDA), is quite crude; it ignores completely any effect the velocity-averaging might have, and transforms the data simply according to the geometry appropriate to the most probable parent beam velocities. Despite the apparent grossness of the approximation, however, this technique does surprisingly well in elucidating the main features of the c.m. scattering and in reproducing the LAB data upon carrying out a rigorous velocity average. The second is a least squares (LS) method which attempts rigorously to solve the two-dimensional integral equation (Eq. (7), Chapter III) relating the intensities through the substitution of a linear series of orthogonal

13. See Chapter III for a discussion.

14. E. A. Entemann, Ph.D. Thesis, Harvard University, Cambridge, Mass., 1967.

functions to represent $I_{cm}(v)$. As expected, this method is capable of extracting fairly exact information in the c.m. from very precise LAB data with a sufficient number of parameters. Given actual LAB data with the usual amount of error (~10% at best), the LS approach is somewhat more limited, but it still can result in a "smooth" representation in the c.m. with a somewhat better fit to the data than could be had with the NNDA.

Chapter II contains the earliest application of these methods, to the reactions of K, Rb, and Cs with CCl_4 . This chapter presents c.m. results for $K + Cs + Br_2$, and $K + HBr$ and DBr derived from the LS analysis. The interested reader is referred to Ref. 4 for further discussion and many examples.

B. Data Analysis and Discussion

The systems cited above were chosen for analysis because, in addition to being very extensively studied both experimentally and theoretically, they represent a wide range of possible kinematic conditions. They are of the general form



where M is an alkali atom and X is either another Br or a hydrogen isotope. In the c.m. system, due to momentum conservation, the final relative velocity v' of the products is partitioned between them according to

$$\frac{u_{MBr}}{m} = \frac{m_X}{m} v', \quad u_X = -\frac{m_{MBr}}{m} v', \quad (1)$$

where m_i is the mass of product i, m the total mass, and the signs are chosen by convention. We see that MBr and X fly apart from their c.m.

with speed inversely proportional to the mass they carry; $(u_{MBr}/u_X) = m_X/m_{MBr}$. The (average) magnitude of V' itself is, of course, determined by the chemical dynamics. It is clear that, in order to be able to discern the structure of the scattering in the c.m. system, i.e., prominent direction and shape of product peak and quantitative estimate of recoil energy, one must observe an appreciable difference between the LAB product distribution and that of the c.m. vectors arising from the various beam velocities. Thus, depending on the absolute size of V' , an unfavorable mass ratio, i.e., detected product (MBr) much heavier than non-detected (X), may prohibit the extraction of quantitative c.m. information from measurements of the LAB product distribution, since MBr is restricted to be near the LAB position of the c.m. in this case. As will be seen, our ability to invert LAB data to an accurate c.m. cross section is directly dependent on the velocity-space displacement of the detected product away from the c.m.

From the foregoing discussion it is clear that the $K + Br_2$ reaction has potentially the best "kinematic resolution", $Cs + Br_2$ should show fair resolution, and for $K + HBr$, DBr the amount of information available about the c.m. scattering should be quite small. Since the recoil energies involved in all these systems are comparable, the above ordering actually holds. For the stripping reactions with Br_2 there is an added difficulty having to do with the angular intensity distributions: the peaks fall very near the parent alkali beam, where the detected M atom background is very large and the subtraction to remove it somewhat uncertain. Moreover, because of the extremely small solid

angle seen by the detector when the velocity analyzer with its narrow slits is in place, there is a "viewing factor" due to the asymmetric shape of the scattering zone which distorts the relative intensities at various angles.⁴ In order to correct for this, the area under the velocity spectrum at each angle was made to equal the total intensity at that angle as measured in an experiment without the analyzer in place. Since the latter measurement also suffers from the same uncertainties at angles close to the M beam, an ambiguous weighting is assigned to an already ambiguous velocity profile. Thus the peak position and shape for the stripping reactions are rendered somewhat less reliable than are the "tails" of the distributions. For K + HBr, DBr, this is not a problem, since the scattered KBr cannot get very close to the K beam.

With this overview, we now examine the results of the analysis. Figures 1 and 2 show the calculated LAB fits (dashed lines) to the "smoothed" experimental data (solid lines) for K, Cs + Br₂ and K + HBr, DBr, respectively. The LS calculations are considered to be well within the experimental errors; runs with more parameters in the c.m. scattering function were tried, with better fits resulting as expected, but examination of the c.m. cross sections thus generated showed clearly that random uncertainties in the data were being fit by allowing too much flexibility. This latter effect is discussed in detail below.

The functional form for the c.m. cross section employed in the analysis is

Fig. 1. Smoothed data (—) and calculated fits (---) for K and Cs + Br₂ velocity analysis data of Ref. 2. For K a 36-term function was used; for Cs a 16-term function; also shown for Cs at $\Theta = 10^\circ, 20^\circ, 30^\circ$ are 4-term (-·-) and 36-term (-···) fits. Vertical scale has been expanded from that of Ref. 2 to show discrepancies more clearly. Normalization within each system is absolute, with the largest experimental intensity assigned a value of ten units.

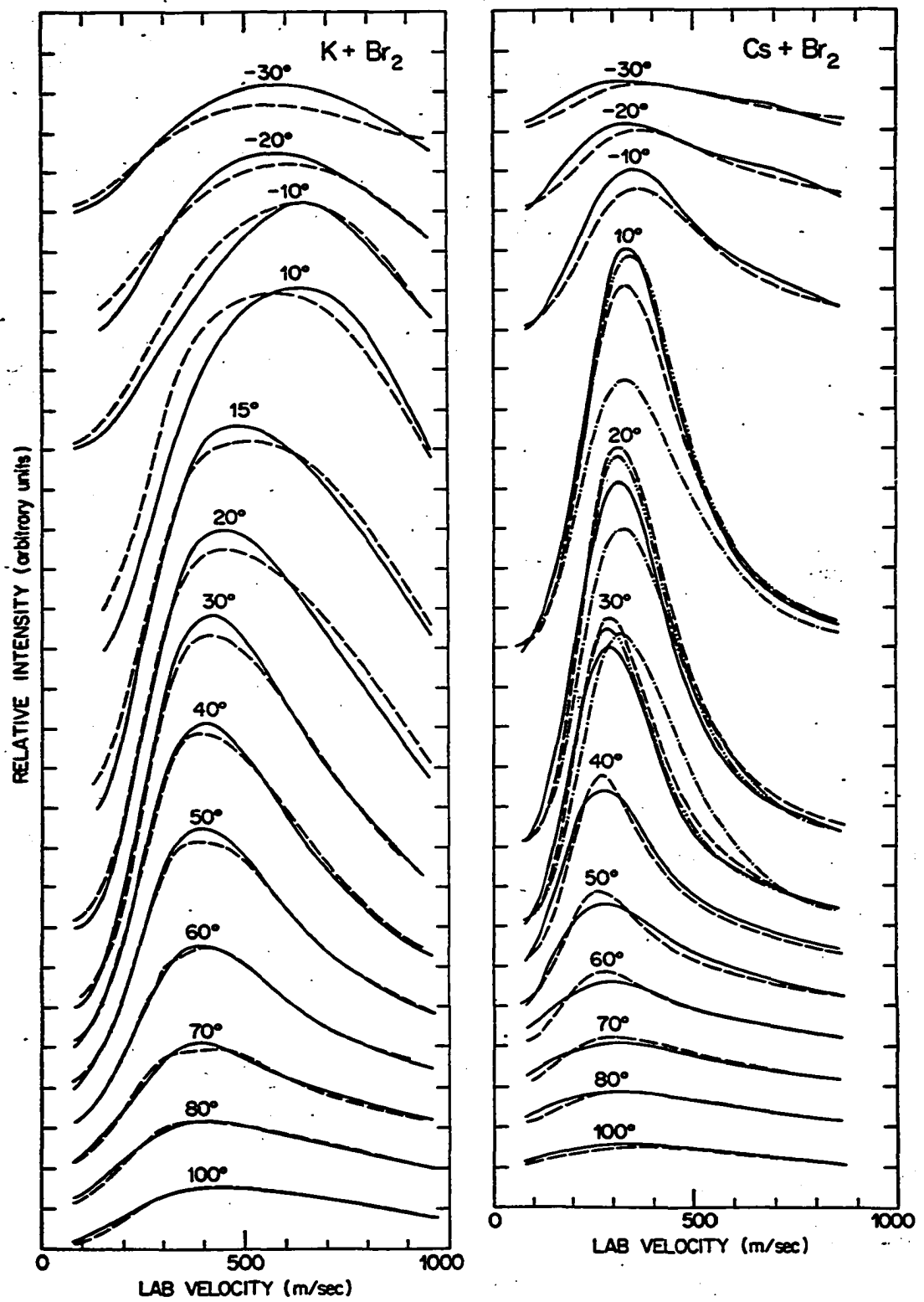
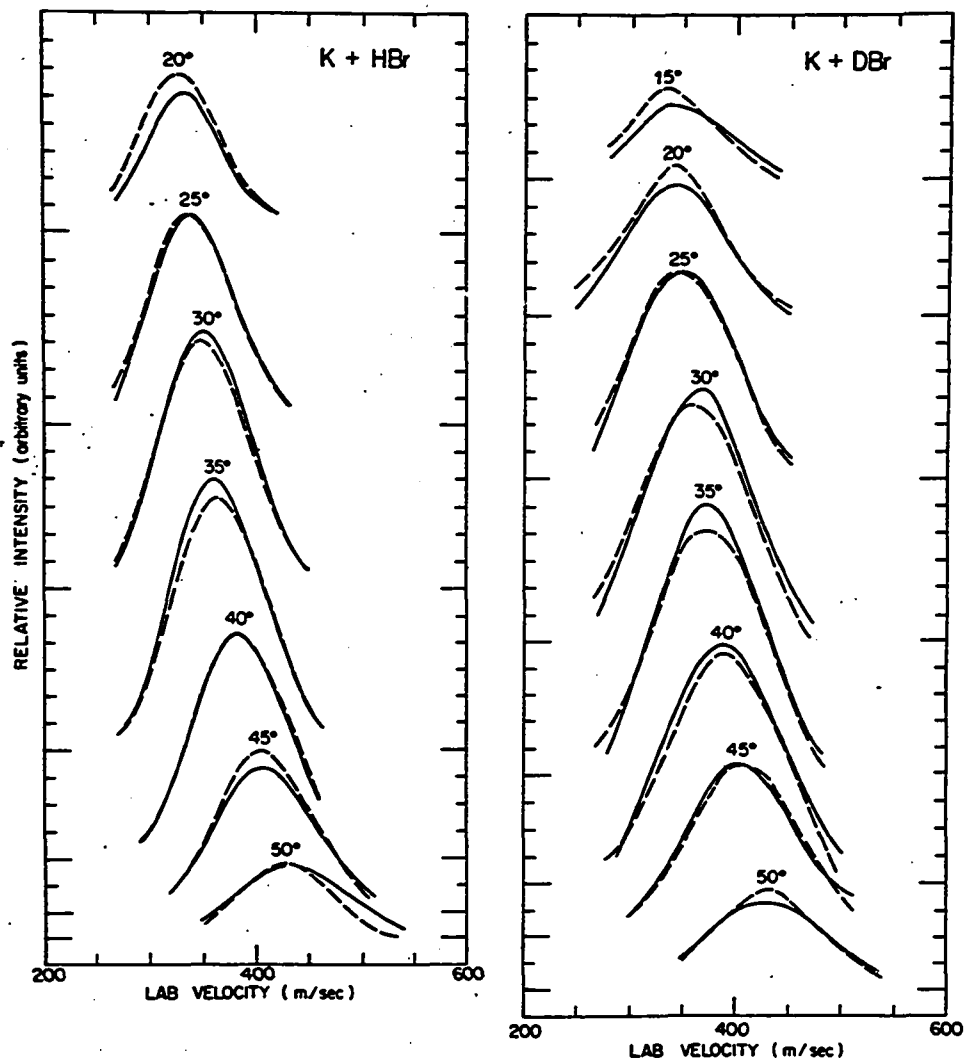


Fig. 2. Smoothed data (—) of Ref. 1 and calculated fits (---) from 16-term functions for K + HBr and DBr. Vertical scale has been expanded from that in Ref. 1 to show discrepancies more clearly. Normalization as in Fig. 1.



$$I_{cm}(u, \theta) = (2u/u_0)^2 \exp(-u/u_0) \sum_{n=0}^{n_{max}} \sum_{l=0}^{l_{max}} a_{nl} L_n^{(4)} (2u/u_0) P_l(\cos\theta), \quad (2)$$

where all symbols have previously been defined (Eq. (19), Chapter III).

In all the calculations described here we have used $n_{max} = l_{max}$. For $K + Br_2$, 36- and 64-term functions with $u_0 = 250$ m/sec were used to fit 585 smoothed data points; the 36-parameter fit is shown in Fig. 1. Four, sixteen and 36 parameters with $u_0 = 100$ m/sec were used in analyzing $Cs + Br_2$ (480 data points); Fig. 1 shows the complete fit obtained with the sixteen parameter run, with the other runs drawn in only at $\theta = 10^\circ, 20^\circ$ and 30° . For $K + HBr$, DBr , functions with 4, 16 and 36 parameters were tried, with u_0 values of 20 and 30 m/sec for HBr (162 data points) and DBr (129 data points) respectively; the crossed beam was assumed to be Maxwellian for these calculations.

Figure 2 shows the 16-term fits for each system. It should be noted that the flexibility in the c.m. cross section (the optimum number of parameters) had to be decreased as the kinematic resolution became worse, to avoid fitting slight discrepancies in the data. Such "over-fitting" can have weird results in the c.m., as we shall discuss below.

Figures 3 and 4 show polar constant-intensity-contour maps of the "optimum" c.m. cross sections obtained for $K + Br_2$, $Cs + Br_2$, $K + HBr$ and $K + DBr$. The maps were generated by the IBM 360/65-Calcomp 575 plotting system, with a program generously lent us by Professor Karplus' group. They are shown only in the regions where they are well-determined by the data. The optimum maps are the same functions which have given the fits of Figs. 1 and 2. The dashed lines show the

Fig. 3. Least squares determination of c.m. angular distributions from primitive laboratory angular distributions for (a) narrow and (b) broad angular shapes (—). Kinematic conditions were appropriate to the H + CsCl reaction of Chapter V. (a): ---, original U(u); ---, peak of U(u) shifted upward by 10%; ----, broader U(u) with original peak position. (b): ---, peak of U(u) shifted upward by 10%; ----, downward by 10%; ----, broader U(u) with original peak position.

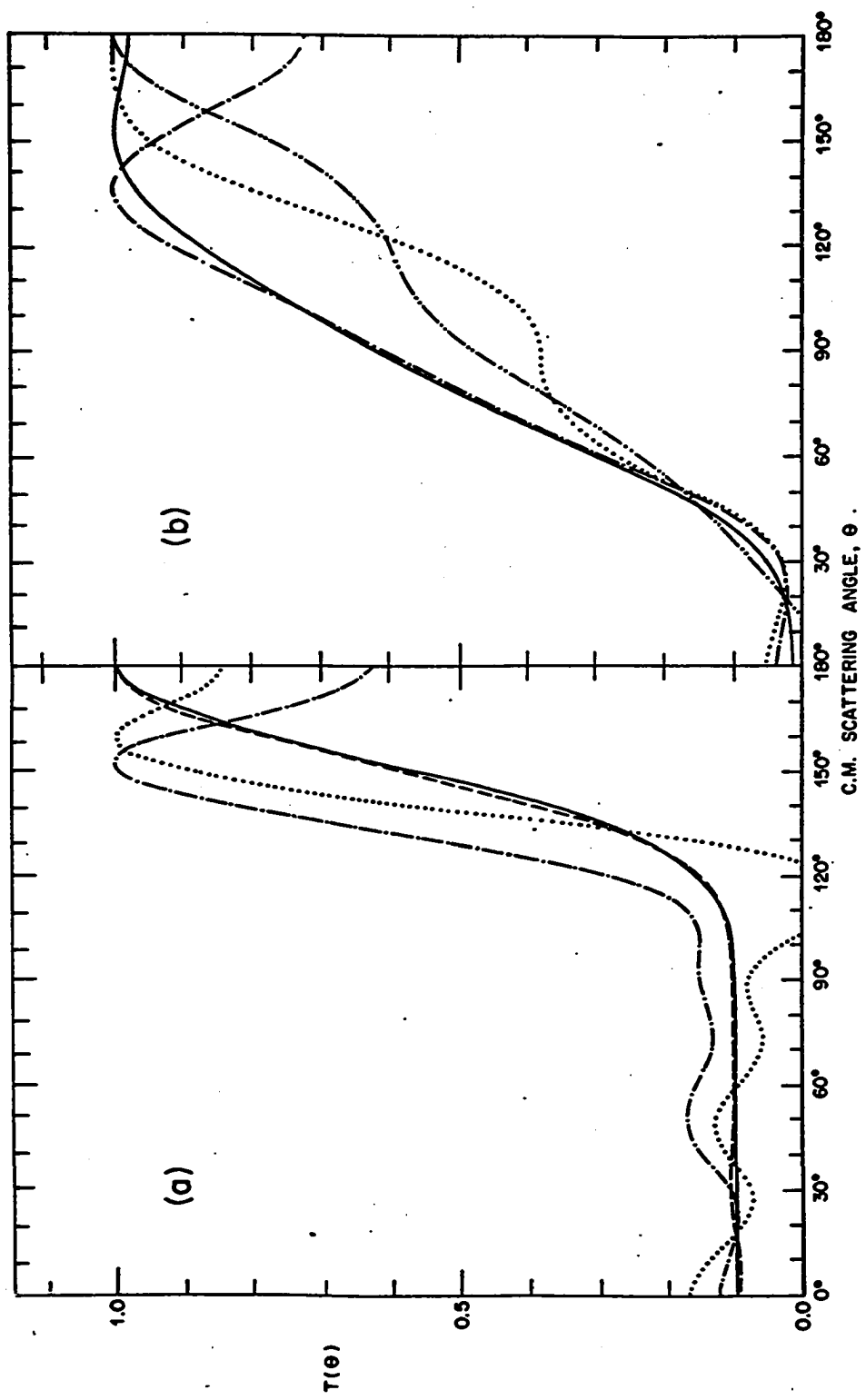
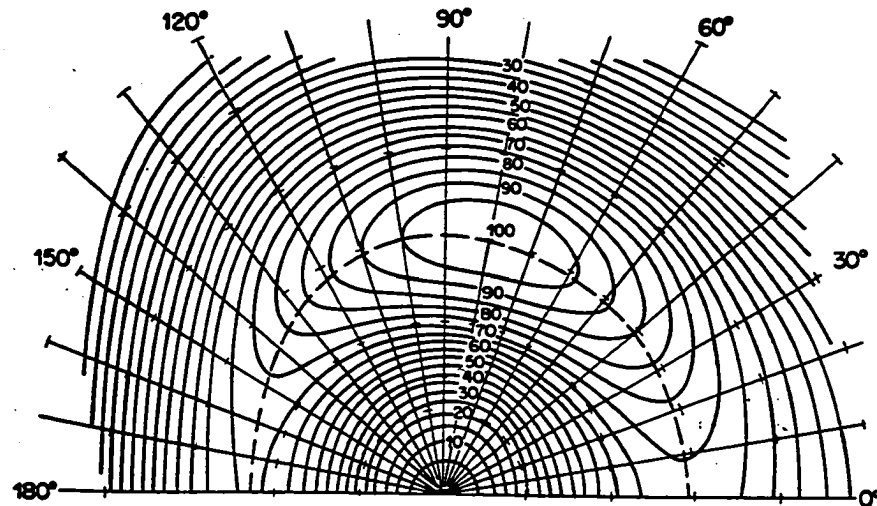
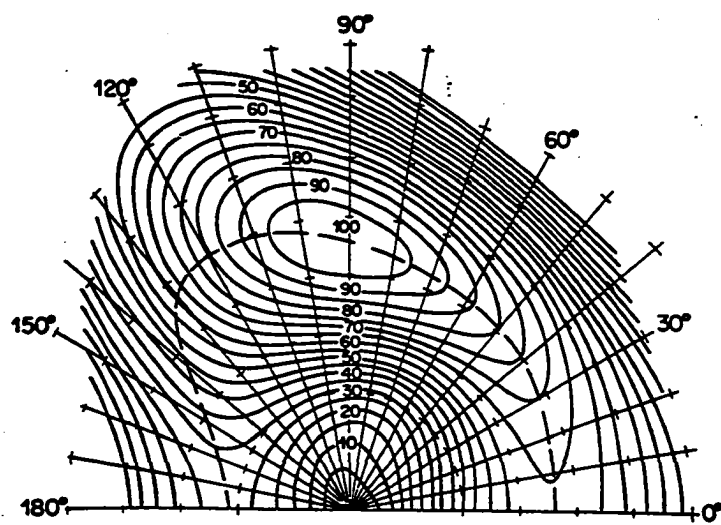


Fig. 4. "Optimum" center-of-mass contour maps for KBr from K + HBr and DBr generated from 16-term functions. Tic marks define 20 m/sec intervals. Note change in velocity scale in going from HBr to DBr.

$K + HBr$



$K + DBr$



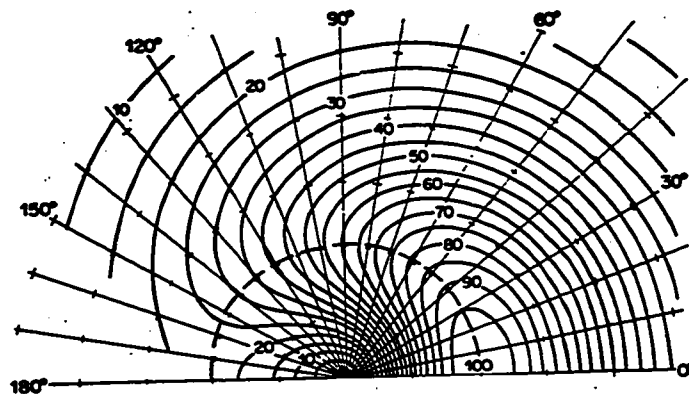
angular paths of slowest descent, i.e., the loci of peaks in the recoil velocity distributions. For "separable" c.m. functions¹⁴ these lines should be semi-circles; their eccentricity indicates the degree to which the direction and size of the recoil velocity vector are correlated. For both K and Cs + Br₂, the MBr product is seen to recoil with greater energy in both the forward ($\theta \sim 0^\circ$) and backward ($\theta \sim 180^\circ$) directions than sideways ($\theta \sim 90^\circ$). This is in qualitative agreement with the NNDA analysis of Ref. 2. Due to the lack of meaningful structure in the K + HBr, DBr data, the degree of coupling between u and θ is somewhat uncertain; in Ref. 1 the data were fit with an assumed separable distribution.

We will use Cs + Br₂ as a canonical example of the limitations imposed by the precision and consistency of the data on the LS analysis, because the kinematic resolution is good enough so that the basic structure of the c.m. cross section is clear, while at the same time the product CsBr recoils slowly enough so that the LAB angular range covers nearly the entire significant region of the cross section. We note first that, as expected, the fit to the data improves as we increase the number of parameters from 4 to 16 to 36, as shown in Fig. 1, though it is still far from "perfect".¹⁵ Figure 5 shows the c.m. maps obtained from the runs and it is here that the effect of trying to fit actual, discrepant data too closely becomes apparent. Of course, one may have too few parameters also, with the result that

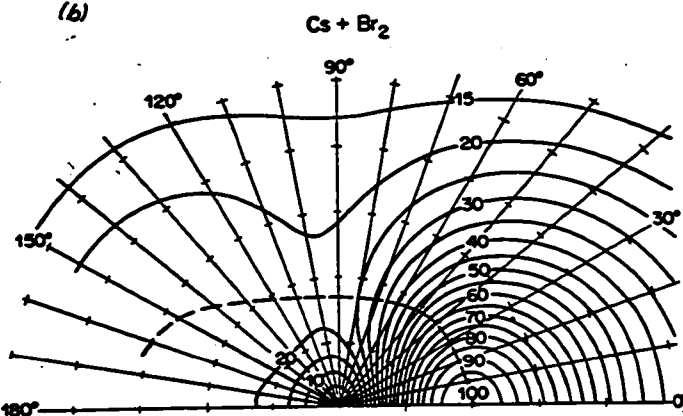
15. We note that the angles chosen, particularly $\Theta = 10^\circ$, are especially sensitive to subtraction and weighting errors; if the data were more "consistent", the fits would probably be better.

Fig. 5. Comparison of center-of-mass maps generated from (a) 4-term,
(b) 16-term, and (c) 36-term fits, for Cs + Br₂.

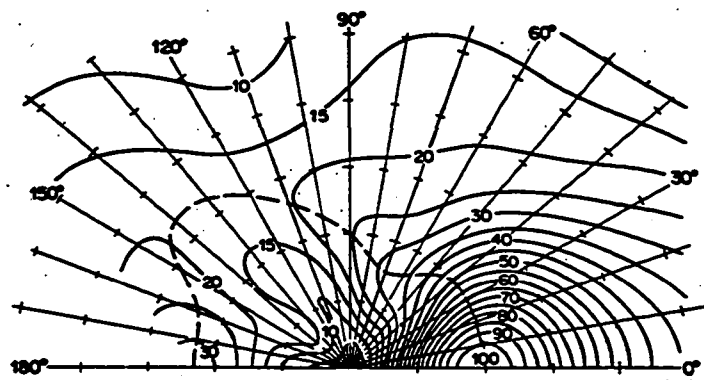
(a)



(b)



(c)



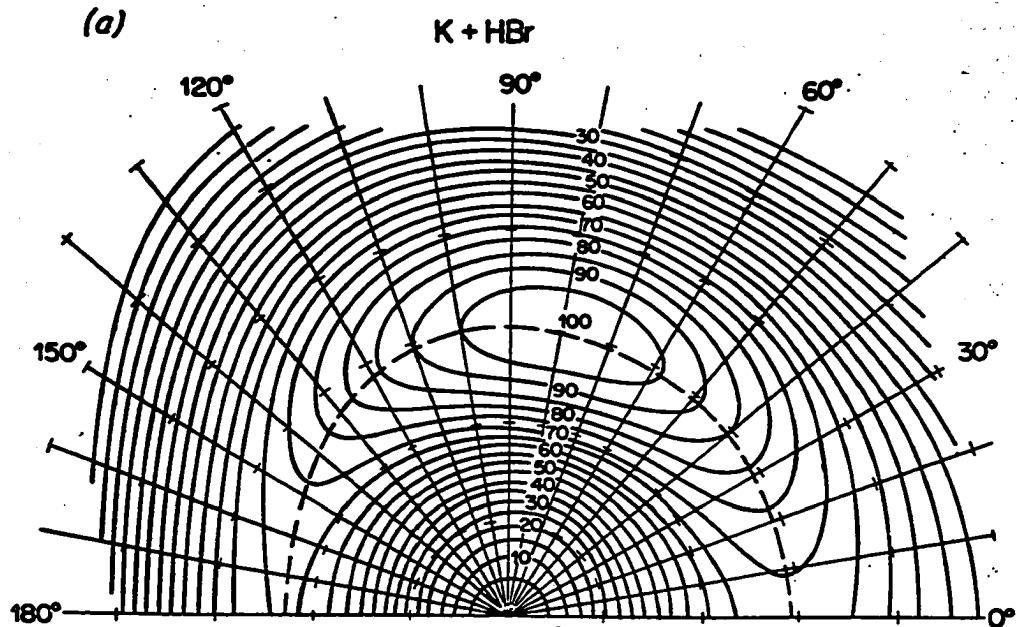
the fit (Fig. 1) is outside the error of the data, so that the uppermost 4-term map does not do justice to the quality of the data. The 16-parameter function does a much better job with fitting the data, while retaining its "smoothing" properties and giving a reasonable-looking c.m. function. On the other hand, the 36-term run, while giving quite a good fit to the data, especially at $\Theta = 10^\circ$ (Fig. 1), has, from inspection of the lowest c.m. map in Fig. 5, quite clearly been allowed too much freedom and has responded to slight noise in the peak heights, positions and shapes of the LAB velocity spectra. In general, then, a balance must be struck between fitting the LAB data closely and getting a reasonably smooth c.m. cross section. Results similar to the above have been found for the other systems analyzed here. Figure 6 compares the 16 and 36 term maps for K + HBr.

It is apparent from the above analysis that we cannot expect to perform a true "unfolding" of the LAB data if it has noise such as found in these systems ($>10\%$, somewhat larger at small LAB angles for the Br_2 reactions). The LS method clearly is capable of such an unfolding, as shown in the preceding chapter, but the "data" used was computer-generated and virtually noise-free. Thus our objective here has had to be more limited, namely, to produce a c.m. representation of the LAB intensities which "smooths out" in a reasonable way any discrepancies in their values.

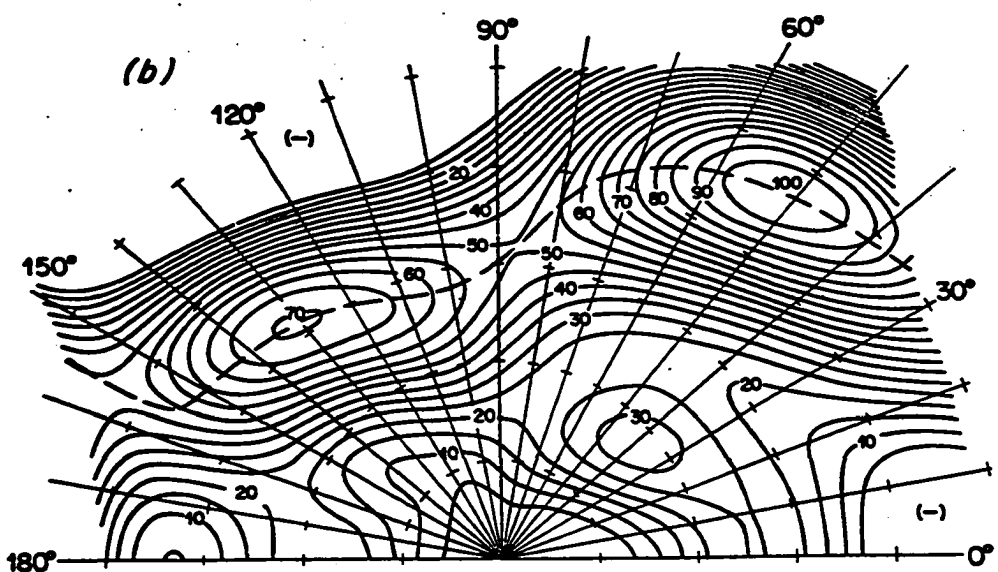
We can now make a quantitative comparison with the NNDA method used in Ref. 2, and the "stochastic" analysis¹⁴ of Ref. 1. The variation of the recoil peak with angle for K and Cs + Br_2 is compared with

**Fig. 6. Comparison of center-of-mass maps generated from (a) 16-term
and (b) 36-term functions for KBr from K + HBr.**

(a)



(b)



the NNDA results in Fig. 7. Angular distributions at various recoil velocities are compared with the stochastic results for K + HBr, DBr in Fig. 8. The NNDA comparison is not completely valid because the LS cross section is required to be symmetric about χ , and hence must compromise in trying to fit data originating from either side of χ in the LAB, whereas the NNDA cross section possesses no inherent symmetry except that provided by the data itself. The NNDA results of Fig. 7 were taken from that side of χ corresponding to positive LAB angles. Comparison with the NNDA contour maps² shows good semiquantitative agreement.

C. Details and Comments

In describing the test calculations in the previous chapter, the numerical computations were laid forth in some detail. Here we will merely point out a few idiosyncrasies and caveats encountered in using the LS method. Many of these details have been brought to light by the calculations of Riley,⁴ who has used the LS program to analyze all of his velocity analysis data. (See the Appendix to Chapter III for a description of the computer program.)

A slight difficulty, which is evident in the data plots (Figs. 1 and 2), is the tendency for "bumpiness" in some of the back-calculated LAB spectra. Investigation has shown that this phenomenon arises in the vicinity of the (most probable) c.m. vector (usually within 20° or so) when the LAB velocity v is passing through the region where $\mu \cdot v \approx 0$ and the u^{-2} factor in the Jacobian is thus varying most rapidly. A finer velocity-averaging grid alleviates this problem, but at the cost

**Fig. 7. Variation of peak in recoil velocity distributions of MBr
with scattering angle for K and Cs + Br₂: (—) LS, (---) NNDA
of Ref. 2.**

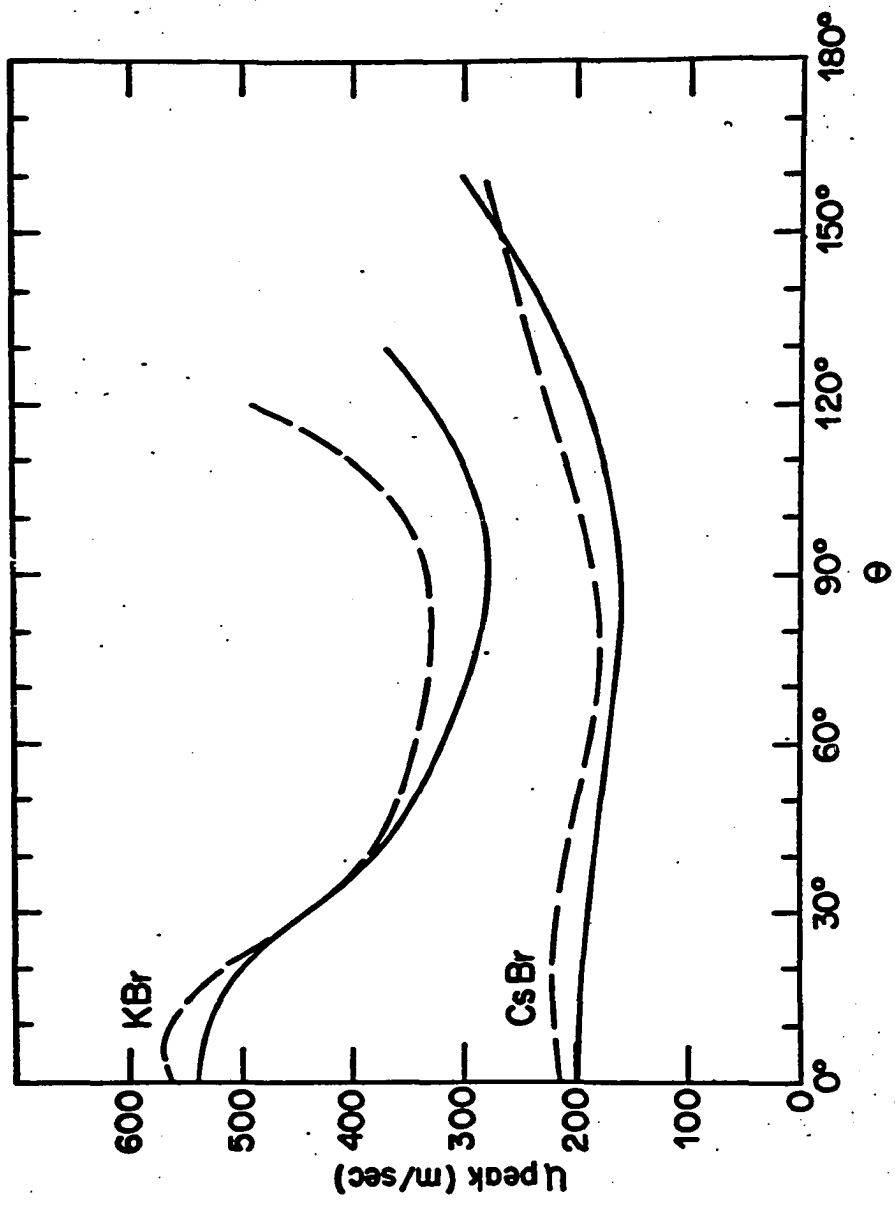
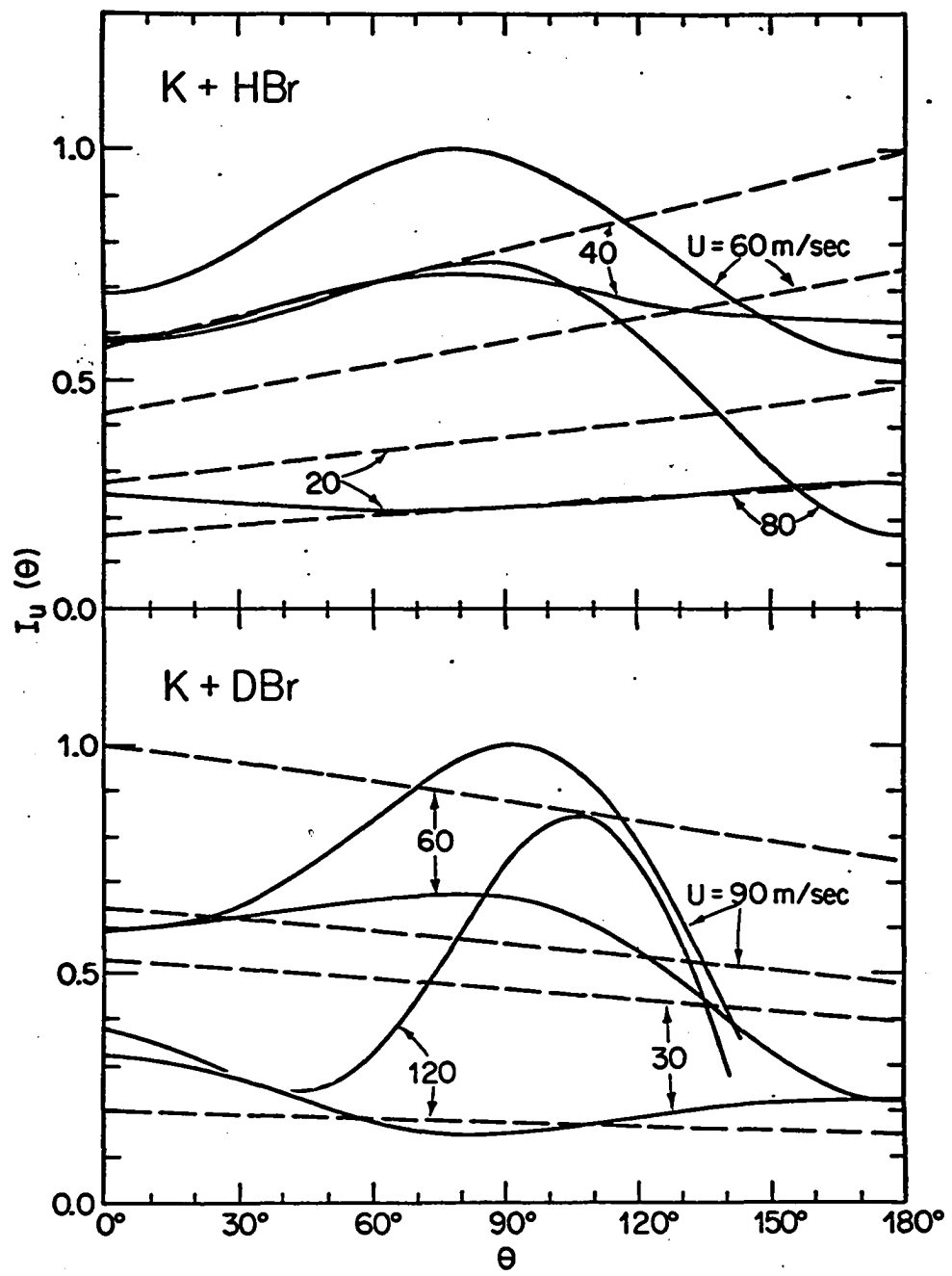


Fig. 8. Comparison of center-of-mass angular distributions at various recoil velocities from the LS analysis (—) with the stochastic fit (---) of Ref. 1, for KBr from K + HBr and DBr.



of much longer computing times. Since it has also been found that the c.m. results are little affected by a finer grid, we have not refined the integration further.

One can discern, from inspection of the c.m. contour maps, that the contours will join smoothly to their "mirror images" below the lower axis, which represents the relative velocity v . This property is due to the nature of the expansion used (Eq. (2)), and is considered physically reasonable and highly desirable. In terms of more conventional angular distribution plots, it implies that each constant- u contour will have zero slope at $\theta = 0^\circ$ and 180° .

All the calculations have been done with a number of parameters ensuring the inclusion of an equal number of even (symmetric about $\theta = 90^\circ$) and odd (antisymmetric about 90°) Legendre functions in order not to introduce a systematic bias into the LS-determined c.m. function. With the auxiliary rule $n_{\max} = l_{\max}$ (see Eq. (2)), this means that we have restricted the a_{nl} matrix to dimensionality 2, 4, 6, ..., or the number of parameters to $2^2, 4^2, 6^2, \dots$

We mention again for completeness the caution about interpretation of the c.m. function at low velocities u and in interpolated or extrapolated velocity-space regions. In these areas, as shown in Chapter III, the results are less trustworthy.

D. Conclusion

This chapter has been intended as a demonstration of the methods of kinematic analysis developed in the preceding chapter, and we have attempted to draw no "chemical" conclusions from the results of the data inversions. Once the c.m. cross section has been obtained in

velocity-space form, it can easily be converted to a function of final translational energy E' and scattering angle θ , and from it can be derived the internal excitation function of the products and its variation with θ . Results in this form are then easily compared to those of trajectory calculations. There seems to be enough detail in the $M + Br_2$ data to confine to a fairly narrow range the possible potential surfaces governing these reactions, and hence to provide very strong evidence for or against any interpretation in terms of electronic structure of the reactants, intermediates and products.

Finally, a word should be said about the merits of the so-called "Cartesian" data plots advocated recently.¹ In our opinion, these are fine for data taken on products with a fairly narrow energy range not near zero. But for data of the $M + Br_2$ type, where the velocity distributions peak low and do not fall off until near zero, this technique tends to make everything peak at zero velocity. In the c.m. the low velocity portion of the cross section, inherently less accurate as mentioned previously, is blown up very much out of proportion to its worth. Since in plotting $I_{cm}(u)/u^2$ for the "Cartesian" representation instead of $I_{cm}(u)$ as in our "polar" representation, an ill-determined region of the scattering function is being exposed, we maintain that the "polar" representation is more meaningful in terms of the data. In addition we feel it to be more consistent with the general interpretation of the cross section for reactive scattering arising from physical theory, particularly as applied to micro-reversibility.

CHAPTER V

**A MOLECULAR BEAM STUDY OF THE REACTIONS OF HYDROGEN AND
DEUTERIUM ATOMS WITH ALKALI HALIDES**

Abstract

Angular distributions of alkali atoms produced in crossed-beam reactions of H and D atoms (at $\sim 2800^{\circ}\text{K}$) with KF, CsF, KCl, CsCl, and KBr (at $\sim 1100-1200^{\circ}\text{K}$) have been measured. For these systems, the reaction exoergicity varies from $\Delta D_0 \sim 17 \text{ kcal/mole}$ for H + KF to -4 kcal/mole for H + KBr; the broad thermal distribution of the reactant energy peaks near 12 kcal/mole with E $\sim 9 \text{ kcal/mole}$ in relative translation and W $\sim 3 \text{ kcal/mole}$ in vibration and rotation of the alkali halide. Cross sections in the center-of-mass (c.m.) system are derived from kinematic analysis of the data, by means of a least-squares technique which takes account of velocity and beam-divergence averaging. The main results are: (1) The reaction cross sections vary from $Q_r \sim 1$ to 25 \AA^2 . The magnitude does not directly correlate with ΔD_0 or the identity of the halogen. For a given halogen, Q_r is 2-4 times larger for the Cs reaction than for K and about 2 times larger for D than for H. (2) The reactively scattered alkali atoms emerge predominantly into the forward hemisphere (c.m. system) with respect to the incident alkali halide. The shape of the angular distribution is similar for K and Cs and for H and D reactions, whereas the peak shifts markedly with the halogen, from strongly forward for the KBr reaction to nearly sideways for the KF and CsF reactions. (3) At wide angles, the distributions of alkali halide scattered without reaction in each case have the form expected for repulsive wall scattering and are similar to that obtained with H or D replaced by He. This indicates that the reaction probability is almost negligibly small in collisions with small impact parameters, in contrast to what

is found for K + HBr and many other reactions. (4) The partitioning of energy between product translation E' (M relative to HX) and internal excitation W' (vibration and rotation of HX) can only be roughly estimated due to the limitations on analysis imposed by the data; it appears that E' is comparable to W and that W' is comparable to $E + \Delta D_0$. These results are qualitatively consistent with a dynamical model which postulates that the motion of H or D is approximately separable from that of the heavier atoms and reaction is most probable for a triangular configuration of H-M-X.

A. Introduction

The reactions of hydrogen atoms with alkali halides, $H + MX \rightarrow HX + M$, offer interesting possibilities for correlation of dynamics with electronic structure. The reactants have an appealingly simple structure, the H atom having only one electron and the salt being well-characterized by a completely ionic, "no-electron bond" model.¹ On the product side, however, the HX bond involves predominantly covalent electron sharing, particularly for the heavier halogens, so that such a simple structural picture no longer applies. These systems are the first to be examined experimentally in which the bond type changes in the direction ionic \rightarrow covalent. In many reactions previously studied involving alkali atoms and covalent halogen-containing molecules,² $M + RX \rightarrow MX + R$, the nature of the bonding changes in the opposite direction, covalent \rightarrow ionic. These latter reactions, including the $M + HX$ case, are usually discussed in terms of the "electron-jump" or "harpoon" mechanism² of Polanyi and Magee,³ where an abrupt transition to the ionic surface occurs at a "crossing radius" determined by the difference between the electron affinity of the halogen group and the ionization potential of the alkali atom. That this change takes place over a short range of reactant

-
1. E. S. Rittner, J. Chem. Phys. 19, 1030 (1951). See also, C. Maltz, Chem. Phys. Letters 3, 707 (1969).
 2. D. R. Herschbach, Advan. Chem. Phys. 10, 319 (1966).
 3. J. L. Magee, J. Chem. Phys. 8, 687 (1940).

separations has been nicely brought out in the recent all-electron potential surface calculation of Balint-Kurti and Karplus⁴ on $\text{Li} + \text{F}_2 \rightarrow \text{LiF} + \text{F}$. Microreversibility suggests that the $\text{H} + \text{MX}$ reactions therefore should perhaps be thought of in terms of a "reverse harpoon".

In the entrance channel the electronic structure in these reactions is analogous to that in the $\text{M}' + \text{MX} \rightarrow \text{M}'\text{X} + \text{M}$ reactions. The latter systems have been studied extensively by Miller and Safron⁵ in this laboratory, and have been shown to react via the formation of a long-lived collision complex. This result correlates nicely with the one-electron calculation of Roach and Child⁶ using a pseudopotential method on the reaction $\text{K} + \text{NaCl} \rightleftharpoons \text{Na} + \text{KCl}$, which gave a potential well for a triangular configuration of the atoms stable with respect to $\text{Na} + \text{KCl}$ by ten kcal/mole. There, of course, the bond type remains ionic for both the reactants and products. Nonetheless it appears that some theoretical information on the reactants side of the potential energy surfaces for $\text{H} + \text{MX}$ might also be had without excessive calculational labor using the one-electronic picture which is likely to hold in that region. In Chapter VI such a calculation will be presented.

4. G. G. Balint-Kurti and M. Karplus (to be published); G. G. Balint-Kurti, Ph.D. Thesis, Harvard University, Cambridge, Mass., 1969.
5. W. B. Miller, S. A. Safron and D. R. Herschbach, Disc. Faraday Soc., 44, 108 (1967); S. A. Safron, Ph.D. Thesis, Harvard University, Cambridge, Mass., 1969; W. B. Miller, Ph.D. Thesis, Harvard University, Cambridge, Mass., 1969.
6. A. C. Roach and M. S. Child, Mol. Phys. 14, 1 (1968).

The extensive work which has been done on the reverse reactions, $M + HX \rightarrow MX + H$, provides another stimulus for the present study, since we can hope to correlate our results with these data through the principle of microreversibility. The nonreactive scattering has been well characterized,⁷ and from it the dependence of reaction probability on energy and impact parameter has been derived by means of an optical model analysis.⁸ The reactive scattering studies⁹ have yielded few definite conclusions, however, because the interpretation is severely handicapped by an unfavorable kinematic situation.^{10,11} Since the MX product, which is detected by the usual surface ionization method, is so much heavier than the H atom and since the reaction exothermicity is low, the conservation laws require MX to have a very small recoil velocity away from the center-of-mass. Hence, the details regarding the preferred direction and magnitude of recoil are hard to discern from measurements in the laboratory frame. Nonetheless, Bernstein and co-workers⁹ have made very careful experiments employing a velocity-selected K beam and velocity analysis of the KBr product of the reactions of K with HBr and DBr. The reactive differential cross sections

-
7. E. F. Greene, A. L. Moursund and J. Ross, *Advan. Chem. Phys.* 10, 135 (1966); J. R. Airey, E. F. Greene, K. Kodera, G. P. Reck and J. Ross, *J. Chem. Phys.* 46, 3287 (1967); and earlier references cited therein.
 8. C. Nyeland and J. Ross, *J. Chem. Phys.* 49, 843 (1968).
 9. C. Riley, K. T. Gillen and R. B. Bernstein, *J. Chem. Phys.* 50, 4019 (1969), and earlier work cited therein.
 10. D. R. Herschbach, *J. Chem. Phys.* 33, 1870 (1960).
 11. S. Datz, D. R. Herschbach, and E. H. Taylor, *J. Chem. Phys.* 35, 1549 (1961).

they derive are still quite uncertain; as shown in Chapter IV, other rather different center-of-mass scattering functions are also compatible with the laboratory intensity distributions. An elegant approach which circumvents the kinematic constraintswas employed by Martin and Kinsey,¹² who detected the radioactive T atoms emerging from the K, Cs + TBr isotopically analogous reactions using an absorption-counting technique. They found the T atom distribution peaked quite sharply backward with respect to the initial TBr direction, implying a "rebound" mechanism. The narrowness of their laboratory distributions, however, requires a center-of-mass angular shape far too sharply peaked to be consistent with the data of Ref. 9, unless a drastic isotope effect is assumed. In addition to the angle- and velocity-distribution studies, measurements of the rotational energy carried by the alkali halide product have been made for the K + HBr and Cs + HBr reactions,^{13,14} The results indicate that essentially all of the available angular momentum goes into the product rotation, as expected from a heuristic argument which again depends primarily on the small H/MX mass ratio.²

In common with other reactions involving H atoms attacking a heavy molecule,¹⁵ the H + MX systems have special dynamical features

-
12. L. R. Martin and J. L. Kinsey, J. Chem. Phys. 46, 4834 (1966).
 13. R. R. Herm and D. R. Herschbach, J. Chem. Phys. 43, 2139 (1965); C. Maltz and D. R. Herschbach, Disc. Faraday Soc. 44, 176 (1967).
 14. C. Maltz, Ph.D. Thesis, Harvard University, Cambridge, Mass., 1969.
 15. Y. T. Lee, R. J. Gordon and D. R. Herschbach, J. Chem. Phys. (to be published), on H + M₂ reactions.

which invite treatment in terms of a model which postulates that the H motion is approximately separable from that of the heavy atoms. A quantitative model of this kind is formulated in Chapter VII and compared there with the experimental findings of this chapter.

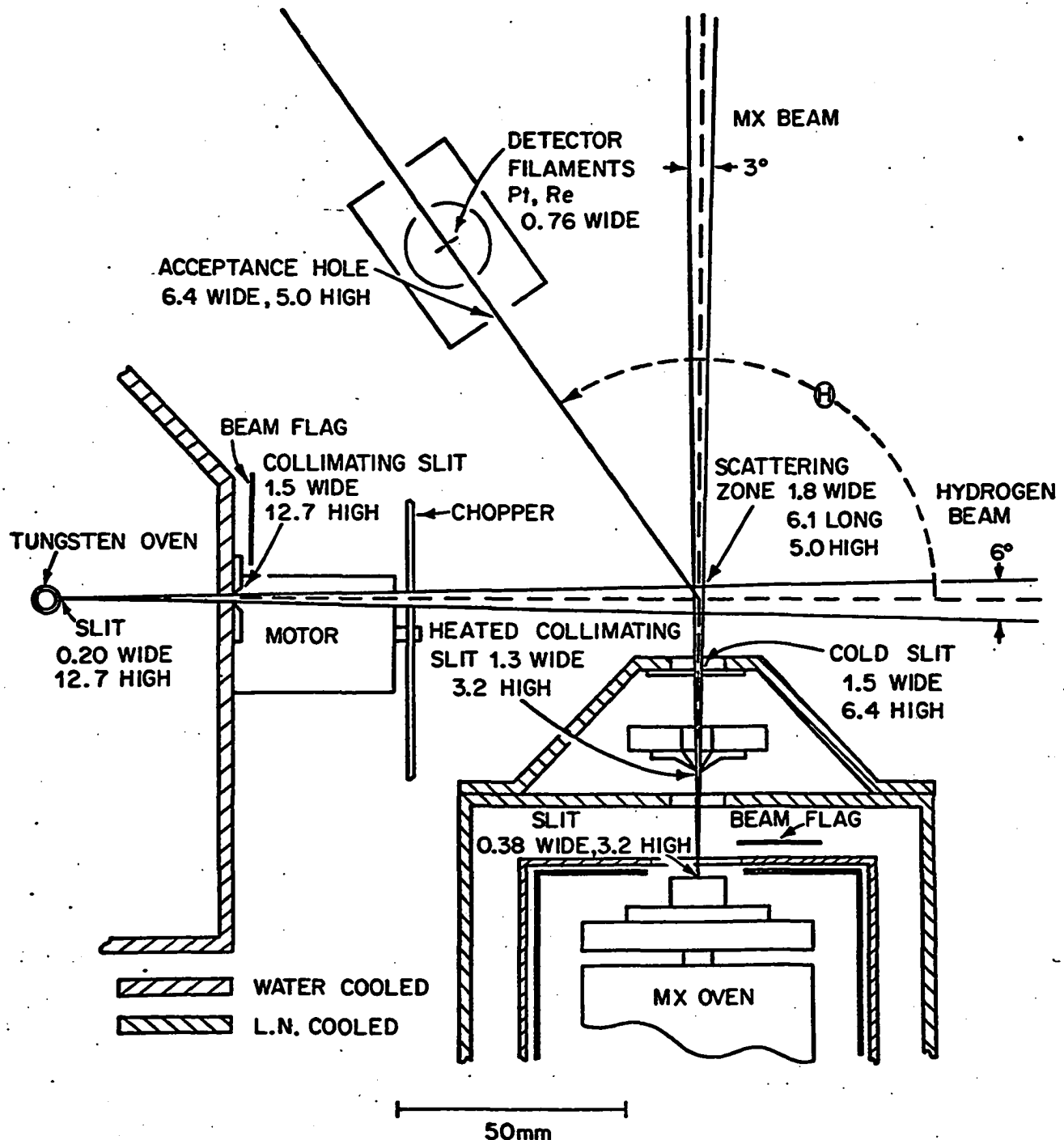
B. Experimental Conditions

The apparatus^{16,17} was essentially the same as in the H + M₂ study.¹⁵ A conventional "upper chamber" with a standard ribbon-shaped slit was mounted on the condensable reactant oven for the MX in place of the "Laval nozzle" pinhole which had been used to generate the M₂ dimers. At first a roll of "crinkly foil" was placed behind the slit, but this was removed when it was found not to affect beam collimation significantly. Also, the orifice of the H atom oven was widened from 0.05 to 0.2 mm in order to increase the scattered intensity. Figure 1 shows the configuration of beam sources and detector used in all of the runs. The distance from the scattering center to the H-beam collimating slit was 9.6 cm, to the H oven 13.4 cm, to the final (cold) MX collimating slit 1.5 cm, to the heated MX slit 3.8 cm, to the MX oven 6.1 cm, and to the filaments on the rotating surface ionization detector 9.5 cm. An auxiliary detector was used to monitor the MX beam intensity, 54 cm from the oven. The H atom beam was formed by thermal dissociation in a tungsten tube heated by direct resistance with 450 A at 2 V a.c. to about 2800°K.^{16,17} The resulting

16. M. A. D. Fluendy, R. M. Martin, E. E. Muschlitz, and D. R. Herschbach, J. Chem. Phys. 46, 2172 (1967).

17. W. C. Stwalley, Ph.D. Thesis, Harvard University, Cambridge, Mass., 1968.

Fig. 1. Schematic of the crossed-beam apparatus. All dimensions are given in mm.



beam, containing about 80% atoms at the pressure used (about 1 torr bled through a capillary), was roughly triangular with a FWHM of $\sim 6^\circ$ as inferred from measurements using a bolometer¹⁸ on a sliding mount opposite the source.

The main chamber of the salt oven was heated so as to produce a pressure of 1-10 torr ($\sim 750\text{-}900^\circ\text{C}$) of salt vapor; the independently heated orifice chamber was kept about $80\text{-}120^\circ$ hotter to prevent condensation. The heated collimating slit was also kept at about 500°C to avert clogging. The slit arrangement resulted in a salt beam about 3° FWHM with a roughly trapezoidal profile.

After a few runs at these high temperatures the salt oven, made of stainless steel #304, began to "fossilize"; the surface became rough and was prone to retain fingerprints and to scratch and nick easily. Toward the end of these experiments, it developed a leak, and has now been replaced for subsequent dimer studies. It may be significant that KF was in the oven when the leak was formed; this salt also corroded the exit slit, enlarging it from 0.37 to 0.50 mm after five or six runs.

The scattering center is surrounded by a copper box attached to a 15l liquid nitrogen reservoir suspended from the bottom of the main vacuum chamber by thin-gauge steel strips and a thin-walled steel fill tube. The copper shield separating the differentially pumped hydrogen chamber from the main chamber is water cooled, and the salt oven is

18. M. A. D. Fluendy, Rev. Sci. Instr. 35, 1606 (1964).

surrounded by a water-cooled copper shield and two liquid N₂ shields, in that order. The interior liquid N₂ shield is independently cooled by a double-walled pipe attached to a "chicken feeder"; the exterior shield is attached to the copper box. The main chamber is evacuated through a water-cooled baffle by a 6" oil diffusion pump, the hydrogen chamber by a 4" pump. The background pressure was $\sim 1-2 \times 10^{-6}$ torr (uncorrected ion gauge reading) in the main chamber and $\sim 2 \times 10^{-5}$ torr in the hydrogen chamber during a typical run. Roughly $7-8 \times 10^{-7}$ torr of the main chamber pressure was due to the hydrogen source; for deuterium this was reduced to $\sim 4-5 \times 10^{-7}$, with a corresponding improvement in the overall pressure.

The factor which has made these experiments feasible, and which distinguishes them from the alkali metal-halogen compound experiments, is that the angular distribution of product M atoms can be measured directly on a "methanated" Pt-8% W filament,¹⁹ without (in principle, at least) having to resort to a subtraction to remove background elastic scattering. The extremely small reactive scattering signals would have been impossible to measure had that been the case here. Miller et al.⁵ also enjoyed this advantage in detecting N' from N + M'X, although the reactive cross sections were much larger ($\sim 200 \text{ \AA}^2$). The reactive signals from H + MX were actually so low that the small, but finite, ionization efficiency, ϵ , of the Pt filament for salt molecules had to be taken into account. Thus, subtraction of signals was still necessary, but not nearly so drastic, since in most cases

19. T. R. Touw and J. W. Trischka, J. Appl. Phys. 34, 3635 (1963).

the remaining reactive signal was of the same order of magnitude as the original Pt signal. For the measurements reported, a 30-mil Pt-8% W ribbon (which had been heated at $\sim 1600^{\circ}\text{K}$ for a few minutes in 10^{-4} torr methane) operated at 1300°K was used to detect the M atoms, and a 30-mil Re ribbon at $\sim 1700^{\circ}\text{K}$ for the total scattering, $M + MX$. The atomic beam was modulated at 10 Hz with a two-blade aluminum chopper, and the scattered signals measured with phase-sensitive lock-in amplification. A reference signal was provided by a light bulb and phototransistor on the chopper mount; the chopper was driven by an f/3 synchronous motor with 15 Hz input voltage to avoid pickup problems.

Prior to each experiment, the alignment of the salt oven was carefully checked. The fact that the oven was tall (14 cm) for its base area (4×5 cm) made it prone to tilt off its three-pin mount when the source flange was replaced, and the slight stiffness of the heating and thermocouple leads sometimes kept it from returning to equilibrium. A removable copper panel in the outer MX oven cold shield allowed access to the oven for readjustment after the flange had been replaced. After the apparatus had been pumped out overnight or longer, liquid N_2 was added to the traps and the salt oven warmed up. When a stable salt beam seemed to be forthcoming, the hydrogen oven was turned on and the gas admitted. The salt beam would become stable after about 3-4 hours, at which time the experiment would be initiated. The Pt filament angle scan would usually be performed first, the signals from the lock-in amplifier being fed to a strip-chart recorder. The signal was taken as the difference in voltage

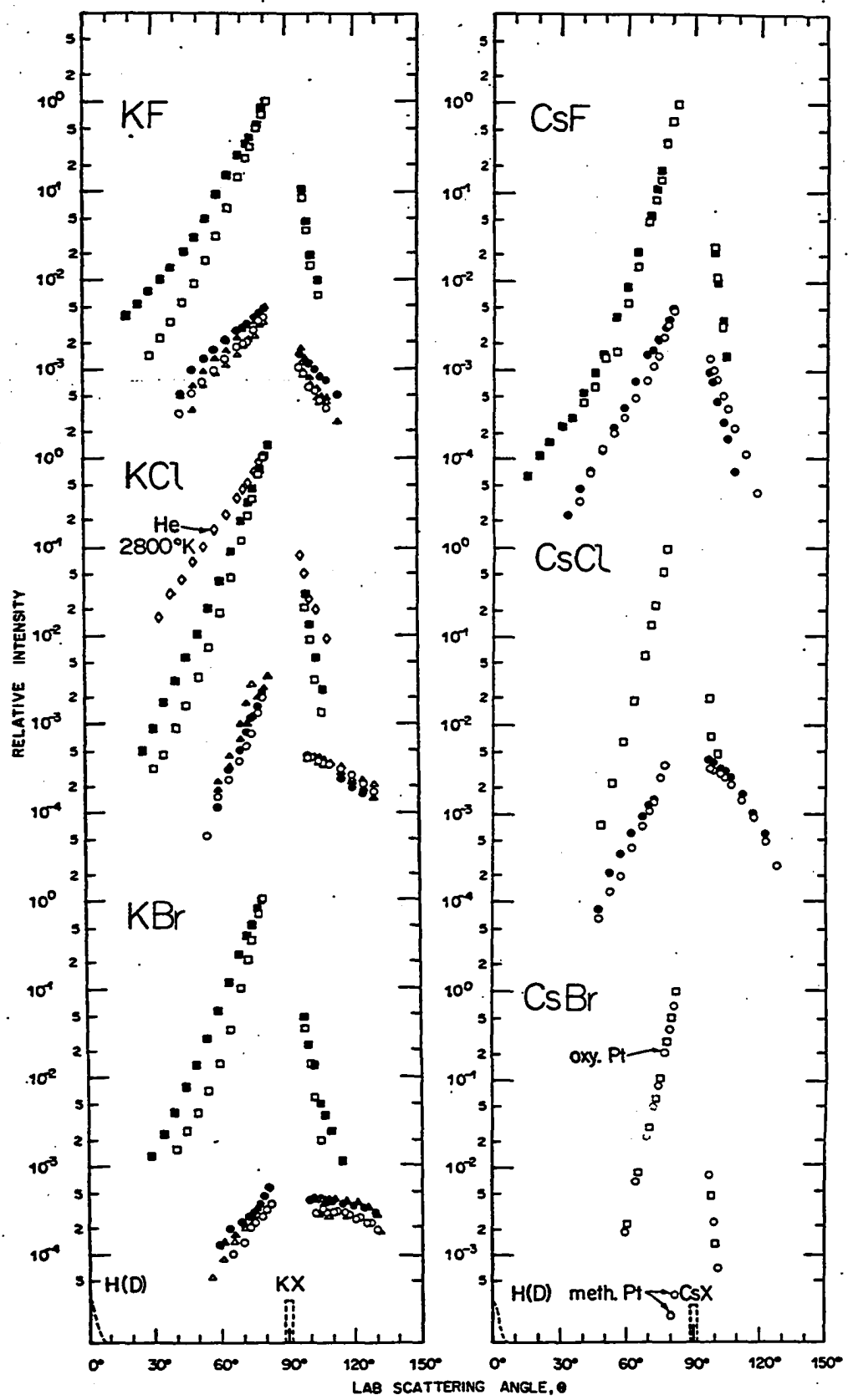
when the H beam flag was opened and closed; two and sometimes three such "flaggings" were executed at each angle. Due to the use of phase-sensitive detection, the flag-closed position usually gave a voltage of zero, except when the angle was within less than $\sim 8^\circ$ of the salt beam; there the response of both filaments became unsteady and sluggish. Every three or four angles a measurement at a reference angle, usually $\pm 20^\circ$ from the salt beam, was interspersed to provide time-normalization. The Re angle scan followed, if the salt beam was still relatively stable. Often this scan could not be completed due to the salt deposit on the exit hole of the inner L.N. cooled shield eventually obstructing the beam path. For later runs this problem was alleviated to some extent by widening the hole. In any event, since the shape of the total scattering as observed on the Re filament reproduced well for various runs on the same system, often only a few measurements on Re were necessary to gauge the relative magnitude of the Re and Pt signals. At the conclusion of each experiment, the positions of the filaments with respect to the salt beam and the detection efficiency ϵ of the Pt ribbon for MX were established by doing beam scans with each filament.

The measured ϵ varied from a maximum of $\sim 0.9\%$ to less than 0.01% from run to run in a seemingly random fashion, independent of how recent the methanation treatment and independent of the system being studied. The work function of the Pt filament, as monitored by the electron emission, did not show any appreciable or systematic changes. The Re filament was always much noisier than Pt, and, after prolonged

operation in the $\sim 10^{-6}$ torr of hydrogen always present, began to show "fatigue" and to lose its detection efficiency. Sometimes oxygenation (flashing in 10^{-4} torr of oxygen) would revive it, sometimes not. It was found that baking the Re overnight in an attempt to reduce the noise level would only hasten this latter effect. (Ironically, as the detection efficiency of Re decreased, so did its noise level.) Consequently, a new Re filament was installed every few weeks to insure that $\sim 100\%$ of the salt molecules were being detected. The accurate measurement of ϵ would of course depend on Re being 100% efficient for MX. Use of the beam flag minimized exposure of the filaments to the salt beam during an experiment.

The primary data are given in Figure 2. For the K salts, where the reactive cross sections are smaller, the two best sets of Pt data are included. Except for the H + CsBr system, it is clear that in each case the Pt signals really do contain a contribution from reactively scattered M atoms. This makes the relative intensities at angles on either side of the MX beam quite different for Pt and Re. Also, on the small-angle side of the beam, where the bulk of the elastic scattering is found, the Pt signal as a rule falls off more gradually than Re. No reactive signal was observed for H + CsBr; since the reaction is endoergic by 9 kcal/mole, this is perhaps not surprising. It became a good test case, however: the Pt ribbon in the MX detecting (oxygenated) mode gave signals which were superimposable on the Re data, and when methanated gave tiny signals at $\Theta = 80^\circ$ and 82° ; when the measured ϵ was used to subtract out the MX

Fig. 2. Primary data collected on the Re (\square , \blacksquare) and Pt (\circ , \bullet , Δ , \blacktriangle) filaments for scattering of six salts by H (open symbols) and D (filled symbols). For KCl, \diamond denotes He on Re; for CsBr, Pt data are shown for both the oxygenated and methanated modes. Re data are normalized so that most intense H point for a given salt is unity, and D is also normalized to H at that point.



contribution, no significant signal remained. These findings bolstered our confidence in regarding the difference in shape of the observed Re and Pt curves as significant.

Since the Re signal was more than an order of magnitude larger than Pt over the entire angular range for every system studied, in correcting the Pt data for the contribution from elastically scattered MX the approximation was made that the Re data represents only the elastic scattering. The error incurred in using this approximation was never greater than 2%. Also, due to the very rapid falloff in the elastic scattering on the large angle side of the beam, neglecting the correction entirely in this angular range resulted in less than 1% error for all systems. (Re was especially noisy in this region, apparently because of the nearness of the H source, making the total scattering data there less reliable. Pt gave no such difficulty.)

The conditions for H + CsF (Fig. 2) were fairly typical of the systems with somewhat larger cross sections: the parent MX beam intensity was 3×10^{-6} A (corresponding to a flux of 5×10^{14} molecules $\text{cm}^{-2} \text{ sec}^{-1}$ at the rotating detector, 2×10^{15} in the scattering zone); at $\theta = 70^\circ$ the total scattering (Re) was 6×10^{-12} A (10^9 molecules $\text{cm}^{-2} \text{ sec}^{-1}$), of which all but 5% was due to elastic scattering, and the Pt signal was 3×10^{-13} A (5×10^7 molecules $\text{cm}^{-2} \text{ sec}^{-1}$) of which about 80% was due to reactively scattered Cs atoms. The ϵ here was somewhat high, 0.90%. The smallest reactive signals observed were those for H + KBr (Fig. 2): the main beam and the total scattering at $\theta = 70^\circ$ were somewhat higher than above, but the total

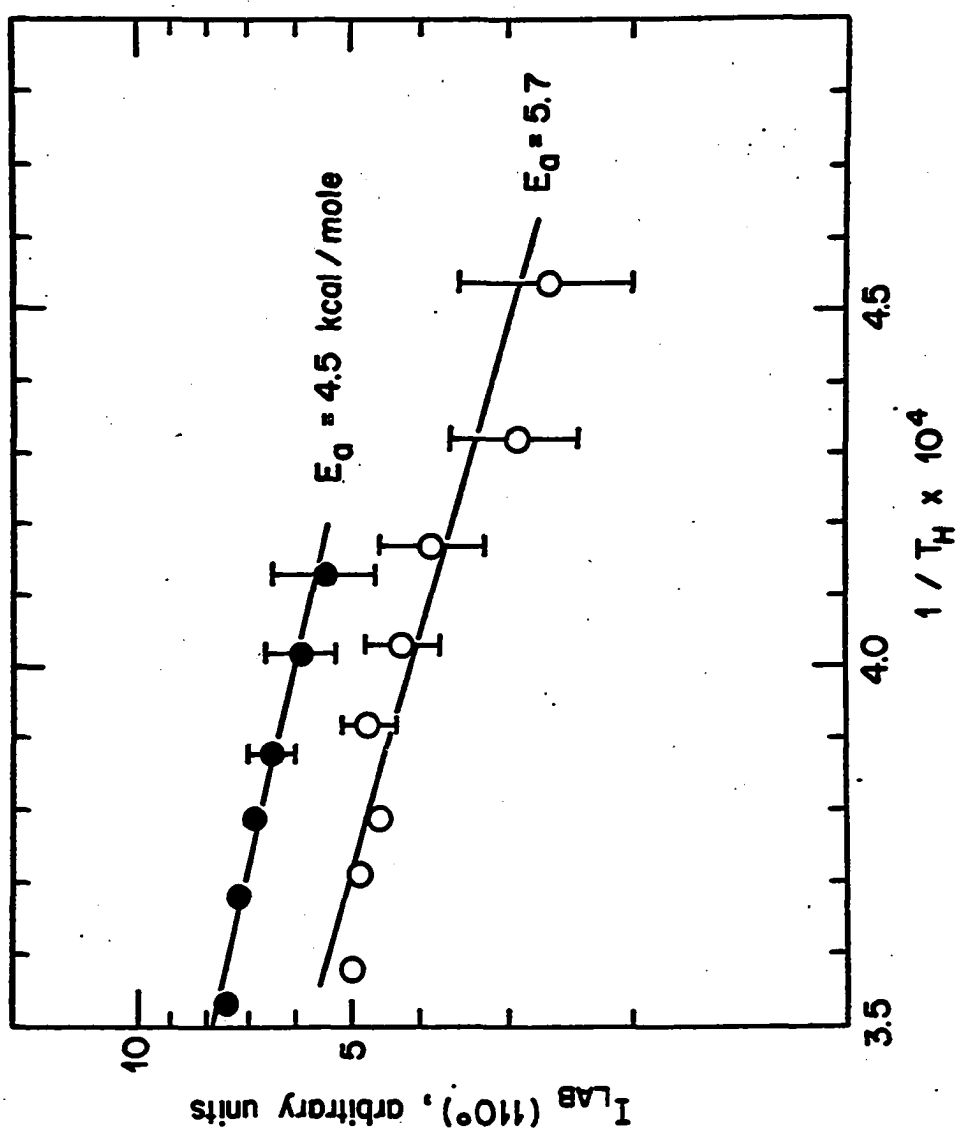
Pt signal was about an order of magnitude less (6×10^6 molecules cm^{-2} sec^{-1}); the measured ϵ of 0.011% left about 90% of this as reactively scattered K.

A temperature-dependence study was carried out on the slightly endoergic H, D + CsCl reactions ($\Delta D_0 = -3.3, -2.0$ kcal/mole, respectively) by measuring the reactive signal at a fixed LAB angle ($\Theta = 110^\circ$) as a function of the H oven temperature. It was possible to remain at the same LAB angle because the temperature range covered (2200-2800°K) affects the H atom velocity by only ~10%, and the origin and LAB orientation of the c.m. system are changed very little ($\approx 0.5^\circ$). In addition, complete angle scans done for three different temperatures verified that the shape of the angular distribution is invariant to changes in this range. The c.m. energy (translational temperature) is determined to better than 99% by the H atom LAB velocity distribution, so that a log (signal) vs reciprocal temperature plot is analogous to an Arrhenius plot, and the slope thus should give the "energy of activation". The results are shown in Fig. 3. The signals were corrected for the variation of the percentage of H atoms in the beam with temperature by normalizing them to the bolometer signal. The apparent activation energies are somewhat higher than the corresponding endoergicities, although the uncertainties, especially at low temperatures, are sizeable.

C. Elastic Scattering

The Re data, treated as purely elastic scattering for subtraction purposes, was also treated as such in analyzing the MX distributions.

Fig. 3. Temperature dependence of the intensity of reactively scattered Cs atoms from H (O) and D (\bullet) + CsCl at $\theta = 110^\circ$. Activation energies are noted. Relative normalization to total cross section ratio.

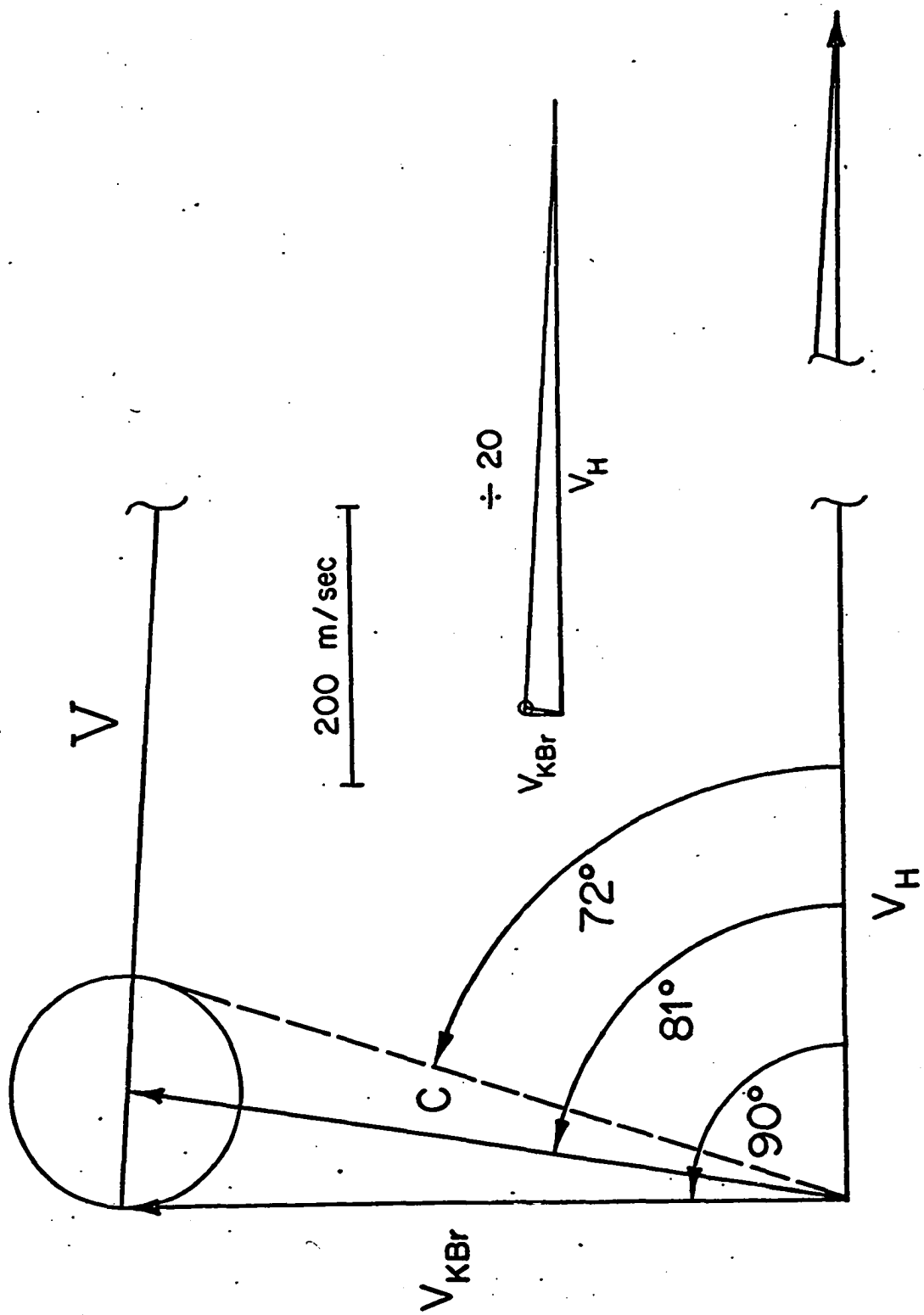


$I_{AB}(110)$, arbitrary units

For a given salt, D is seen to give more intensity at wide angles than H, as expected because of its greater mass; but when transformed into the center-of-mass (c.m.) system, this type of superficial dependence on the laboratory (LAB) position of the c.m. velocity vector ξ should disappear.

Figure 4 shows a kinematic diagram for the most probable velocities of the parent beams for the H + KBr system. (We define the c.m. scattering angle θ with respect to the initial c.m. H(D) atom direction; but to avoid confusion we will use $\theta' = 180^\circ - \theta$ to describe the MX elastic scattering so that forward and backward scattering of the salt correspond respectively to $\theta' = 0^\circ$ and $\theta' = 180^\circ$.) The circle indicates the locus of c.m. velocities μ which the KBr may possess assuming purely elastic scattering. Since the radius u of this circle is smaller than the magnitude of ξ , it is clear, for a ray drawn through the circle at LAB angle Θ , that two c.m. angles θ' correspond to that Θ , and that therefore two different regions of the c.m. intensity distribution $I_{cm}(\theta')$ contribute to the observed intensity $I_{LAB}(\Theta)$. Any scattering observed at Θ 's corresponding to rays outside the circle is, of course, unaccountable for the set of beam velocities chosen. But, due to the spread in ξ and μ caused by the beam velocity distributions and imperfect collimation, scattering is observed at much wider angles than the limits indicated by V_{KBr} and the dashed ray in Fig. 4. For the purpose of the analysis, however, only the most probable kinematic diagram was taken into account, and data not "allowed" by the chosen diagram were ignored. As mentioned

Fig. 4. Kinematic diagram for H + KBr. v_H and v_{KBr} are the most probable beam velocities, C is the center-of-mass velocity, and V the relative velocity. Inset on right shows complete diagram reduced by a factor of 20.



above, the LAB \rightarrow c.m. transformation remains double-valued,

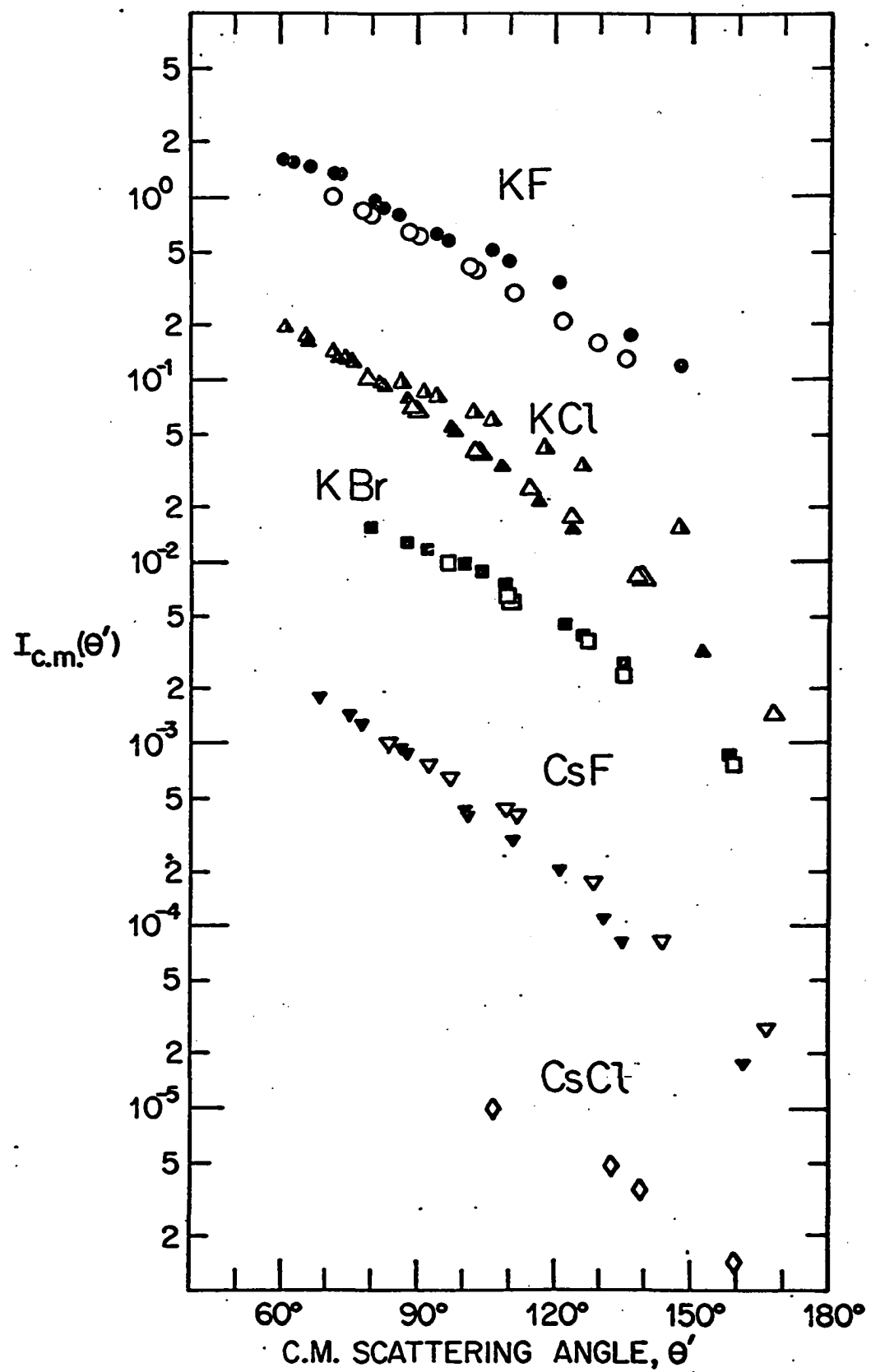
$$I_{LAB}(\theta) = J_i I_{cm}(\theta'_i) + J_o I_{cm}(\theta'_o), \quad (1)$$

where the subscripts "i" and "o" refer to the inner and outer intersections with the μ circle and $J_{i(o)}$ is the intensity Jacobian for that intersection. In this case, the inner "branch" cannot be neglected, as has usually been done,²⁰ since the elastic scattering circle is small enough in all cases to make the Jacobians comparable, and the inner branch usually comes from smaller θ' where the scattering is more intense. The problem is handled by using an iterative scheme to solve (1) for $I_{cm}(\theta')$ which makes use of the fact that the inner and outer branches are part of the same curve; details of this method may be found in an appendix to this chapter.

The resulting c.m. elastic scattering distributions are shown in Fig. 5. Since the c.m. vector is very close to the salt beam for all systems, and measurements near the beam could not be accurately made because of its breadth, most of the observed data transformed into the backward hemisphere in the c.m. system. The curves show a slightly bowed shape characteristic of repulsive wall scattering (here with the $\sin\theta'$ factor left in for later analysis). This is consistent with the small reaction cross sections involved. The fact that the LAB pt curves fall well below R_e even at the points which transform into $\theta' \sim 180^\circ$ indicates that even for purely backward scattering

20. In the past, it has only been necessary to make this approximation in the fixed-velocity analysis for reactive scattering, but the transformation relations are identical to those for elastic. See Chapter III of this thesis.

Fig. 5. Center-of-mass intensity curves for the elastic scattering of five salts by H (open symbols) and D (filled symbols). For KCl, A denotes He. Normalization for each salt is the same as in Fig. 2.



(near-zero impact parameter) a large percentage of collisions do not result in reaction. In addition, as shown in Fig. 5, the purely nonreactive He + KCl data when transformed shows some similarity to the other curves, although it does not fall off as rapidly as H and D + KCl. It should be noted, however, that the transformation procedure we have used is much more accurate for He, since the larger c.m. recoil velocity of the salt makes the single-kinematic-diagram approximation more reliable. The CsBr data could not be transformed at all.

D. Reactive Scattering

Figures 6-10 show the LAB angular distributions of M atoms formed in these reactions. The points on the small-angle ($\Theta < 90^\circ$) side of the MX beam generally show more scatter than the large-angle ($\Theta > 90^\circ$) points due to the subtraction involved in the correction for MX detection on Pt, and are considered less reliable. Nonetheless the agreement between runs, within scatter, serves to define the shape and peak positions of the distributions within a fairly narrow range.

The kinematics for these systems, dominated as they are by the light mass and high energy (~ 0.4 eV) of the H and D atoms, are all remarkably similar; the position of the most likely c.m. vector ranges from $\Theta = 76^\circ$ for D + KF to 83° for H + CsCl. The dashed curves on the figures indicate the centroid distributions for each system;¹¹ it is seen that all the product curves are fatter and are displaced to larger Θ , indicating a preference for recoil of the M atoms into the backward hemisphere in the c.m. system with respect to the initial relative velocity V (see Fig. 4). This implies that the HX products

Fig. 6. Arbitrarily normalized laboratory angular distributions of Cs atoms from the reactions of H and D with CsF at the beam temperatures indicated. Dashed curves are centroid distributions; solid curves are calculated from a least squares kinematic analysis.

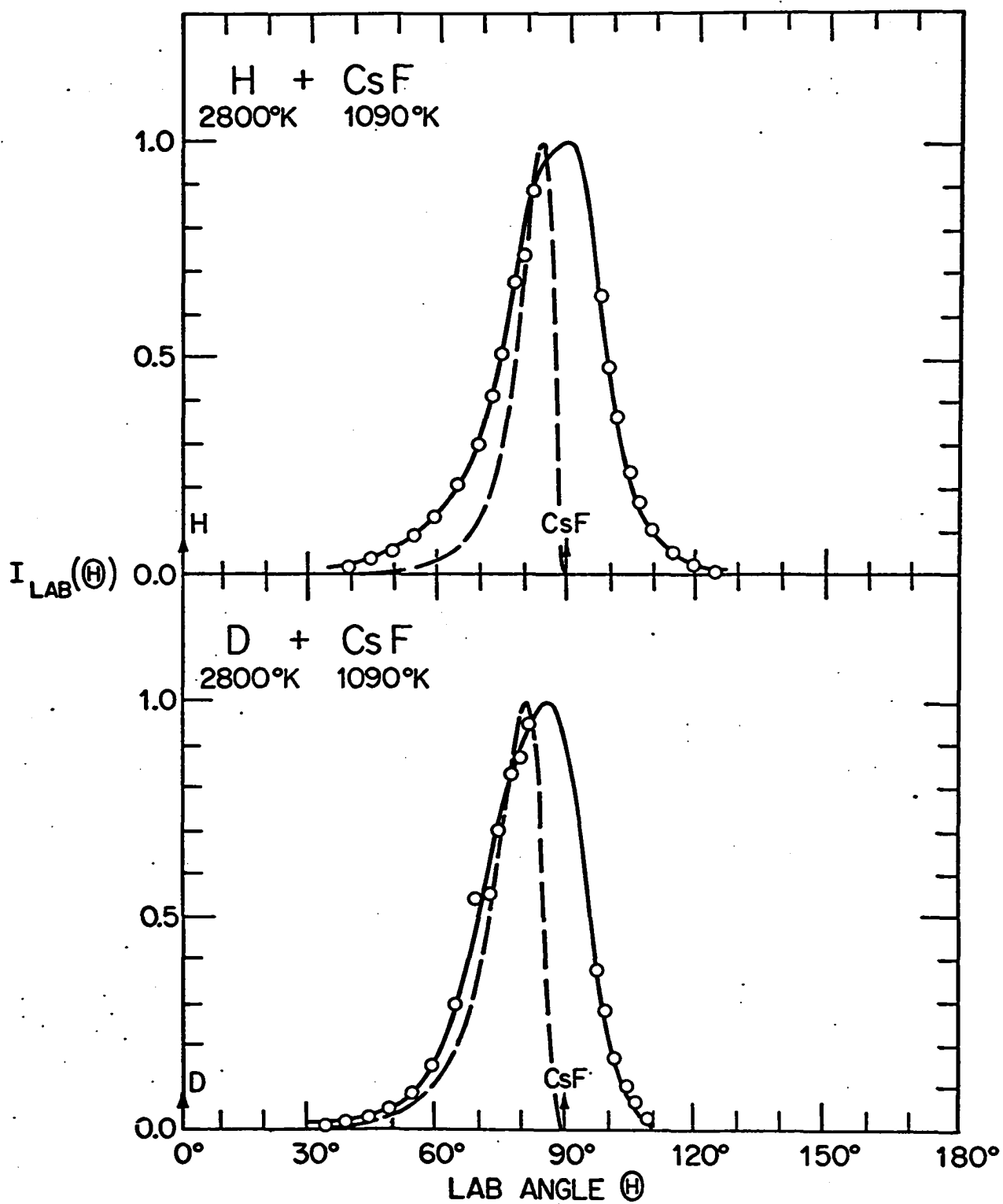


Fig. 7. Laboratory angular distributions of K from H and D + KF.

Notation as in Fig. 6.

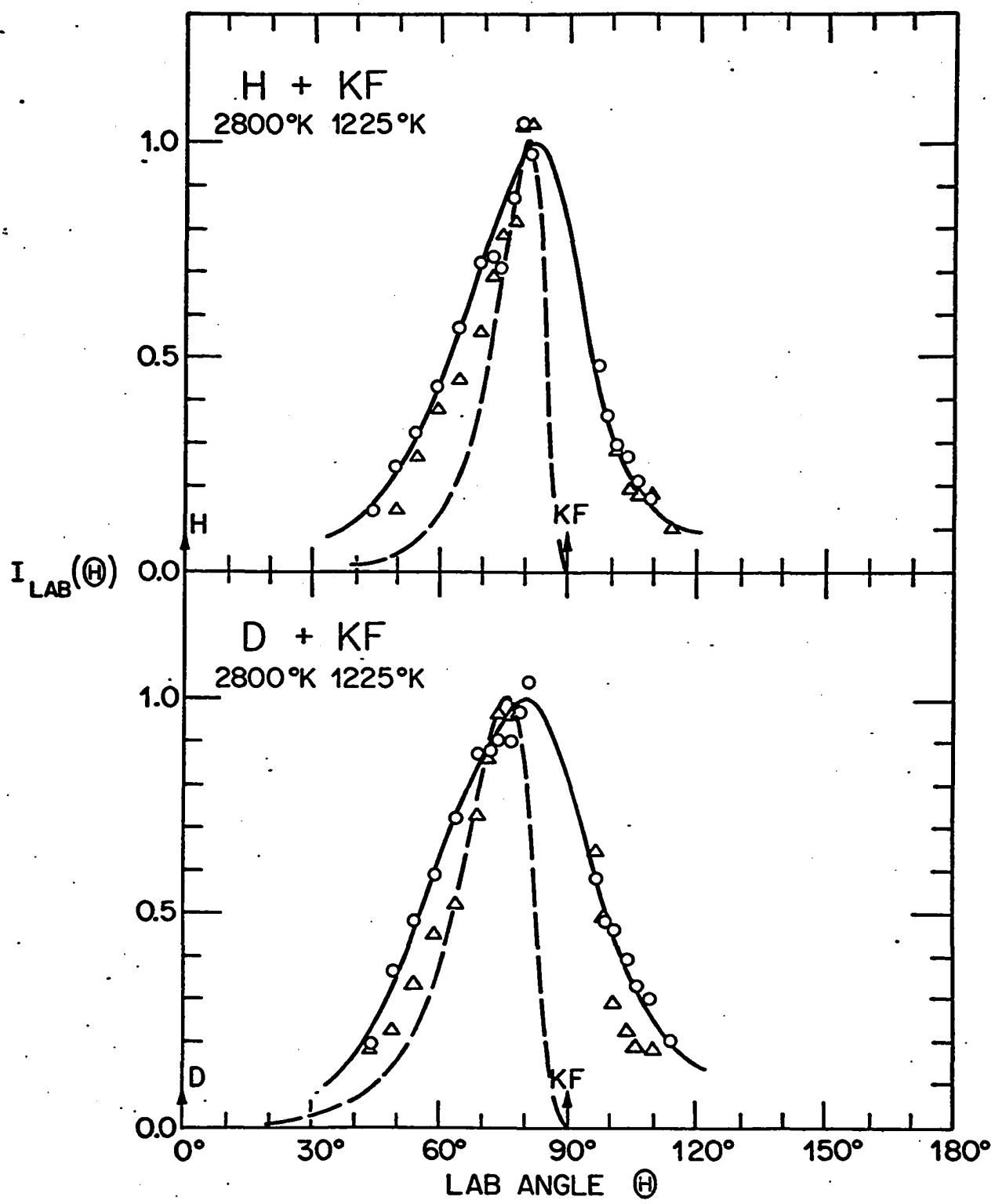


Fig. 8. Laboratory angular distributions of Cs from H and D + CsCl.

Notation as in Fig. 6.

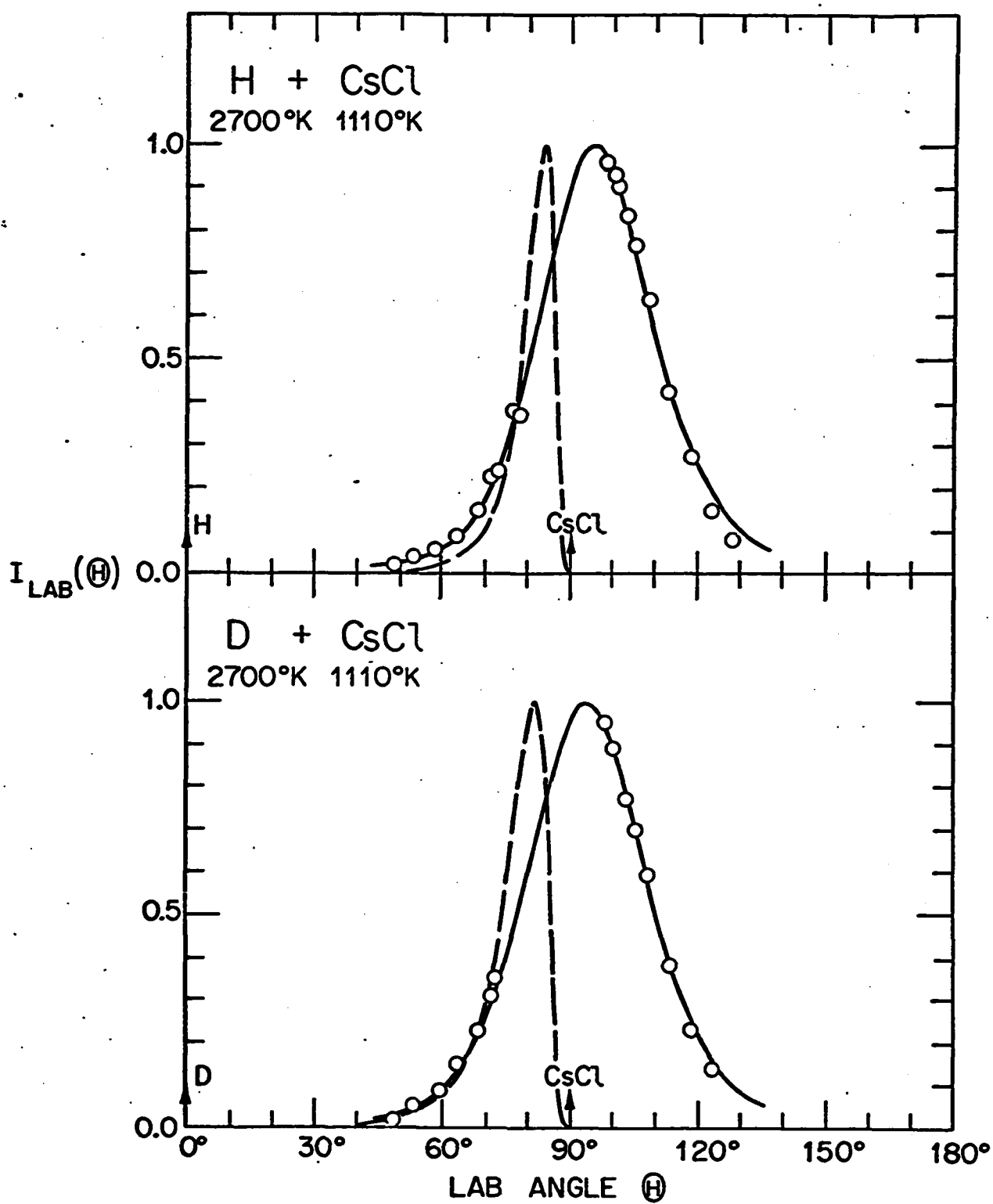


Fig. 9. Laboratory angular distributions of K from H and D + KCl.

Notation as in Fig. 6.

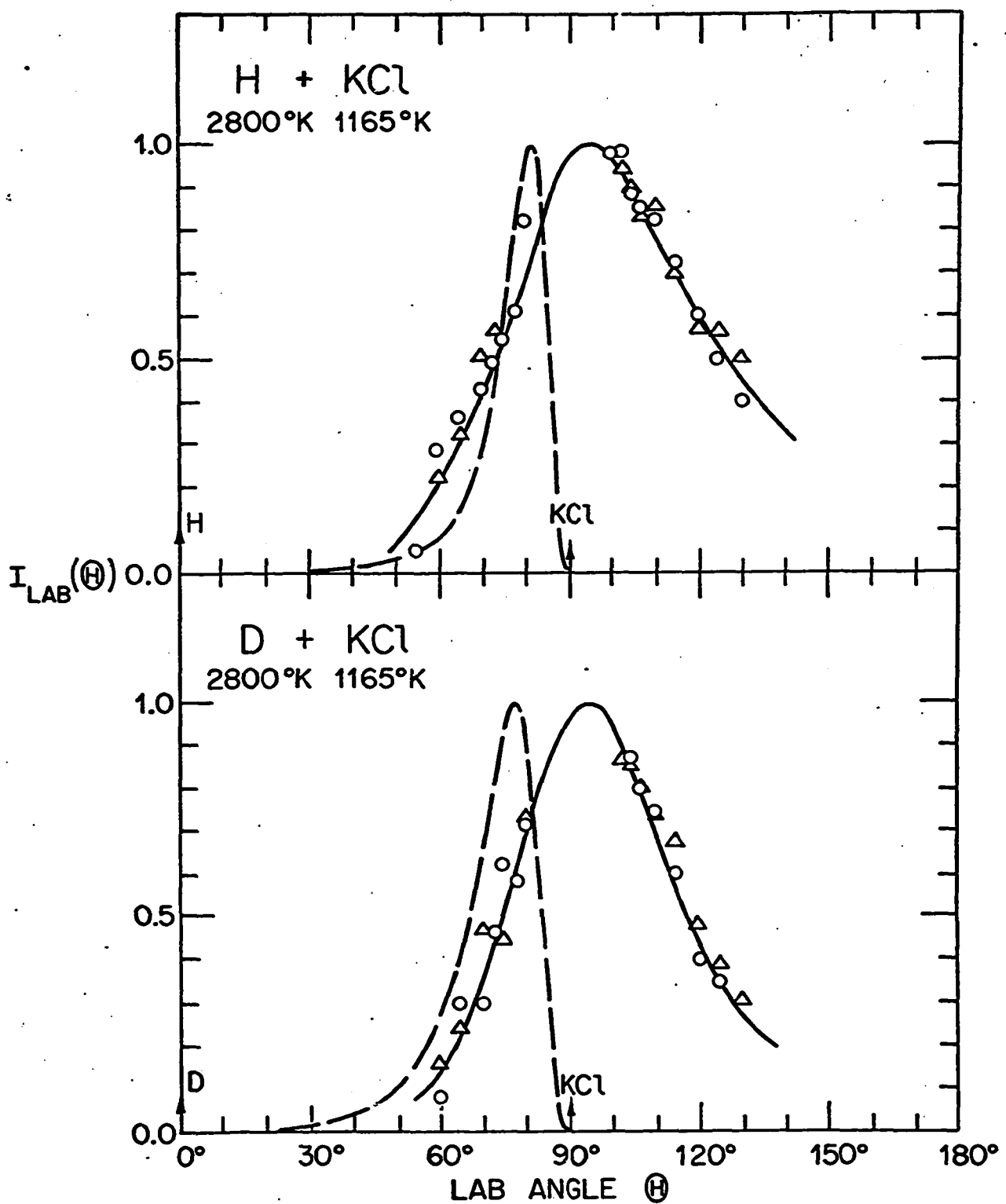
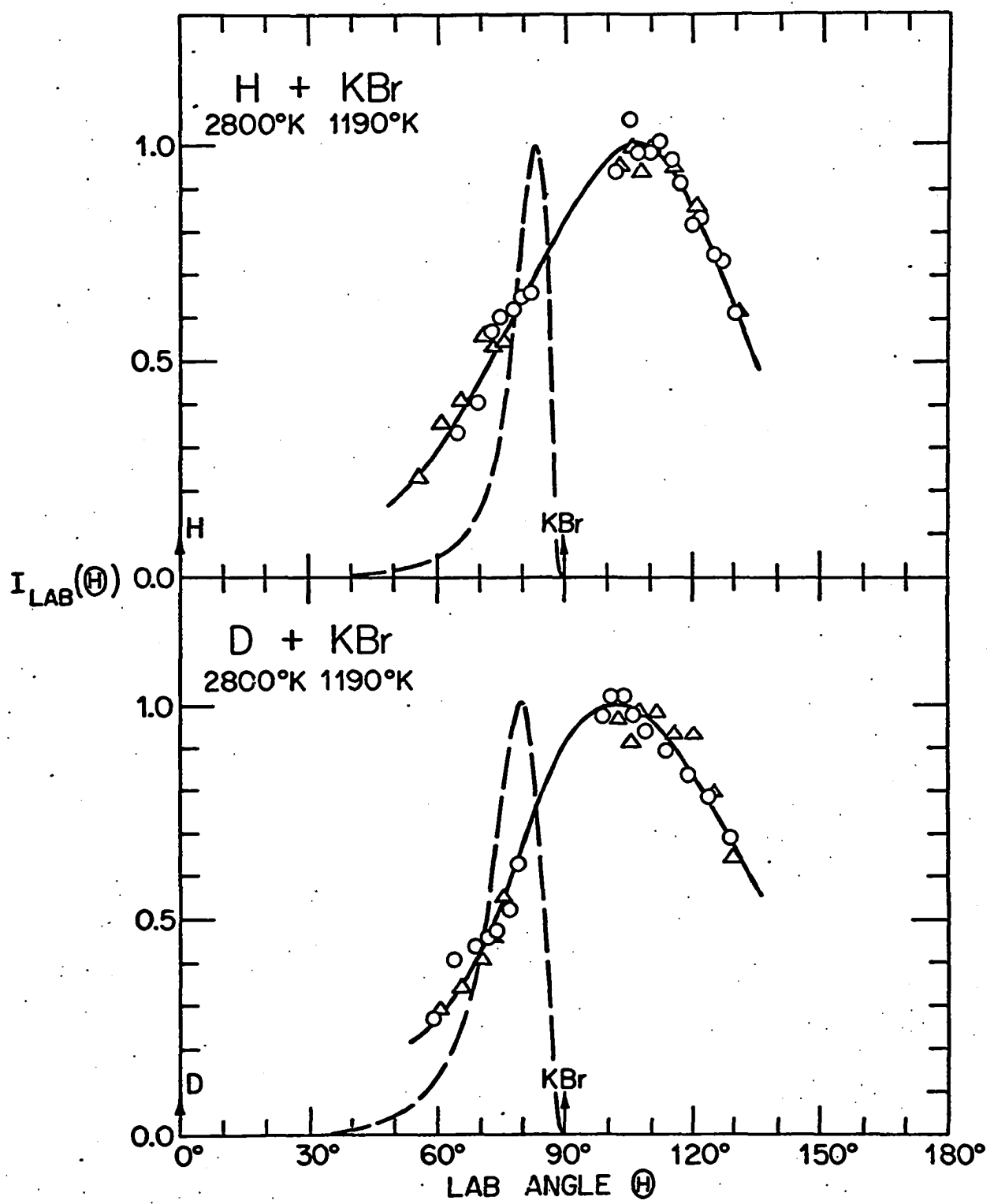


Fig. 10. Laboratory angular distributions of K from H and D + KBr.

Notation as in Fig. 6.



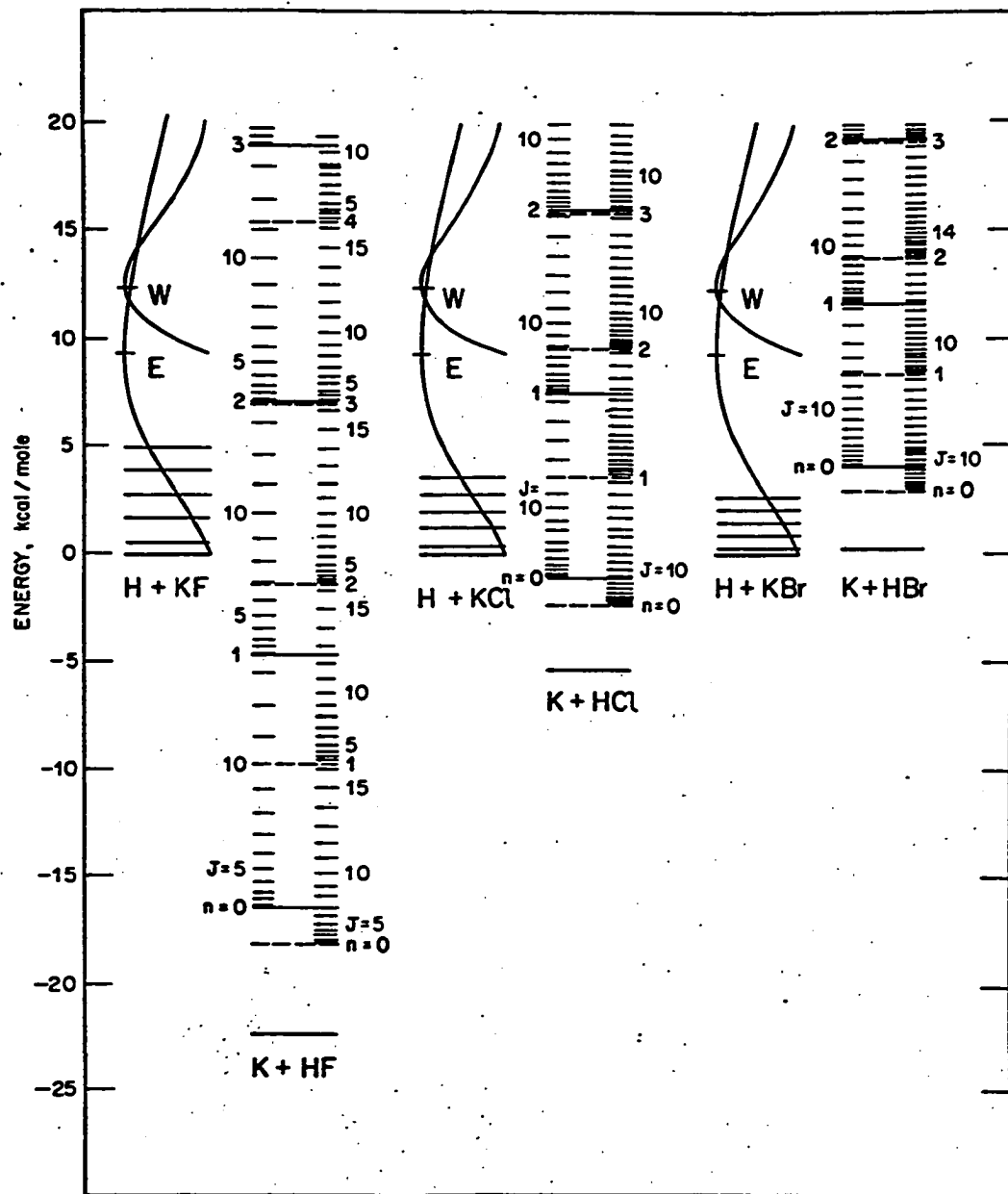
must prefer the forward hemisphere through momentum conservation. The displacement to wider angles is slight for the fluorides, indicating either a small recoil velocity away from the c.m., or more of a tendency to peak sideways. For the chlorides it is more pronounced, and for KBr the LAB peak is fairly well resolved on the far side of the salt beam. This trend seems to be outside experimental uncertainties by a good margin.

Due to the high kinetic energy of the H and D atoms after thermal dissociation, and also to the rather high temperatures needed for vaporization of MX, the distribution in total energy is peaked around 12 kcal/mole, and is very broad. Energy conservation requires that

$$E' + W' = E + W + \Delta D_0, \quad (2)$$

where $E(E')$ and $W(W')$ are the initial (final) translational and internal energies, respectively, and ΔD_0 the difference in dissociation energies of the HX and MX bonds, measured from the ground vibrational states. Figure 11 is an energy diagram for the KX reactions with H and D. The reactions of H and D with KCl, KBr and CsCl are all nearly thermoneutral or slightly endoergic, and thus, even with the high incoming energy, not much internal excitation of HX can take place, the second vibrational level usually being out of reach. This is not the case with the fluorides; there the exoergicities are sufficiently large to allow $n = 2$, or even $n = 3$ for DF. The very small displacement from centroid for the fluorides suggests that HF and DF may be so excited. A kinematic analysis to put the observed data in the c.m. frame should help to determine what can be said about the energy partitioning.

Fig. 11. Energy level diagram for the reactants and products of the $H + KX \rightarrow HX + K$ reactions. The curves show the distributions in translational (E) and internal (W) energies of the reactants, and the positions of the first five vibrational levels are indicated for KX. For the products the vibration-rotation levels are indicated for HX (left side) and DX (right side) by the n and J quantum numbers. All levels are drawn in the harmonic oscillator-rigid rotor approximation. Zero of energy in each case is with respect to reactants.



The analysis of this type of (so-called "primitive") experiment has been the subject of recent study,^{21,22} and improved, more rigorous methods have resulted. Entemann²¹ has developed a technique which allows a c.m. cross section for reaction with distributions both in angle and recoil speed to be transformed into the LAB with averaging over beam velocities and divergence. The author has extended the method so that the c.m. angular distribution may be determined by a least-squares fit to the LAB data for an assumed recoil distribution.²² A "separable" form is assumed for the c.m. scattering function.^{21,23}

$$I_{cm}(\theta, u, V) = T(\theta)U(u)V(V), \quad (3)$$

and the dependence on V is ignored by setting $V(V) = 1$. The possible endoergicity of the reaction is taken care of in the averaging procedure by including a damping factor which allows the diatomic reactant to contribute its internal energy if the initial kinetic and chemical energies are not sufficient to produce a given final kinetic energy.²⁴ In trial calculations on the most endoergic system, H + KBr, it was found that, for typical LAB velocities, all but the very smallest

- 21. (a) E. A. Entemann, Ph.D. Thesis, Harvard University, Cambridge, Mass., 1967; (b) E. A. Entemann and D. R. Herschbach, Disc. Faraday Soc. 44, 297 (1967).
- 22. Chapter III of this thesis.
- 23. A "primitive" experiment in general does not allow an assessment of the degree to which the magnitude and angle of μ are coupled; hence Eq. (3) is used. See Chapter III of this thesis for a discussion.
- 24. J. D. McDonald, unpublished; mentioned in W. B. Miller, Ph.D. Thesis, Harvard University, Cambridge, Mass., 1969, and in Ref. 5.

(low energy) kinematic diagrams did not have to call upon this factor. Thus the LAB \leftrightarrow c.m. transformation is not appreciably influenced by the endoergicity in some of these reactions, due to the high initial energy. For the $U(u)$ function, in the absence of a priori information, a flux Boltzmann shape was chosen

$$U(u) = (u/u_0)^3 \exp\left[\frac{3}{2}(1 - (u/u_0)^2)\right], \quad (4)$$

where u_0 is the peak of the distribution and $U(u_0) = 1$. The peak position was retained as a parameter and varied to give a best fit to the data. The coefficients of a series of six Legendre polynomials in $\cos\theta$ used to represent $T(\theta)$ were determined by a least-squares fit to the data for each value of u_0 . The solid curves in Figs. 6-10 represent the best fits obtained using this analysis.

The measurements of Stwalley¹⁷ on hydrogen atom beams and of Miller et al.²⁵ on salt beams under similar conditions suggest that the beam velocity distributions are somewhat Laval, both with Mach numbers of the order of unity. Therefore an approximation to a Mach 1 distribution,

$$n(v) = (v/v_p)^8 \exp[8(1 - (v/v_p))],$$

where v_p is taken as $1.3\sqrt{2kT/m}$, was used for each beam in performing the velocity averaging. The c.m. cross section was averaged over 36 combinations of parent beam velocities and transformed to give LAB velocity spectra at the desired Θ 's, and these spectra were then integrated to give the total flux density at each angle to be compared

25. W. B. Miller, S. A. Safron, G. A. Fisk, J. D. McDonald, and D. R. Herschbach, J. Chem. Phys. (to be published).

with experiment. The Legendre coefficients were determined beforehand by velocity-averaging each term in the series for $T(\theta)$ and applying the standard least squares technique.²⁶

The "goodness" criterion used for a given LAB fit was the standard deviation, defined by $\sigma = [S/N]^{1/2}$, where S is the sum of the squares of the differences between the calculated and observed data points, and N is the number of data points. Plots of σ versus u_0 for all the systems are shown in Fig. 12. $\sigma(u_0)$ always exhibits a distinct but sometimes shallow minimum, and hence the c.m. results suffer from considerable uncertainty. In Fig. 13 this uncertainty is roughly quantified with a plot of the peaks in the c.m. angular distribution which give the best possible fit for a given u_0 versus u_0 . The open circles indicate the nominal "best fit", and the solid lines terminated by crosses indicate the range of $(u_0, \theta_{\text{peak}})$ which give "reasonable" fits to the data, i.e., fits believed to be within the error of the data. The figure has been drawn for H only, but D is quite similar.

The c.m. angular distributions from the best data fits are shown in Fig. 14, within an error in peak position as indicated in Fig. 13. Usually the angular peaks have no greater than a 30° uncertainty, but the value to assign to u_0 is quite uncertain. Since the recoil energy $E' = u_0^2$, this makes the energy disposal very ill-defined. Table I indicates the nominal value of E' with upper and lower bounds in parentheses and the nominal internal excitation of HX, W' , again

26. See, for example, A. Ralston, "A First Course in Numerical Analysis", Ch. 6, McGraw-Hill, New York, 1965.

Fig. 12. Standard deviation of angular distribution fits as a function of peak c.m. recoil velocity u_0 for KF (\circ , \oplus); KCl (Δ , \blacktriangle), KBr (\square , \blacksquare), CsF (∇ , \triangledown), and CsCl (\lozenge , \diamond) with H (open symbols) and D (filled symbols). Units of u_0 are 10^4 cm/sec. The Cs curves are displaced downward by two orders of magnitude.

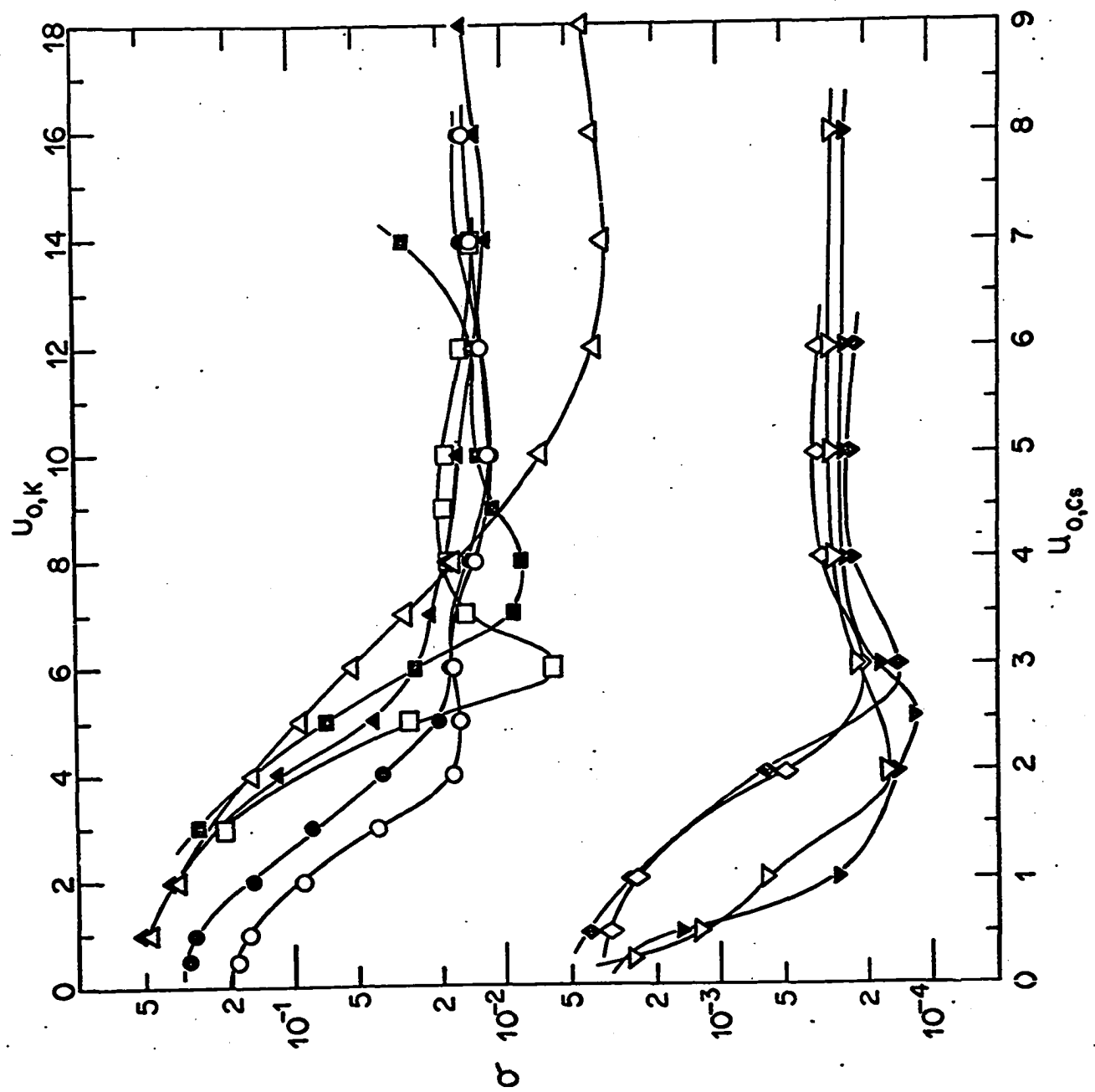


Fig. 13. Fitted center-of-mass angular peak positions as a function of peak recoil velocity for five salts reacting with H. Circles denote nominal best fits, and solid lines terminated by crosses denote regions where acceptable fits are obtained.

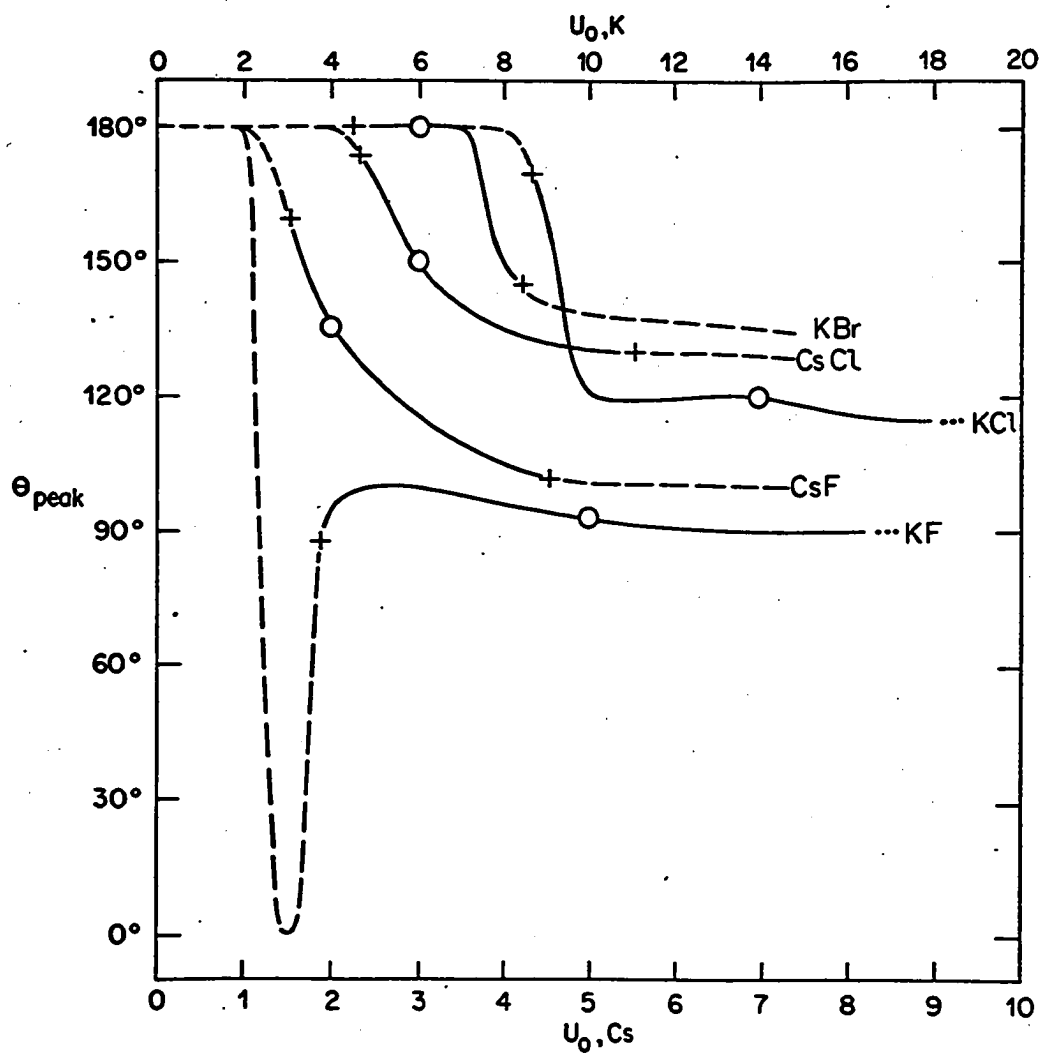


Fig. 14. Nominal best-fit center-of-mass angular distributions for H(—) and D(---) reacting with five salts. The curves are drawn only in the regions where they are well-determined by the laboratory data.

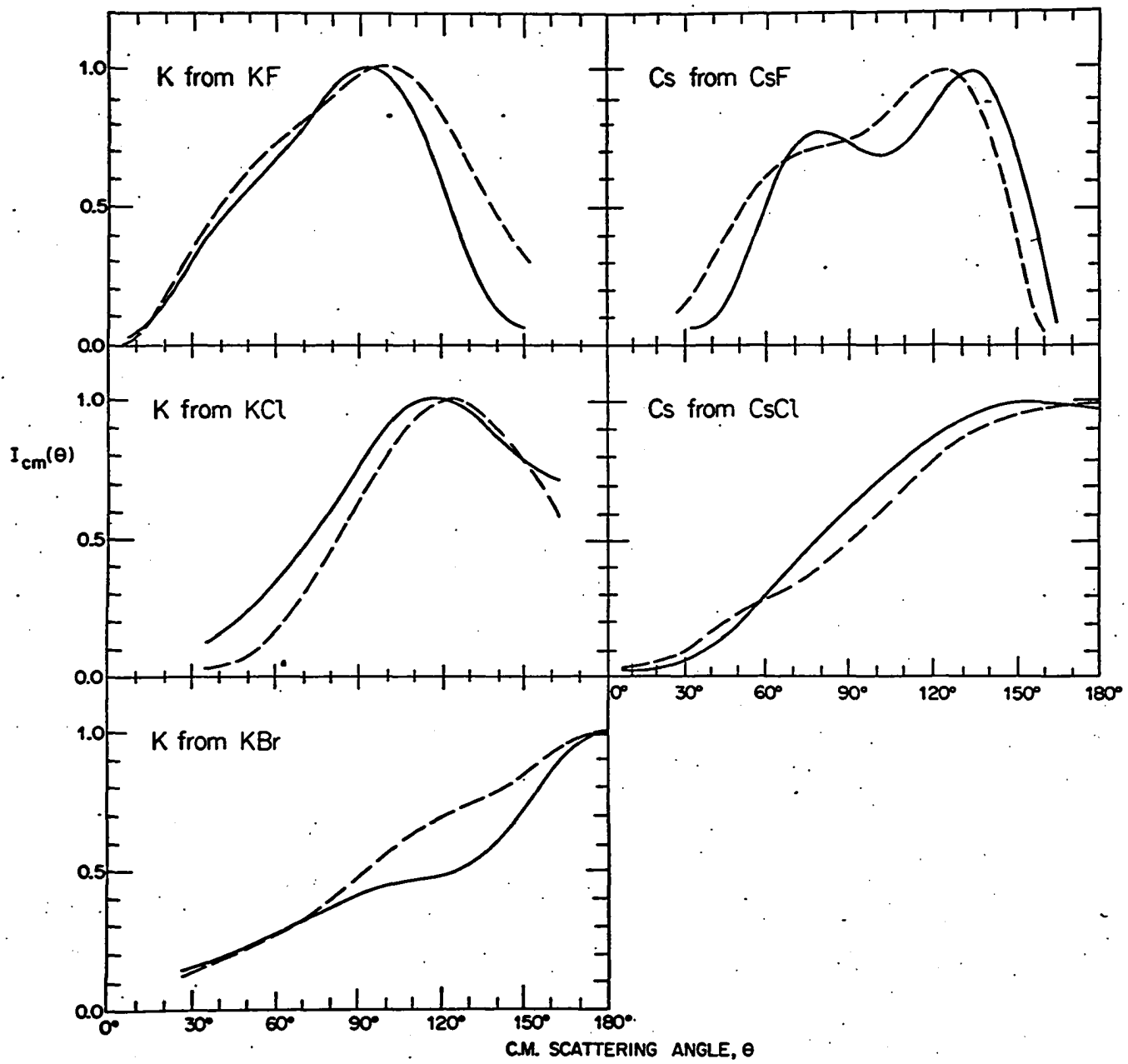


Table I. Energy disposal^a

Salt	KF	CsF	KCl	CsCl	KBr
$E'(E'_-, E'_+)$	9(2,30)	3(2,20)	12(3,14)	4(2,9)	2(1,4)
$W'(W'_-, W'_+)$	21(0,28)	24(7,25)	2(0,9)	5(0,7)	6(4,7)

^aEnergies given in kcal/mole, for the H reactions only. E' is the translational recoil energy of the products, and W' the internal excitation of HX above the ground vibrational state. The notation " $E'(E'_-, E'_+)$ " indicates "nominal best fit value (lower bound, upper bound)", and similarly for W' .

within limits, for H only; D agrees within one or two kcal/mole in all cases.

The trend mentioned earlier of progressively more backward peaking as the halogen involved is changed from F to Br as deduced from examination of the LAB data is indeed carried over into the c.m. The shoulder-like structure in the $\theta < 90^\circ$ portion of the Cs atom distributions from H, D + CsF is probably spurious, due to the blurring effect of the averaging for the low recoil velocities involved,²² but nonetheless for both the Cs and K fluoride systems there appears to be considerable intensity in the forward ($\theta < 90^\circ$) hemisphere. The curves for different alkalis but the same halogen show some similarity, indicating that the identity of the halogen may play a more decisive role in determining the shape of the angular distributions than does that of the alkali, as has been found earlier in the M + X₂ reactions.²⁷ The fact that the distributions resulting from H and D reactions with a given salt are so similar (as is the LAB data) rules out any large dynamic isotope effect.

As indicated in Table I, the internal excitation for the HF and DF products may be quite substantial according to the nominal result, but there is a possibility that this is not so. It should be noted that the KF and KCl nominal recoil energies are especially uncertain owing to the extremely shallow minima in $\sigma(u_0)$ (Fig. 12); values for the other systems are regarded as more well-determined. These other

27. J. H. Birely, R. R. Herm, K. R. Wilson and D. R. Herschbach, J. Chem. Phys. 47, 993 (1967).

values seem to indicate that, since W , the initial internal MX energy, is ~ 3 kcal/mole, that, to a fair approximation $E' = W$ and $W' = E + \Delta D_0$; the error limits on the KF and KCl values do allow this interpretation.

E. Total Reaction Cross Sections

Due to the nature of the kinematics of these reactions, none of the three most widely used methods for calculating the total reaction cross section²⁷ can be used. Small angle elastic scattering could not be observed, and hence the semiclassical small angle scattering formula cannot be employed to normalize the data. The lack of a complete elastic scattering distribution also prohibits the use of total cross section normalization, and the fact that a salt beam attenuation could not be observed prevents normalizing the total amount of MX scattered out of the beam. The method chosen here is less satisfactory than the ones alluded to, but it seems adequate for the purpose of establishing an upper bound on the cross section.

The results of Fig. 5 can all be extrapolated without much ambiguity to $\theta' = 180^\circ$. It was therefore decided to normalize the elastic scattering so that the magnitude of $I_{cm}(180^\circ)$ would equal that of the hard sphere cross section, given by

$$I_{cm}^{(hs)} = \frac{1}{4} R^2 \quad (5)$$

where R is the radius of the sphere, taken to be $r_H + \frac{1}{2} R_{MX}$; $r_H = a_0$ and R_{MX} is the equilibrium internuclear distance of MX.²⁸ Of course,

28. The value chosen for R might be thought to be an underestimate, since covalent radii are larger than those used for H and MX, but the fairly high collision energy (0.4 eV) warrants the use of a smaller R value.

back scattering corresponds to collisions with near-zero impact parameter, and such collisions might be thought to have a considerable likelihood of producing reaction; however, as mentioned in the elastic scattering analysis, the data seem to indicate that the factor by which (5) should have been attenuated is fairly close to unity. Once the normalization is obtained, the experimentally determined ratio of elastic to reactive scattering can be used to put the c.m. reactive cross section in absolute units. Then

$$Q_r = N \iint T(\theta) U(u) d\omega du, \quad (6)$$

where Q_r is the desired total reaction cross section and N is the normalization constant, given by

$$N = \left\{ \frac{1}{4} R^2 / [I_{cm}^{el}(180^\circ)]_{rel} \right\} \cdot \left\{ [I_{LAB}^{react}(\Theta_N)]_{rel} / [I_{LAB}^{react}(\Theta_N)]_{calc} \right\}.$$

The first bracketed factor in N puts the c.m. elastic scattering in absolute units and the second normalizes the calculated c.m. reactive cross section $T(\theta)U(u)$ to the same units. The normalization angle Θ_N was arbitrarily chosen, usually in a region where the data were smooth, if possible. The form chosen for the angular distribution permits the easy evaluation of the angular integral, and $U(u)$ is also easily integrated to give

$$\begin{aligned} Q_r &= N(4\pi a_0) \left(\frac{2}{9} e^{\frac{3}{2}} u_0 \right) \\ &= 12.515 N a_0 u_0 \end{aligned} \quad ((6a)$$

where a_0 is the coefficient of the zeroth order Legendre polynomial in the $T(\theta)$ series.

The R values and resulting total cross sections, along with possibly relevant bond lengths, are given in Table II. The cross section values suffer from uncertainties in the raw data itself, the elastic scattering subtraction for the Pt data, the elastic scattering LAB \rightarrow c.m. transformation, the hard sphere radius R, and the reactive transformation as reflected in the values of a_0 and u_0 used; but the magnitudes should not be more than a factor of 10 off and are, as stated, expected to be overestimates. The isotope ratios for a given salt should be the most accurately determined; we see that D is favored over H by about 2:1. The ratios of the CsX to KX cross sections are also regarded as much more reliable than the absolute numbers; here Cs seems favored over K by $\sim 2\text{-}4:1$ for a given halogen.

F. Discussion

The most striking mechanical aspect of these reactions is the large mass disparity between H and MX and the consequent difference in time scale for their relative motions. In these experiments the initial velocities of H and MX relative to their c.m. are in the ratio $\sim 100:1$; the H atom has traveled 10 Å in the time MX can move 0.1 Å. Likewise, the typical collision duration is $\sim 10^{-14}$ sec, whereas a rotational period of MX is $\sim 10^{-12}$ sec and a vibrational period is $\sim 10^{-13}$ sec. Thus, during the collision, unless strong chemical forces act, MX has rotated through only $\sim 2^\circ$ of arc and vibrated by only 0.05 Å. This situation is identical in kind, if not in degree, to that in the case of electrons and nuclei, where the small mass ratio and time scale for motion of the electrons enables the Born-Oppenheimer

Table II. Total reaction cross sections^a

Salt	R	R_{HX}	R_{MX}	R_{MH}	Q_x	H	D
KF	1.61	0.92	2.17	2.24	4	7	
KCl	1.87	1.27	2.67		3	4	
KBr	1.94	1.41	2.82		1.5	3	
CsF	1.70		2.35	2.49	10	25	
CsCl	1.98		2.91		6	12	

^aUnits are Å for the R's, and Å² for Q_x .

approximation to be made. Though the mass ratio H/M or X is at best 1/100 compared with 1/2000 or better for m_e/m_n , the same type of uncoupling of the Schrodinger equation of motion should hold as an approximation. We thus expect that the dynamically conserved quantities associated with the motion of H relative to the MX force center should remain independent of the heavy atom motion (to some degree of approximation), just as the energy and angular momentum of the electrons in a molecule are conserved independently of the nuclear rotation and vibration for a given nuclear state. We are thus led to consider a model for the H + MX reactions in which the orbital angular momentum of H with respect to MX, λ , is conserved, and must therefore become the rotational angular momentum of HX, λ' :

$$\lambda = \lambda'.$$

This also implies that the thermal rotational angular momentum of MX, λ , must end up as the orbital angular momentum of the M and HX products, λ' :

$$\lambda = \lambda'.$$

The conservation law for the total angular momentum J ,

$$J = \lambda + \lambda = \lambda' + \lambda'$$

has thus been broken down into two laws.

We can arrive at this same "uncoupling" postulate from another approach based on the quantization of rotational energy levels. From the small size of the reaction cross sections, we can deduce that impact parameters which lead to reaction are fairly small, probably on the order of equilibrium H-X bond lengths (0.9-1.4 Å). This implies,

for the most probable relative velocity $V \sim 9 \times 10^5$ cm/sec, that the orbital angular momentum $L = \mu V b$ is $\sim 10-15$ K for reactive collisions. The rotational energy spacing in HX for this much angular momentum is ~ 1 kcal, while for thermal KF (which has the largest rotational spacings of any of the salts studied) at 39 K (thermal peak) the spacing is only ~ 0.06 kcal. Thus angular momentum quanta cannot be exchanged between L and J without also exchanging rather large energy chunks into or out of MX vibration or product translation. Since the probabilities for such energy transfers are low unless there is an accidental resonance, we then conclude that, in general, the angular momentum conditions of the preceding paragraph should be reasonable. Both these arguments also apply, though with less rigor, to the deuterium reactions.

Because of the small "size" and mass of H and D, it is also true that the angular momenta associated with their motion will usually be considerably smaller than those of heavier atoms. The rotational angular momentum of MX in these experiments is $J \sim 50$ K, while, as mentioned above, $L \sim 10-15$ K. Independent of any assumption about uncoupling, the total angular momentum must be conserved; since J for a given collision is isotropically distributed in space and also dominates the vector sum $\mathbf{J} = \mathbf{L} + \mathbf{J}$, \mathbf{J} is also nearly isotropic. To say that this is true for collisions which lead to reaction, however, assumes that there are no molecular orientation effects which weight certain orientations of \mathbf{J} with respect to \mathbf{V} more heavily. The observed angular distributions of products must reflect the

distribution in θ , and a nearly isotopic θ distribution would lead to an isotropic angular distribution. The observed data are without much doubt not consistent with such a distribution; the c.m. angular distributions derived from kinematic analysis are fairly broad, but quite anisotropic, and definite trends in peak position have been established. The notion advanced above that MX is a "fixed target" would enhance the chances for observation of an orientational preference. The one-electron potential energy surfaces presented in Chapter VI give a strong indication of preferred geometry, implying that orientation effects as reflected in the reactive scattering are quite likely and also that trends with the identity of the halogen can be expected. A quantitative comparison between a predictive dynamic model employing the orientational assumption and the data presented here is given in Chapter VII, the results of which indicate that the observed scattering is quite consistent with such a model. The values of the orientation parameter obtained from the dynamic analysis correlate nicely with the trends observed in the energy surfaces.

In line with the considerations above, the partitioning of available energy can now be more quantitatively discussed. The fact that the CsCl and KBr reaction endoergicities are due solely to the zero-point motion of H, which can in both cases easily be met by the H atom translational energy, these small energy barriers can perhaps be ignored. In addition, the temperature dependence studies of the H, D + CsCl reactions indicate that there are no "activation barriers" more than one or two kcal/mole in excess of the endoergicities. We

thus postulate, consistently with the above discussion, that any reaction exoergicity goes into vibrational excitation of the HX bond, and that the final relative energy of the products is simply a reflection of the internal motion possessed by MX before reaction. This implies, roughly, that $E' \approx W$ and $W' = E + \Delta D_0$. As we have already pointed out, such an interpretation is not inconsistent with the results of the kinematic analysis. The dynamic model calculations of Chapter VII take complete account of the distributions in E and W , and use a modification of our simple energy assumption to predict the form of the translational energy distribution of the products.

Our energetic and angular momentum suppositions presented above correspond exactly to the predictions of the Spectator Stripping (SS) model²⁹ for the case where the attacking atom is very light. In the SS model the important parameter is a mass ratio, given for our case by

$$\cos^2 \beta = \frac{m_H m_M}{m_{HX} m_{MX}} = 0.01, \beta \approx 90^\circ.$$

The model predicts the product recoil energy to be, approximately,

$$E' = E \cos^2 \beta + W \sin^2 \beta \quad (7)$$

and the angular momentum partitioning to be determined by

$$\begin{aligned} J' &= J \cos^2 \beta + \lambda \sin^2 \beta \\ \lambda' &= \lambda \sin^2 \beta + J \cos^2 \beta. \end{aligned} \quad (8)$$

For $\beta = 90^\circ$ these expressions become identical to those proposed in our discussion. In its usual form, however, SS uses an isotropically

29. D. R. Herschbach, Appl. Optics, Chemical Lasers Suppl. 2, 128 (1965).

distributed χ , and for our systems this would necessarily lead to a nearly isotropic angular distribution.

A reasonable heuristic interpretation can also be given, within the limits of the model developed, of the isotope effect favoring D over H by ~2:1 in total reaction cross section. The observed effect suggests that the different zero-point energies (ZPE) of HX and DX might be a factor. If we make the somewhat arbitrary assumption that any chemical energy cannot be released unless H has enough translational energy to meet the ZPE requirement, then the ZPE acts like an "activation energy". We then can write

$$\frac{\langle v_{DQ_r}^{(D)} \rangle}{\langle v_{HQ_r}^{(H)} \rangle} = e^{-(ZPE_D - ZPE_H)/RT_H}, \quad (9)$$

or, approximately,

$$\frac{Q_r^{(D)}}{Q_r^{(H)}} \approx \left(\frac{m_D}{m_H}\right)^{1/2} e^{(ZPE_H - ZPE_D)/RT_H}. \quad (9a)$$

Eq. (9a) gives ratios ranging from 1.6 to 1.7 (due largely to the reduced mass factor), in fairly good agreement with the observed ratios. A fact which also supports this interpretation is that the observed E_a 's for H, D + CsCl (5.7, 4.5 kcal) are closer to H, DCI ZPE's (4.3, 3.0) than to the endoergicities (3.3, 2.0).

G. Comparison with M + HX Reactions

Before proceeding to apply the principle of microreversibility in comparing our results for the reactions of H and D with KBr to the extensively studied reactions of K with HBr, DBr and TBr, we will

summarize briefly what is known about these reverse reactions:

(1) From an optical model analysis of the nonreactive scattering at various initial energies,^{7,8} the total reaction cross sections for both HBr and DBr are found to be nearly independent of initial energy. In addition, the probability for reaction is near unity for small impact parameters, indicating little or no orientational preference for reaction. The isotope ratio $Q_r(K+HBr)/Q_r(K+DBr)$ found from these studies is $\sim 1.3 \pm 0.2$.

(2) The reactive scattering studies^{9,12} have yielded seemingly contradictory results concerning the angular distribution of the KBr product, as mentioned in the introduction. Information on the product recoil energy distribution is also quite uncertain. The reactive scattering experiments⁹ give an isotope ratio $Q_r(K+HBr)/Q_r(K+DBr)$ of 1.4 ± 0.2 , which agrees well with the ratio inferred from the non-reactive scattering.⁷

(3) Electric deflection analysis of the CsBr product from the analogous Cs + HBr reaction^{13,14} has revealed that the mean rotational angular momentum J' of CsBr is nearly the same as that expected from the condition $k = J'$ which should hold for these reactions.² We can thus estimate $J' = 100$ K for the K + HBr case.

The microreversibility principle³⁰ in its most detailed form states that a given reaction path (a trajectory) is time reversible, i.e., if the final kinetic and internal energies and exit impact

30. J. C. Light, J. Ross and K. E. Shuler, in "Basic Theory of Gas Dynamics and Reactions", A. Hochstim, Ed. (Interscience, New York, 1969).

parameter b' were made the initial ones, the path would be retraced exactly to the original initial conditions. The mathematical statement is

$$(2J+1)\mu EI(\theta, E, E', \alpha, \alpha', b, b') = (2J'+1)\mu'E'I'(\pi-\theta, E', E, \alpha', \alpha, b', b), \quad (10)$$

where θ is measured with respect to the forward (unprimed) c.m. atomic reactant direction, $\alpha(\alpha')$ is the collection of quantum numbers defining the initial (final) internal diatomic states, and the premultiplying factors arise from phase space volumes needed to go from the equality of the transition probabilities for the forward and reverse reactions to a relation involving cross sections. In terms of angular distributions, in an idealized two-state system the preferential orientation of the product relative velocity v' with respect to v should be identical for forward and reverse reactions. In reality, we must be content at best with having to integrate Eq. (10) over impact parameter, since a beam experiment has no way of selecting b ; and in practice there are usually many other quantities which must be averaged over before (10) can be applied. In classical kinetics use of (10) with appropriate averaging leads to the principle of detailed balancing relating the rate constants for the forward and reverse processes.³⁰

For our application we will regard the forward direction as $K + HBr \rightarrow KBr + H$. Eq. (10) implies that for forward and reverse reactions run under approximately complementary energy conditions, the c.m. angular distributions with respect to the initial atom direction in each case should be nearly the same. Here we are in clear

disagreement with the K + TBr results,¹² since there the KBr by inference recoils backwards from the initial K direction, while we find HBr and DBr preferring the forward direction with respect to the incoming H and D atoms. It must be emphasized, however, that the energies are not complementary in these cases. Figure 15 shows a schematic diagram of the energies involved; it is clear that our reactants H + KBr have about 6-7 kcal/mole more energy on the average than is possessed by the products of the forward reaction.

We will now proceed to integrate (10) over initial impact parameter and final solid angle to obtain³⁰

$$(2J+1)\mu EQ(E, E', \alpha, \alpha') = (2J'+1)\mu'E'Q'(E', E, \alpha', \alpha), \quad (11)$$

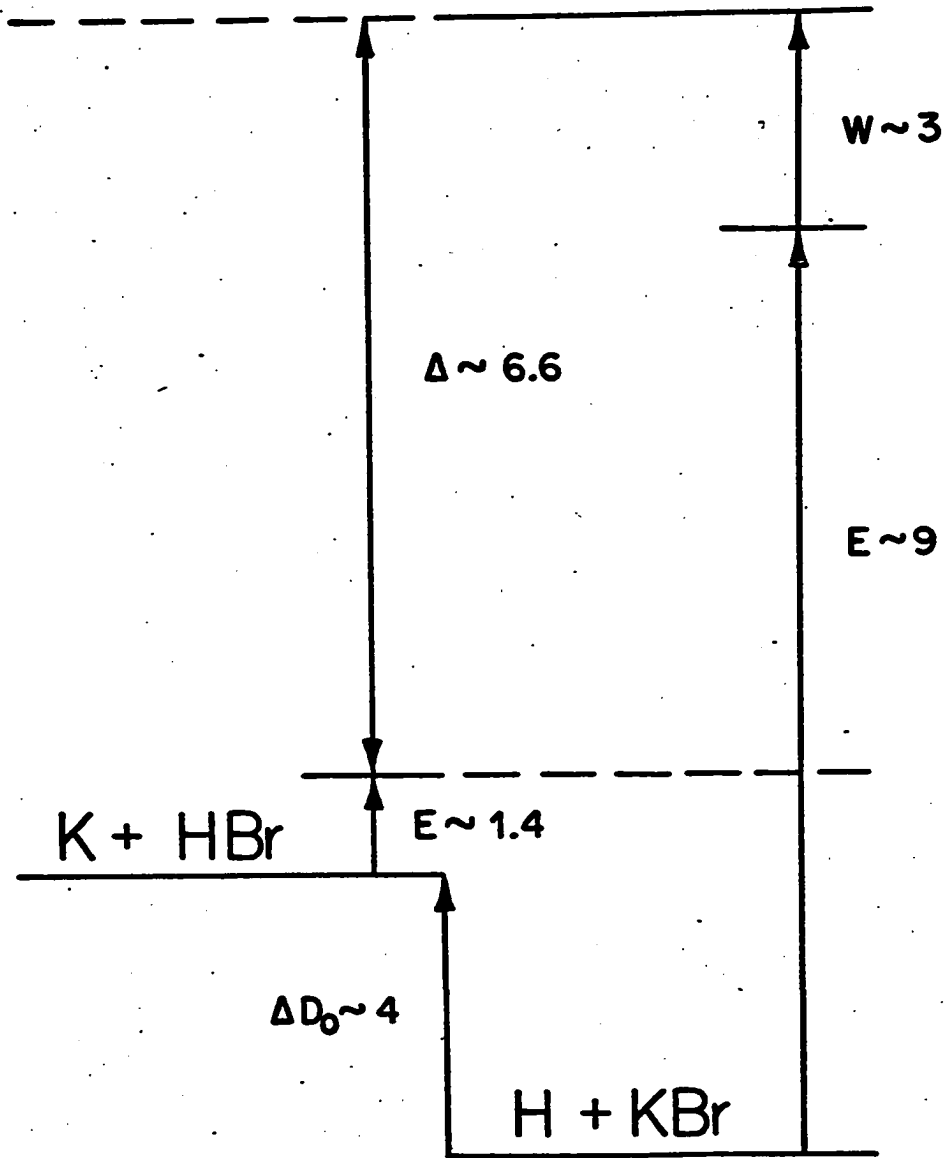
where the remaining quantities, if they depend on angle, are understood to stand for their angle-averaged values. In a simple two-state approximation, we can put in the most probable values for the variables and calculate the numerical ratio of the total reaction cross sections. Under the conditions of the forward experiment,⁹ $E \sim 2.8$ kcal/mole and $J_{HBr} \sim 3$ K. As above, we estimate $J'_{KBr} \sim 100$ K and, since the data for the forward reaction are at least not inconsistent with our model for energy disposal, we take $E' \sim W_{HBr} + \Delta D_{O,H} = 4.1$ kcal. Substituting into Eq. (11) we get for the H reaction,

$$(7)(26)(2.8)Q_H = (200)(1)(4.1)Q'_H,$$

$$Q'_H = 0.6 Q_H,$$

implying that $Q'(H+KBr) = 20 \text{ \AA}^2$ at $E' = 4.1$ kcal. In order to obtain our value of 1.5 \AA^2 , E' would have to be so large as to violate energy conservation. Of more interest is the prediction of the

Fig. 15. Schematic energy diagram for the reaction $K + HBr \rightleftharpoons KBr + H$;
the energy in the forward direction is that of Ref. 12 (W has
been omitted, since it is only ~0.4 kcal).



of the isotope ratio. For the D reaction, $J_{D\text{Br}} \sim \sqrt{2} J_{H\text{Br}}$, $\mu_D' = 2 \mu_H'$, and $E_D' = E_H'/\sqrt{2}$ (from our model), so that $Q_D' \approx 0.6 Q_D$ also. We therefore have

$$\frac{Q_H'}{Q_D'} = \frac{Q_H}{Q_D},$$

i.e., microreversibility predicts that the isotope ratios should be the same for the forward and reverse directions at these energies. As mentioned, in the Wisconsin and Brown experiments the isotope ratio is ≈ 1.4 , whereas for the reverse reactions we have found it to be ≈ 0.5 . The same calculation carried out for our most probable initial conditions, again making use of our model ($\zeta = \zeta'$, $J_{H\text{Br}} = J_{D\text{Br}}/\sqrt{2} = 10 K$, $J_{K\text{Br}}' = 75 K$, $E_H' = E_D' = 9 \text{ kcal}$, $E_H = E_D = 3 \text{ kcal}$), yields $Q_H' = 1.1 Q_H$, $Q_D' = (1.1/\sqrt{2}) Q_D$, and therefore.

$$\frac{Q_H'}{Q_D'} = \sqrt{2} \frac{Q_H}{Q_D}.$$

If the ratio for the forward reaction can be extrapolated to higher product energies (more internal excitation of H(D)Br, according to our model), this finding clearly is inconsistent with our experimental result, since it would predict $Q_H'/Q_D' \approx 2.0$, just the inverse of our observed ratio. We have carried out an energy average of Eq. (11), but the results for the isotope ratio are nearly the same as we have quoted for each set of initial conditions. This inconsistency will be discussed in the following section.

H. Correlation with Electronic Structure

The special dynamical features of H atom reactions outlined above strongly suggest that an orientational preference is responsible for the marked anisotropy of the observed product angular distributions, and the apparently small probability for reaction even at near-zero impact parameters as deduced from the small reactive/elastic scattering ratio. This in turn implies that a concerted electronic mechanism intimately involving all three atoms in a preferred geometrical configuration may govern these reactions. Both the potential surface calculations, to be presented in Chapter VI, and the dynamic model calculations of Chapter VII point to a triangular configuration as being most favored, and strengthen the qualitative arguments given here. The simplest electronic interpretation that can be given is that the presence of the H atom is quite essential for the electron transfer to the alkali ion necessary for reaction to occur. On the other hand, the nonreactive scattering studies indicate that orientational effects are not important for the reverse reaction, since the probability for reaction is near unity for sufficiently small b . A simple calculation shows that the classical rotational period of H about Br is $\sim 4 \times 10^{-13}$ sec at 300°K, whereas the typical relative velocity of K and HBr is 1×10^{13} Å/sec, so that the H atom cannot be considered just a high speed "blur" which is always available for electron transfer purposes. Thus, we might expect that any orientational preference would be manifest in the reaction probability at small b . These considerations suggest an interesting speculation. If

the forward reaction proceeds via an "electron jump", then it seems that the "harpooning" electron goes directly to the halogen from the nonreactive studies, but our results seem to show that to put an electron back on the alkali ion, the H atom is needed as an intermediary. This implies that perhaps our application of microreversibility to these reactions has not been valid, since the forward and reverse reactions appear not to be occurring in the same region of the potential surface governing the interactions. Hence the apparent inconsistency in isotope ratios may not be a contradiction at all, but may be a valuable clue as to the intimate electronic mechanism involved here.

Appendix. Elastic Scattering Transformation Procedure

This appendix describes a general program to transform in-plane laboratory (LAB) elastic scattering data into the center-of-mass (c.m.) system for a given pair of parent beam velocities and a beam intersection angle of 90° . The transformation relations and appropriate Jacobian have been given elsewhere;^{21a} the transformation used here is analogous to that presented in Chapter III of this thesis. The main change in this program from an earlier version^{21a} is that, in the event the c.m. recoil velocity u is less than C , the velocity of the c.m., the contribution from the "inner branch" is taken into account, rather than ignored as an approximation. Ignoring the inner branch would be especially misleading for the systems considered in this chapter, since the inner branch actually makes the larger contribution to the LAB intensity.

The method used to find a consistent set of outer and inner branch c.m. intensities which reproduce the LAB data is as follows. We will shorten the notation of Eq. (1) of the text by letting

$I_{LAB}(\theta) \rightarrow I_L$ and $I_{cm}(\theta_{i(o)}) \rightarrow I_{i(o)}$. Eq. (1) becomes

$$I_L = J_i I_i + J_o I_o. \quad (A1)$$

In order to start an iterative procedure, we make the assumption that the outer branch is predominant (it will later be seen that the method works even if this assumption is not valid), and take

$$I_o^{(0)} = J_o^{-1} I_L, \quad (A2)$$

where the superscript denotes the order of approximation. We can thus

generate a unique approximation to the actual c.m. intensity; we then interpolate (or extrapolate) the resulting curve to find an approximate set of I_i , $I_i^{(0)}$, which, of course, should lie on the same curve. If we then calculate the approximate LAB intensity corresponding to the set of $(I_o^{(0)}, I_i^{(0)})$, it will of necessity be too large. We need some procedure for correcting the I_o so that the LAB intensities are reproduced with the interpolates I_i . Taking differences of (A1),

$$\delta I_L = J_i \delta I_i + J_o \delta I_o. \quad (A3)$$

If the magnitudes of the increments δI_i and δI_o are roughly comparable, then an approximate corrector for $I_o^{(n)}$ is given by

$$\delta I_o^{(n)} = (J_i + J_o)^{-1} \delta I_L^{(n)}, \quad (A4)$$

and we then have

$$I_o^{(n+1)} = I_o^{(n)} - \delta I_o^{(n)}, \quad (A5)$$

where

$$\delta I_o^{(n)} = (J_i + J_o)^{-1} [J_i I_i^{(n)} + J_o I_o^{(n)} - I_L] \quad (A6)$$

and the $I_i^{(n)}$ have been obtained from $I_o^{(n)}$ by interpolation. Eq. (A5) represents the desired iterative scheme for taking the inner branch contribution into account; it is easily seen that the corrector goes to zero as the actual I_L is approached, as it should.

In practice it was thought that $\delta I_o^{(n)}$ would have to be multiplied by a "convergence factor" less than unity in order to prevent oscillation during the iteration, but this proved to be unnecessary. Convergence within 15 iterations (sometimes as few as 5) was found for

all the systems analyzed in this chapter, independent of the fact that the outer branch usually did not make the major contribution to the LAB intensity. The convergence for any one point might be somewhat non-uniform due to the coupling between points induced by the interpolation procedure, but on the whole each iteration was always an improvement on the previous one.

Table IA defines the punched card input and gives a Fortran listing of the program, decknamed NEST (Nominal Elastic Scattering Transformation). The program time on the IBM 7094 computer is \approx 30 sec for 10 LAB points with the iteration, \approx 1 sec without; the time increases linearly with the number of points. (This program has been run on the IBM 1620 computer, showing times of 5-10 min.) The iteration timing is determined by the logarithmic interpolation used, requiring the computation of ALOG and EXP for each data point.

Table IA. NEST input and listing

<u>Variable</u>	<u>Meaning</u>
.....	(The first card to be read contains a "1" in col. 1 followed by user's comments.)
VA,VBC.....	Velocities of the A ($\theta = 0^\circ$) and BC beams corresponding to the most probable kinematic diagram.
GA,GBC.....	masses of A and BC in a.m.u.
NTHL.....	number of LAB angles and intensities to be analyzed.
IABC.....	indicates, if non-zero, that input data is for A atom; if zero BC molecule is assumed.
ISIN.....	indicates, if non-zero, that $I_{cm}(\theta)\sin\theta$ is desired form of output; otherwise just $I_{cm}(\theta)$ will be calculated.
TH,PL arrays.....	the set of LAB angles and intensities.

```

C NEST
C NOMINAL NEWTON DIAGRAM TRANSFORMATION OF 'PRIMITIVE' ELASTIC
C SCATTERING DATA TO C.M. SYSTEM FOR INTERSECTION ANGLE OF 90 DEG.
C IF INPUT DATA IS FOR ATOM A, IABC=1, IF FOR BC MOLECULE, IABC=0.
C IF I(THCM)*SIN(THCM) IS DESIRED, ISIN=1. ISIN=0 RESULTS IN I(THCM)
C ONLY.
C FOR U.GE.C ONLY ONE THCM CORRESPONDS TO THL, AND THE TRANSFORMATION
C IS SINGLE-VALUED AND UNIQUE. THE OUTPUT LABELED 'OUTER BRANCH ONLY'
C IN THIS CASE REPRESENTS THE EXACT C.M. INTENSITY FOR MONOCHROMATIC
C INITIAL CONDITIONS.
C FOR U.LT.C TWO THCM'S CORRESPOND TO THL FOR THL RAY INTERSECTING
C THE CIRCLE U FORMS AROUND THE TIP OF C, AND NO THCM'S TO THL NOT
C INTERSECTING THIS CIRCLE. FOR THE FORMER CASE THESE INTERSECTIONS
C DEFINE INNER AND OUTER BRANCHES COMING FROM DIFFERENT REGIONS OF
C I(THCM) WHICH CONTRIBUTE TO THE OBSERVED INTENSITY. THE PROGRAM USES
C AN ITERATIVE SCHEME TO FIND I(THCM) WHICH REPRODUCES THE DATA WITH
C BOTH BRANCHES TAKEN INTO ACCOUNT.
C
      DIMENSION PL(20),PL1(20),PCO(20),PCI(20),THCO(20),THCI(20),
      1 AJO(20),AJI(20),THCA(20),PCL(20),TH(20)
      LOGICAL BC,SINE
      DATA Y,F/.01745329,1./
100 READ(5,1000)
      READ(5,1001) VA,VBC,GA,GBC,NTHL,IABC,ISIN
      READ(5,1006) (TH(I),PL(I),I=1,NTHL)
      WRITE(6,1000)
      WRITE(6,1002)
      WRITE(6,1001) VA,VBC,GA,GBC,NTHL,IABC,ISIN
1000 FORMAT(55H
1001 FORMAT(4F10.3,5X,3I5)
1002 FORMAT(1H07X2HVA7X3HVBC8X2HGA7X3HGBC6X14HNTHL IABC ISIN)
1006 FORMAT(2F10.0)
      BC=IABC.EQ.0
      SINE=ISIN.NE.0
      G=GA+GBC
      CX=GA*VA/G
      CY=GBC*VBC/G
      C2=CX*CX+CY*CY
      C=SQRT(C2)
      THLC=ATAN(CY/CX)
      V=SQRT(VA*VA+VBC*VBC)
      IF(BC) GO TO 52
      U=GBC/G*V
      GO TO 53
52  U=GA/G*V
53  CONTINUE
      U2=U*U
      COSTV=VA/V
      SINTV=VBC/V
      D=U-C
      MTHL=0
      DO 10 I=1,NTHL

```

```

ISW=0
T=TH(I)*Y
A=ABS(T-THLC)
COSTL=COS(T)
SINTL=SIN(T)
COSA=COS(A)
A=C*COSA
B=U2+C2*(COSA*COSA-1.)
IF(B) 95,95,1
1 B=SQRT(B)
VL=A+B
2 VL2=VL*VL
UXL=VL*COSTL-CX
UYL=VL*SINTL-CY
UX=UXL*COSTV-UYL*SINTV
UY=UXL*SINTV+UYL*COSTV
IF(ISW) 3,3,7
3 THCO(I)=ATAN2(ABS(UY),UX)/Y
IF(BC) THCO(I)=180.-THCO(I)
AJO(I)=2.*VL2*VL/(U*ABS(U2+VL2-C2))
PCO(I)=PL(I)/AJO(I)
IF(D) 6,10,10
6 VL=A-B
ISW=1
GO TO 2
7 THCI(I)=ATAN2(ABS(UY),UX)/Y
IF(BC) THCI(I)=180.-THCI(I)
AJI(I)=2.*VL2*VL/(U*ABS(U2+VL2-C2))
GO TO 10
95 MTHL=MTHL+1
10 CONTINUE
NTHL=NTHL-MTHL
WRITE(6,1005)
DO 105 I=1,NTHL
PC=PCO(I)
IF(SINE) PC=PC*SIN(THCO(I)*Y)
WRITE(6,1004) TH(I),PL(I),THCO(I),PC
105 CONTINUE
1004 FORMAT(2(CPF10.2,1PE12.4))
1005 FORMAT(18H00 OUTER BRANCH ONLY/7X3HTHL10X2HIL6X4HTHC08X4HICM0)
IF(D) 101,100,100
101 CONTINUE
ITER=0
11 DO 12 I=1,NTHL
THCA(I)=THCO(I)
PCL(I)= ALOG(ABS(PCO(I)))
12 CONTINUE
CALL SORT(NTHL,THCA,PCL)
DO 16 I=1,NTHL
T=THCI(I)
DO 13 J=1,NTHL
IF(T-THCA(J)) 14,14,13
13 CONTINUE
J=NTHL
GO TO 15

```

```

14 IF(J-1)145,145,15
145 J=2
15 PCI(I)=EXP((PCL(J)-PCL(J-1))/(THCA(J)-THCA(J-1))*(T-THCA(J-1))
1 +PCL(J-1))
16 CONTINUE
DO 17 I=1,NTHL
17 PL1(I)=AJ0(I)*PCO(I)+AJI(I)*PCI(I)
IF(ABS(PL(NTHL)-PL1(NTHL))-5.E-4*PL(NTHL)) 21,21,18
18 CONTINUE
DO 19 I=1,NTHL
19 PCO(I)=PCO(I)-(PL1(I)-PL(I))/(AJ0(I)+AJI(I))*F
ITER=ITER+1
WRITE(6,1010) ITER
WRITE(6,1011) (PL(I),PL1(I),I=1,NTHL)
GO TO 11
21 WRITE(6,1012)
DO 22 I=1,NTHL
PC=PCO(I)
PCC=PCI(I)
IF(.NOT.SINE) GO TO 22
PC=PC*SIN(THCO(I)*Y)
PCC=PCC*SIN(THCI(I)*Y)
22 WRITE(6,1013) TH(I),PL(I),PL1(I),THCO(I),PC,THCI(I),PCC
GO TO 100
1010 FORMAT(6H0ITER=,I2/9X3H0BS8X4HCALC)
1011 FORMAT(1P2E12.4)
1012 FORMAT(1H06X3HTHL10X2HIL5X7HIL,CALC6X4HTHC08X4HICM06X4HTHC18X4HICM
1I)
1013 FORMAT(F10.2,1P2E12.4,2(0PF10.2,1PE12.4))
END

```

C SORTS IN ASCENDING ORDER.

```

SUBROUTINE SORT(N,X,Y)
DIMENSION X(20),Y(20)
DO 20 I=2,N
SAVE=X(I-1)
J1=I-1
DO 10 J=I,N
IF(X(J)-SAVE)5,10,10
5 J1=J
SAVE=X(J)
10 CONTINUE
SAVE=X(I-1)
X(I-1)=X(J1)
X(J1)=SAVE
SAVE=Y(I-1)
Y(I-1)=Y(J1)
Y(J1)=SAVE
20 CONTINUE
RETURN
END

```

CHAPTER VI

ONE-ELECTRON POTENTIAL ENERGY SURFACES FOR THE REACTIONS

OF HYDROGEN ATOMS WITH ALKALI HALIDES

Abstract

A method patterned after the pseudopotential technique of Roach and Child is used to calculate potential energy surfaces for the reactions of hydrogen atoms with LiF, KF, KCl and KBr on a one-electron model. The results for LiF show some resemblance to the all-electron calculation of Balint-Kurti. Surfaces for the K salts have qualitative features and trends which correlate well with experimental results on these reactions (Chapter V), as interpreted in terms of a dynamic model (Chapter VII). The possible nature of the electronic mechanism for these reactions is examined.

A. Introduction

The complexities of the many-electron atomic and molecular problems have long prohibited the construction of reliable three-atom potential energy surfaces for chemical reactions from first principles. The Hartree-Fock self-consistent-field (SCF) method is the best known for the atomic problem; in terms of energy magnitudes important in chemical bonding, its limitations are quite severe due to the treatment of electron correlation as an average-field effect.¹ The molecular orbital (MO) method for systems with many nuclei must ultimately rely on linear combinations of SCF atomic orbitals (LCAO) and thus suffers from the same energetic deficiencies.² Only in the limit of a full configuration interaction (CI) of a set of SCF-LCAO-MO's corresponding to the (approximate) ground state and all the excited states of the molecular system, can an accurate description of the electronic energy surface as a function of the internuclear geometry be obtained (in the Born-Oppenheimer approximation). Unfortunately, such a CI calculation may be very slowly convergent due to the use of the SCF basis, where electron correlation effects have not been properly accounted for. For the case of only two nuclei, a direct CI-VB (valence bond) expansion in determinants of more appropriate (confocal

-
1. J. C. Slater, "Quantum Theory of Atomic Structure", Vol. II (McGraw-Hill, New York, 1960), Chapters 17, 18.
 2. J. C. Slater, "Quantum Theory of Molecules and Solids", Vol. I, electronic structure of molecules (McGraw-Hill, New York, 1963). The excellent discussions throughout this book have served as the conceptual basis for some of the introduction.

elliptic) functions has provedn practicable for a reasonably small number of electrons and has yielded results which are considerably more reliable.³ But there is no comparable method for three or more nuclei, and thus the CI-SCF-LCAO-MO approach must be resorted to. Recently, Balint-Kurti and Karplus⁴ have extended a semiempirical method originally proposed by Moffit⁵ in which the atomic energies are "calibrated" to match experiment (correcting all the elements in the atomic Hamiltonian) and the resulting "corrected" SCF atomic wavefunctions used in a CI-VB calculation of three-nuclei surfaces. Electronic energies have now been calculated as a function of nuclear coordinates for the reactive systems Li + F₂, Li₂ + F and H + LiF by this technique; the last of these is, of course, of great interest to us, being for the same types of atoms as considered here.

The structure of atoms and the role played by this structure in chemical bonding suggests that many atoms can be considered as consisting of an essentially imperturbable "core" of electrons tightly bound by the nuclear charge and a set of a few outer "valence" electrons which are almost solely responsible for the longer-wavelength electronic spectra of the atoms and for their chemical interactions with other atoms and molecules. This type of model is especially

3. C. S. Lin, J. Chem. Phys. 50, 2787 (1969), on LiH⁺ is relevant to the present work.
4. G. G. Balint-Kurti, Ph.D. Thesis, Harvard University, Cambridge, Mass., 1969; the method is briefly outlined in G. G. Balint-Kurti and M. Karplus, J. Chem. Phys. 50, 478 (1969).
5. W. Moffit, Proc. Roy. Soc. (London) A210, 245 (1951).

accurate for alkali atoms, which all exhibit hydrogen-like Rydberg spectra. Furthermore, the alkali ion cores, as Rittner's calculations⁶ have strikingly shown, behave remarkably like classical charged spheres in ionic halide compounds. The alkali valence electron can be thought of as moving in an effective central field due to the nucleus and core electrons. Since the SCF approximation is the most accurate for this case, the wavefunction for the electron outside the ionic core should closely resemble the exact SCF result, the best approximant to which has been given by Clementi.⁷ This line of thinking prompted Roach and Child⁸ (RC) to treat the three-atom system NaKCl as a one-electron problem, with the Cl atom retaining an extra electron at all configurations, in accord with the known ionic character of NaCl and KCl. The wavefunction for the electron was simply expressed as a linear combination of Slater-type orbitals⁹ (STO's) on Na and K. This approach, based on empirical structural evidence and chemical intuition, made workable what would be an almost intractable problem if approached ab initio. One might question the accuracy of such an intuitive model, but calculations of RC on Na_2^+ and K_2^+ demonstrate surprisingly good results without nearly the calculational labor that an SCF-MO treatment would have entailed.

-
6. E. S. Rittner, J. Chem. Phys. 19, 1030 (1951).
 7. E. Clementi, Document No. 7440, ADI Auxiliary Publications Project, Photoduplication Service, Library of Congress, Washington, D. C.
 8. A. C. Roach and M. S. Child, Mol. Phys. 14, 1 (1968).
 9. J. C. Slater, Phys. Rev. 36, 57 (1930).

The apparent success of the RC approach has prompted us to apply a similar treatment to the systems $H + MX \rightarrow HX + M$, where M is an alkali atom and X a halogen. Such a treatment might result in some insight into the nature of the chemical interaction in these systems, even though it could not be expected to be as representative of the actual electronic structure here as it must be for $M^+ + MX \rightarrow M^+X + M$. The reason for this is that the H-X interaction involves predominantly covalent electron sharing (in contrast to MX), and the RC model is obliged to regard the interaction as being purely $H^+ - X^-$. We have attempted to cope with this problem by taking account of the X^- electrons in a purely mechanical way using an adaptation of Pauling's model¹⁰ for hydrogen halides. In any case, the halogen atom does exist as X^- as the reactants approach, so that we can hope to obtain a fair description at least of the entrance valley for these reactions.

B. Pseudopotential Formulation

The general prescription for setting up the electronic calculation presented by RC has been closely followed here. The wavefunction for the electron, which enters with H and is presumed to leave with M, is expanded as

$$\Psi = C_1 |1s_H\rangle + C_2 |ns\rangle + C_3 |np_{\sigma}\rangle + C_4 |np_{\pi}\rangle, \quad (1)$$

where the ns and np orbitals belong to M and the C's are expansion coefficients. The Hamiltonian for the model is, in atomic units,

$$\mathcal{H} = -\frac{1}{2} \nabla^2 + V(H^+) + V(M^+) + V(X^-) + V_{core} \quad (2)$$

10. L. Pauling, Proc. Roy. Soc. (London) A114, 181 (1927).

$$= \mathcal{H}_0 + V_{\text{core}},$$

Here \mathcal{H}_0 includes the kinetic energy of the electron and its coulombic interaction with the ion cores. V_{core} includes the coulombic interaction among the ion cores, which can rigorously (in the Born-Oppenheimer approximation) be added in after the electronic energies have been found, and in addition contains core-polarization terms involving the electron, which are treated as first-order perturbations to the eigenvalues of \mathcal{H}_0 .

As RC point out, there is a serious problem with using Eq. (1): the valence wavefunction must be orthogonal to all the core wavefunctions in order to avoid violating the Pauli exclusion principle through allowing the electron to penetrate into the cores. In order to avoid the explicit introduction of the core wavefunctions, RC instead propose to modify the core potentials, in analogy to the method of pseudopotentials,¹¹ in an attempt to reproduce the energetic effects of orthogonalization. The forms they introduce are

$$V(M^+) = -\frac{1}{r} \quad r > \sigma \quad (3)$$

$$= 0 \quad r \leq \sigma,$$

$$V(X^-) = \frac{1}{r}, \quad (4)$$

where σ is the gaseous ionic radius of M^+ as defined by Rittner.⁶ For our problem, we assume for simplicity that $V(H^+) = -1/r$ with no cutoff, since the proton does not possess a core of electrons. The

11. B. J. Austin, V. Heine, and L. J. Sham, Phys. Rev. 127, 276 (1962).

argument for (3) and (4) presented by RC is, briefly, that the increased potential energy of the electron inside a foreign core is almost cancelled by a concomitant increase in kinetic energy, and that therefore the core region can energetically be neglected as far as foreign orbitals are concerned. Effectively, (3) prevents the electron from entering the M^+ core through the barrier produced by the cutoff, and $V(X^-)$ of (4) is electrostatically purely repulsive. The choice of a as the cutoff radius appears justified by the success of the Na_2^+ and K_2^+ calculations of RC; in addition we have carried out calculations on LiH^+ which are in good qualitative agreement with those of Lin,³ and which are described below.

Upon substituting the expansion (1) into the zero-order Schrödinger equation, $\mathcal{H}_0\psi = E\psi$, multiplying by each of the basis orbitals in turn and integrating over all space, we obtain¹²

$$\sum_{i=1}^4 (H_{ij} - ES_{ij})C_i = 0, \quad j = 1, 2, 3, 4, \quad (5)$$

where we have numbered the orbitals according to the "C" subscripts in (1), $H_{ij} = \langle i | \mathcal{H}_0 | j \rangle$, and $S_{ij} = \langle i | j \rangle$ are the overlap integrals. The existence of a non-zero solution for the C's requires that the secular determinant vanish,

$$|H_{ij} - ES_{ij}| = 0,$$

which yields a fourth degree polynomial in E whose roots are the

12. The same set of equations is obtained if we use Eq. (1) as a variational function and set $\frac{\partial E}{\partial C_j} = 0, j = 1, 2, 3, 4$.

eigenvalues for the electronic energy. A set of C's for each root can easily be found by substitution into (5), and thus the wavefunctions can be determined.

C. Evaluation of Integrals

As in the RC procedure, all kinetic and one-center potential energy integrals are evaluated empirically, e.g.,

$$\langle 2 | \frac{1}{2} v^2 + V(M^+) | 2 \rangle = -I(M,s) \quad (7)$$

where $I(M,s)$ is an isolation potential, and, e.g.,

$$\langle 1 | \frac{1}{2} v^2 + \frac{1}{2} V(H^+) + \frac{1}{2} V(M^+) | 2 \rangle = -\frac{1}{2} [I(M,s) + I(H)] \langle 1 | 2 \rangle. \quad (8)$$

In the case of only one electron, this procedure is exact for these integrals. All the other two- and three-center integrals should be determined only by the outer lobes of the true valence wavefunctions, since, in a true pseudopotential theory, the pseudowavefunction has no inner lobes which would otherwise be needed to insure orthogonality to the core. The orthogonality constraint is taken care of by the form of the pseudopotential, so that single-lobed functions which approximate the true wavefunctions outside the core are the only reasonable choices in this problem. For this reason RC chose single-term STO's with orbital exponents adjusted to give a good fit to Clementi's SCF functions⁷ (which are quite accurate for alkalis). For Li we chose to use the exponent from Clementi's minimum-basis-set SCF results.¹³ It will be seen later that the MH^+ interaction as calculated on the model is rather insensitive to the exact choice for the

13. E. Clementi and D. L. Raimondi, J. Chem. Phys. 38, 2686 (1963).

exponent. The basis functions are thus given by

$$\begin{aligned} |1\rangle &= |1s_H\rangle = \pi^{-\frac{1}{2}} \exp(-r), \\ |2\rangle &= |ns\rangle = N_n r^{n-1} \exp(-\delta r), \\ |3\rangle &= |np_\sigma\rangle = \sqrt{3} N_n r^{n-1} \exp(-\delta r) \cos\theta, \\ |4\rangle &= |np_\pi\rangle = \sqrt{3} N_n r^{n-1} \exp(-\delta r) \sin\theta \cos\phi, \end{aligned} \quad (9)$$

where $N_n = \{(2\delta)^{2n+1}/[4\pi(2n)!]\}^{\frac{1}{2}}$ is the s-orbital normalization constant and δ the orbital exponent. Geometrically, we have confined the three atoms to lie in the XZ plane, with M and H along the Z axis and, for convenience, the X^- ion in the +X half-plane.

Due to the symmetry of the s and p functions on M, some of the off-diagonal terms in the Hamiltonian and overlap matrices are zero.

For $S_{ij} = S_{14} = S_{23} = S_{24} = S_{34} = 0$, and we have for H

$$\left. \begin{aligned} H_{11} &= I(H) + V(M^+)_{11} + V(X^-)_{11}, \\ H_{22} &= I(M,s) + V(H^+)_{22} + V(X^-)_{22}, \\ H_{33} &= I(M,p) + V(H^+)_{33} + V(X^-)_{33}, \\ H_{44} &= I(M,p) + V(H^+)_{44} + V(X^-)_{44}, \end{aligned} \right\} \quad (10)$$

$$\left. \begin{aligned} H_{12} &= \frac{1}{2}[I(H)+I(M,s)]S_{12} + \frac{1}{2}V(H^+)_{12} + \frac{1}{2}V(M^+)_{12} + V(X^-)_{12}, \\ H_{13} &= \frac{1}{2}[I(H)+I(M,p)]S_{13} + \frac{1}{2}V(H^+)_{13} + \frac{1}{2}V(M^+)_{13} + V(X^-)_{13}, \\ H_{14} &= V(X^-)_{14}, \\ H_{23} &= H_{24} = H_{34} = 0. \end{aligned} \right\} \quad (11)$$

The fourteen two-center and three three-center integrals in (10) and (11) were evaluated using the algorithms outlined in Harris and

Michels' review of STO integrals;¹⁴ an appendix to this chapter contains the computational details. The integrals involving the discontinuous M^+ potential had to be corrected for the region inside the M^+ core; it was found that approximating the foreign basis orbital $|1s_H\rangle$ by a linearized Taylor series expansion around the position of the M nucleus as used by RC was quite inaccurate for small internuclear separations, so the corrections were evaluated exactly. Figure 1 shows a comparison of the exactly and approximately corrected integral $V(M^+)_{11}$ as a function of M-H separation for various values of σ , the ionic radius; the mathematics is again given in the appendix. The integral evaluation procedures were programmed for arbitrary quantum numbers, so that different alkali atoms could be studied and compared. Since the dimensionality of the secular determinant was only four, it was explicitly expanded and the roots obtained using the Laguerre iterative procedure;¹⁵ thus the zeroth-order electronic energies and wavefunctions were determined.

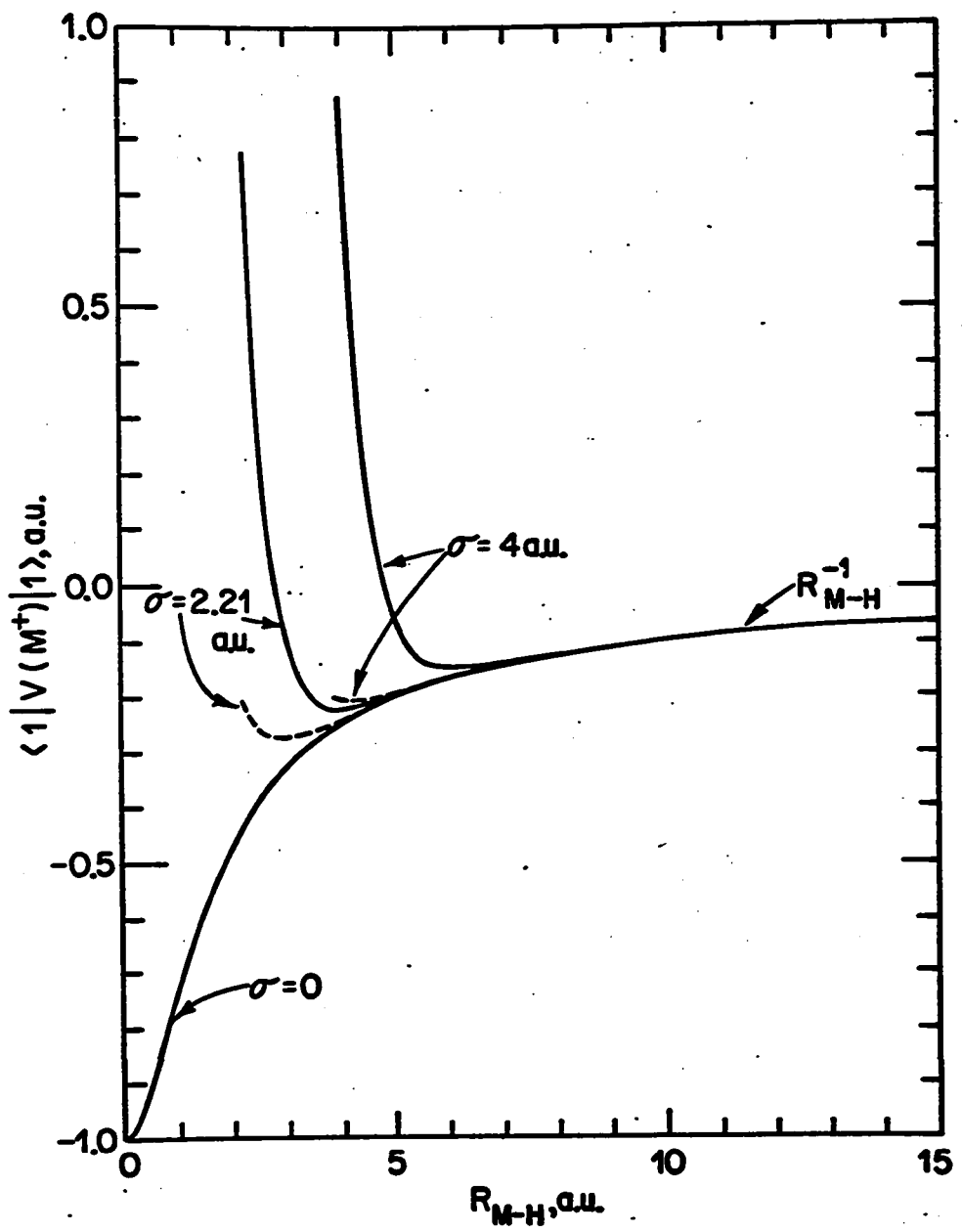
D. Pairwise Core Interactions

In exact analogy to an ab initio calculation, the core interactions can be added in after the electronic energies have been found. Unlike the "bare nuclei" case, however, these cores are polarizable (with the exception of the proton) and, in addition to the mutual polarization of the cores, the electron also induces core dipoles.

14. F. E. Harris and H. H. Michels, *Advan. Chem. Phys.* 13, 205 (1967).

15. See, for example, A. Ralston, "A First Course in Numerical Analysis" (McGraw-Hill, New York, 1965), Ch. 8.

Fig. 1. Comparison of exact (—) and approximate (---) hydrogenic expectation values for the alkali ion pseudopotential $V(M^+)$ as a function of the M-H internuclear distance for three values of σ , the M^+ ionic radius.



The three-body polarization problem will be considered in detail later; for now we will consider the interactions between the pairs M^+X^- , M^+H^+ and H^+X^- .

According to the simple ionic Rittner model⁶ for M^+X^- , the (assumed) point-charge interactions are counterbalanced for small internuclear distances R by a theoretically reasonable exponential repulsion term of the form $A \exp(-R/\rho)$, which reflects the Pauli repulsion of the ion core electrons. The potential energy as a function of the internuclear distance is written (in a.u.)

$$V(R) = A \exp(-R/\rho) - \frac{1}{R} - \frac{(\alpha_{M^+} + \alpha_{X^-})}{2R^4} - \frac{C_6}{R^6}, \quad (12)$$

where the α 's are ion polarizabilities and C_6 is the van der Waals force constant, estimated via¹⁶

$$C_6 = \frac{\alpha_{M^+}\alpha_{X^-}}{M^+ X^-} \cdot \frac{I_{M^+} I_{X^-}}{(I_{M^+} + I_{X^-})}, \quad (13)$$

where the I 's are ionization potentials. We have neglected the induced-dipole-induced-dipole interactions, which go as R^{-7} . More recent experimental data was used, namely, the equilibrium internuclear distance R_e and vibration frequency ω_e , to recalculate A and ρ , and thus determine the binding energy. Table I lists A and ρ for all the alkali halides, along with the predicted and experimental dissociation energies into neutral atoms; it can be inferred from the good agreement in energies that the ionic Rittner model is reliable

16. F. London, Z. Physik 63, 245 (1930).

Table I. Alkali halide repulsion constants and binding energies^a

Molecule ^b	A	ρ	D_e , calc	D_e , expt ^c
LiF	25.97	.5128	139.6	138.8
LiCl	36.36	.6163	107.3	112.4
LiBr	37.99	.6531	93.2	100.4
LiI	41.11	.7030	75.4	84.6
NaF	16.82	.6420	111.4	114.2
NaCl	66.95	.6172	93.8	97.5
NaBr	68.78	.6496	82.1	86.4
NaI	62.78	.7108	66.6	72.3
KF	36.03	.6378	113.8	117.6
KCl	104.55	.6421	99.2	101.4
KBr	82.40	.6999	86.7	90.5
KI	60.87	.7850	71.3	76.2
RbF	80.42	.5816	117.5	116.0
RbCl	106.55	.6666	98.1	100.4
RbBr	110.94	.6961	86.9	89.9
RbI	73.85	.7903	71.6	76.1
CsF	108.71	.5838	122.3	119.4
CsCl	127.29	.6811	101.6	105.8
CsBr	92.60	.7479	89.2	95.6
CsI	52.38	.8707	73.1	81.6

^aA and ρ , parameters in the overlap repulsion term $A \exp(-r/\rho)$, are given in a.u.; the dissociation energies, measured from the bottom of the well, in kcal/mole. D_e , calc was computed via $D_e = -V_{MX}(R_e) - I(M) + E(X)$, where $V_{MX}(R)$ is the Rittner potential using the constants of Table III, and $I(M)$, $E(X)$ are also given in Table III.

^bSee also C. Maltz, Chem. Phys. Letters 3, 707 (1969), for calculations on the K and Cs salts.

^cTaken from L. Brewer and E. Brackett, Chem. Rev. 61, 425 (1961).

for these species.

The Pauli overlap repulsion used in the M^+X^- potential clearly does not apply to the $M^+ - H^+$ or $H^+ - X^-$ cases, since the proton has no electronic core. In fact, the only way in which repulsion can arise, in an electrostatic framework, is through penetration of the proton into the electronic core until the nuclear repulsion counter-balances the attraction of the electron distribution. This in turn implies that we can no longer make use of the point-charge interaction approximation, at least at internuclear distances comparable to the spatial extent of the core electronic wavefunction, and also that we must know something about the core wavefunction.

A simple electromechanical theory was developed long ago by Pauling¹⁰ as a qualitative description of the bonding in the hydrogen halides which makes use of the proton penetration idea. Platt¹⁷ has more recently extended the model to all the hydrides. It seems especially appealing for the halides, since equilibrium H-X separations are all smaller than the corresponding X^- ionic radii. Pauling considered only the charge-charge interaction, but we wish to extend the model to include polarization effects, in keeping with our general scheme.

The outer shell of 8 electrons in X^- is assumed to be described by a single electron density function $\delta\rho(r)$, where $\int \rho(r) dr = 1$; the nucleus and inner shells are taken as forming a single tight "ball" of net electrical charge +7. The potential energy of a proton situated

17. J. R. Platt, J. Chem. Phys. 18, 932 (1950).

at a distance R from the X^- nucleus is then the sum of the repulsion due to the nuclear ball and the attraction due to the extranuclear charge distribution ρ :

$$V(R) = \frac{7}{R} - 8 \int \frac{\rho(x)}{|x-R|} dx. \quad (14)$$

We now perform a multipole expansion of $|x-R|^{-1}$, taking care to use the proper convergent expansion depending on whether r is greater or less than R ; we obtain

$$V(R) = \frac{7}{R} - 8 \left[\int_0^R \rho(x) \left(\frac{1}{R} + \frac{r}{R^2} P_1(\cos\theta) + \frac{r^2}{R^3} P_2(\cos\theta) + \dots \right) dx + \int_R^\infty \rho(x) \left(\frac{1}{r} + \frac{R}{r^2} P_1(\cos\theta) + \frac{R^2}{r^3} P_2(\cos\theta) + \dots \right) dr \right], \quad (15)$$

where the terms in the integrals represent the charge-charge, charge-dipole, charge-quadrupole, etc., interactions between the proton and ρ (the P_ℓ are the Legendre polynomials). If we assume that ρ is spherically symmetric, i.e., that X^- remains undistorted by the presence of H^+ , we obtain the result given by Pauling,¹⁰

$$V_o(R) = \frac{7}{R} - 8 \left[\int_0^R \frac{\rho(r)}{R} r^2 dr + \int_R^\infty \frac{\rho(r)}{r} r^2 dr \right], \quad (16)$$

where ρ is now radially normalized, $\int_0^\infty \rho(r)r^2 dr = 1$. Pauling employed hydrogen-like radial wavefunctions $\chi_n(r)$ to represent ρ via

$$\rho(r) = |\chi_n(r)|^2. \quad (17)$$

For simplicity we use Slater-type radial functions,⁹

$$\chi_n(r) = N r^{n-1} \exp(-\delta r), \quad (18)$$

where $N = [(2\delta)^{2n+1}/(2n)!]^{1/2}$ and $\delta = (Z-S)/n$; the screening constant S can be chosen according to Slater's rules. Substitution of (17) and (18) in (15) yields, upon integrating and combining terms.

$$V_0^{(n)}(R) = \frac{1}{R} [7 - 8(1 - e^{-x}) \sum_{i=0}^{2n-1} \frac{2n-i}{2ni!} x^i)], \quad (19)$$

where $x = 2\delta R$. It is clear physically that the proton should greatly distort the outer-shell electrons of X^- , particularly in the equilibrium R region, so that (19) is not a very good approximation. In order to bring in the charge-dipole terms in Eq. (15), we must allow for distortion of ρ .

We write the distorted electron density on X^- as

$$\rho(x) = \rho(r)(1 + a(R)\cos\theta), \quad (20)$$

where $\rho(r)$ is our zeroth-order Slater density of Eq. (17), and the distortion parameter "a" depends on the nearness of the proton. Since the halide ion in the absence of perturbation must be spherically symmetric, we require $a(\infty) = 0$. In using the form (20) we see from Eq. (15) that we can retain our result (19) as the zeroth-order potential, and that the polarization correction will be directly proportional to $a(R)$. At large R , the semi-infinite integral in (15) becomes negligible, so that the correction becomes

$$V_1(R) \xrightarrow[\text{large } R]{} 8 \int \rho(x) \frac{r}{R^2} P_1(\cos\theta) d\tau \rightarrow \frac{-8 a(R) \langle r \rangle}{3R^2}, \quad (21)$$

where $\langle r \rangle = \int \rho(r)rd\tau$. Since the spatial extent of ρ becomes negligible for sufficiently large R , we know from simple electrostatics that

$$V_1(R) \underset{\text{large } R}{=} -\frac{\alpha}{2R^4}, \quad (22)$$

where α is the electric polarizability of the halide ion. Comparing Eqs. (21) and (22), we obtain

$$\alpha(R) = \frac{3}{16} \frac{\alpha}{R^2 \langle r \rangle}, \quad (23)$$

which vanishes at $R = \infty$ as required. Carrying out the integrations of Eq. (15) fully, we find

$$V_1^{(n)}(R) = -\frac{\alpha}{2R^4} \left(1 - e^{-x} \sum_{i=0}^{2n} \frac{(2n+1)(2n)(2n-1) - i(i-1)(i-2)}{(2n+1)(2n)(2n-1)i!} x^i \right), \quad (24)$$

where as before $x = 2\delta R$. The total $H^+ - X^-$ potential is then given by

$$V^{(n)}(R) = V_0^{(n)}(R) + V_1^{(n)}(R), \quad (25)$$

where $n = 2$ for F^- , 3 for Cl^- , and 4 for Br^- .

The qualitative effect of what we have done in taking account of the finite spatial extent of the X^- outer shell is, from inspection of Eqs. (19) and (24), to attenuate both the attractive coulombic and polarization interactions at small R , since the expressions in parentheses involving the exponential go to zero at $R = 0$. Thus the coulomb repulsion of the nuclear ball eventually dominates the interaction at sufficiently small R .

In comparing the potentials generated with this model with experiment, we find poor agreement for both binding energy and equilibrium

internuclear distance if we choose the screening constants using Slater's rules. If we allow the orbital exponent δ to be a free parameter, however, we can get fair to good agreement for internuclear distance and fair results for vibration frequency by adjusting δ to give the correct binding energy; the qualitative trends with halogen in these quantities are correctly given. Table II compares the calculated and observed parameters, and Fig. 2 shows the potential curves, with Morse curves drawn in for comparison. The model, naturally, incorrectly predicts ionic dissociation, so the energy scale of Fig. 2 is with respect to dissociated ions as zero.

The same model can be used for the $M^+ - H^+$ interaction, although it is not nearly so important to include the details of the core repulsion in this case, since the M^+ ions are not nearly so polarizable as X^- and the charge-charge potential is repulsive at all separations. With the exception of Li^+ , the expression corresponding to Eq. (19) for the charge-charge interaction is obtained simply by replacing 7, the charge of the nuclear ball, by 9, and the charge-dipole term is identical to Eq. (24) for all the alkalis, where $n = 1$ for Li, 2 for Na, and 3 for K. For Li, the 7 and 8 in Eq. (19) must be replaced by 3 and 2, respectively. In the absence of experimental "calibration", Slater screening constants are used.

The problem of including repulsive interactions between the proton and M^+ , X^- can also be approached from another, more empirical direction, with a basically different philosophy in mind. Particularly with regard to $H^+ - X^-$, in the spirit of valence-bond theory the

Table II. Pauling model for H⁺-X⁻

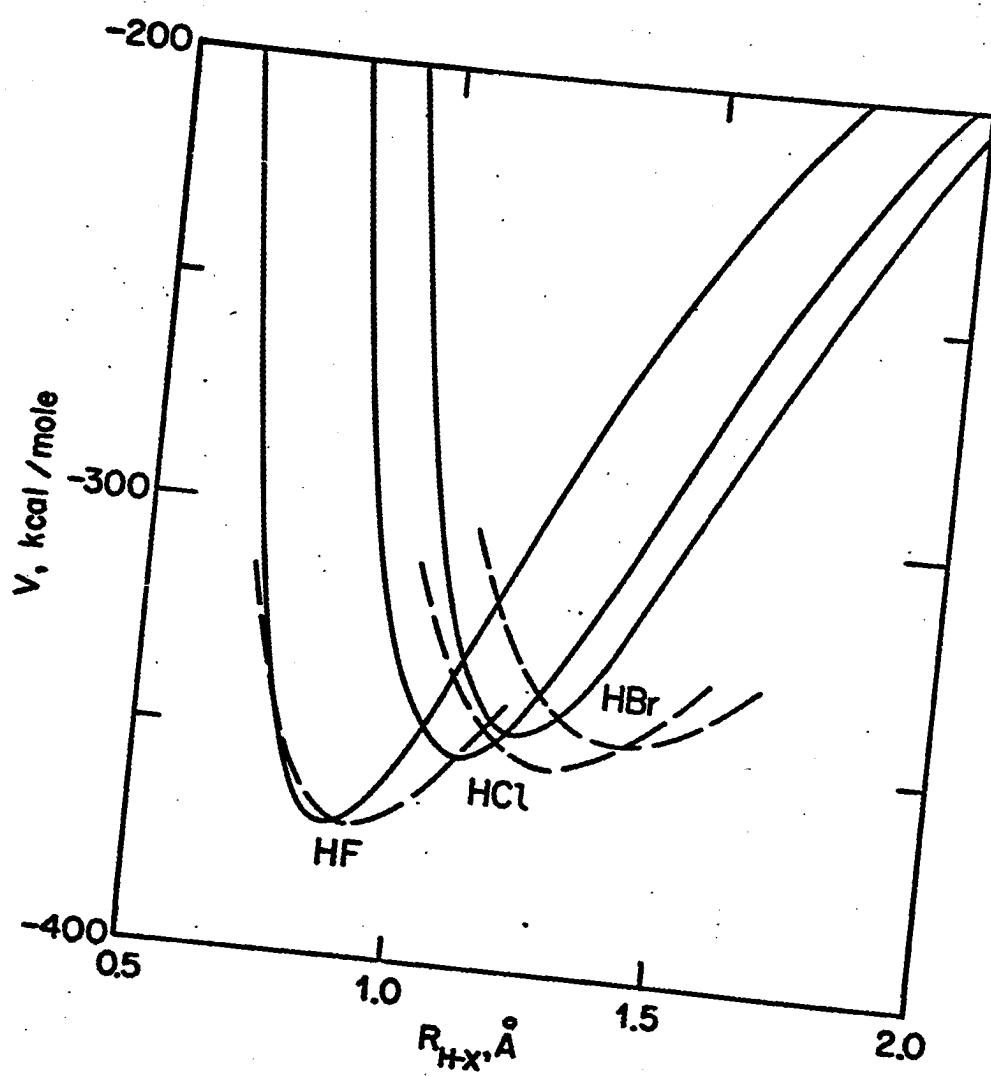
X ⁻	Slater δ	Adj. δ ^a	D _e ^(ions) ^b	R _e , expt ^c	R _e , calc	ω _e , expt ^c	ω _e , calc
F ⁻	2.42	1.84	0.5899	0.92	0.87	4140	5240
Cl ⁻	1.92	1.85	0.5628	1.27	1.11	2990	4820
Br ⁻	1.51	2.15	0.5533	1.41	1.22	2650	4670

^aValue of δ giving correct ion dissociation energy.

^bCalculated from D_e + I(H) - E(X); D_e, dissociation energy into atoms measured from bottom of potential well, taken from G. Herzberg, "Spectra of Diatomic Molecules" (D. Van Nostrand Co., Inc., Princeton, N. J., 1950); I(H) = 0.5 a.u.; E(X), electron affinity of the halogen atom, is listed in Table III.

^cTaken from G. Herzberg, ibid.

Fig. 2. Potential curves for hydrogen halides according to Pauling model. Dashed curves are the corresponding Morse potentials. Zero of energy is that of the separated ions H^+ and X^- .



interaction in the entrance valley of the potential surface can be regarded as being the "ionic part" of the overall H-X interaction, and the repulsive term empirically chosen assuming a non-zero ionic radius for H^+ and using a Badger's Rule type of correlation to estimate the force constant. This approach was tried, but the binding energy obtained for the ions lay above the asymptote for dissociation of the atoms, and the resulting potential surfaces were everywhere repulsive. The theory of these interactions as outlined above was considered to be more consistent with the general character of the one-electron model, and, within the limits imposed by such a picture, fairly realistic.

E. Three Center Polarization

We now turn to the three-body polarization interaction problem. The main complication over the two-body cases we have been considering is that the vector nature of the polarizing fields must be taken into account. If we again neglect the interactions of the induced dipoles with each other, the ξ_j fields at each core are independent of one another, and the energy of interaction ϕ can be written as

$$\phi = -\frac{1}{2} \sum_j \alpha_j \xi_j^2, \quad (26)$$

where the index "j" runs over all the cores. Since we assume $\alpha_{H^+} = 0$, in this case the sum includes only M^+ and X^- . As RC point out, the problem of including terms in the ξ_j due to the electron, as represented by the zeroth-order wavefunction, is greatly simplified if we regard the weight of each basis function $|i\rangle$, $|c_i|^2$, as a fractional

point charge (in atomic units) residing at the orbital center, and any p-character of the wavefunction as resulting in a point electric dipole at the origin of the p basis functions. Thus the core charges on the orbital centers are effectively partially screened, and the M center becomes both a partial charge and dipole field source. Denoting the charges on M and H by Q_M , Q_H and the M dipole by D_M , and using Eq. (1), it is clear that

$$Q_M = |C_1|^2, Q_H = \sum_{i=2}^4 |C_i|^2 = 1 - Q_M \quad (27)$$

and

$$D_M = \langle M | \vec{x} | M \rangle, \quad (28)$$

where $|M\rangle = \sum_{i=2}^4 C_i |i\rangle$ is that part of the basis residing on M. For the geometry previously defined,

$$D_M = 2C_2 C_3 \langle 2 | z | 3 \rangle \hat{k} + 2C_2 C_4 \langle 2 | x | 4 \rangle \hat{i}; \quad (28a)$$

all other dipole matrix elements are zero, since the dipole operator connects only even and odd states. By symmetry $\langle 2 | z | 3 \rangle = \langle 2 | x | 4 \rangle$, and using the definitions (9), it is easily shown that $\langle 2 | z | 3 \rangle = \langle r \rangle / \sqrt{3}$, where $\langle r \rangle$ is the mean orbital radius $\langle 2 | r | 2 \rangle$. Thus we have finally

$$D_M = \frac{2}{\sqrt{3}} \langle r \rangle C_2 (C_3 \hat{k} + C_4 \hat{i}). \quad (29)$$

In order to conform with electrostatic convention, the negative of (29) must be used, so that D_M points toward the positive pole.

Using the well-known formulae

$$\vec{E}_{\text{charge}} = \frac{Q}{R^2} \hat{R}, \quad (30)$$

$$\vec{E}_{\text{dipole}} = \frac{D}{R^3} [3(\hat{D} \cdot \hat{R}) \hat{R} - \hat{D}], \quad (31)$$

where the hat denotes a unit vector, the dipole $\hat{D} = \frac{1}{\alpha} \vec{D}$, and \hat{R} is directed from field source to field point, it is now very easy to substitute into Eq. (27) and find

$$\begin{aligned}\phi = & -\frac{\left(\frac{\alpha}{M^+} + Q_M^2 \frac{\alpha}{X^-}\right)}{2R_{MX}} - \frac{\alpha Q_H^2}{2R_{HX}} - \frac{\alpha Q_H^2}{2R_{MH}} + \frac{\alpha Q_H}{R_{MH}^2 R_{MX}^2} (\hat{R}_{MX} \cdot \hat{R}_{MH}) \\ & - \frac{\alpha Q_H}{R_{HX} R_{MX}} (\hat{R}_{HX} \cdot \hat{R}_{MX}) - \frac{2\alpha Q_M D_M}{R_{HX}} (\hat{D}_M \cdot \hat{R}_{MX}) \\ & - \frac{\alpha Q_H D_M}{R_{HX} R_{MX}} \left[-\hat{D}_M \cdot \hat{R}_{HX} + 3(\hat{D}_M \cdot \hat{R}_{MX})(\hat{R}_{MX} \cdot \hat{R}_{HX}) \right] \\ & - \frac{\alpha D_M^2}{R_{MX}^2} [1 + 3(\hat{D}_M \cdot \hat{R}_{MX})^2],\end{aligned}\quad (32)$$

where the directions of the radial unit vectors are indicated by the identity and order of the indices. All the dot products are simply evaluated from the nuclear geometry and Eq. (29). In order to account for the effects of core penetration by the proton, the second and third terms in Eq. (32) were attenuated by factors of the form in Eq. (24). To avoid the complications of a multicenter multipole expansion on the M^+ and X^- shells, three-body terms in Eq. (32) were left unaltered. With the aid of Eqs. (12), (19) and (32), the total core interaction including the approximate electronic contribution to the polarization is

$$V_{core} = V_{o,HX}(R_{HX}) + V_{o,MH}(R_{MH}) + A \exp(-R_{MX}/\rho) - \frac{1}{R_{MX}} - \frac{C_6}{R_{MX}^6} + \phi. \quad (33)$$

All the terms except ϕ are common to all four surfaces; ϕ , since it contains the electronic terms, changes depending on the zeroth-order wavefunction.

F. Summary of Empirical Parameters

Empirical data used in the calculations to be presented include the s- and p-ionization potentials of the alkali atoms,¹⁸ the atomic SCF results for the valence orbital exponents ξ and hence the mean radii $\langle r \rangle$,^{7,13} the polarizabilities α ,¹⁹ the ionic ionization potential I_{\pm} ,^{18,20} the gaseous ionic radii σ , and the alkali halide overlap repulsion parameters A and ρ (Table I). The ionic radii were recalculated by a least-squares fit to present spectroscopic values for $R_e(MX)$ assuming $\sigma_{K^+} = 2.211$ a.u.²¹ Table III contains a complete compilation of these atomic data for all the alkalis and halogens where available.

G. Calculations on MH^+ Molecule Ions

In order to test the method of calculation, electronic potential energy curves were computed for the molecule ions LiH^+ , NaH^+ and KH^+ with rather interesting and perhaps accurate results. These species

18. W. F. Meggers, C. H. Corliss, and B. F. Scribner, "Tables of Spectral Line Intensities" (National Bureau of Standards Monograph 32-Part I, 1961).
19. J. R. Tessman, A. H. Kahn, and W. Shockley, Phys. Rev. 92, 890 (1953).
20. R. S. Berry and C. W. Reimann, J. Chem. Phys. 38, 1540 (1963), electron affinities of halogen atoms.
21. L. Pauling, "The Nature of the Chemical Bond" (Cornell University Press, Ithaca, New York, 1944), p. 344.

Table III. Empirical atomic data.^a

Atom	I.P.(s)	I.P.(p)	I.P. ion	α_{ion}	σ_{ion}	δ
H	0.50000			0	0	1.000
Li	0.19814	0.13023	2.7797	0.1957	0.994	0.6396
Na	0.18886	0.11157	1.7384	1.721	1.600	0.850
K	0.15952	0.10022	1.1693	8.105	2.211	0.736
Rb	0.15351	0.09565	1.0108	12.13	2.432	-
Cs	0.14310	0.09091	0.9216	21.17	2.652	-
F			0.12670	5.122	1.855	
Cl			0.13278	20.07	2.828	
Br			0.12359	27.87	3.118	
I			0.11257	41.84	3.547	

^aAll values given in atomic units (a.u.); $a_0 = 0.529167 \text{ \AA}$ and 1 a.u. of energy = 27.2107 eV = 627.505 kcal/mole. These conversions are based on the study of E. R. Cohen and J. W. M. DuMond, Revs. Mod. Phys. 37, 537 (1965). Sources for the values are enumerated in the text.

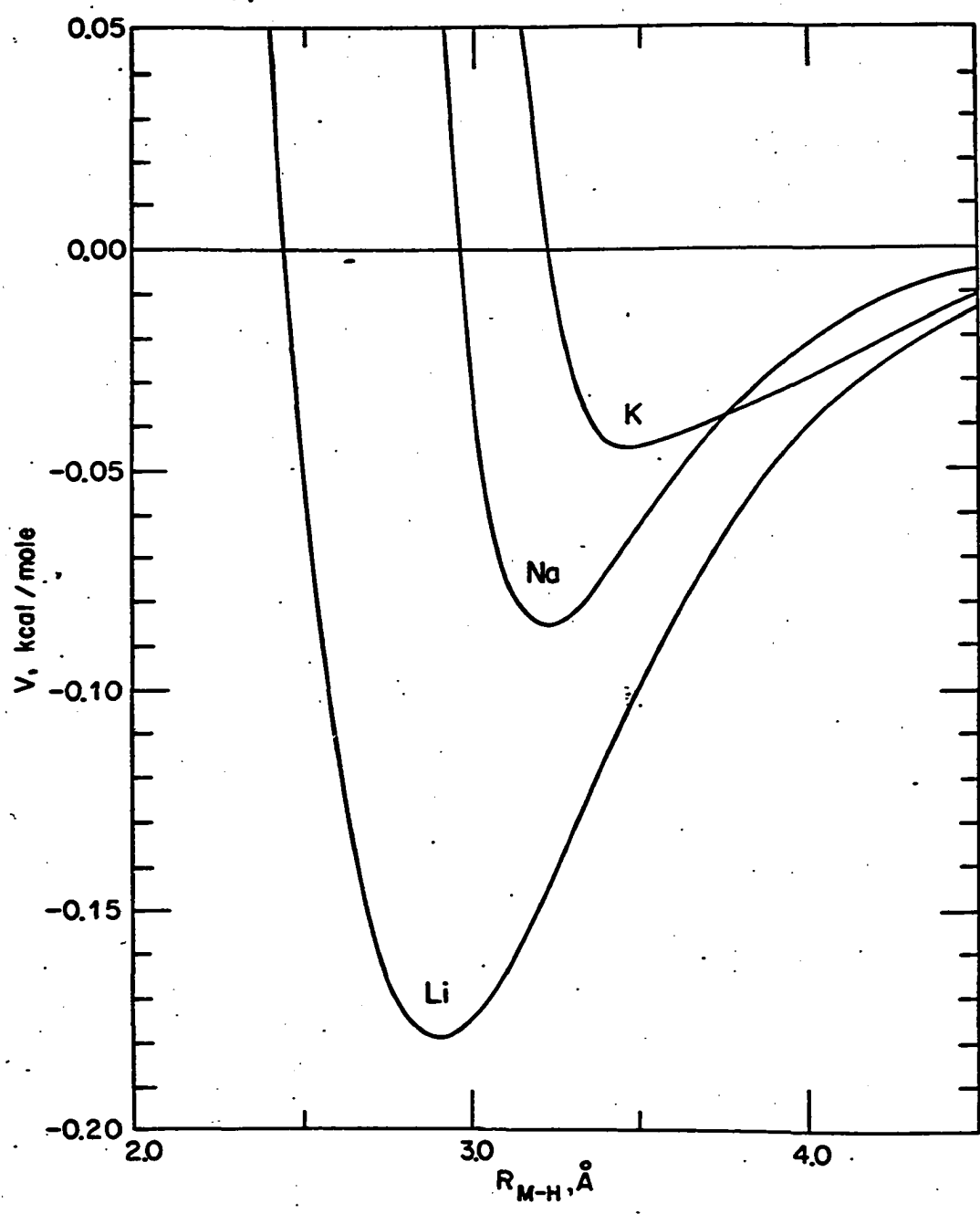
have not been observed spectroscopically, indicating that the ionized states of the corresponding MH molecules are at most only slightly attractive, and/or have equilibrium internuclear distances much larger than those of the neutral. Lin³ has performed a CI calculation which indicates that the equilibrium internuclear distance, if the molecule ion is stable at all, is greater than $4.25 a_0 = 2.25 \text{ \AA}$. NaH^+ and KH^+ have never been treated to the knowledge of the author.

The present calculations are in qualitative agreement with Lin's prediction. Lin's calculations lie about 11.8 kcal/mole higher in energy with respect to the dissociated alkali ion and H atom at $R_{\text{Li-H}} = 2.0 \text{ \AA}$. The gradients dV/dR at that point compare fairly well, -8.1 kcal/ \AA from Lin's work, -5.7 here. We predict no stable species for any of the MH^+ , but we do find tiny potential wells (incapable of supporting bound states) at very large internuclear separations. These results are presented in Table IV, and Fig. 3 shows the potential curves; the orbital exponents corresponding to both the minimum-basis-set SCF¹³ and full SCF⁷ wavefunctions for Na and K were used in the calculations. The full SCF exponent results are shown and listed for Na and K, the minimum basis set for Li. The two orbital exponents δ for Na are nearly identical (full SCF, 0.850; minimum SCF, 0.836) so that the calculated curves gave identical R_e values and differed by only 0.003 kcal at the minimum. For K the δ 's are not so similar (0.736 and 0.874), and consequently the minimum SCF exponent gave a shallower well by 0.020 kcal and a larger R_e by 0.2 \AA . Considering the size of the energies being dealt with, these results show that all

Table IV. MH^+ molecule ion

Molecule Ion	kcal/mole		\AA	
	D_e Ion	D_e Neutral	R_e Ion	R_e Neutral
LiH^+	0.179	58	2.94	1.60
NaH^+	0.085	47	3.23	1.89
KH^+	0.045	43	3.47	2.24

Fig. 3. Potential curves for the alkali hydride molecule ions.
Zero of energy is that of separated H and M^+ .

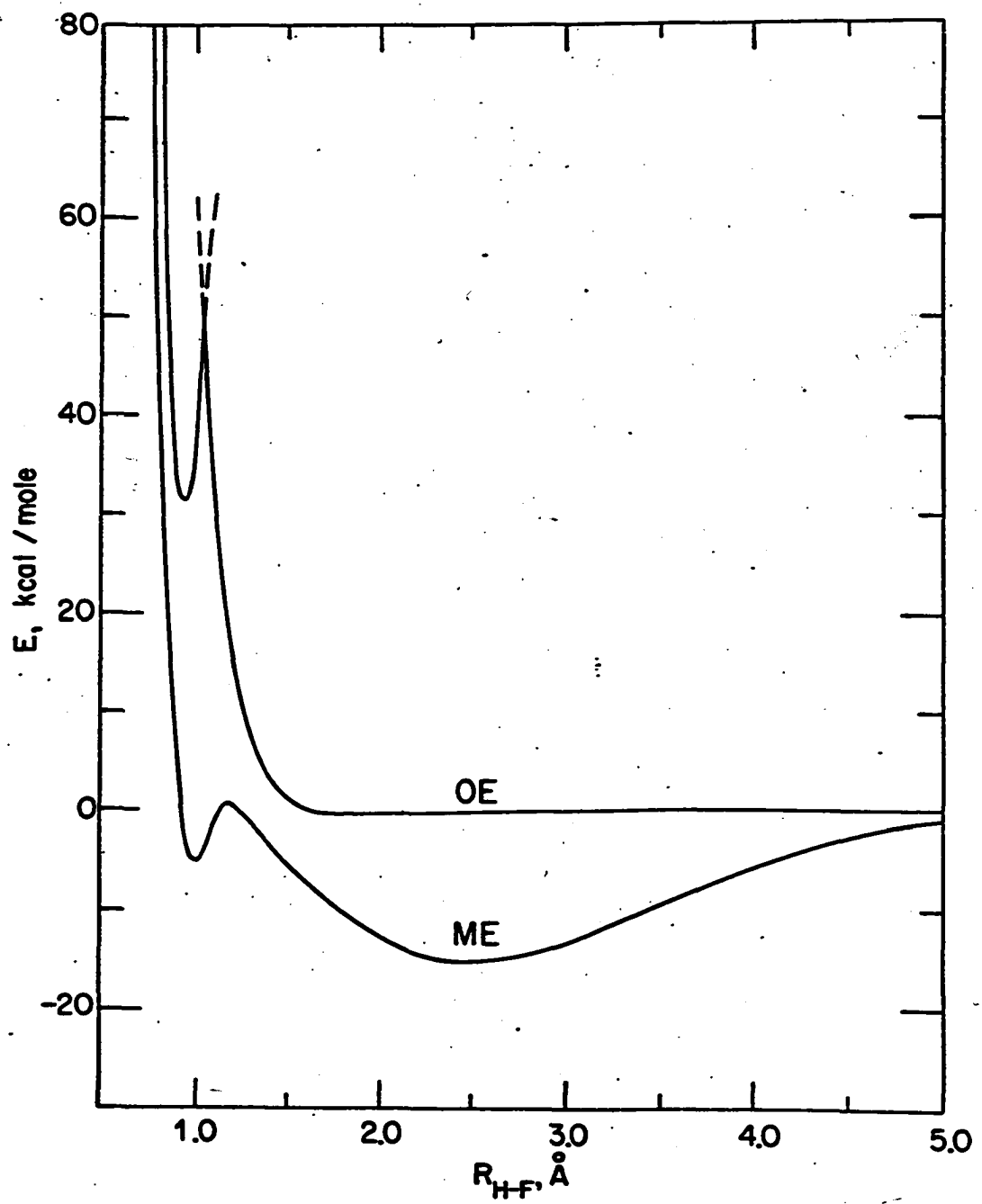


the calculations should be fairly insensitive to the choice of δ . The well depths and equilibrium separations for the MH molecules are listed for comparison. At these internuclear distances, which are rather large compared with the dimensions of the M^+ ions, the core potential $V_0(R)$ (cf. Eq. (19)) reduces to $+1/R$, and the contribution to the well depth from polarization is completely negligible. These small wells are due to the inclusion of the p M function in the basis; without it the energy curves are purely repulsive.

H. Results and Discussion

Calculations based on the theory outlined above were carried out for the systems H + LiF, KF, KCl, and KBr. In an effort to assess the validity and reliability of the one-electron model, the H + LiF calculations were compared with the all-electron calculations of Balint-Kurti⁴ (BK). His calculations were done for a linear H-F-Li geometry; the results of comparison on the reactant side are shown in Fig. 4. Here we notice the first unusual feature of the one-electron calculations: a curve-crossing occurs for the entrance reactive channel. This curve crossing must be due to the polarization interaction ϕ , since the zeroth order electronic energies, as roots of a secular determinant, cannot cross, and the other terms in V core, as pointed out, are common to all four surfaces. The zeroth-order electronic ground state puts most of the electron on H even for small H-F separations and an excited state with most of the electron on Li then must cross this ground state due to the very strong polarization interaction between H^+ and F^- . As can be seen, the crossing is

Fig. 4. Comparison of one-electron (OE) model with many-electron (ME) calculation of Balint-Kurti, Ref. 4. Curves represent a cut in the linear H-F-Li potential surface for $R_{\text{Li}-\text{F}} = 1.59 \text{ \AA}$. Zero of energy is that of the separated reactants H + LiF.

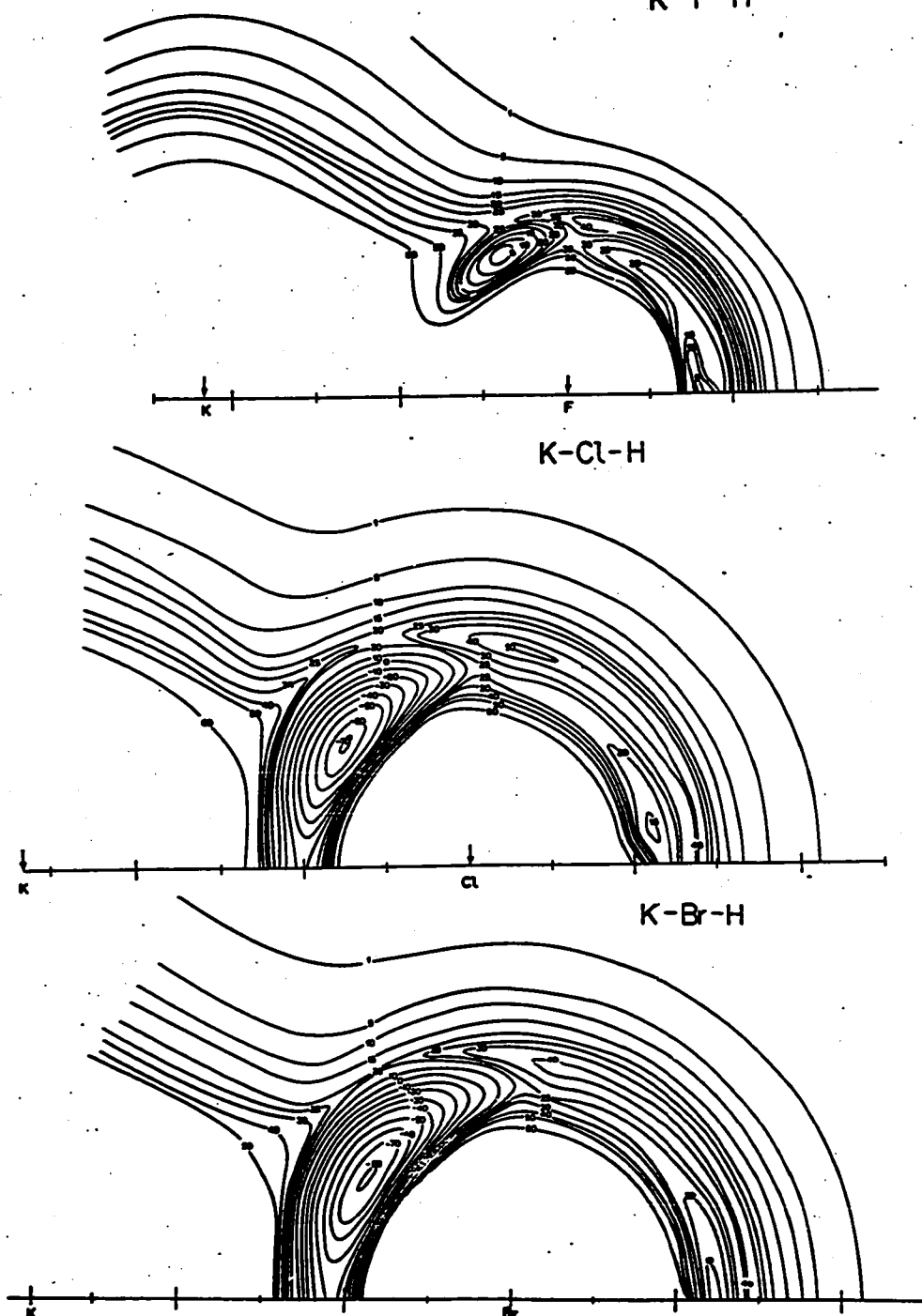


extremely steep; we thus expect quite a large interaction energy between the resonant states to reduce the size of the crossing barrier drastically. In the BK result there can be no curve-crossing since the entire energy is the result of solving the secular equations, but nonetheless it shows a qualitatively similar "bump" just before the inner well, indicating that the electronic wavefunction is changing rapidly in this region.⁴ The inner wells both occur near the equilibrium H-F distance (1.01 Å for BK, 0.87 Å for this work), although the one-electron well is unstable with respect to reactants. We cannot reproduce the long-range attraction of BK, since our H atom is not polarizable. From this comparison, we may conclude that while the model will not give reliable long-range behavior for the entrance channel, it may impart a reasonable qualitative idea of the "close-in" interactions for these systems. The BK calculations were not extended to non-linear configurations, but we can hope that our model may give some reliable indication of any preferred geometry.

The experimental results of the previous chapter seem to imply some geometrical effect and trends with halogen for the reactions of H with KF, KC1 and KBr; it was therefore of particular interest to carry out calculations for these three systems. The results are presented in Fig. 5. In accord with the ideas discussed in the previous chapter concerning the mechanics of H atom systems, where the motion of H is approximately "separable" from that of the heavy atoms, we have "clamped" the KX nuclei in their equilibrium positions and show the potential energy as a function of the position of the H atom with

Fig. 5. Angular dependences of the one-electron potential energy surfaces for the reactions of H with KF, KCl and KBr, for each salt at its equilibrium internuclear distance. Major tic marks are 1 Å apart; energy contours are given in kcal/mole.

K-F-H



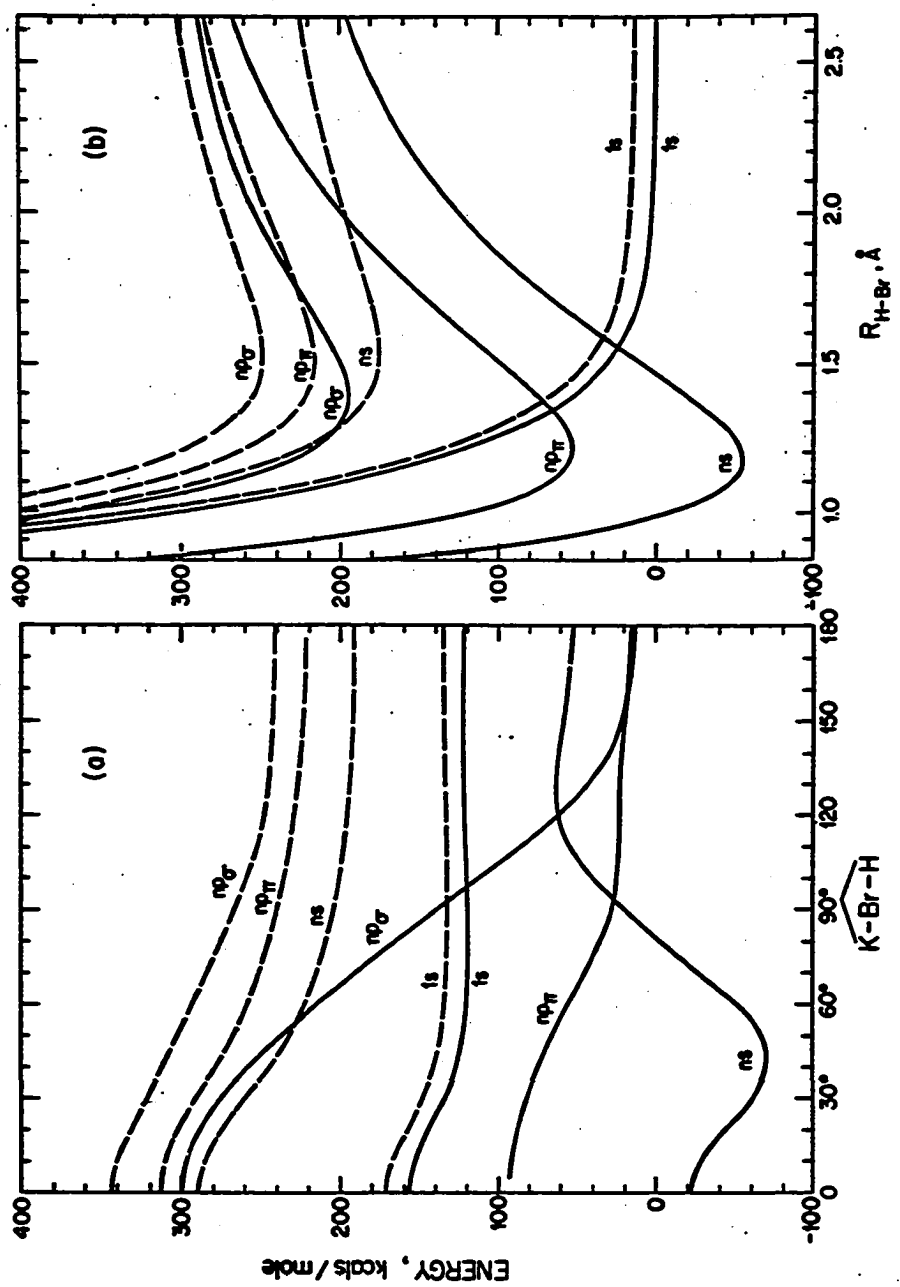
respect to the diatomic. The features of note are the following:

(1) Each surface has a well for a triangular configuration, with depth ranging from ~ 0 kcal/mole for KF to -80 for KBr. (2) The position of the well shifts in toward the internuclear axis as F \rightarrow Br. (3) A "curve-crossing barrier" similar to that in Fig. 4 surrounds each halide ion of height ~ 40 kcal, but it is reduced to 20-30 kcal in the vicinity of the well. Figure 6 shows the variation of the four surfaces for H + KBr when (a) sweeping around the Br⁻ ion at the equilibrium H-Br distance and (b) coming in at $\overbrace{K\ Br\ H} = 60^\circ$, both for $R_{KBr} = R_e$.

The wells in each case occur for an H-X separation very close to the equilibrium position (see Table II). The shift toward the axis as F \rightarrow Br correlates nicely in a qualitative way with the results of the dynamic model calculations, to be presented in the next chapter, as applied to the data of Chapter V. This correlation will be discussed in more detail in Chapter VII. As we mentioned above in discussing H-F-Li, we expect a substantial interaction energy to reduce the crossing barrier a good deal. The fact that it is already lower by ~ 10 -20 kcal near the well region suggests that this region will be greatly favored for reactive collisions over linear H-X-K and other less triangular configurations.

Since the model is not expected to be realistic as the products depart, we have not examined the surfaces for larger KX distances, except to confirm that, at very large R_{KX} , the HX diatomic curves are recovered.

Fig. 6. Behavior of the four one-electron surfaces for H + KBr, without (---) and with (—) the polarization interactions included. (a) $R_{\text{HBr}} = 1.22 \text{ \AA}$, $R_{\text{KBr}} = 2.72 \text{ \AA}$, angle $\overbrace{\text{K-Br-H}}$ varied. (b) $R_{\text{KBr}} = 2.72 \text{ \AA}$, angle $\overbrace{\text{K-Br-H}} = 60^\circ$, R_{HBr} varied.



In a situation where a perturbation has caused curve crossing and core penetration can occur, the zeroth-order one-electron wavefunctions may not be too relevant, but it is nonetheless of interest to consider the form of the ground and excited wavefunctions when the perturbation has made these states resonant. To better than 90%, the crossing corresponds to an electron transfer from H to K, which is the qualitative picture upon which the one-electron model relies in attempting to describe these reactions. But because the $H^+ - X^-$ polarization interaction in actuality implies, for small H-X separations and hence partial core penetration, a partial charge transfer to the proton, we are forced to think that, in a qualitative way, the model bears witness to a highly concerted electronic mechanism intimately involving the X^- electrons. In effect, an electron transfer from X^- to H "pushes" the H electron over to the alkali.

It is clear that any conclusions we have drawn from the calculations must remain qualitative because of the necessarily inadequate treatment of the role played by the X^- electrons in the overall electronic structure, especially in "close" configurations. Nonetheless there appear to be two ways in which the present calculations could be improved: (1) Expanding the one-electron basis set to include the 2s and 2p (or perhaps just 2p) orbitals on H would enable a better calculation of the long-range forces acting on the H atom by allowing for polarization, and might also serve to reduce the curve-crossing barriers somewhat. This change, however, would not be likely to affect the crossing states at small R_{HX} appreciably, since these

Filmed as received
without page(s) VI-36.

UNIVERSITY MICROFILMS.

Appendix. Computational Details

A Fortran IV computer program was written to perform the calculations described in the text. The program breaks down into three main steps: calculation of the integrals of Eqs. (10) and (11), solution of the secular equation (5) to obtain the energies and wavefunctions, and calculation of the coulombic, repulsive, and core-polarization contributions to the energy. The third of these has been treated in some detail in the text, the second is rather trivial, and so our main concern here will be with the first stage.

As mentioned in the text, the algorithms used to calculate the two- and three-center one-electron integrals are those of Harris and Michels (HM) (Ref. 14). Their great advantage over the use of explicit formulae lies in their generality; arbitrary values for the STO quantum numbers can be handled by allowing the computer to perform the algebraic manipulations necessary for a particular case. We will give a brief outline of these methods here, and will include certain details omitted by HM in their review.

Two-center Integrals

For the specialized three-body, two-orbital-center geometry of the problem, the general Euler rotational transformations for STO's considered by HM are not needed, since orbitals with the appropriate $\sigma, \pi, \delta, \dots$, symmetry can be selected beforehand. The general real STO is written as

$$|a\rangle = N_{n_a l_a m_a} r_a^{n_a - 1} \exp(-\delta_a r_a) P_{l_a}^{m_a} (\cos \theta_a) \cos m_a \phi_a, \quad (A1)$$

where, for in-plane orbitals, $m_a > 0$, and the normalization constant is given by

$$N_{nm} = \left[\frac{(2\delta)^{2n+1}}{(2n)!} \frac{(l+m)!}{(l-m)!} \frac{(2l+1)}{2\pi(1+\delta_{mo})} \right]^{\frac{1}{2}}. \quad (A2)$$

For convenience, we will omit the normalization in what follows. We write the general two-center integral as $\langle a|\Theta|b\rangle$, where Θ can be unity (overlap integral), $1/r_a$ or $1/r_b$ (nuclear attraction integrals) and the orbitals may or may not be on the same center. We will assume that the spherical coordinate (s.c.) systems of $|a\rangle$ and $|b\rangle$ each have the vector $R = \vec{b} - \vec{a}$ (\vec{a} and \vec{b} the position vectors of the nuclei) as the common polar axis, and that they are "in phase", i.e., their $\phi = 0$ half-planes coincide. The natural coordinates to use for a two-center problem are the confocal elliptic coordinates (e.c.) ξ, η, ϕ ; for a given fixed distance between the centers (R), the transformation equations for s.c. \rightarrow e.c. are

$$r_a = \frac{R}{2}(\xi + \eta)$$

$$r_b = \frac{R}{2}(\xi - \eta)$$

$$r_a \sin\theta_a = r_b \sin\theta_b = \frac{R}{2} \sqrt{(\xi^2 - 1)(1 - \eta^2)} \quad (A3)$$

$$r_a \cos\theta_a = \frac{R}{2}(\xi\eta + 1)$$

$$r_b \cos\theta_b = \frac{R}{2}(\xi\eta - 1)$$

$$\phi_a = \phi_b = \phi.$$

The last four of Eqs. (A3) result from our orientational assumptions about the s.c. systems. We now wish to write $\langle a|\Theta|b\rangle$ in terms of

e.c. The explicit expression for the Legendre function is

$$P_l^m(x) = (1-x^2)^{m/2} \sum_{k=0}^{\lfloor \frac{l-m}{2} \rfloor} a_k x^{l-m-2k}; \quad (A4)$$

$$a_k = \frac{m!(-1)^{m+k}}{2^k} \binom{l}{k} \binom{2l-2k}{l} \binom{l-2k}{l-2k-m}$$

where $\lfloor x \rfloor$ is the largest integer contained in x , and the curved brackets denote binomial coefficients. Since the volume element in e.c. is $d\tau = \frac{R}{2} r_a r_b d\xi d\eta d\phi$, the integrand can be written as

$$\begin{aligned} f &= \frac{R}{2} r_a^{n_a} r_b^{n_b} \exp[-\delta_a r_a - \delta_b r_b] P_l^m(\cos \theta_a) P_l^m(\cos \theta_b) \cos m_a \phi \cos m_b \phi \mathcal{O} \\ &= \frac{R}{2} r_a^{n_a-l_a} r_b^{n_b-l_b} \exp[-\delta_a r_a - \delta_b r_b] (r_a \sin \theta_a)^{l_a} (r_b \sin \theta_b)^{l_b} \\ &\quad \times \left[\sum_{k_a} \sum_{k_b} a_{k_a} a_{k_b} r_a^{2k_a} r_b^{2k_b} (r_a \cos \theta_a)^{l_a-m_a-2k_a} (r_b \cos \theta_b)^{l_b-m_b-2k_b} \right] \\ &\quad \times \cos m_a \phi \cos m_b \phi \mathcal{O} \\ &= \frac{R}{2} r_a^{n_a+n_b+1} \exp[-\delta \xi - \zeta \eta] [(\xi^2-1)(1-\eta^2)]^{\frac{m_a+m_b}{2}} \left[\sum_{k_a} \sum_{k_b} a_{k_a} a_{k_b} (\xi+\eta)^{n_a-l_a+2k_a} \right. \\ &\quad \left. \times (\xi-\eta)^{n_b-l_b+2k_b} (\xi\eta+1)^{l_a-m_a-2k_a} (\xi\eta-1)^{l_b-m_b-2k_b} \right] \cos m_a \phi \cos m_b \phi \mathcal{O}, \quad (A5) \end{aligned}$$

where $\delta = \frac{R}{2}(\delta_a + \delta_b)$ and $\zeta = \frac{R}{2}(\delta_a - \delta_b)$. The only effect of \mathcal{O} is possibly to reduce n_a or n_b by one, so that the above expression is still completely general (n_a, n_b are ≥ 1 by definition) with \mathcal{O} omitted. We can trivially carry out the integration $\int_0^{2\pi} d\phi$, and find that this gives

a factor $\pi(1 + \delta_{mo})\delta_{m_a m_b}$, where $m = m_a = m_b$ for a non-zero integral.

Using the binomial expansion

$$(x \pm y)^n = \sum_{i=0}^n (\pm 1)^i \binom{n}{i} x^{n-i} y^i, \quad (A6)$$

we can write the integrand as

$$f' = \int_0^{2\pi} f d\phi = \pi(1 + \delta_{mo}) \left(\frac{R}{2}\right)^{n_a + n_b + 1} \sum_{p=0}^N \sum_{q=0}^N C_{pq} \xi^p \eta^q \exp[-\delta\xi - \zeta\eta], \quad (A7)$$

where $N = n_a + n_b$ and the C_{pq} can be generated, for a and b distinct center, from

$$\begin{aligned} C_{n_a + n_b} &= (2i_1 + i_3 + i_4 + i_5 + i_6), \quad \ell_a + \ell_b = 2(m + k_a + k_b) + 2i_2 + i_3 + i_4 - (i_5 + i_6) \\ &(-1)^{i_1 + i_2 + i_4 + i_6} \frac{\ell_a \ell_b}{k_a k_b} \binom{m}{i_1} \binom{m}{i_2} \binom{n_a - \ell_a + 2k_a}{i_3} \binom{n_b - \ell_b + 2k_b}{i_4} \binom{\ell_a - m - 2k_a}{i_5} \\ &\times \binom{\ell_b - m - 2k_b}{i_6} \end{aligned} \quad (A8)$$

and

$$C_{pq} = \sum_{k_a} \sum_{k_b} \sum_{i_1} \dots \sum_{i_6} c_{pq}. \quad (A9)$$

If a and b are the same center, obvious modifications of (A8) suffice to give the C_{pq} matrix in this case also. We note that for a single orbital center $\ell_a = \ell_b$ must obtain for a non-vanishing integral. The integral of Eq. (A7) over ξ and η thus is broken down into a sum of products of one-dimensional integrals; we have

$$\langle a | \mathcal{O} | b \rangle = \pi(1 + \delta_{mo}) \left(\frac{R}{2}\right)^{n_a + n_b + 1} \sum_p \sum_q C_{pq} A_p(\delta) B_q(\zeta), \quad (A10)$$

where

$$A_p(\delta) \equiv \int_1^{\infty} d\xi \xi^p e^{-\delta\xi},$$

$$B_q(\zeta) \equiv \int_{-1}^1 dn n^q e^{-\zeta n};$$
(A11)

these subintegrals are conveniently evaluated by recursion as described by HM.

For our problem, in the case where $\mathcal{C} \leq V(M^+)$ the result (A10) must be corrected for the "core contribution", since $V(M^+)$ vanishes inside the M^+ ionic radius σ . Because there are only three such integrals ($V(M^+)_{11}$, $V(M^+)_{12}$, $V(M^+)_{13}$), we chose to treat them separately rather than attempting to find a general expression for an arbitrary pair of STO's. As mentioned in the text, these core integrals are easily done in closed form; thus a good comparison can be made with the RC approximation to the core correction, as described below. We will work out in detail $V(M^+)_{11}^{\text{core}}$ since it is the easiest ($|1\rangle \equiv |1s_H\rangle$) and the differences between it and the RC approximation are most readily seen.

In s.c. we have

$$V(M^+)_{11}^{\text{core}} = \int_0^{\sigma} dr_M r_M^2 \int_0^{\pi} d\theta_M \sin\theta_M \int_0^{2\pi} d\phi_M \frac{1}{r_M} e^{-2r_H}. \quad (\text{A12})$$

By the law of cosines, $r_H = (R^2 + r_M^2 - 2Rr_M \cos\theta_M)^{1/2}$, where R is the M-H internuclear distance. The ϕ_M integration gives a factor of 2π , and, noting that

$$\sin \theta_M d\theta_M = \frac{r_H}{R r_M} dr_H,$$

the θ_M integral becomes

$$\frac{1}{R r_M} \int_{R-r_M}^{R+r_M} dr_H r_H e^{-2r_H}.$$

This is easily evaluated, and we then have

$$V(M^+)_{11}^{\text{core}} = \pi \frac{e^{-2R}}{R} [(1+2R) \int_0^\sigma \sinh(2r) dr - \int_0^\sigma 2r \cosh(2r) dr]$$

(the M subscripts have been dropped for convenience). The radial integrals are readily done, and we finally obtain

$$V(M^+)_{11}^{\text{core}} = \pi \frac{e^{-2R}}{R} \{(1+R)[\cosh(2\sigma)-1] - \sigma \sinh(2\sigma)\}. \quad (\text{A13})$$

In the RC approximation, we take

$$|1\rangle \approx (|1\rangle)_M + \left(\frac{\partial |1\rangle}{\partial z}\right)_M z \quad (\text{A14})$$

which results in

$$|1\rangle \approx e^{-R}(1+z). \quad (\text{A14a})$$

When the square of (A14a) is substituted into (A13), terms through order z being retained, and the integrations performed, one obtains

$$V(M^+)_{11}^{\text{core}} \approx 2\pi\sigma^2 e^{-2R}. \quad (\text{A15})$$

In order to compare this result with (A13), we note that the approximation (A14) will be good for $R \gg \sigma$; so we first let R become very large, whereupon (A13) becomes

$$V(M^+)_{11}^{\text{core}} \xrightarrow[R \rightarrow \infty]{ } \pi e^{-2R} [\cosh(2\sigma) - 1]. \quad (\text{A16})$$

If we expand the hyperbolic cosine, we find

$$V(M^+)_{11}^{\text{core}} \approx 2\pi e^{-2R} [\sigma^2 + \frac{1}{3}\sigma^4 + \frac{4}{15}\sigma^6 + \dots], \quad (\text{A16a})$$

to which (A15) is still an approximation, good only for $\sigma \ll 1$, which is not the case physically (see Table III of the text). Retention of more terms in (A14) would, of course, improve the result, but at the expense of more labor than the exact form (A13) requires. Fig. I of the text shows a comparison of these two formulae applied to the correction of $V(M^+)_{11}$; the approximate form fails at small R as expected.

$V(M^+)_{11}$ is expected to be the worst case for the RC method, since the presence of the M valence function, which vanishes at the origin, will lessen the error incurred in using (A14). Nonetheless, $V(M^+)_{12}^{\text{core}}$ and $V(M^+)_{13}^{\text{core}}$ were also done exactly, with the results

$$V(M^+)_{12}^{\text{core}} = 4\pi \frac{e^{-R}}{R} [(1+R)S_{n-1}(\sigma, \delta) - C_n(\sigma, \delta)], \quad (\text{A17})$$

$$\begin{aligned} V(M^+)_{13}^{\text{core}} &= 4\pi \frac{e^{-R}}{R^2} [(3+3R+2R^2+R^3)S_{n-2}(\sigma, \delta) \\ &\quad - (3+3R+2R^2)C_{n-1}(\sigma, \delta) + 2(1+R)S_n(\sigma, \delta) - C_{n+1}(\sigma, \delta)], \end{aligned} \quad (\text{A18})$$

where n is the principal M STO quantum number (assumed ≥ 2), δ is the orbital exponent, and

$$\begin{Bmatrix} S_j(\sigma, \delta) \\ C_j(\sigma, \delta) \end{Bmatrix} = \int_0^\sigma dx x^j e^{-\delta x} \begin{Bmatrix} \sinh x \\ \cosh x \end{Bmatrix}. \quad (\text{A19})$$

S_j and C_j are most easily evaluated using the coupled recursion formulae.

$$(1-\delta^2)S_j = \sigma^j [(1-\delta^2)S_0 + 1] - j[\delta S_{j-1} + C_{j-1}], \quad (A20)$$

$$(1-\delta^2)C_j = \sigma^j [(1-\delta^2)C_0 + \delta] - j[\delta C_{j-1} + S_{j-1}],$$

($j > 1$), with

$$S_0 = (1-\delta^2)^{-1} [e^{-\delta\sigma} (\delta \sinh\sigma + \cosh\sigma) - 1], \quad (A21)$$

$$C_0 = (1-\delta^2)^{-1} [e^{-\delta\sigma} (\delta \cosh\sigma + \sinh\sigma) - \delta].$$

Three-center Integrals

We now turn to the consideration of those integrals in which the repulsion of the X^- ion is averaged over STO's on the M and H orbital centers. These integrals are formally equivalent to the three-center nuclear attraction integrals treated in IM. We again use e.c. with the orbital centers as foci, and employ the Neumann expansion

$$\frac{1}{r_{12}} = \frac{2}{R} \sum_{l=0}^{\infty} \sum_{m=-l}^l (-1)^m (2l+1) \left[\frac{(l-|m|)!}{(l+|m|)!} \right]^2 P_l^m(\xi_2) Q_l^m(\xi_1) P_l^m(n_1) P_l^m(n_2) \\ \times e^{im(\phi_2 - \phi_1)}, \quad (A22)$$

where (ξ_1, n_1, ϕ_1) and (ξ_2, n_2, ϕ_2) are the coordinates of the (1,2) vectors in the e.c. system, and $\xi_{>}(<)$ is the greater (lesser) of ξ_1 and ξ_2 , to express the distance of the electron from the X^- center in terms of e.c. Here also we can take advantage of the three-body geometry to simplify the algebra. The integral we wish to evaluate is $\langle a | r_{X^-}^{-1} | b \rangle$; if we take the X^- ion, whose e.c. we denote by (Ξ, H, Φ) , to be in the $\phi = 0$ half-plane of the STO's, then we have $\Phi = 0$. The manipulation procedure used to break down the integral is very similar to that in the two-center case, being complicated by the introduction of the Neumann series for $r_{X^-}^{-1}$. The expression for the integrand is

$$f = \left(\frac{R}{2}\right)^{n_a+n_b} \sum_{l=0}^{\infty} \sum_{m=-l}^l (-1)^m (2l+1) \left[\frac{(l-|m|)!}{(l+|m|)!} \right]^2 P_l^m(H) \exp[-\delta\xi - \zeta n]$$

$$\begin{aligned} & \times \left[(\xi^2 - 1)(1-n^2)^{\frac{n_a+n_b}{2}} \left[\sum_{k_a} \sum_{k_b} a_{k_a} a_{k_b} (\xi + n)^{n_a - l_a + 2k_a} (\xi - n)^{n_b - l_b + 2k_b} \right] \right. \\ & \times \left. (\xi n + 1)^{l_a - m_a - 2k_a} (\xi n - 1)^{l_b - m_b - 2k_b} \right] P_l^m(\xi_<) Q_l^m(\xi_>) P_l^m(n) e^{im\phi} \cos m_a \phi \cos m_b \phi, \end{aligned} \quad (A23)$$

where use has been made of Eqs. (A3) and (A4), and all symbols have already been defined. Again the ϕ integration is trivial, yielding a factor of

$$\frac{\pi}{2} (\delta_{m, m_a+m_b} + \delta_{m, -(m_a+m_b)} + \delta_{m, m_a-m_b} + \delta_{m, m_b-m_a}).$$

Since $(-1)^m = (-1)^{|m|}$ and the Legendre functions arising from the Neumann expansion depend only on $|m|$, we can confine our attention to $m \geq 0$, and the factor becomes

$$\pi (\delta_{m, m_a+m_b} + \delta_{m, |m_a-m_b|}),$$

implying that the integral's only contributing terms arise from $m = m_{\pm}$, where $m_{\pm} = |m_a \pm m_b|$. We note that if one or both of m_a, m_b are zero, both the δ -functions are satisfied, and the m summation of (A23) reduces to a single term. We can now write

$$\begin{aligned} f' & \equiv \int_0^{2\pi} f d\phi = \pi (1 + \delta_{m_<, 0}) \left(\frac{R}{2}\right)^{n_a+n_b} \sum_{m=m_{\pm}}^{\infty} \sum_{l=m}^{\infty} (-1)^m (2l+1) \left[\frac{(l-n)!}{(l+m)!} \right] \\ & \times P_l^m(H) \sum_{p=0}^{N_m} \sum_{q=0}^{N_m} C_{pq} \exp[-\delta\xi - \zeta n] \xi^p n^q [(\xi^2 - 1)(1-n^2)]^{\frac{m}{2}} P_l^m(n) P_l^m(\xi_<) Q_l^m(\xi_>), \end{aligned} \quad (A24)$$

where $m_- = \min(m_a, m_b)$, $N_m = n_a + n_b - m_+ + 2m_{\delta, m, m_-}$, and the C_{pq}^m are obtained from equations very similar to (A8) and (A9). Although $[(\xi^2 - 1)(1 - \eta^2)]^{m_+/2}$ appears in (A23), it is still possible to write the power as $m/2$ in (A24) because either $m_+ = m_-$ or they differ by an even integer; in the latter case we can write $m_+/2 \equiv (m_+ - m_-)/2 + m_-/2$ and absorb the integral powers into the C_{pq}^m . Upon integrating (A24) over ξ and η we finally obtain

$$\langle a | r^{-1} | b \rangle = \pi(1 + \delta_{m_-, 0}) \left(\frac{R}{2}\right)^{n_a + n_b} \sum_{m=m_{\pm}} (-1)^m \sum_{l=m}^{\infty} (2 + l) P_l^m(H) \sum_p \sum_q C_{pq}^m I_{lq}^m(\xi) \\ \times [Q_l^m(\Xi) K_{lp}^m(\Xi, \delta) + P_l^m(\Xi) L_{lp}^m(\Xi, \delta)], \quad (A25)$$

where

$$I_{lq}^m(\xi) = \frac{(l-m)!}{(l+m)!} \int_{-1}^1 d\eta e^{-\xi \eta} \eta^q (1-\eta^2)^{\frac{m}{2}} P_l^m(\eta), \\ K_{lp}^m(\Xi, \delta) = \frac{(l-m)!}{(l+m)!} \int_1^{\Xi} d\xi e^{-\delta \xi} \xi^p (\xi^2 - 1)^{\frac{m}{2}} P_l^m(\xi), \\ L_{lp}^m(\Xi, \delta) = \frac{(l-m)!}{(l+m)!} \int_{\Xi}^{\infty} d\xi e^{-\delta \xi} \xi^p (\xi^2 - 1)^{\frac{m}{2}} Q_l^m(\xi). \quad (A26)$$

In practice, the l summation can be truncated fairly early, since the series is usually rapidly convergent.

The $P_l^m(H)$ and $P_l^m(\Xi)$ were evaluated using standard recursion relations given in HM; the $Q_l^m(\Xi)$ were obtained from downward recursion in a manner analogous to that used by HM for \tilde{Q}_l^m , a modified Legendre function defined by HM. The procedure described by HM for getting the $I_{lq}^m(\xi)$ recursively proved satisfactory. Instead of using two methods for evaluating the $K_{lp}^m(\Xi, \delta)$ depending on the value of $(\Xi - 1)\delta$,

double precision recursion for all values of the parameters was used, with good results. For the $L_{ip}^m(\Xi, \delta)$, instead of using the numerical integration for a certain set of the L's as recommended by HM, a recursion formula similar to Eq. (184) of HM was developed and used in double precision successfully. (It should be noted that the statement in HM, p. 260, referring to the Lobatto quadrature applied to the L's apparently does not hold in general; Gauss-Laguerre quadrature was found to be much more accurate.) The L recursion usually began to fail at $k > 6$, but at that point these subintegrals were no longer contributing significantly to the overall result, a conclusion reached from study of many orbital combinations and nuclear configurations. The use of recursion rather than numerical integration for the L's resulted in an increased computation efficiency by a factor of ~ 2.5 over that quoted by HM. (See below.) Finally, in order to use the recursion relation (192) of HM successfully, one must take into account the special case

$$L_{m,p}^m(\Xi, \delta) = L_{m+1,p-1}^m(\Xi, \delta) + \frac{(-1)^m}{(2m+1)!!} C_{p-1}(\Xi, \delta), \quad (A27)$$

where $n!!$ denotes $n(n-2)(n-4)\dots 2$ or 1, and

$$C_k(\Xi, \delta) = \int_{\Xi}^{\infty} d\xi \xi^k e^{-\delta\xi}. \quad (A28)$$

The C_k can also be generated recursively from

$$C_k(\Xi, \delta) = k\delta^{-1} C_{k-1}(\Xi, \delta) + \Xi^k C_0(\Xi, \delta) \quad (A29)$$

with $C_0(\Xi, \delta) = \delta^{-1} e^{-\delta\Xi}$. The $C_k(\Xi, \delta)$ are just a generalization of the $A_p(\delta)$ of Eq. (A11): $C_k(1, \delta) = A_k(\delta)$.

Numerical Examples and Computation Times

The procedures outlined above for the two- and three-center integrals were extensively tested for $n = 1, 2$, $l = 0, 1$, $m = 0, 1$ against numerical values produced by the programs of Pitzer²³ and Stevens.²⁴ For the two-center integrals, a minimum accuracy of 6 significant figures on the IBM 7094 computer and 5 on the 360/65 was found for single-precision calculations; similar results were obtained for the three-center case. Table IA gives some numerical comparisons.

The integrals were programmed so as to give maximum efficiency when working with a large number of nuclear configurations, so a comparison of computation times might be somewhat unreliable. HM quote a time of <100 msec on the 7094 for all two-center integrals arising from a single charge distribution; we have found times of 22 msec per individual integral for the 7094 and 6 msec for the 360/65. A more direct comparison can be made in the three-center case: HM claim 300 msec/integral, and we have found times of 120 msec on the 7094, 50 msec on the 360/65, due largely to the different evaluation method for the L integrals mentioned in the preceding section.

23. R. M. Pitzer, Ph.D. Thesis, Harvard University, Cambridge, Mass., 1963.

24. R. M. Stevens, J. Chem. Phys. (to be published).

Table IA. Numerical comparisons for two- and three-center one-electron integrals.^a

Orbital Centers		ϕ	Radii			Integral Values	
A n _m , δ	B n _m , δ		R _{AB}	R _{AC}	R _{BC}	P. or S.	This work
100, 1.000	200, 1.625	1	2.08250	-	-	0.56390	0.56390
200, 1.625	200, 1.625 ^b	r_B^{-1}	2.91588	-	-	0.34122	0.34121
200, 1.625	200, 1.625	r_B^{-1}	"	-	-	0.19585	0.19585
210, 1.625	200, 1.625	r_A^{-1}	"	-	-	0.18283	0.18283
210, 1.625	210, 1.625 ^b	r_B^{-1}	"	-	-	0.38330	0.38329
211, 1.625	211, 1.625	r_A^{-1}	"	-	-	0.094039	0.094039
200, 1.4223	200, 1.4223	r_C^{-1}	3.35430	2.26013	4.90459	0.097786*	0.097789
200, 1.4223	210, 1.4587	"	"	"	"	-0.11545*	-0.11545
210, 1.4587	200, 1.4223	"	"	"	"	0.85667*	0.85668
200, 1.4223	211, 1.4587	"	"	"	"	-0.011361*	-0.011361
210, 1.4587	210, 1.4587	"	"	"	"	-0.089593*	-0.089591
210, 1.4587	211, 1.4587	"	"	"	"	0.0071071*	0.0071063
211, 1.4587	211, 1.4587	"	"	"	"	0.051618*	0.051619

Orbital Centers

A n _m , δ	B n _m , δ	○	Radii	Integral Values			
			R _{AB}	R _{AC}	R _{BC}	P. or S.	This work
100, 5.7	200, 1.625	r _C ⁻¹	2.91588	2.08250	4.11295	0.014120	0.014120
210, 1.625	100, 5.7	"	"	"	"	0.012943	0.012943

^aAtomic units are used. In the column labeled "P. or S.", the values are ethane integrals from Ref. 23, except for entries marked with an asterisk, which are diborane integrals calculated by the program of Ref. 24, values kindly given to us by E. Switkes. In the column labeled "This work" the values were calculated on an IBM 360/65 in single precision (7.2 significant figures) using algorithms of Ref. 14.

^bOrbitals are on same center.

CHAPTER VII
IMPULSIVE MODEL FOR HYDROGEN ATOM REACTION DYNAMICS

Abstract

A dynamic model is presented for hydrogen atom reactions based on the assumption that the motion of H is approximately separable from that of the reactant diatomic, which is composed of heavy atoms. The model can take into account orientational preferences for reaction as well as possible repulsion between the products. Calculations using this model are compared with reactive scattering data for the H + MX reactions described in a previous chapter, with good agreement for a suitable choice of orientation. Correlations with an approximate potential energy surface for these reactions, also presented previously, are discussed.

A. Introduction

The Born-Oppenheimer approximation "is valid only because electrons are so much lighter than nuclei and move so much faster."¹ If we wish to make the same statement about the chemical reactions of hydrogen atoms with heavy-atom molecules, we must replace "electrons" with "H atoms", "nuclei" with "heavy atoms", and then remove the two "so"'s, because such an approximation cannot be as good for H atoms vs heavy atoms. In fact, because of the presence of inelastic "chemical" forces due to the structure within the atoms, we cannot even expect the translational energy of H to be conserved, but we nonetheless suspect that the mechanical effect on the heavy atoms of the H atom motion should be small. Any strong forces due to the initial chemical interaction should affect the H atom much more than the heavy diatomic reactant. On the other hand, if some of the available energy is released as the products depart, the relative radial motion of HB and C from the reaction $H + BC \rightarrow HB + C$ will receive a boost, while the angular or transverse motion should hardly be affected, since the small mass of H puts the center-of-mass of HB very near to the B nucleus.

How much of the chemical and collisional energy goes into HX vibration and how much into product translation will depend intimately on the form of the potential surface governing the reaction.

1. J. C. Slater, "Quantum Theory of Molecules and Solids", Vol. I, electronic structure of molecules (McGraw-Hill, New York, 1963), p. 11.

Because of the light mass of H and the disparity of time scales for motion mentioned in Chapter V. in discussing the $H + MX \rightarrow HX + M$ reactions, in addition to the above considerations, we can still postulate that the angular motion of H is approximately separable from that of the heavy atoms, so that a "Spectator Model" type of result still holds, i.e., that

$$k = k', \lambda = \lambda'.$$

Although the Spectator energy condition cannot hold in general if we allow for product repulsion, it appears that a fairly consistent interpretation can be given to the experimental results of Chapter V if we postulate just such a condition:

$$E' = W, W' = E + \Delta D_0.$$

It should be emphasized, as was made clear in Chapter V, that these angular momentum and energy postulates are Spectator predictions only in the limit that either the reactant or product atom is very light compared to the others.

The experimental data of Chapter V and the potential surface calculations of Chapter VI both seem to indicate that, in the light of the time-scale and angular momentum arguments of Chapter V, molecular orientation effects have a prominent role in producing the observed anisotropies in the angular distributions of products from the $H + MX$ reactions, MX an alkali halide. Since those arguments are based on mechanical considerations common to any H atom-heavy molecule reaction, we might expect that in general orientational preferences for reaction latent in the form of the potential surface should be

manifested by anisotropies in the observed reactive scattering. Such anisotropies have recently been found in studies on the D + XY reactions, X and Y halogens.² In addition, trajectory calculations on D + H₂³ show orientation effects, even though the diatomic, H₂, is not so heavy.

It is thus highly desirable to formulate a quantitative and predictive model which embodies the possibility of product repulsion, the postulated angular momentum uncoupling, and an allowance for orientational effects, so that comparisons can be made with experimental data which allow inferences as to the nature of the potential surface for reaction.

Two other models have previously been introduced as general interpretations of impulsive reaction dynamics, an elastic hard sphere model⁴ based on a simplified application of the Optical Model, and the Direct Interaction with Product Repulsion (DIPR) model.⁵ The present impulsive model contains specialized mechanical assumptions which make it difficult to compare with these, except to note that the shapes of the angular distributions predicted by our model arise

-
2. J. D. McDonald, P. R. LeBreton, Y. T. Lee and D. R. Herschbach, J. Chem. Phys. (to be published).
 3. M. Karplus, R. N. Porter and R. D. Sharma, J. Chem. Phys. 40, 2033 (1964).
 4. D. R. Herschbach, Advan. Chem. Phys. 10, 319 (1966).
 5. P. J. Kuntz, M. H. Mok, E. M. Nemeth and J. C. Polanyi, J. Chem. Phys. 50, 4623 (1969).

from rather different kinematic assumptions than those underlying the other models.

A Spectator model for collinear collisions only which employs the same angular momentum assumptions has been introduced as a dynamical interpretation of the reactive scattering in the $H + M_2$ reactions.⁶ We will later derive this Spectator model as a special case of the present development.

B. Kinematic Formulation

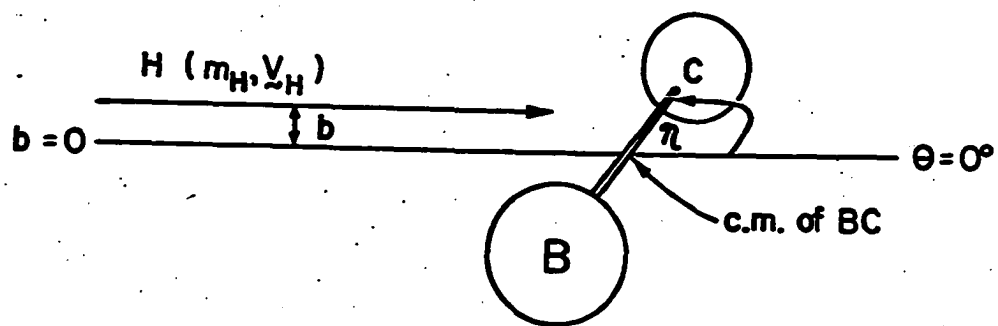
We define the orientation angle η of the B-C axis, directed from B to C, with respect to the direction of the initial relative c.m. velocity V , defined to be the initial c.m. direction of approach of the H atom, as shown in Fig. 1(a). For purposes of the model, we will assume that the maximum initial impact parameter b_{\max} which can lead to reaction is smaller than the geometrical "size" of the heavy diatomic, roughly represented by its equilibrium internuclear distance R_e , so that dynamic effects associated with reaction at larger b 's are ignored, and the orientation angle η takes on a clearer meaning. (This assumption will definitely be inadequate if there is a strong long-range attraction, but because the polarizability of H is small, it seems to be reasonable.) For simplicity we consider only one unique angle η , intending later to average over the allowed range in η . Initially we will develop the theory in the internal (int) c.m. system of the diatomic; subsequently the transformations to the c.m.

6. Y. T. Lee, R. J. Gordon and D. R. Herschbach, J. Chem. Phys. (to be published).

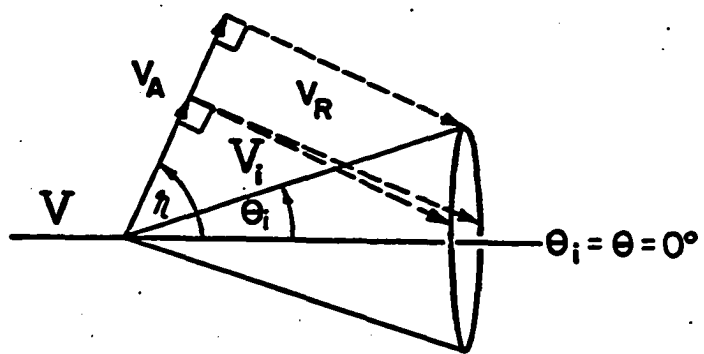
**Fig. 1. (a) Schematic physical picture invoked by the H atom model;
 η is the orientation angle. (b) Geometry involved in relating
component velocities.**



(a)



(b)



and LAB systems will be described.

The number density probability for forming a given final relative int velocity v_i with int scattering angle θ_i defined with respect to χ is the result of compounding the distributions in internal motion of BC, which we write symbolically as

$$P(v_i, \theta_i) = C [P_V(v_V) \cdot P_R(v_R) \cdot P_I(v_I)] \quad (1)$$

where C is an integral operator which accomplishes the composition, and the operands are the distributions in the vibrational, rotational and impulsive components of the internal motion, respectively.

Miller⁷ has treated the distribution-composition problem in some detail. Essentially, the operator C must integrate over all possible combinations of the velocity components consistent with the constraints imposed by the transformations relating them to the resultant v_i . Vectorially, we have

$$v_i = v_I + v_V + v_R \quad (2)$$

The impulsive component has by choice been limited to occur along the B-C axis; since the vibrational velocity is also radial, these vectors may be added algebraically. The rotational contribution, on the other hand, is perpendicular to the molecular axis, so we have

$$(v_i)^2 = (v_I + v_V)^2 + v_R^2 \quad (2a)$$

for the magnitudes. But, as Fig. 1(b) shows, different combinations of $v_A \equiv v_I + v_V$ and v_R can give rise to the same set (v_i, θ_i) , since

7. W. B. Miller, Ph.D. Thesis, Harvard University, Cambridge, Mass., 1969.

this set defines the edge of a cone with half-angle θ_i . Thus there is no unique relation corresponding to (2a) for the angular dependence, but there are limits on the magnitudes of v_A and v_R which can contribute which are expressible in terms of θ_i and η . We arbitrarily choose to define these limits through the upper and lower bounds for the axial velocity v_A as follows:

$$\text{for } \beta < \pi/2, v_< = \begin{cases} 0 & , \theta_i + \eta \geq \pi/2 \\ v_i |\cos(\theta_i + \eta)|, & " < " \end{cases}$$

$$v_> = \begin{cases} 0 & , \theta_i - \eta \geq \pi/2 \\ v_i |\cos(\theta_i - \eta)|, & " < " \end{cases}; \quad (3)$$

$$\text{for } \beta > \pi/2, v_< = \begin{cases} 0 & , \theta_i + \eta \geq 3\pi/2 \\ v_i |\cos(\theta_i + \eta)|, & " < " \end{cases}$$

$$v_> = \begin{cases} 0 & , \eta - \theta_i \geq \pi/2 \\ v_i |\cos(\eta - \theta_i)|, & " < " \end{cases}$$

where $v_{<}(>)$ is the lower (upper) limit on v_A .

Having now more precisely defined the geometry we can consider the explicit form which \mathcal{C} must take in Eq. (1). Miller⁴ considers the case where unique relations between the variables exist; in an obvious generalization of his formulae, the principal result can be written as

$$P(x_1, x_2, \dots, x_n) = \int d\xi_1 \int d\xi_2 \dots \int d\xi_N P_1(\xi_1) P_2(\xi_2) \dots P_N(\xi_N) \\ \times \delta(x_1 - f_1(\xi_1 \dots \xi_N)) \delta(x_2 - f_2(\xi_1 \dots \xi_N)) \dots \delta(x_n - f_n(\xi_1 \dots \xi_N)), \quad (4)$$

where the integrals cover the defined domains of the P_j , $\delta(x)$ is the Dirac δ -function, the f_i are the constraints relating the x_i to the ξ_j , and N , the number of "basic" probability functions $P_j > n$, the number of independent variables x_i . We can identify C for this case as

$$C = \int d\xi_1 \dots \int d\xi_N \delta(x_1 - f_1(\xi_1 \dots \xi_N)) \dots \delta(x_n - f_n(\xi_1 \dots \xi_N)). \quad (5)$$

We now suggest an intuitive generalization of (5) for the case where explicit f_i 's do not exist, but the ξ_j can be limited to certain intervals which depend on the x_i . It consists in replacing the δ -functions in (5) by products of heaviside h -functions as

$$\delta(x_i - f_i(\xi)) \rightarrow h(x_i - f_i^<(\xi))h(f_i^>(\xi) - x_i), \quad (6)$$

where $f_i^{<}, f_i^{>}(\xi)$ express the delimiting relationships, and the h -functions are defined by

$$h(x) = \begin{cases} 1, & x \geq 0 \\ 0, & x < 0. \end{cases} \quad (7)$$

In the limit that $f_i^< \rightarrow f_i^>$, using $h(x)h(-x) = \delta(x)$, we see that Eq. (5) can be recovered.

For our problem, it is convenient to do the compounding in two independent steps. This is possible because the impulsive and vibrational velocities are axial, orthogonal to the rotational, and the composition of the first two component distributions can be considered separately. The axial probability is

$$\begin{aligned} P_A(v_A) &= \int dv_V \int dv_I P_V(v_V) P_I(v_I) \delta(v_A - (v_V + v_I)) \\ &= \int dv_V P_V(v_V) p_I(v_A - v_V). \end{aligned} \quad (8)$$

Eq. (1) can then be written, using Eqs. (5) and (6),

$$P(v_i, \theta_i) = \int dv_A \int dv_R P_A(v_A) P_R(v_R) \delta(v_i - \sqrt{v_A^2 + v_R^2}) h(v_A - v_<) h(v_> - v_A), \quad (9)$$

where the arguments of the h-functions have been written in a way clearly indicative of their effect on the integral, and the $v_{<,>}$ have been defined in Eqs. (3). Carrying out the integration over v_R ,

$$P(v_i, \theta_i) = v_i \int dv_A P_A(v_A) P_R(\sqrt{v_i^2 - v_A^2}) / \sqrt{v_i^2 - v_A^2} h(v_A - v_<) h(v_> - v_A). \quad (10)$$

The square root denominator arises because of the quadratic relationship (2a). The role of the h-functions clearly will be to set the integration limits, unless the P_A , P_R function domains narrow them or $v_< \rightarrow v_>$. Inspection of Eqs. (3) reveals that the latter will happen when $\eta \rightarrow 0, \pi$; in this event we obtain

$$\begin{aligned} P_{0,\pi}(v_i, \theta_i) &= v_i \int dv_A P_A(v_A) P_R(\sqrt{v_i^2 - v_A^2}) / \sqrt{v_i^2 - v_A^2} \delta(v_A - v_i \cos \theta_i) \\ &= v_i P_A(v_i \cos \theta_i) P_R(v_i \sin \theta_i). \end{aligned} \quad (11)$$

This result becomes identical to that found by Lee et al.⁶ if $P_I(v_I) \rightarrow \delta(0)$ and therefore $P_A \rightarrow P_V$. For $\eta \neq 0, \pi$, Eq. (10) is simply

$$P_\eta(v_i, \theta_i) = v_i \int_{v_<}^{v_>} dv P_A(v) P_R(\sqrt{v_i^2 - v^2}) / \sqrt{v_i^2 - v^2}. \quad (12)$$

where the "A" subscripts have been dropped for convenience. We note that all the angular dependence is contained in the limits $v_{<, >}$ through Eqs. (3). The spherical flux distribution in V_i , i.e., the differential reactive cross section in the int system is given by

$$I_{int}^{(n)}(v_i, \theta_i) dv_i d\omega_i = v_i P_n(v_i, \theta_i) dv_i d\theta_i$$

or

$$I_{int}^{(n)}(v_i, \theta_i) = \frac{v_i}{\sin \theta_i} P_n(v_i, \theta_i) \quad (13)$$

for a given orientation. The extra factor of v_i is needed because P is inherently a number density distribution.

In order to carry the analysis further, we must introduce explicit forms for the basic probability distributions. For simplicity we assume

$$P_I(v_I) = \delta(v_I - v_0), \quad (14)$$

since a priori there is no criterion for choosing a more complicated dependence on the impulse. Equation (8) then yields

$$P_A(v_A) = P_V(v_A - v_0). \quad (15)$$

The vibrational and rotational velocity distributions we choose in accord with those in Birely's treatment of the Spectator model.⁸ The vibrational function is obtained from the harmonic oscillator (H.O.) momentum-space eigenfunctions; we write it as

$$P_V(v_V) = (\sqrt{\pi} Q \alpha_V)^{-1} \sum_{n=0}^N f_n (2^n n!)^{-1} \exp[-(v_V/\alpha_V)^2] H_n^2(v_V/\alpha_V), \quad (16)$$

8. J. H. Birely, Ph.D. Thesis, Harvard University, Cambridge, Mass., (1966).

where

$$f_n = \exp[-nhv/kT],$$

$$Q = \sum_n f_n,$$

$$\alpha_v = \sqrt{hv/\mu_{BC}},$$

$H_n(x)$ is the n th order Hermite polynomial, and N is an upper limit to the sum determined either by the size of f_N or by the limited range of validity of the H.O. approximation. The rotational distribution is taken to be classical (a good approximation for a heavy-atom diatomic),

$$P_R(v_R) = 2\alpha_R^{-2} v_R \exp[-(v_R/\alpha_R)^2], \quad (17)$$

where $\alpha_R = \sqrt{2kT/\mu_{BC}}$. Using Eqs. (15), (16), and (17) in (12), we have

$$P_n(v_i, \theta_i) = 2(\sqrt{\pi} Q \alpha_R^2 \alpha_v)^{-1} v_i \sum_{n=0}^N f_n (2^n n!)^{-1} \\ \times \int_{v_i}^{v_o} dv \exp[(v^2 - v_i^2)/\alpha_R^2 - (v - v_o)^2/\alpha_v^2] H_n^2 \left(\frac{v - v_o}{\alpha_v} \right), \quad (18)$$

where the sum and integral have been interchanged. Defining $\delta \equiv 1 - (\alpha_v/\alpha_R)^2$, $\delta \geq 0$ for the results to follow to be valid, Eq. (18) can be written, after some algebra,

$$P_n(v_i, \theta_i) = 2(\sqrt{\pi} Q \alpha_R^2)^{-1} v_i \exp[(\delta^{-1} v_o^2 - v_i^2)/\alpha_R^2] \\ \times \sum_{n=0}^N f_n (2^n n!)^{-1} \int_{\xi_o}^{\xi_o} d\xi H_n^2(\xi + \xi_o) \exp(-\delta \xi^2), \quad (19)$$

where we have substituted $\xi = (v - \delta^{-1} v_o)/\alpha_v$, $\xi_o = (\delta^{-1} - 1)v_o/\alpha_v$,

and $\xi_{\delta} = (v_{<,\delta} - \delta^{-1} v_0)/\alpha_V$. The integrals in (19) are easily evaluated in closed form, since the square of the Hermite polynomial is just

$$H_n^2(x) = \sum_{j=0}^n a_{nj} x^{2j}, \quad (20)$$

and defining

$$K_l(\delta, \xi_0, \xi_<, \xi_>) = \int_{\xi_<}^{\xi_>} d\xi (\xi + \xi_0)^l \exp(-\delta \xi^2), \quad (21)$$

we have upon integration by parts and rearrangement,

$$\begin{aligned} K_{l+2} &= \xi_0 K_{l+1} + (2\delta)^{-1} \\ &\times [(l+1)K_l - (\xi_> + \xi_0)^{l+1} e^{-\delta \xi_>} + (\xi_< + \xi_0)^{l+1} e^{-\delta \xi_<}] \end{aligned} \quad (22)$$

with

$$\begin{aligned} K_0 &= \sqrt{\pi}(2\delta)^{-1} [\operatorname{erf}(\sqrt{\delta}\xi_>) - \operatorname{erf}(\sqrt{\delta}\xi_<)], \\ K_1 &= \xi_0 K_0 + (2\delta)^{-1} [e^{-\delta \xi_<} - e^{-\delta \xi_>}]. \end{aligned} \quad (23)$$

Thus the desired result may finally be written as

$$\begin{aligned} P_n(v_i, \theta_i) &= 2(\sqrt{\pi} Q \alpha_R^2)^{-1} v_i \exp[(\delta^{-1} v_0^2 - v_i^2)/\alpha_R^2] \\ &\times \sum_{n=0}^N f_n (2^n n!)^{-1} \sum_{j=0}^n a_{nj} K_{2n}(\delta, \xi_0, \xi_<, \xi_>). \end{aligned} \quad (24)$$

Use of the relation (13) then enables us to calculate the scattered intensity at a given v_i for orientation n and impulse velocity v_0 . If we consider only those molecules in the ground vibrational state, (24) takes the simple form

$$P_n(v_i, \theta_i) = (\delta \alpha_R^2)^{-1} v_i \exp[(\delta^{-1} v_0^2 - v_i^2)/\alpha_R^2] [\operatorname{erf}(\sqrt{\delta}\xi_>) - \operatorname{erf}(\sqrt{\delta}\xi_<)]. \quad (24a)$$

We can now use the technique of Entemann⁹ to transform and velocity-average the result (24) into the LAB and c.m. systems.

Before we do so, however, we must consider the initial relative kinetic and chemical energy dependence of our derived cross section. The impulse velocity v_o certainly must depend on the energy available; it cannot exceed the value

$$v_o^{(\max)} = [2(E + \Delta D_o)/\mu']^{1/2}, \quad (25)$$

where E is the initial kinetic energy, ΔD_o the reaction exoergicity and μ' the reduced mass of the products. v_o may also be coupled to n , so for generality we allow $v_o = \sqrt{f(n)} v_o^{(\max)}$ where $f(n)$ is the fraction of the available energy going into radial translation and is < 1 . In the event that $E + \Delta D_o < 0$ (endoergic reaction) $v_o \equiv 0$ and the diatomic is required to possess vibrational velocity greater than

$$v_v^{(\min)} = [-2(E + \Delta D_o)/\mu']^{1/2} \quad (26)$$

in order for reaction to occur.

The velocity-space transformations are a matter of elementary kinematics. From an intensity distribution of a certain type of particle as a function of its vector velocity v_a measured in a certain coordinate system "a", we can derive the intensity spectrum in any other system "b" moving with velocity v with respect to "a" from⁹

$$I_b(v_b) = \frac{v_b^2}{v_a^2} I_a(v_a) \quad (27)$$

9. E. A. Entemann, Ph.D. Thesis, Harvard University, Cambridge, Mass., 1967; see also Chapter III, this thesis.

where we transform the velocity-space coordinates via

$$x_b = x_a - \eta. \quad (28)$$

If we wish to include the effect of a distribution in η which makes (28) non-unique, the Entemann method may be used to velocity-average the right-hand side of (27). A computer program based on Eq. (24) with the energy restrictions noted above and on a modification of Entemann's program⁹ was written to perform calculations to test the validity of the model presented here by comparing it with actual data for various ranges of η . A description of this program is contained in an appendix. The allowed range of η was averaged over using

$$I_{int}(v_i, \theta_i) = \int dn w(n) I_{int}^{(n)}(v_i, \theta_i), \quad (29)$$

where $w(n)$ was taken as a Gaussian of variable width.

C. Comparison with Experimental Data on H + MX

The impulsive H atom model was formulated with a view toward correlating the experimental data on the H + MX reactions described in Chapter V. These results showed not only pronounced anisotropy in the c.m. angular distributions, but also a definite trend in peak position from nearly sideways ($\theta \sim 90^\circ$) to backwards ($\theta \sim 180^\circ$) as the halogen was varied from F → Cl → Br. The kinematic analysis also indicated that the energy in product translation is roughly comparable to the initial internal excitation in MX. For the model analysis this implied that at most small values of the energy fraction $f(\eta)$ would be needed. First the best fit for each system was found for a unique angle η and $f(\eta) = 0$; for the CsX systems these fits were quite

adequate, but not as good for the KX reactions, as shown by the dashed lines in Fig. 2. But by the addition of a small impulse ($f \sim 0.05$ - 0.10) the KX systems were also fit adequately, also as shown in Fig. 2. In general the fits were quite sensitive to the choice of n . Also shown for H + KBr are the results of averaging over a range of n for the full width at half maximum of the Gaussian $w(n)$ of 40° and 90° . The 90° curve is definitely too broad, indicating that, within the limits of the model and the data, only a fairly narrow range of n is accessible to reaction. Figure 2 demonstrates that the model as formulated is consistent with the LAB distributions observed. Figure 3 presents integrated c.m. angular distributions, which also compare well with those derived from the kinematic analysis of Chapter V (see Fig. 14, Chapter V). The angular and recoil dependences of these c.m. functions, however, are not "separable" as was assumed for the kinematic analysis. The model predicts only a small kinematic isotope effect, in accord with the data, so results for the H reactions only have been presented.

D. Discussion

For reactions involving a heteronuclear diatomic reactant (such as MX) there are certain orientations which are physically inaccessible to reaction due to the finite "size" of the nonreactive atom (M), if one accepts the nonadiabatic assumption of the model. For H + MX, the optimum orientation angles found by comparison with the data are all outside the excluded range, which is, as we have defined it, $n \approx 180^\circ$. Since the data show little displacement toward the

Fig. 2. Smoothed representations of M atom laboratory angular distributions for the reactions of H with five salts (—) compared with model calculations as indicated. The dotted portions of the experimental curves denote regions where data was not taken due to nearness of the MX beam.

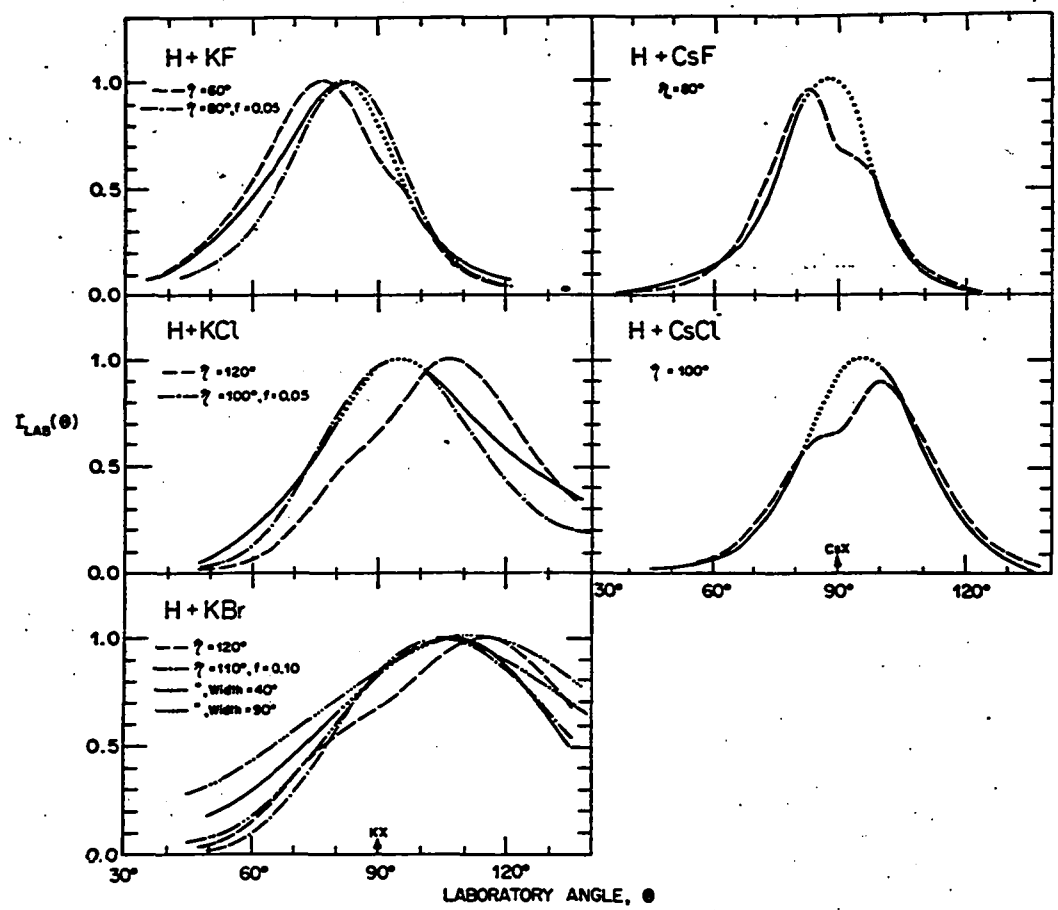
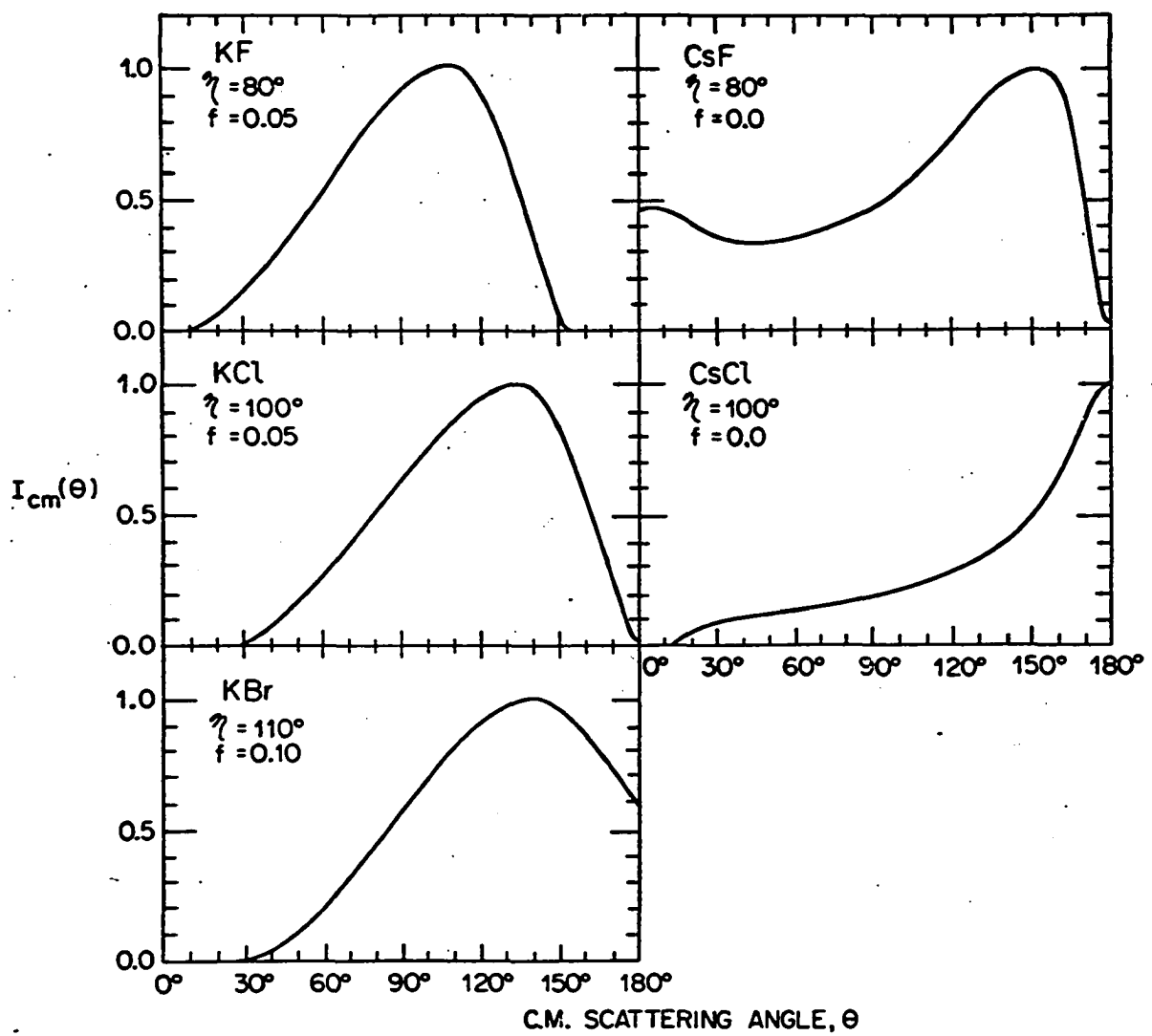


**Fig. 3. Integrated c.m. angular distributions corresponding to
(- -) of Fig. 2 for Cs and (- -) for K.**



small LAB angle side of the most probable c.m. vector, which fact indicates very little "rebound" character, we can also conclude that $\eta \sim 0^\circ$ is not very likely. This does not mean that no reaction can occur if $\eta \sim 0^\circ$, but only that, due to the geometrical $\sin\eta$ weighting, $\eta \sim 0^\circ$ has been weighted down compared to other "allowed" orientations. Hence, using very crude observations we can narrow the effective range of η considerably.

If one has a reliable potential surface for a reaction, it may be examined to see if any orientational effect is possible. The one-electron potential surfaces presented in Chapter VI for H + MX cannot be expected to be quantitative, but comparison with more rigorous many-electron treatments for H + LiF suggests that it may be used to give qualitative estimates of the kind needed here. The barriers found in the entrance channels corresponding to linear and near-linear H-X-K configurations hints that these orientations may be less favored; the data also imply this, as mentioned above. It is difficult to assign explicit values for η because of the uncertainties in the curve-crossing regions of the surfaces, but it seems clear from the well positions that $\eta = 90^\circ$ should be favored, that only a fairly narrow range of η should allow reaction, and that the movement of the well toward the KX axis as F \rightarrow Cl \rightarrow Br might require that η should increase as the identity of the halogen is varied in this way. In this light the values for η calculated from our dynamic model of $\eta = 80^\circ$, 100° and 110° for H + KF, KC1 and KBr are very consistent, and provide a satisfying interpretation for the observed trends in the scattering.

At present, the interpretation of these results in terms of the electronic mechanisms for these reactions remains speculative, but the conclusion that a triangular configuration is preferred for reaction nonetheless appears reasonably well established. The n 's found suggest that the preferred angle MHX is greater than 90° , as obtained from the energy surfaces. If the one-electron picture is adopted, the results of the previous chapter show that the electron is more easily transferred to the alkali (the ground state surface becomes that in which the M atom has most of the electron) in such a configuration. For this geometry the perturbative polarization interactions cause the $M - H^+ - X^-$ surface to cross $M^+ - H - X^-$ (the zeroth order ground state); dominant terms in the polarization energy arise from the concerted action of the (partially shielded) M^+ and H^+ on X^- . Since H^+ is much closer to X^- than is M^+ in the favored configuration, the polarization corresponds roughly to a transfer of charge to H^+ while M^+ retains, in zeroth order, the electron which entered on H .

From our findings here, it appears that the impulsive model may have some relevance for reactions of this type both as a guide to interpretation of the observed data and as a clue to the possible electronic mechanism by which the reaction proceeds. In order to test the model further, data on other H atom reactions and possibly velocity analysis of the M atom product in the $H + MX$ reactions is needed.

Appendix. H Atom Impulsive Model Calculation

In this appendix is described a computer program referred to in the text to calculate LAB and c.m. product velocity vector distributions from Eq. (24) and the energy assumptions following it. Input to the program includes the masses of all the atoms, the beam velocity distributions and other kinematic parameters, the vibrational and rotational temperatures of the diatomic reactant, its fundamental vibrational frequency ω_e , and the reaction exothermicity. A unique orientation angle η and an energy fraction for impulse $f(\eta)$ is specified; or several values of η , $f(\eta)$ can be given over which the program is to average with a weighting $w(\eta)$ which uses the Entemann $T(\theta)$ function. The actual operation of the program is very similar to the conventional kinematic programs (see the appendix to Chapter III). The velocity-averaging is performed using a trapezoidal rule over a user-specified integration grid, and the transformations performed from the int system to the LAB and c.m. as described in the text and in Chapter III. The first five harmonic oscillator levels are included (see Eq. (24)). The program has been given the main deckname HIMOR (Hydrogen atom Impulsive Model with Orientation), and a listing, Table IA, follows this description. Program times on the IBM 360/65 computer average about 40 sec for complete LAB and c.m. distributions for one orientation angle.

...HIMOR FORTRAN IV LISTING...

```

C HIMOR
C CALCULATES THE VELOCITY-AVERAGED LAB AND C.M. CROSS SECTIONS FOR THE
C PRODUCT B ATOM OF THE REACTION H+BC=HC+B ASSUMING AN IMPULSIVE DIS-
C SOCIATION AT A PREFERRED ORIENTATION FOR REACTION. .A. IS THE
C ORIENTATION OF ATOM B WRT THCM=0 DEG., AND .FRC. IS THE FRACTION OF
C THE AVAILABLE TRANSLATIONAL AND CHEMICAL ENERGY ALLOWED TO CONTRIBUTE
C TO THE RADIAL DEPARTURE SPEED.
      DIMENSION P(100),THL(50),UCM(20),TH(19),DXS(19,20),FLUX(50)
      DIMENSION FABG(400),E(400),VBCX(400),VDCY(400),COSTV(400),
1 SINTV(400),FA(20),VA(20),VAPAR(5),VBCPAR(5),A(17),FRC(17),SA(17),
2 CA(17),VOJ(20),FAX(5),VCM(20),WG(17),APAR(6)
      COMMON AR,AR2,AV,F(5),D,TD,SQD,DI,VVMIN,VP,TI,CI,SI
      DATA Y/.01745329/
      VF(E)=28.95*SQRT(E/RMU)
      CALL CLOCK1
C READ INPUT PARAMETERS.
100 READ(5,1000)
      READ(5,1001) GA,GB,GC,TR,TV,OMEGA
      READ(5,1002) NVA,NVBC,NGAM,GAMMA,HWIDBC,DELTDO
      READ(5,1001) (VAPAR(I),I=1,5)
      READ(5,1001) (VBCPAR(I),I=1,5)
      READ(5,1003) NV,NTHL,DV
      READ(5,1004) (THL(I),I=1,NTHL)
      READ(5,1006) NU,DU
C CALCULATION OF NEWTON DIAGRAM WEIGHTS AND TRANSFORMATION PARAMETERS.
      CALL CNEWT(NVA,NVBC,VAPAR,VBCPAR,GA,GB,GC,NGAM,GAMMA,HWIDBC,
1 FABG,E,VBCX,VDCY,COSTV,SINTV,VA,FA)
C INITIALIZATION.
      NGRID=NVA*NVBC*NGAM
      G=GB+GC
      RMU=GB*GC/G
      AR=1.2897*SQRT(TR/RMU)
      AR2=AR**2
      AV=1.0898*SQRT(OMEGA/RMU)
      D=1.-(AV/AR)**2
      SQD=SQRT(D)
      DI=1./D
      TD=D+D
      EX=EXP(-1.4387*OMEGA/TV)
      F(1)=1.-EX
      DO 1 I=2,5
      F(I)=EX*F(I-1)
1 CONTINUE
      GHC=GA+GC
      G=G+GA
      RMU=GB*GHC/G
      GF=G/GHC
      GFC=GA/G
      GV=1.19503E-3*GA
      DO 31 I=1,NVA
      FA(I)=FA(I)*VA(I)
      VCM(I)=GFC*VA(I)

```

```

EAV=GV*VA(I)**2+DELTDO
IF(EAV.LT.0.) GO TO 315
VOJ(I)=VF(EAV)
GO TO 31
315 VOJ(I)=-VF(-EAV)
31 CONTINUE
NU1=NU+1
C WRITE INPUT PARAMETERS.
  WRITE(6,1000)
  WRITE(6,1020)
  WRITE(6,1001) GA,GB,GC,TR,TV,OMEGA,AR,AV
  WRITE(6,1021)
  WRITE(6,1002) NVA,NVBC,NGAM,GAMMA,HWIDBC,DELTDO
  WRITE(6,1022) (VAPAR(I),I=1,5)
  WRITE(6,1023) (VBCPAR(I),I=1,5)
  WRITE(6,1024)
  WRITE(6,1003) NV,NTHL,DV
  WRITE(6,1005) (F(I),I=1,5)
1000 FORMAT(5H
1001 FORMAT(8F10.3)
1002 FORMAT(3I5,5X,6F10.3)
1003 FORMAT(2I5,F10.3)
1004 FORMAT(16F5.0)
1005 FORMAT(24H0VIBRATIONAL POPULATIONS/5F10.6)
1006 FORMAT(15,F10.0)
1020 FORMAT(1H07X2HGA8X2HGB8X2HGC8X2HTR8X2HTV5X5HOMEGA8X2HAR8X2HAV)
1021 FORMAT(1H01X3HNVA1X4HNVBC1X4HNGAM10X5HGAMMA4X6HHWIDBC4X6HDELTDO)
1022 FORMAT(7H VAPAR,5F10.3)
1023 FORMAT(7H VBCPAR,5F10.3)
1024 FORMAT(5H0 NV1X4HNTHL8X2HDV)
1025 FORMAT(16H0THE TIME IS NOW,F8.3)
  FAX(1)=F(1)+F(3)/2.+.375*F(5)
  FAX(2)=2.*(F(2)-F(3))+3.*(F(4)-F(5))
  FAX(3)=2.*F(3)-4.*F(4)+7.*F(5)
  FAX(4)=4.*(F(4)/3.-F(5))
  FAX(5)=2.*F(5)/3.
  DO 17 I=1,5
17  F(I)=FAX(I)
101 CONTINUE
  TIME=CLOCK(I)
  WRITE(6,1025) TIME
C READ ORIENTATION AND IMPULSE PARAMETERS.
  READ(5,1002) NA
  IF(NA.LE.0) GO TO 100
  READ(5,1004) (A(I),FRC(I),I=1,NA)
  READ(5,1001) (APAR(I),I=1,6)
  WRITE(6,1012) (A(I),I=1,NA)
  WRITE(6,1013) (FRC(I),I=1,NA)
  WRITE(6,1026) (APAR(I),I=1,6)
1026 FORMAT(3X4HAPAR,6F10.3)
  DO 2 I=1,NA
    SA(I)=SIN(A(I)*Y)
    CA(I)=COS(A(I)*Y)
    FRC(I)=SQRT(FRC(I))
    WG(I)=THDIST(A(I),APAR)

```

```

2 CONTINUE
C CALCULATE LAB DISTRIBUTION.
DO 30 ITHL=1,NTHL
  TL=THL(ITHL)*Y
  CT=COS(TL)
  ST=SIN(TL)
  FLX=0.
  DO 20 IV=1,NV
    VL=IV*DV
    VX=VL*CT
    VY=VL*ST
    FL=0.
    DO 10 IJK=1,NGRID
      EAV=E(IJK)+DELTDO
      VVMIN=0.
      VO=VF(ABS(EAV))
      IF(EAV.GT.0.) GO TO 3
      VVMIN=VO
      VO=0.
3 CONTINUE
  UIX=VX-VBCX(IJK)
  UY=VY-VBCY(IJK)
  UI=SQRT(UIX**2+UY**2)
  VP=GFT*UI
  CI=(UIX*COSTV(IJK)-UY*SINTV(IJK))/UI
  SI=ABS(UIX*SINTV(IJK)+UY*COSTV(IJK))/UI
  TI=ATAN2(SI,CI)/Y
  SUM=0.
  DO 5 I=1,NA
    5 SUM=SUM+WG(I)*CMORSP(A(I),CA(I),SA(I),FRC(I)*VO)
    FL=FL+FABG(IJK)*(VL/UI)**2*SUM
10 CONTINUE
  P(IV)=FL
  FLX=FLX+FL
20 CONTINUE
  FLUX(ITHL)=FLX
  FLX=FLX*DVT
  WRITE(6,1010) THL(ITHL),FLX
1010 FORMAT(5H0THL=,F6.1,4X5HFLUX=,1PE11.4)
  WRITE(6,1011) (P(IV),IV=1,NV)
1011 FORMAT(1X,1P10E10.3)
30 CONTINUE
  FM=0.
  DO 305 I=1,NTHL
    IF(FM.LT.FLUX(I)) FM=FLUX(I)
305 CONTINUE
  DO 307 I=1,NTHL
    FLUX(I)=FLUX(I)/FM
307 CONTINUE
  WRITE(6,1030)
  WRITE(6,1031) (THL(I),FLUX(I),I=1,NTHL)
1030 FORMAT(28HINORMALIZED LAB DISTRIBUTION/1H06X3HTHL6X4HFLUX)
1031 FORMAT(F10.1,F10.4)
  TIME=CLOCK(I)
  WRITE(6,1025) TIME

```

```

C CALCULATE C.M. DISTRIBUTION.
DO 335 ITH=1,19
335 DXS(ITH,NU1)=0.
DM=0.
DO 50 ITH=1,19
TH(ITH)=10*(ITH-1)
IF(ITH.EQ.1) TH(ITH)=.01
IF(ITH.EQ.19) TH(ITH)=179.99
C=COS(TH(ITH)*Y)
S=SIN(TH(ITH)*Y)
DO 50 IU=1,NU
U=IU*DU
UCM(IU)=U
UX=U*C
UY=U*S
FL=0.
DO 40 J=1,NVA
VVMIN=0.
VO=VOJ(J)
IF(VO.GT.0.) GO TO 34
VVMIN=-VO
VO=0.
34 CONTINUE
UIX=VCM(J)+UX
UI=SQRT(UIX**2+UY**2)
CI=UIX/UI
SI=ABS(UY/UI)
TI=ATAN2(SI,CI)/Y
VP=GF*UI
SUM=0.
DO 35 I=1,NA
35 SUM=SUM+WG(I)*CMORSP(A(I),CA(I),SA(I),FRC(I)*VO)
FL=FL+FA(J)*(U/UI)**2*SUM
40 CONTINUE
DXS(ITH,IU)=FL
IF(DM.LT.FL) DM=FL
DXS(ITH,NU1)=DXS(ITH,NU1)+FL
50 CONTINUE
DO 60 IU=1,NU
DO 60 ITH=1,19
60 DXS(ITH,IU)=DXS(ITH,IU)/DM
DM=0.
DO 65 ITH=1,19
IF(DM.LT.DXS(ITH,NU1)) DM=DXS(ITH,NU1)
65 CONTINUE
DO 66 ITH=1,19
66 DXS(ITH,NU1)=DXS(ITH,NU1)/DM
WRITE(6,1017)
NR=1
IF(NU.GT.10) NR=2
DO 70 IR=1,NR
N1=10*(IR-1)+1
N2=MIN0(N1+9,NU)
WRITE(6,1014) (UCM(IU),IU=N1,N2)
WRITE(6,1016)

```

```

IF(N2.EQ.NU) N2=NU1
DO 70 ITH=1,19
70 WRITE(6,1015) TH(ITH),(DXS(ITH,IU),IU=N1,N2)
    WRITE(6,1018)
1012 FORMAT(13H0ORIENTATIONS,20F5.0)
1013 FORMAT(13H ENERGY FRACS,20F5.2)
1014 FORMAT(1H08X1HU,10F10.2)
1016 FORMAT(6H THCM)
1015 FORMAT(F6.1,4X,10F10.5)
1017 FORMAT(18H1C.M. DISTRIBUTION)
1018 FORMAT(1H1)
GO TO 101
END

```

C CALCULATION OF NEWTON DIAGRAM WEIGHTS AND TRANSFORMATION PARAMETERS.

SUBROUTINE CNEWT(NVA,NVBC,VAPAR,VBCPAR,GA,GB,GC,NGAM,GAMMA,HWIDBC,

- 1 FABG,E,VBCX,VBCY,COSTV,SINTV,VA,FA)
- DIMENSION FABG(400),E(400),VBCX(400),VBCY(400),COSTV(400),
- 1 SINTV(400)
- DIMENSION VA(20),VBC(20),FA(20),FBC(20),GAM(9),FG(9)
- DIMENSION VAPAR(5),VBCPAR(5)
- GF=.001195*GA*(GB+GC)/(GA+GB+GC)
- NH=NGAM/2+1
- FNH=NH
- DO 1 K=1,NGAM
- GAM(K)=GAMMA+FLOAT(K-NH)*HWIDBC/FNH
- FG(K)=1.
- 1 IF(HWIDBC.NE.0.) FG(K)=1.-ABS(GAM(K)-GAMMA)/HWIDBC
- FNH=(NVA+1)/2
- DO 2 I=1,NVA
- VA(I)=VAPAR(I)*FLOAT(I)/FNH
- 2 FA(I)=UDIST(VA(I),VAPAR)
- FNH=(NVBC+1)/2
- DO 3 J=1,NVBC
- VBC(J)=VBCPAR(1)*FLOAT(J)/FNH
- 3 FBC(J)=UDIST(VBC(J),VBCPAR)
- SUM=0.
- IJK=0
- DO 4 K=1,NGAM
- GMK=GAM(K)*.0174533
- CG=COS(GMK)
- SG=SIN(GMK)
- DO 4 I=1,NVA
- V1=VA(I)
- DO 4 J=1,NVBC
- V2=VBC(J)
- IJK=IJK+1
- V=SQRT(V1**2+V2**2-2.*V1*V2*CG)
- E(IJK)=GF*V**2
- FABG(IJK)=V*FA(I)*FBC(J)*FG(K)
- VBCX(IJK)=V2*CG
- VBCY(IJK)=V2*SG
- COSTV(IJK)=(V1-V2*CG)/V

```

• SINTV(IJK)=V2/V*SG
4 SUM=SUM+FABG(IJK)
  NGRID=NVA*NVBC*NGAM
  DO 5 IJK=1,NGRID
5 FABG(IJK)=FABG(IJK)/SUM
  RETURN
END

```

C PARAMETRIC FORM FOR VELOCITY DISTRIBUTIONS.

```

FUNCTION UDIST(U,PAR)
DIMENSION PAR(5)
R=U/PAR(1)
IF(R.GT.1.) GO TO 2
A=PAR(2)
B=PAR(3)
1 UDIST=R**A*EXP((1.-R**B)*A/B)
RETURN
2 A=PAR(4)
B=PAR(5)
GO TO 1
END

```

C CALCULATES INT C.M. INTENSITY FOR AN ORIENTED HEAVY-ATOM REACTANT
C MOLECULE ASSUMING IMPULSIVE DISSOCIATION WITH A HYDROGEN ATOM AS
C REACTING PARTNER.

```

FUNCTION CMORSP(A,CA,SA,VO)
DIMENSION E(10)
COMMON AR,AR2,AV,F(5),D,TD,SQD,DI,VVMIN,V,T,C,S
DATA Y,NTYPE/.01745329,2/
AM=A-90.
AP=A+90.
VMIN=0.
IF(AM) 1,1,2
1 IF(T.GE.AP) GO TO 4
IF(T.LT.-AM) GO TO 25
GO TO 3
2 IF(T.LE.AM) GO TO 4
IF(T.GT.(180.-AM)) GO TO 25
GO TO 3
25 VMIN=V*ABS(C*CA-S*SA)
3 VMAX=V*ABS(C*CA+S*SA)
IF(VVMIN.LE.0.) GO TO 29
IF(VVMIN.GT.VMAX) GO TO 4
IF(VVMIN.GT.VMIN) VMIN=VVMIN
GO TO 295
29 CONTINUE
IF(VO.GT.VMAX) GO TO 4
IF(VO.GT.VMIN) VMIN=VO
295 CONTINUE
FRM=V**2/S*EXP((VO**2/D-V**2)/AR2)
X1=SQD*(VMIN-VO/D)/AV

```

```

X2=SQD*(VMAX-V0/D)/AV
E(1)=.886227/D*(ERF(X2)-ERF(X1))
GO TO (31,32),NTYPE
31 CMORSP=FRM*E(1)
RETURN
32 CONTINUE
EX1=EXP(-X1**2)
EX2=EXP(-X2**2)
X0=(DI-1.)*V0/AV
X1=X1/SQD+X0
X2=X2/SQD+X0
X1I=X1*EX1
X2I=X2*EX2
E(2)=X0*E(1)-(EX2-EX1)/TD
DO 35 I=3,9
E(I)=X0*E(I-1)+((I-2)*E(I-2)-X2I+X1I)/TD
X1I=X1I*X1
X2I=X2I*X2
35 CONTINUE
36 CONTINUE
CMORSP=0.
DO 38 I=1,5
38 CMORSP=CMORSP+F(I)*E(2*I-1)
CMORSP=CMORSP*FRM
RETURN
4 CMORSP=0.
RETURN
END

```

C PARAMETRIC GAUSSIAN FORM FOR C.M. ANGULAR DISTRIBUTIONS.

```

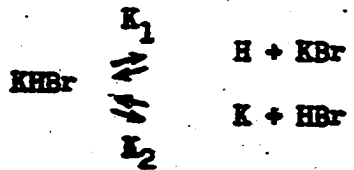
FUNCTION THDIST(THCM,THPAR)
DIMENSION THPAR(6)
X1=THCM-THPAR(1)
X2=THCM-THPAR(2)
IF(X1.GE.0..AND.X2.LE.0.) GO TO 2
IF(X2.GT.0.) GO TO 3
H=THPAR(3)
C=THPAR(4)
X=X1
GO TO 4
2 THDIST=1.
RETURN
3 H=THPAR(5)
C=THPAR(6)
X=X2
4 THDIST=(1.-C)*EXP(-.6931472 *(X/H)**2)+C
RETURN
END

```

GENERAL APPENDIX:
POSSIBLE OBSERVABILITY OF KHBr

The potential surface calculations of Chapter VI indicate that a nearly linear K-H-Br complex may be stable with respect to H + KBr by as much as 80 kcal/mole (see Fig. 5, Chapter VI). A simple electrostatic calculation, using the known H atom polarizability for the charge-induced-dipole interactions and repulsions scaled from those for H with the isoelectronic rare gases, gives a well depth of 23 kcal, also for a triangular configuration. This indicates that the electronic calculation may not be too unreasonable. The experimental crossed-beam findings for the reaction H + KBr of Chapter V as interpreted through the dynamical model of Chapter VII imply that an approach of H broadside on KBr is indeed favored for reaction. Observation of a collision complex would not be possible under the single-collision conditions of a beam experiment, since the "complex" could not hold together long enough even to produce the characteristic forward-backward center-of-mass peaking because of the high-frequency motion of H. Under higher pressure conditions, however, where additional collisions might allow K-H-Br to exist as a stable species, we might hope to observe it spectroscopically. We present here some equilibrium calculations which demonstrate the degree of observability of this species under appropriate conditions.

We choose a vessel temperature of 1000°K to keep the KBr in the vapor state. The total pressure is assumed to consist initially of 1 torr each of H and KBr. In general we must take into account the equilibria



The equilibrium constants are calculated from the partition functions and the standard energy changes for each reaction. For these purposes the K-H-Br complex was assumed to be linear, and its three vibrational frequencies were taken as 213 cm^{-1} (symmetric stretch), 2650 cm^{-1} (asymmetric stretch) and 1000 cm^{-1} (bending). The well depth for the complex was varied from 80 to 5 kcal/mole with respect to H + KBr. Table I shows the resulting K's; it may be observed that K_2 is always smaller than K_1 by more than an order of magnitude. Neglecting the partial pressures of K and HBr, therefore, the fraction α of the total pressure due to KHBr is

$$\alpha = (X + 1 - \sqrt{2X + 1})/X ,$$

where $X = p_0/K_1$ and p_0 is the initial total pressure, 2 torr.

Table I gives the α 's also. According to these calculations, if the well depth were only 5 kcal/mole, roughly 10^{-9} torr of K-H-Br should be present in the vessel, probably undetectable. If the well depth actually is 80 kcal, K-H-Br should be formed exclusively under these conditions.

Table I. Equilibrium Calculations for KHBr^a

Well depth kcal/mole	K_1	atm	K_2	α
80	3.2×10^{-12}	1.2×10^{-13}		1.000
40	1.8×10^{-3}	5.4×10^{-5}		0.33
20	33.	1.2		2.5×10^{-6}
5	5.9×10^4	2.1×10^3		1.4×10^{-9}

^aFor a temperature of 1000°K and total initial pressure of 2 torr.